ISTANBUL TECHNICAL UNIVERSITY ★ GRADUATE SCHOOL OF SCIENCE ENGINEERING AND TECHNOLOGY

COMPARATIVE STUDY OF COMBUSTION MODES IN INTERNAL COMBUSTION ENGINES USING CFD SIMULATIONS

M.Sc. THESIS

Mobin MAJIDI DOLAT ABADI

Department of Mechanical Engineering

Automotive Engineering Program

DECEMBER 2016

ISTANBUL TECHNICAL UNIVERSITY ★ GRADUATE SCHOOL OF SCIENCE ENGINEERING AND TECHNOLOGY

COMPARATIVE STUDY OF COMBUSTION MODES IN INTERNAL COMBUSTION ENGINES USING CFD SIMULATIONS

M.Sc. THESIS

Mobin MAJIDI DOLAT ABADI
(503131713)

Department of Mechanical Engineering

Automotive Engineering Program

Thesis Advisor: Prof. Dr. Cem SORUŞBAY

DECEMBER 2016

İSTANBUL TEKNİK ÜNİVERSİTESİ ★ FEN BİLİMLERİ ENSTİTÜSÜ

İÇTEN YANMALI MOTORLARDA FARKLI YANMA MODLARININ SAD YAKLAŞIMI KULLANARAK KARŞILAŞTIRILMASI

YÜKSEK LİSANS TEZİ

Mobin MAJIDI DOLAT ABADI
(503131713)

Makine Mühendisliği Anabilim Dalı

Otomotiv Programı

Tez Danışmanı: Prof. Dr. Cem SORUŞBAY

ARALIK 2016

Mobin MAJIDI DOLAT ABADI, a M.Sc. student of ITU Graduate School of Science Engineering and Technology 503131713 successfully defended the thesis entitled "COMPARATIVE STUDY OF COMBUSTION MODES IN INTERNAL COMBUSTION ENGINES USING CFD SIMULATIONS", which he prepared after fulfilling the requirements specified in the associated legislations, before the jury whose signatures are below.

Thesis Advisor :	**Prof. Dr. Cem SORUŞBAY** Istanbul Technical University	.....
Jury Members :	**Prof. Dr. Muammer ÖZKAN** Yıldız Technical University	.....
	Assist. Prof. Hikmet ARSLAN Istanbul Technical University	.....
		.....

Date of Submission : **22 January 2017**
Date of Defense : **22 December 2016**

To my dear family,

FOREWORD

I would like to express my gratitude to my advisor Prof. Dr. Cem SORUŞBAY for his wonderful guidance and trusting me to go in a research direction of great personal interest. He contributed actively in all steps of this research from analyzing data to writing paper, and finally preparing this thesis.
I am very thankful to Res.Assist. Muhammet AYDIN and Res.Assist. Öncel ÖNCÜOĞLU for their valuable technical contributions and advices.
Finally, I would like to express my thanks and appreciation to my parents and siblings for their encouragement, extensive support and patience as I pursue this degree.

December 2016 Mobin MAJIDI DOLAT ABADI

TABLE OF CONTENTS

Page

FOREWORD ..... **ix**
TABLE OF CONTENTS ..... **xi**
ABBREVIATIONS ..... **xv**
SYMBOLS ..... **xvii**

LIST OF TABLES ..... **xix**

LIST OF FIGURES ..... **xxiii**
SUMMARY ..... **xxix**
ÖZET ..... **xxxi**
1. INTRODUCTION **1**
1.1 Purpose of Thesis 2
1.2 Literature Review 2
1.2.1 Historical background 2
1.2.2 Advanced combustion models 3
1.2.2.1 Low temperature combustion 3
1.2.2.2 Homogeneous charge compression ignition (HCCI) 6
1.2.2.3 Premixed charge compression ignition (PCCI) 12
2. COMPUTATIONAL METHOD FOR ENGINE SIMULATION **23**
2.1 Introduction 23
2.2 CFD Simulation Methodology Using AVL FIRE® 24
2.2.1 Pre-processing 24
2.2.2 Flow solver and solution algorithm 25
2.2.3 Post-processing 28
2.3 Computational Meshes 29
2.4 Basic Fluid Mechanical Equations 32
2.4.1 Conservation equations 32
2.4.1.1 Mass conservation (continuity equation) 32
2.4.1.2 Momentum equation 35
2.4.1.3 Energy equation 37
2.4.1.4 Species transport 38
2.4.2 Equations of state 40
2.5 Turbulence 41
2.5.1 Turbulence modeling 41
2.5.2 k-ε model 43
2.6 Combustion Models 45
2.6.1 SI combustion 45

2.6.1.1 Coherent flame model (flame surface density model) 46
2.6.1.2 Extended coherent flame models (ECFM) 48
2.6.2 CI combustion..... 51
2.6.2.1 ECFM-3Z model..... 52
2.6.2.2 Eddy breakup model 53
2.7 Multiphase Spray Module 55
2.7.1 Basic equations 56
2.7.1.1 Momentum..... 56
2.7.2 Submodels 58
2.7.2.1 Evaporation..... 58
2.7.2.2 Break-up model 60
2.7.2.3 Turbulence dispersion model 62
2.7.2.4 Spray-wall interaction..... 63
2.8 Ignition Model 65
2.8.1 Spherical model 65
2.9 Pollutant Model 65
2.9.1 NO model 66
2.9.2 Soot model..... 68
3. COMPARATIVE STUDY; VALIDATION, PARAMETRIC STUDY AND MODIFICATION TO NATURAL GAS FUELED HCCI ENGINE..... 73
3.1 Experimental Data 74
3.2 Pre-Processing Of Simulation 77
3.2.1 Meshing 77
3.2.2 Operating mode 81
3.2.3 Boundary conditions..... 82
3.2.4 Initial conditions 83
3.2.5 Solver control 85
3.2.6 Turbulence model 86
3.2.7 Combustion model..... 86
3.2.8 Ignition 87
3.2.9 Pollutant model..... 88
3.2.10Summary..... 88
3.3 Simulation Results And Validation 91
3.3.1 In-cylinder pressure comparison 92
3.3.2 Rate of heat release comparison 94
3.3.3 Engine specific output 99
3.3.4 Specific fuel consumption comparison..... 103
3.3.5 NO_x emissions..... 106
3.4 Parametric Study 107
3.4.1 Effect of EGR 108
3.4.1.1 In-cylinder pressure 108
3.4.1.2 In-cylinder mean temperature..... 109
3.4.1.3 Rate of heat release and accumulated heat release 111
3.4.1.4 Exhaust emissions..... 113
3.4.1.5 Engine specific output..... 118

3.4.2 Effect of equivalence ratio 121
3.4.2.1 In-cylinder pressure 122
3.4.2.2 In-cylinder mean temperature 123
3.4.2.3 Rate of heat release and accumulated heat release 124
3.4.2.4 Exhaust emissions 126
3.4.2.5 Engine specific output 131
3.4.3 Effect of spark timing 133
3.4.3.1 Maximum brake torque 133
3.4.3.2 In-cylinder pressure 134
3.4.3.3 In-cylinder mean temperature 136
3.4.3.4 Rate of heat release and accumulated heat release 137
3.4.3.5 Exhaust emissions 139
3.4.3.6 Engine specific output 143
3.5 Simulation Results By Using Natural Gas As Fuel 146
3.5.1 Rate of heat release and accumulated heat release comparison 148
3.5.2 In-cylinder mean temperature and in-cylinder pressure comparison 151
3.5.3 Emissions 152
3.5.4 Engine specific output 155
3.6 Natural Gas fueled HCCI Combustion Modeling 157
3.6.1 Introduction 157
3.6.2 Pre-processing of simulation 160
3.6.3 Simulation results 165
4. SIMULATION OF LOW TEMPERATURE COMBUSTION DIESEL ENGINE 181
4.1 Introduction 181
4.2 Conventional DI Diesel Engine Modeling 186
4.2.1 Pre-processing of simulation 186
4.2.2 Simulation results 196
4.2.2.1 Engine load 197
4.2.2.2 Combined effects of EGR and engine load 205
4.3 Simulation of Low Temperature Combustion Diesel Engine Using Double Injections 219
4.3.1 Effect of injection ratio 219
4.3.2 Effect of EGR 229
4.3.3 Effect of first injection duration with different EGR ratios 231
5. CONCLUSIONS AND RECOMMENDATIONS 239
5.1 Conclusion 239
5.2 Recommendations And Future Work 258

REFERENCES 259
CURRICULUM VITAE 287

ABBREVIATIONS

AFR : Air to Fuel Ratio
ATDC : After Top Dead Center
BC : Boundary Conditions
BDC : Bottom Dead Center
BMEP : Brake Mean Effective Pressure
BSFC : Brake Specific Fuel Consumption
BTDC : Before Top Dead Center
CA : Crank Angle
CAD : Crank Angle Degrees
CFD : Computational Fluid Dynamics
CFM : Coherent Flame Model
CI : Compression Ignition
CNG : Compressed Natural Gas
CO : Carbon Monoxide
CO_2 : Carbon Dioxide
CR : Compression Ratio
DI : Direct Injection
ECFM : Extended Coherent Flame model
ECFM-3Z : 3-Zone Extended Coherent Flame Model
EGR : Exhaust Gas Recirculation
ESE : Engine Simulation Environment
EVC : Exhaust Valve Closing
EVO : Exhaust Valve Opening
HC : Hydrocarbons
HCCI : Homogeneous Charge Compression Ignition
HRR : Heat Release Rate
HTHR : High Temperature Heat Release
ICE : Internal Combustion Engine
IMEP : Indicated Mean Effective Pressure
ISFC : Indicated Specific Fuel Consumption
ITHR : Intermediate Temperature Heat Release
IVC : Intake Valve Closing
IVO : Intake Valve Opening
LES : Large Eddy Simulation
LHV : Lower Heating Value
LTC : Low Temperature Combustion
LTHR : Low Temperature Heat Release
MBT : Maximum Brake Torque
MK : Modulated Kinetics
NG : Natural Gas

NO_x : Nitrogen Oxides
PCCI : Premixed Charge Compression Ignition
PFI : Port Fuel Injection
PM : Particulate Matter
PREDIC : PREmixed lean DIesel Combustion
RANS : Reynolds-Averaged Navier-stokes
RPM : Revolutions Per Minute
SI : Spark Ignition
SIMPLE : Semi-Implicit Method for Pressure-Linked Equations
SOC : Start Of Combustion
SOFI : Start Of First Injection
SOI : Start Of Injection
SOS : Start Of Spark
SOSI : Start Of Second Injection
TDC : Top Dead Center
TKE : Turbulent Kinetic Energy
UHC : Unburned Hydrocarbons
VVT : Variable Valve Timing

SYMBOLS

ϕ	: Equivalence ratio
K	: Kelvin
T	: Temperature
t	: Time
d	: Diameter
u	: Vector velocity in Cartesian space
u, v, w	: Velocity vector components in a Cartesian coordinate system
ρ	: Density
∇	: Vector operator, gradient, nabla
$\nabla \cdot \mathbf{A}$	: Divergence of a vector field **A**
Nu	: Nusselt number
Le	: Lewis number
Pr	: Prandtl number
Sc	: Schmidt number
Re	: Reynolds number
We	: Weber number
Oh	: Ohnesorge number
Kn	: Knudsen number
τ_a	: Break-up time
τ	: Shear stress
Λ	: Wavelength
ψ	: Angle
μ	: Molecular viscousity
C_D	: Drag coefficient
C_P	: Cunningham correction factor
c_p	: Specific heat capacity at constant pressure
c_v	: Specific heat capacity at constant volume
e	: Specific internal energy
E	: Energy
f	: Body force
F	: Force
h	: Enthalpy
k	: Specific turbulent kinetic energy
fu	: Fuel
tot	: Total
D_i	: Diffusion coefficient for species i
μ_t	: Turbulent viscosity
R	: Specific gas constant
l	: Length
S_L	: Laminar burning velocity

σ	: Flame surface density
ω_L	: Mean laminar fuel consumption rate per unit surface
m	: Mass
S_{ij}	: Shear tensor
S_k, S_ε	: Source term
γ	: Ratio of specific heats of in-cylinder gases
M	: Torque
N	: Engine speed
n_R	: Number of crank revolutions for each power stroke
p	: Pressure
W_i	: Indicated work per cycle
p_{mi}	: Mean indicated pressure
p_{me}	: Mean effective pressure
P_i	: Indicated power
P_e	: Effective power
P_f	: Friction power
$\dot{m}_a$	: Air mass flow rate
$\dot{m}_f$	: Fuel mass flow rate
Q_m	: Energy content of mixture
$\dot{Q}$	: Convective heat flux
$\dot{q}$	: Heat flux per unit area
α	: Convective heat transfer coefficient
V	: Volume
m_f	: Fuel mass
y^+	: Non-dimensional distance from wall
x, y, z	: Coordinates in a Cartesian system
ε	: Dissipation rate of turbulent kinetic energy
η	: Efficiency
η_v	: Volumetric efficiency
η_m	: Mechanical efficiency
η_{com}	: Combustion efficiency
th	: Thermal
λ	: Air-fuel ratio
V_d	: Displacement volume

LIST OF TABLES

1.1 Comparison of Otto four-stroke and Otto-Langen engines, adapted from (Heywood, 1988). ... 3

2.1 Coefficients of standard k–ε-model. ... 44

2.2 Parameters used in laminar burning velocity Eq.(2.33). ... 47

3.1 Modified test engine specifications (Doğru, 2013). ... 75

3.2 Experimental data (Doğru, 2013). ... 76

3.3 Computational grids specification used for sector mesh generation... 77

3.4 Time discretization ... 81

3.5 Utilized boundary conditions. ... 82

3.6 Initial conditions of baseline simulations. ... 85

3.7 Required inputs for spherical ignition model. ... 87

3.8 SI engine baseline simulation set-up. ... 88

3.9 Experimental and simulated peak cylinder pressures and related crank angles. ... 94

3.10 SOC and combustion duration of experimental and simulations. ... 99

3.11 Engine specific output. ... 100

3.12 Calculated and measured fuel mass flow rates. ... 105

3.13 Peak cylinder pressures and related crank angles with different EGR rates. ... 109

3.14 Peak cylinder temperatures and related crank angles with different EGR rates. ... 110

3.15 Start of combustion position and combustion duration with different EGR rates. ... 112

3.16 Engine specific output with different EGR rates. ... 120

3.17 Peak cylinder pressures and related crank angles with different equivalence ratios. ... 123

3.18 Peak cylinder temperatures and related crank angles with different equivalence ratios. ... 124

3.19 Start of combustion position and combustion duration with different equivalence ratios. ... 126

3.20 Engine specific output with different equivalence ratios. 133
3.21 Peak cylinder pressures and related crank angles with different spark timings. 135
3.22 Start of combustion position and combustion duration with different spark timing. 138
3.23 Engine specific output with different spark timing. 145
3.24 Properties of natural gas and gasoline. 147
3.25 Amount of intake air and supplied fuel. 148
3.26 LHV of fuels and energy content of mixtures. 150
3.27 Start of combustion position and combustion duration of gasoline and natural gas engines. 151
3.28 Peak cylinder pressures and related crank angles of natural gas and gasoline combustion. 152
3.29 Soot and unburned hydrocarbon emissions of natural gas and gasoline engines. 155
3.30 Gasoline and natural gas engine specific output. 157
3.31 Verified SI engine and modified HCCI engine specifications 161
3.32 Computational grid specification used for sector mesh generation. ... 161
3.33 Time discretization 162
3.34 Utilized boundary conditions for HCCI engine. 163
3.35 Initial conditions of HCCI engine simulation. 164
3.36 Peak cylinder pressures and related crank angles for different engines. 167
3.37 Start of combustion position and combustion duration for different engines. 169
3.38 NO_x emissions of different engines. 174
3.39 Unburned hydrocarbon emissions of simulated engines 176
3.40 Specific outputs of different engines. 178
4.1 Simulated diesel engine specifications 187
4.2 Computational grids specification used for diesel engine sector mesh generation. 187
4.3 Time discretization 188
4.4 Utilized boundary conditions for simulation of diesel engine. 189
4.5 Initial conditions for baseline simulation of diesel engine. 190
4.6 Injected fuel mass and injection timing. 191
4.7 Adopted submodels for spray modeling. 192

4.8 Diesel engine baseline simulation set-up. 192
4.9 Injected fuel mass for different loads. 197
4.10 Ignition delay and premixed combustion duration under different loads. 199
4.11 Engine specific output for different loads. 204
4.12 Overall equivalence ratio of mixture with different EGR rates. 205
4.13 Peak in-cylinder pressures with different EGR rates. 207
4.14 Ignition delay with different EGR rates. 207
4.15 Engine specific output with different EGR ratios (Medium load). 215
4.16 Engine Specific output with with different EGR ratios (Low load). 216
4.17 Investigated injection ratios. 220
4.18 Peak cylinder pressures and related crank angles of different injection ratios. 221
4.19 Specific engine output with different injection ratios. 228
5.1 Optimum results. 257

LIST OF FIGURES

2.1 Segregated SIMPLE solution procedure for Pressure-Based solver (Versteeg and Malalasekera, 2007). 28

2.2 Rate of mass flows into the fluid element (Versteeg and Malalasekera, 2007). 33

2.3 Stress components on three faces of fluid element (Versteeg and Malalasekera, 2007). 36

2.4 Different WAVE break-up models (AVL, 2013). 61

3.1 Original piston (left) and modified piston (right) geometries (Doğru, 2013). 74

3.2 Grid resolutions. 78

3.3 Effects of grid resolutions on in-cylinder pressure. 79

3.4 Generated 3D sector mesh used in SI engine simulations (72° sector). 80

3.5 Boundary conditions (schematic). 83

3.6 In-cylinder pressure comparison between experimental and simulation results @1500[rpm]. 93

3.7 In-cylinder pressure comparison between experimental and simulation results @1660[rpm]. 93

3.8 In-cylinder pressure comparison between experimental and simulation results @1800[rpm]. 94

3.9 Heat release rate comparison between experimental and simulation results @1500[rpm]. 95

3.10 Heat release rate comparison between experimental and simulation results @1660[rpm]. 95

3.11 Heat release rate comparison between experimental and simulation results @1800[rpm]. 96

3.12 Accumulated heat release comparison between experimental and simulation results @1500[rpm]. 96

3.13 Accumulated heat release comparison between experimental and simulation results @1660[rpm]. 97

3.14 Accumulated heat release comparison between experimental and simulation results @1800[rpm]. 97

3.15 Brake mean effective pressure comparison between experimental and simulation results. 101
3.16 Effective power comparison between experimental and simulation results. 102
3.17 Effective torque comparison between experimental and simulation results. 102
3.18 Supplied and burnt fuel mass fraction of case-44 103
3.19 Supplied and burnt fuel mass fraction of case-30. 104
3.20 Supplied and burnt fuel mass fraction of case-35. 104
3.21 Brake specific fuel consumption comparison between experimental and simulation results. 105
3.22 NO_x emissions comparison between experimental and simulation results. 106
3.23 The effect of EGR on in-cylinder pressure. 109
3.24 The effect of EGR on mean temperature. 111
3.25 The effect of EGR on rate of heat release. 112
3.26 The effect of EGR on accumulated heat release. 113
3.27 The effect of EGR on intake oxygen. 114
3.28 The effect of EGR on NO_x emissions. 115
3.29 **(Cont.)** In-cylinder distributions of temperature and NO_x emissions with different EGR @ 20 [CAD] ATDC. 116
3.30 The effect of EGR on soot emissions. 117
3.31 The effect of EGR on CO emissions. 118
3.32 The effect of EGR on HC emissions. 119
3.33 The effect of EGR on IMEP and indicated power. 120
3.34 The effect of EGR on ISFC. 121
3.35 The effect of equivalence ratio on in-cylinder pressure. 122
3.36 The effect of equivalence ratio on mean temperature. 123
3.37 The effect of equivalence ratio on rate of heat release. 125
3.38 The effect of equivalence ratio on accumulated heat release. 125
3.39 The effect of equivalence ratio on NO_x emissions. 127
3.40 **(Cont.)** In-cylinder distributions of temperature and NO_x emissions with different equivalence ratios @ 20 [CAD] ATDC. 128
3.41 The effect of equivalence ratio on soot emissions. 129
3.42 The effect of equivalence ratio on CO emissions. 130

3.43 The effect of equivalence ratio on HC emissions. 130
3.44 The effect of equivalence ratio on IMEP and indicated power. 131
3.45 The effect of equivalence ratio on ISFC. 132
3.46 The effect of spark timing on brake torque. 134
3.47 The effect of spark timing on in-cylinder pressure. 135
3.48 The effect of spark timing on mean temperature. 136
3.49 The effect of spark timing on rate of heat release. 137
3.50 The effect of spark timing on accumulated heat release. 138
3.51 The effect of spark timing on NO_x emissions. 139
3.52 **(Cont.)** In-cylinder distributions of temperature and NO_x emissions in 20 [CAD] ATDC for different spark timings. 141
3.53 The effect of spark timing on soot emissions. 141
3.54 The effect of spark timing on CO emissions. 142
3.55 The effect of spark timing on HC emissions. 143
3.56 The effect of spark timing on IMEP and indicated power. 144
3.57 The effect of spark timing on ISFC. 144
3.58 Mass fraction of burnt gasoline and natural gas engines. 149
3.59 Heat release rate of gasoline and natural gas engines. 149
3.60 Accumulated heat release of gasoline and natural gas engines. 150
3.61 Mean in-cylinder temperature of gasoline and natural gas engines. 151
3.62 In-cylinder pressure of gasoline and natural gas engines. 152
3.63 NO_x and CO emissions of gasoline and natural gas engines. 153
3.64 In-cylinder distributions of temperature and NO_x emissions for natural gas and gasoline fueled SI engines in different crank angles. 154
3.65 IMEP and indicated power of gasoline and natural gas engines. 156
3.66 ISFC of gasoline and natural gas engines. 156
3.67 A comparison of SI, CI and HCCI engines, adapted from (William and Charles, 2011). 159
3.68 Grid resolution. 162
3.69 Generated 3D sector mesh used in HCCI engine simulations (72° sector). 162
3.70 In-cylinder pressure of SI-Gasoline, SI-NG and HCCI-NG engines. 166
3.71 In-cylinder mean temperature of SI-Gasoline, SI-NG and HCCI-NG engines. 167
3.72 Heat release rate of SI-Gasoline, SI-NG and HCCI-NG engines. 169

3.73 Accumulated heat release of SI-Gasoline, SI-NG and HCCI-NG engines. 170
3.74 IMEP and indicated power of SI-Gasoline, SI-NG and HCCI-NG engines. 171
3.75 ISFC of SI-Gasoline, SI-NG and HCCI-NG engines. 172
3.76 P-V diagram of ideal Otto-cycle (NASA, 2015)..... 173
3.77 LTC, SI, conventional CI and HCCI combustion regions on a ϕ-T map with NO_x -soot contour, adapted from (Kamimoto and Bae, 1988; Dec, 2009)..... 175
3.78 ϕ-T plot of HCCI-NG engine. 175
3.79 In-cylinder distributions of temperature and unburned equivalence ratio for HCCI-NG engine. 177
4.1 Identifying diesel combustion phases, adapted from (Heywood, 1988). 183
4.2 Conceptional model of diesel combustion, (Dec, 1997; Flynn et al., 1999). 184
4.3 LTC, SI and conventional CI combustion regions on a ϕ-T map with NO_x -soot contour, (Kamimoto and Bae, 1988). 186
4.4 Grid resolution. 188
4.5 Generated 3D sector mesh used in simulations (72° sector). 188
4.6 The effect of injection quantity on rate of heat release..... 198
4.7 The effect of injection quantity on accumulated heat release..... 198
4.8 The effect of injection quantity on mean combustion temperature. ... 199
4.9 The effect of injection quantity on NO_x emissions..... 200
4.10 In-cylinder distributions of temperature and NO_x emissions for different loads @ 2 [CAD] ATDC 201
4.11 The effect of injection quantity on soot emissions. 202
4.12 ISFC of different cases..... 202
4.13 ϕ-T plots with different injection quantities. 203
4.14 The effect of EGR on in-cylinder pressure of Case-11..... 206
4.15 The effect of EGR on in-cylinder pressure of Case-12..... 206
4.16 The effect of EGR on in-cylinder temperature of Case-11. 208
4.17 The effect of EGR on in-cylinder temperature of Case-12. 209
4.18 The effect of EGR on heat release rate of Case-11..... 209
4.19 The effect of EGR on heat release rate of Case-12..... 210

4.20 The combined effect of EGR and injection quantity on NO_x emissions. 211
4.21 The combined effect of EGR and injection quantity on soot emissions. 212
4.22 The effect of EGR on IMEP and indicated power of Case-11 213
4.23 The effect of EGR on IMEP and indicated power of Case-12 214
4.24 The combined effect of EGR and injection quantity on ISFC. 215
4.25 ϕ-T plots of medium load with different EGR ratios. 217
4.26 ϕ-T plots of low load with different EGR ratios. 218
4.27 Injected fuel mass. 221
4.28 The effect of injection ratio on in-cylinder pressure. 222
4.29 The effect of injection ratio on temperature 222
4.30 The effect of injection ratio on rate of heat release 223
4.31 The effect of injection ratio on accumulated heat release. 224
4.32 In-cylinder distributions of temperature and NO_x emissions with different injection ratios @ 2 [CAD] ATDC 225
4.33 The effect of injection ratio on NO_x emissions. 226
4.34 The effect of injection ratio on soot emissions. 226
4.35 The effect of injection ratio on IMEP and indicated power. 227
4.36 The effect of injection ratio on ISFC. 228
4.37 The effect of EGR on NO_x emissions. 229
4.38 The effect of EGR on soot emissions. 230
4.39 The effect of EGR on indicated power. 230
4.40 The effect of EGR on ISFC. 231
4.41 The effect of first injection duration on mean temperature with 5% EGR 233
4.42 The effect of first injection duration on NO_x emissions with 5% EGR 234
4.43 The effect of first injection duration on NO_x emissions with 10% EGR 234
4.44 The effect of first injection duration on soot emissions with 5% EGR. 235
4.45 The effect of first injection duration on soot emissions with 10% EGR 235
4.46 The effect of first injection duration on indicated power with 5% EGR 236

4.47 The effect of first injection duration on indicated power with 10% EGR..... 236
4.48 The effect of first injection duration on ISFC with 5% EGR. 237
4.49 The effect of first injection duration on ISFC with 10% EGR. 237

COMPARATIVE STUDY OF COMBUSTION MODES IN INTERNAL COMBUSTION ENGINES USING CFD SIMULATIONS

SUMMARY

Internal combustion engines did not become a practical reality until the 1860s. Because of wide-spreading markets of internal combustion engines, researches and developments of IC engines, maybe less fundamental, have continued ever since to improve engine efficiency and exhaust emissions.

In fact, both of SI and CI engines have their own advantages and disadvantages. Although CI engine has higher compression ratio which results in a higher thermal efficiency and better fuel economy than SI engine, diesel engine operates in more limited speed range and produces higher levels of nitrogen oxides (NO_x) and particulate matter (PM) emissions.

Nowadays, decreasing of energy resources, high fuel price and environmental protection led the researchers to design the engines which maximize power and fuel economy while minimizing exhaust emissions. In order to achieve these goals some advanced combustion strategies such as Low Temperature Combustion (LTC), Homogeneous Charge Compression Ignition (HCCI) and Premixed Charge Compression Ignition (PCCI) have been introduced. Advanced combustion concepts are receiving increased attention for the reason that they can be a practical solution used in piston engines to meet the increasingly stringent emission regulations. In addition to the need for advanced combustion models to be utilized in future engines, the ability of using alternative fuels such as methane in these concepts is indispensable.

Computational Fluid Dynamics (CFD) tools provide a detailed description of the fluid flow and transport phenomena occurring in the system, employing simplified kinetic mechanisms in order to develop current high computational effort. Noticeable advantages of CFD make it a promising way to realize flow patterns that are difficult, expensive or impossible to study using experimental techniques. Indeed, in parallel with novel combustion concepts and alternative fuel usage, 3D computational fluid dynamics simulation of in-cylinder spray formation/propagation, combustion and pollutant formation processes is receiving increasing attention during engine and combustion system development. Nowadays, CFD has been successfully defined for the calculation of fluid flow, mixture formation and combustion in internal combustion engines as a supplementary tool to in-cylinder pressure analysis, combustion diagnostics and optical mixture formation.

In this study, commercially available AVL FIRE® CFD code is used to perform the simulations. Boundary fitted computational grids are generated by Engine Simulation Environment Diesel (ESE Diesel) tool, then in-cylinder processes are simulated via Workflow Manager tool. The combustion chamber of engine is considered as a closed thermodynamic system and the governing equations for unsteady, compressible, turbulent flow and thermal fields are solved from the intake valve closing (IVC) to exhaust valve opening (EVO).

In the first part of current study, simulated SI engine is validated by available

experimental test results. To understand the grid sensitivity of multi-dimensional engine CFD, five different grid resolutions are adopted and compared. The selected mesh represents a compromise between computational time and accuracy, but is found to give adequately grid independent results. In favor of assessing the predictive accuracy and reliability of the CFD simulations, it is critical to perform validation studies over various engine operating conditions. In this regard, in-cylinder pressure, heat release rate, specific fuel consumption, brake mean effective pressure, brake power and emissions predictions are compared with the measured experimental results at three different engine speeds of 1500[rpm], 1660 [rpm] and 1800[rpm]. The results of the simulation are in good qualitative and quantitative agreement with the corresponding experimental data. Then a comprehensive parametric study of individual influences of exhaust gas recirculation, equivalence ratio and spark timing on the performance and exhaust emissions of the simulated gasoline engine is investigated at a fixed engine speed of 1500 [rpm]. In order to carry on the study, additional simulations are done by applying the natural gas (methane) as an alternative fuel and the performance and emission characteristics of CNG engine are compared with those of validated gasoline engine.

Since the primary focus of this research is the examination of different combustion strategies for reducing NO_x and soot emissions along with engine performance improvement, in addition to conventional natural gas fueled SI engine, a low temperature combustion strategy known as Homogeneous Charge Compression Ignition (HCCI) is developed by using natural gas as fuel. In order to prepare a reasonable comparison, the natural gas fueled HCCI engine is considered to operate under the same load of verified gasoline engine.

Additionally in the second part of this research, first a conventional single cylinder diesel engine under full load condition at engine speed of 1500[rpm] is simulated with AVL FIRE® CFD code, and then the individual and combined effects of EGR and engine load on combustion and engine-out emissions are studied. Moreover, in order to achieve the partially premixed compression ignition and lower temperature combustion of diesel engine, the effects of multiple injection strategies including injection ratio and first injection duration on performance and exhaust emissions of diesel engine are investigated.

İÇTEN YANMALI MOTORLARDA FARKLI YANMA MODLARININ SAD YAKLAŞIMI KULLANARAK KARŞILAŞTIRILMASI

ÖZET

İçten yanmalı motorlar temel olarak buji ateşlemeli ve sıkıştırmalı ateşlemeli motorlar olarak iki gruba ayrılmaktadır. Uzun bir tarihsel geçmişe sahip olan bu motorların günümüzde hala teknolojik olarak geliştirilmesine yönelik birçok çalışma yapılmaktadır. Ancak içten yanmalı motorları geliştirmek, yeni teknolojiler üretmek adına yapılan tasarım geliştirme ve test çalışmaları uzun vakitler alan, yüksek maliyet ve işçilik gerektiren zahmetli çalışmalardır. Bu zahmetli çalışmaların bir ön adımı olması ve doğabilecek sorunları önceden tahmin etmek amacıyla gerçeğe yakın fiziksel ve matematiksel modeller oluşturulmakta ve bu modeller her geçen gün gelişmeye devam etmektedir. İçten yanmalı motorlarda sonlu hacimler yöntemini kullanan bu modeller hesaplamalı akışkanlar dinamiğine, yanma fiziği ve kimyasına dayanmaktadır. Yanma odası sonlu hacimlere bölünerek kütlenin, momentumun ve enerjinin korunum denklemleri bu küçük hacimlere uygulanmaktadır.

Hesaplamalı akışkanlar dinamiği (CFD) için geliştirilmiş yazılımlar son zamanlarda içten yanmalı motorlardaki akış, ısı transferi, yanma ve emisyon problemlerinin çözümü için matematiksel modelleme sırasında sıklıkla kullanılmaktadır. Böylece daha tasarım aşamasındayken problemler sebepleriyle beraber görülerek deneme yanılma sürecine girilmeden çözümler geliştirilip tasarım süreci kısaltılmakta ve optimize edilmiş ürünler piyasaya sürülerek rekabet şansı artırılmaktadır.

Bu çalışma kapsamındaki simülasyonlar AVL FIRE® CFD programı kullanılarak, ESE Diesel adlı alt programıyla ağ yapısı oluşturulduktan sonra Workflow Manager yazılımıyla çözülmüştür. Hücre sayılarının kabadan hassasa doğru değişmesiyle simülasyon sonuçlarının çok değiştiği görülmektedir. Seçilen hücre sayısı çözümu etkilemeyeck şekilde olduğu tespit edildikten sonra, bilgisayar gücü ve çözüm süreleri göz önünde bulundurularak 56000 civarındaki hücre sayılarıyla asıl simülasyonlar gerçekleştirilmiştir. Çalışmanın ilk aşamasında, öncelikli olarak 9,1 sıkıştırma oranındaki yanma odasına sahip bir buji ateşlemeli motorun deneysel ve simülasyon sonuçlarının farklı motor hızlarında örtüşmesi amaçlanmıştır. Model doğrulandıktan sonra EGR, hava fazlalık katsayısı ve ateşleme avansi parametrelerinin motor performansı ve kirletici emisyonlara olan etkisi incelenmiştir. AVL FIRE® yazılımı ile krank açısına bağlı olarak silindir içindeki basınç, maksimum basınçlar, ortalama ve maksimum sıcaklılar, yakıt tüketimi, yakıt miktarındaki değişim, ısı açığa çıkışı, güç, ortalama efektif basınç, oluşan HC, is, CO ve NO_x miktarları incelenmiştir. 3 boyutlu grafikler için ESE Diesel programı kullanılmıştır.

Kalibrasyon amaçlı simülasyonlar sonucunda yanma hızları ve ateşleme avanslarının da ayarlanması gerektiği görülmüştür ve farklı avans değerleri uygulanarak ayarlama yapılmıştır. Ayrıca simülasyon ve deneylerdeki tutuşma gecikmesi sürelerinin farklı olduğu görülerek simülasyonlarda, deneylerdeki ateşleme avansları yerine güncelleştirilmiş değerler kullanılmıştır.

EGR sisteminin amacı, motora giren taze havanın belirli oranlarda yanma ürünleri ile karıştırılması sonucu alev sıcaklığının düşürülmesidir. Böylece NO_x emisyonları azaltılmaktadır. Bu çalışmada farklı EGR miktarları % 0, 5, 10, 13, 15, 18, 20 uygulanarak, egzoz gaz resirkülasyonunun güç, yakıt tüketimi ve egzoz emisyonlarına etkisi incelenmiştir.

Motorlarda en ekonomik çalışma fakir karışımla sağlanmaktadır. Maksimum güç için ise zengin karışıma ihtiyaç vardır. Motorun değişik çalışma koşullarında hava-yakıt oranının iyi bir şekilde sağlanması, değişimin minimum düzeyde kalması gerekmektedir. Bu çalışmada hava yakıt oranı değiştirilerek, farklı karışımlarda motor performansı ve kirletici emisyonları incelenmiştir.

Ulaşım sektörü için alternatif yakıtlar aramanın başlıca nedenleri; süratle tükenmekte olan petrol rezervleri, sınırlı sayıdaki petrol üreticilerine bağımlılığın azaltılması ve çevrenin korunması şeklinde özetlenebilir. Son yıllarda artış gösteren taşıt sayısı ile birlikte etkin hale gelen hava kirliliği de, daha temiz bir yanma sağlayabilecek alternatif yakıt arayışlarındaki diğer bir faktördür. Alternatif yakıtların; kaynak ve potansiyel yakıt temini, emniyet, zehirlilik ve sağlığa zararlılık, motor performansı ve emisyonları ve tekrar yakıt temini gibi kriterler açısından incelenmesi gerekir. Doğal gaz, bu kriterler bakımından olumlu ve motor yakıtı olarak kullanılabilecek en önemli alternatif yakıtlardan birisidir. Bolluk, düşük maliyet ve temiz yanma karakteristikleri ve dağıtım sistemlerinin var oluşuna ek olarak daha düşük araç emisyonlarına imkan vermesi, doğal gazı son derece elverişli bir alternatif yakıt yapmaktadır. Doğal gaz hacimsel olarak 80–95% metan (CH_4) gazından oluşmaktadır. Sıkıştırılmış doğal gaz (CNG), gelecekte taşıtların enerji ihtiyacını daha büyük oranda karşılayabilecek olan çevreci ve önemli bir alternatif yakıt olarak görülmektedir. Deneysel çalışmalar, doğal gazın hem buji ile ateşlemeli hem de sıkıştırma ile ateşlemeli motorlarda önemli modifikasyonları gerektirmeksizin ve dikkate değer performans kaybına yol açmaksızın kullanılabileceğini göstermektedir. Bu tezde, doğal gaza dönüştürülen buji ile ateşlemeli bir motorunda, doğal gazın güç, yakıt tüketimi ve egzoz emisyonları bakımından etkisi değerlendirilmiştir. Yapılan araştırmada, benzin motorunun doğal gazla çalıştırılmasının moment ve güç değerlerinin bir miktar azalttığı görülmektedir.

Homojen-karışımlı sıkıştırmalı ateşlemeli (HCCI) motorlar, geleneksel buji ile ateşlemeli ve sıkıştırma ile ateşlemeli motorlardan tamamen farklıdır. Bu yeni yanma teknolojisine göre çalışan motorlar, her iki geleneksel motorun avantajlarına aynı anda sahip olabilmektedir. Silindir içerisinde ya da dışında homojen ve seyreltilmiş olarak hazırlanan dolgu, herhangi bir kısılma işlemine tabi olmadan silindire alınır. Ön-karışımlı homojen dolgunun sıkıştırılması sonucunda, alev gelişimi olmaksızın yanma odasında birden fazla bölgede eşzamanlı ve ani olarak gerçekleşen yanma olayında NOx oluşumuna yeterli zaman tanınmadığı ve ön-karışımlı yanma gerçekleştiği için de partiküllerinin oluşumu önlendiği için emisyonlar bakımından avantaj sağlar. Çalışmada ilk aşamanın son bölümünde doğal gaz yakıtlı bir HCCI motorun AVL FIRE® yazılımı kullanılarak modellemesi yapılarak, simülasyon sonuçları benzin ve doğal gaz yakıtlı geleneksel buji ile ateşlemeli motorun simülasyon sonuçları ile karşılaştırılarak, bu yeni yanma teknolojisinin avantajları ve dezavantajları incelenmiştir.

Çalışmanın ikinci kısmında ise, dört zamanlı, tek silindirli, doğal emişli, direkt püskürtmeli ve tam yükte çalışan bir dizel motorunun yanma, performans ve emisyon analizi için AVL FIRE® programında bir simülasyon gerçekleştirilmiştir. Simülasyon sonucunda; bu motor referans alınarak krank mili açısına bağlı olarak 1500 [devir/dakika] motor dönme sayısında, farklı hava fazlalık katsayılarında (1.2

, 2.0 ve 3.0) ve farklı EGR oranlarında (% 5, 10, 20), silindir basıncı, sıcaklık ve motor performans eğrileri elde edildikten sonra yakıt tüketimi ve egzoz emisyonları bakımından karşılaştırılması yapılmıştır.

Daha sonra yapısal değişiklik yapılmayan dizel motorda toplam yakıt kütlesi sabit kalacak şekilde ana püskürtmeye ek olarak ilk püskürtme de yapılmıştır. Çift püskürtme yöntemi ile yapılan bu çalışmada ilk püskürtme süresi sabit tutularak (35 KMA), ilk püskürtülen yakıt miktarının performans ve emisyon değerlerine olan etkileri araştırılmıştır. İlk püskürtülen yakıt miktarları toplam yakıt miktarlarının sırası ile % 20 ,30 ve 40'ı olacak şekilde yapılmış ve yine bu koşularda sırası ile %5, %10, %13, %15, %18 ve %20 EGR uygulanmıştır. Bununla birlikte, ilk püskürtmenin süresi gibi püskürtme sistemi parametrelerinin; yanma olayı, performans ve emisyonlar üzerine olan etkisi incelemiştir. Sonuçlara göre ilk püskürtülen yakıt yüzdesi çoğaldıkça bu yöntemın avantajları azalmakta ve NO_x emisiyonlarinın artışı ile birlikte güç kaybı da görülmektedir, bu nedenle ilk püskürtülen yakıtın kütleleri sabit tutularak, püskürtme süreleri sırası ile 35, 40, 45, 50, 55 KMA arasında değiştirilerek ve %5 ve %10 EGR kullanılarak püskürtme süresi ve EGR nin birleşik etkisi motor performansından ödün vermeden emisyonlara olan etkisi incelenmiştir. Yapılan koşu sonuçlarına dayanarak yakıt miktarı arttıkça püskürtme süresini uzatarak istenilen sonuçları elde etmek mümkündür. Yapılan tüm koşular tek püskürtmeli koşuların sonuçları ile karşılaştırılmıştır ve buna göre optimum yakıt yüzdesi, ilk püskürtme süresi ve EGR miktarlarını seçerek performans ve emisyonlarda iyileşme sağlanmıştır.

1. INTRODUCTION

In an internal combustion engine (ICE), the ignition and combustion of fuels occurs inside the engine. The main application of internal combustion engines is converting the chemical energy contained in the fuel to mechanical power. Combustion is the basic chemical process of releasing energy from a fuel and air mixture. In this process, reactants (fuel-air mixture) and burned products acting as working fluids. In order to provide the desired power output these working fluids interact with mechanical components of engine to transfer the work. There are two types of internal combustion engines which have found wide applications in transportation and power generation because of their relative low-cost, high durability simplicity and high power/weight ratio; the spark-ignition (SI) engines and compression-ignition (CI) or diesel engines. In comparison with the conventional SI engines, due to the higher compression ratios, CI engines perform higher thermal efficiencies and better fuel economy. However, these advantages come with some drawbacks such as e.g. higher noise levels, more limited engine speed, diminished start ability and higher levels of NO_x and soot emissions. Thus, it will be more beneficial to take the advantages of both engine types. Additionally, stringent emission regulations, depletion of fossil based fuels and high fuel costs persuaded the researchers to develop cleaner and more efficient engines. In this regard, advanced combustion strategies such as Low Temperature Combustion (LTC), Homogeneous Charge Compression Ignition (HCCI) and Premixed Charge Compression Ignition (PCCI) have been introduced. These advanced strategies are capable of simultaneously reducing NO_x and soot emissions while maintaining their high thermal efficiency. Furthermore, in addition to the development of advanced combustion models to meet the strict emission regulations and produce high thermal efficiencies, using alternative fuels such as natural gas seems to be a promising way to achieve this goal.

1.1 Purpose of Thesis

The primary focus of this research is the examination of different combustion strategies for reducing NO_x and soot emissions along with engine performance improvement. The secondary objectives of this research are investigation of the effects of various parameters such as EGR and equivalence ratio on engine-out emissions and performance characteristics.

1.2 Literature Review

1.2.1 Historical background

Internal combustion engines did not become a practical reality until the 1860s. In 1867, Otto and Langen presented the more successful progress of an atmospheric engine. This engine had some drawbacks such as low thermal efficiency and excessive weight. In order to solving mentioned problems, Otto had introduced an engine cycle with four piston strokes: an intake stroke, a compression stroke before ignition, an expansion or power stroke where work was delivered to the crankshaft and an exhaust stroke. Table 1.1 demonstrates the distinction of Otto engine in comparison with previous atmospheric type. In after years, Otto's achievement affords engineers and researchers an opportunity to attaining further developments. For instance, by the 1880's two-stroke internal combustion engine has been successfully introduced by Clerk, Robson and Benz (Heywood, 1988, pp. 2-3).

A new concept of internal combustion engine has been announced by Diesel in 1892. In his patent, air alone is inducted into the cylinder so its temperature increased during the compression stroke and the liquid fuel injected directly into the heated air to initiate the combustion just before the combustion process required to start (Heywood, 1988, pg. 4). Because of wide-spreading markets of internal combustion engines, researches and developments of internal combustion engines, maybe less fundamental, have continued ever since to improve engine efficiency and exhaust emissions.

In fact, both of SI and CI engines have their own advantages and disadvantages. By considering CI engines, although they have higher compression ratios which result higher efficiencies than SI engines, diesel engines produce higher levels of nitrogen oxides (NO_x) and particulate matter (PM) emissions. In this regard, since the

Table 1.1 : Comparison of Otto four-stroke and Otto-Langen engines, adapted from (Heywood, 1988).

Specifications	Otto-Langen	Otto four-stroke
Brake horse power	2	2
Weight [lb]	4000	1250
Piston displacement [in^3]	4900	310
Power strokes per min	28	80
Shaft speed [rev/min]	90	160
Mechanical efficiency [%]	68	84
Overall efficiency [%]	11	14
Expansion ratio	10	2.5

1920's, attempts have been employed to achieve a hybrid internal combustion engine to combine the best features of SI engines and CI engines. Stratified-charge engine is one of the results of these efforts (Heywood, 1988, pp. 37-38). however complex and expensive fuel injection equipment have been used in these types of engines.

1.2.2 Advanced combustion models

1.2.2.1 Low temperature combustion

Low temperature combustion strategies which are capable of simultaneously reducing NO_x and soot emissions are classified in two categories: those in which there is a short time between the fuel injection and ignition time so, short ignition delay preclude through the air-fuel premixing and those in which the injection timing is early enough to prepare a homogeneous mixture, also ignition timing is controlled by chemical kinetics. By considering the first category, various methods such as low compression ratios, high levels of cooled EGR and retarded injection timing have been employed to decrease the flame temperature and extend the ignition delay.

Smokeless rich diesel combustion which has a high efficiency of conventional diesel engine and produces very low NO_x and PM emissions was developed by Sasaki and Iguchi (2000). An analyzing of low temperature non-sooting combustion with a simplified mixing model and a detailed chemical kinetic model which is capable of explaining most of low temperature combustion characteristics was conducted

by Aceves and Flowers (2005). Very high levels of EGR is required to keep the temperature low enough to avoid the PM formation, while this level of EGR limits the operation range of smokeless combustion to low power outputs. In order to get higher power outputs NO_x trap was used which caused losses in the efficiency of system. Kook et al. (2005)analyzed the effects of various EGR rates and injection timing. In this study intake charge is diluted by applying high levels of EGR or in another word, N_2 and CO_2 were added to fresh air. This action decreases the flame temperature and affect the local charge equivalence ratio which results a change in ϕ-T plane and afford the opportunity of avoiding PM and NO_x formation. Similar study was developed by Li et al. (2007b) to show the effect of intake charge dilution by using different dilution gasses including nitrogen, argon and carbon dioxide.

Alriksson and Denbratt (2006) performed a series of experiments with a single-cylinder test engine by utilizing high EGR rates and reducing compression ratios in order to extend the engine load ranges. Although the results showed a great reduction in NO_x and PM emissions, fuel consumption and formation rate of HC and CO were increased. In an analogous experimental study by McTaggart-Cowan et al. (2012), various significant engine operating parameters have been employed and changed in order to record the most effective parameters on low temperature combustion model. They have introduced two parameters which, low temperature combustion model showed a drastic sensitivity to their variations. EGR rate and amount of injected fuel were those two parameters as long as both of them altered the concentration of oxygen in the intake charge. Results indicated that high increment of EGR Rate and injected fuel mass causes an intense enhancement in amount of HC and CO emissions and decrease the combustion stability. Caton (2011) prepared a different study and used a thermodynamic cycle to figure out the cylinder wall temperature effects on the efficiency and emissions of an engine in which, both conventional and low temperature model were tested. According to the results, by raising wall temperature, NO_x emissions of low temperature model was near zero, also showed a slight improvement in efficiency. On the other side, there was not any noticeable development in the efficiency of conventional model, moreover, NO_x emissions were increased by wall temperature growth.

Further numerical and experimental studies about low temperature combustion strategy have been conducted by numerous researches and investigated the influences of various

parameters such as EGR rates, equivalence ratios, fuel jets (injector types), injection pressure, compression ratios, supercharging, high charge density using variable intake valve closing timing (IVCT), advanced injection strategies and piston geometries (Pickett and Siebers, 2004; Fang et al., 2006; Musculus et al., 2007; Yun and Reitz, 2007; Beatrice et al., 2008; Kumar and Zheng, 2008; Han et al., 2009; Su et al., 2009; Asad and Zheng, 2009; Kashdan et al., 2009; Mendez et al., 2009; Li et al., 2009; Ehleskog et al., 2009; Knight et al., 2011; Asad et al., 2013; Michailidis et al., 2013). Additionally, some studies visualized the combustion process with high-speed cameras and optical diagnostic images (Fang et al., 2006; Musculus et al., 2007).

Anselmi et al. (2010) presented a research to improve the emissions, fuel economy and combustion noise of low temperature combustion by using close-space multiple injection strategies. This method takes the advantage of time between fuel injection and start of combustion in order to prepare a desirable air-fuel mixture. In a similar study, Han and Bae (2012) demonstrated the effect of fuel injection pressure on conventional and low temperature diesel combustion. The results illustrated that the combustion phase of low temperature diesel combustion was considerably affected by injection pressure because of longer premixing time. Developed atomization and boosted evaporation of fuel droplets which is achieved by higher injection pressure resulted in shorter ignition delay and combustion duration in low temperature diesel combustion model. In case of engine-out emissions, CO and HC emissions decreased in both regimes and this is because of higher flame temperature in conventional engine and reduced fuel-rich mixture in low temperature combustion model. The reduction of soot emission was higher in conventional diesel combustion. Other research was done by Cong et al. (2010), to evaluate the effects of fuel injection timing and injection pressure at fixed engine speed on combustion characteristics. A complementary experimental study was accomplished by Kitamura and Ito (2010), in which, a different injection strategy, pressure modulated multiple-injection coupled with swirl control, was tested to avoid soot and noise emissions of high-load low temperature combustion engine. Very low levels of NO_x and PM emissions were produced by using high pressure injection in this experiment.

In addition to fuel injection strategies, in recent years, the idea of optimizing low temperature combustion by implementing various fuel types was pursued by numerous researchers as well. A simulation was prepared by Ra and Reitz (2009) using

multi-dimensional CFD code, KIVA-ERC-CHEMKIN, to inspect the influences of fuel composition on low temperature diesel combustion. Fuels were varied in terms of auto-ignition ability, viscosity and volatility.Michailidis et al. (2013)investigated the effects of gas-blended fuels on cyclic behavior, emissions and efficiency of low temperature combustion. Gas-blended fuels resulted a reduction in NO_x and soot emissions but not in proportion to its blend ratio. In a related experimental study,Gao et al. (2012) applied ethanol-blended diesel fuel where, ethanol was induced from intake port and diesel was injected directly in to the cylinder. The results indicated low NO_x and soot emissions, however fuel efficiency dropped off. In order to optimizing the low temperature combustion model, various biodiesel-blended fuels were prepared by Tompkins et al. (2014); Lee et al. (2014); Soloiu et al. (2013); Gharehghani et al. (2015). Palm biodiesel that has a higher cetane number and density than soy biodiesel showed a better torque and emission characteristics in addition to a lower rates of heat release which caused less sensitivity to EGR rates (Tompkins et al., 2014). In another case, 60%-biodiesel-blended diesel fuel was the best choice to obtain the desired results (Lee et al., 2014).

1.2.2.2 Homogeneous charge compression ignition (HCCI)

The first study which applied HCCI concept in a four-stroke engines was done by Najt and Foster (1983). They called it Compression Ignition Homogeneous Charge (CIHC) in which high levels of EGR were used to made a high temperature mixture in order to initiate the auto-ignition. Three different types of fuel with various octane number were examined and according to the results of this study, while high temperature hydrocarbon oxidation controlled the process of energy release, the process of ignition is controlled by low temperature hydrocarbon kinetics and ignition tendency of low octane number fuels which have a low ignition point is higher. Another experimental study in a four-stroke engine was developed by Thring (1989). The common term of homogeneous charge compression ignition (HCCI) which is used nowadays was presented by this author. His study affords the opportunity of diesel-like fuel economy at part-load conditions because the engine operates with very lean mixture in absence of throttling and also delivers a power density similar to SI engines because accedes to operate at full-load condition with homogeneous charge. Although he found that it is not possible to operate at high loads in HCCI mode at that moment and the

homogeneous mixture should be preheated by using heating equipment, or high levels of EGR, or both. He confirmed that high EGR rates and high intake temperatures are essential conditions to apply HCCI concept to his test engine.

Despite traditional SI and CI engines in which, respectively, spark and fuel injection controls the start of combustion and combustion rate depends on flame propagation speed or the injection duration, combustion timing of HCCI concept is controlled by chemical kinetics and intensely depends on initial condition, fuel quality and thermodynamic history experienced during the compression stroke.

Peng et al. (2003) checked the effects of equivalence ratios, EGR rates and different compression ratios by using of n-heptane as fuel which induced from a port injector in a single-cylinder four-stroke engine. This study focused on the effect of these parameters on knock limit, combustion rates, engine load and exhaust emissions. According to the results of this study, diesel fuel type HCCI combustion is more accessible than gasoline fuel type HCCI combustion because it can favorably operate at near room temperature in a wide range of equivalence ratios and EGR rates. They found that EGR rates strongly affect the auto-ignition timing, while combustion durations largely depend on equivalence ratios. Although the results showed an extremely reduction in NO_x and soot emissions, HC and CO emissions were still in high levels and misfire which caused incomplete combustion would increase these emissions more.

Additionally, Gray and Ryan (1997) developed an experiment based on HCCI concept in which wide range of compression ratios, intake temperatures, EGR rates and air-fuel ratios were tested for two fuels and the result of this experimental study revealed a drastically reduction in PM and NO_x emissions by using HCCI model, although the HC emission was approximately twice of that from the conventional diesel engine. Dec and Sjöberg (2003) performed an analogous experimental and computational study of HCCI combustion over various equivalence ratios, intake temperatures, engine speeds, compression ratios and a small variation in intake pressure. They used a single-cylinder engine using iso-octane as fuel to investigate the HC and CO emissions sources at low loads and in terms of computational part of study single-zone model with full chemistry mechanisms for iso-octane was used by them to determine the behavior of bulk-gases. Coupled with previous studies, the effect of intake temperature was tested by several researchers. Persson et al. (2004) figured out an experiment in which, a heat exchanger was utilized to change the intake charge temperature. Test engine was

operated in HCCI mode, using camshafts with low lift and negative valve overlap. Collected data were compared with SI mode and indicated that NO_x emissions and CO emissions were lower whereas, HC emissions were gently higher for HCCI model. Besides that, engine efficiency showed improvement in HCCI mode, however, until engine did not run out of the HCCI operating range, intake air temperature alteration did not significantly affect the HCCI combustion. Agarwal (2011) analyzed the cyclic variation of ignition timing of HCCI combustion with changing inlet air temperature and air-fuel ratio at various engine speeds. According to the outcomes, as inlet temperature growth, results richer mixture, combustion timing distribution predominantly diverged from normal distribution. In a computational study, using n-Dodecane as fuel, to achieving proper evaporation and mixing of fuel, intake air was preheated. Compared to conventional engine with early injection and in absence of preheating, peak pressure increased, while revealed a reduction in emissions (Renganathan and Rajagopal, 2014). Similarly, Gowthaman and Sathiyagnanam (2016) checked the impact of intake air temperature and fuel injection pressure on the efficiency and emissions of a HCCI engine compared to a conventional diesel engine. They exhibited that, although higher charge temperature developed fuel vaporization and reduced NO_x and soot emissions at a specific condition, this model limited the operation range of HCCI engine due to the high knocking intensity and misfiring as well as higher fuel injection pressure which caused high levels of HC and NO_x . Investigations that have formed by Juttu et al. (2007); Bression et al. (2008); Singh and Agarwal (2016); Sundararajan et al. (2016); Jamsran et al. (2016) are in good agreement with previous studies.

By contrast to conventional engines, operating range of HCCI engines bounded to low-load conditions, by virtue of enormously rapid pressure rise (high combustion rate) occurred in high load conditions and resultant knock and misfire, also ignition timing is controlled by chemical kinetics which is complicated and makes it difficult to control. Additionally, although HCCI engines are capable of simultaneous reduction in NO_x and soot emissions, due to the early injection, low temperature and wall wetting of fuel they lead to higher HC and CO emissions. In this regard, numerous researches have been done to expand operating range of HCCI engines.

Çinar et al. (2016) carried out an experimental research, employing various equivalence ratios and constant inlet air temperature where, a blend of n-heptane

and iso-octane used as fuel. In this research, two different cam mechanism were adjusted to change the intake valve lift in contemplation of gaining diverse amounts of trapped EGR. Low lift cams resulted a reduction in rate of heat release and in-cylinder pressure along with a higher level of trapped EGR and as a consequence, combustion timing was retarded. However, high lift cams showed better thermal efficiencies. Kawasaki et al. (2014) induced nitrogen oxides into the intake charge and figured out the effects of this action on the combustion characteristics of a natural gas fueled HCCI engine. NO and NO_2 was inducted in two uniform and non-uniform ways. In case of uniform mixing, auto-ignition timing was singularly advanced and adding either NO or NO_2 resulted an intense heat release. On the other hand, non-uniform mixing of nitrogen oxides with air-fuel mixture, by inducing NO and air-fuel mixture individually into the combustion chamber, two peaks appeared in rate of heat release diagram. Furthermore, advanced combustion phasing and higher combustion pressure was achieved by retarding the NO induction timing and keeping its amount constant. Also, high amount of NO_x helped auto-ignition more effectively than uniform mixing. In another detailed research, the effects of EGR components was numerically and experimentally surveyed in two steps, first the effect of adding EGR to supercharged HCCI combustion and the second one was the effect of individually induced nitrogen and carbon dioxide into the inlet air manifold. Despite both of nitrogen and carbon dioxide had impacts on retarding HCCI combustion, carbon dioxide resulted more dilution and leaded to misfire (Munehiro Matsuishi et al., 2015). Takashi Shimada (2015) visualized the in-cylinder pressure oscillations and the effect of internal EGR on knock characteristics of HCCI combustion by taking high-speed photographs of the entire bore area. Obtained results showed that, in-cylinder pressure oscillations were suppressed by adding internal EGR, which also balanced combustion by delaying the ignition timing.

Reducing emissions through the utilizing different fuel injection strategies is followed by numerous researchers. Effects of narrow spray angle and dual injection on exhaust emissions was the subject of study that have done by Kim and Lee (2007). Collected results showed that, with the advance of first injection timing, the dual injection strategy reduced NO_x emission, while using narrow spray angle limited CO and HC emissions in an acceptable range. Similar researches illustrated that, a remarkable reduction in PM and NO_x emissions were achieved by using narrow angle injector

with suitable EGR rate and dual injection strategy, whereas fuel consumption increased slightly (Lechner et al., 2005; Park et al., 2013). In a numerical study, Yu et al. (2015) carried out the effects of spray cone angle on emissions and mixture formation. According to their results, soot and CO emissions were significantly affected by wall wetting region. Since mixture formation and exhaust emissions of wall wetting region were directly controlled by spray cone angle, employing narrow cone angle injector reduced wall film built in the early injection, developed the oxidation of soot and CO and as a consequence, improved the exhaust emissions. An innovative dual-injection strategy was applied in a single cylinder HCCI diesel engine by Das et al. (2016), in favor of gathering the effects of second injection timing, EGR rates and premixed equivalence ratios on emissions and combustion characteristics. As expected, these parameters had noticeable effects on combustion controlling process. Although, peak pressure rise rate and in-cylinder peak pressure can be suppressed by external cooling EGR which produced lower NO_x and PM emissions, amount of HC and CO emissions were still higher than conventional diesel engine. In a supplementary experimental study, the impacts of multiple fuel injection strategies on combustion characteristics of a HCCI engine were observed (Mathivanan et al., 2016). In this experiment, diesel fuel was injected in five timed pulses. In first step, first, middle and last injection pulse durations were varied while all other injection pulse durations remained equal, and in second step, the effect of last injection pulse was checked. Although first injection pulse duration did not affect the combustion phasing as the last injection pulse retarded, retarding the last pulse and decreasing the duration of that reduced NO_x emissions. Experiment results demonstrated that, due to a better combustion phasing and higher heat release rates, multiple pulse injection showed lower engine-out emissions and higher thermal efficiency than single pulse injection.

A large range of studies gathered the alternative fuels usage and fuel composition effects on operating range of HCCI combustion. Ogawa et al. (2003) accomplished an investigation to optimize the ignition timing, clamping down the extremely fast combustion and try to enlarge the operating range of an HCCI engine by using selective fuels with different low-temperature oxidation characteristics. In order to increase the ignition, light naphtha, which represents two-stages ignition, was inducted from intake manifold and a low ignitable fuel or water, which does not represent low temperature oxidation, directly injected early in the compression stroke to suppress the

ignition. Polat (2016) tested various blends of ethanol (additive fuel) and diethyl ether (main fuel) at the same time with increasing intake air temperature and compression ratio. By considering the results, start of combustion was delayed and HCCI engine operating was not possible with using higher amount of ethanol, very lean mixture, because of its high octane number and high auto-ignition temperature. Furthermore, increase of intake air temperature, eventuated an increase in combustion duration and combustion of HCCI was advanced. Besides that, Bahng et al. (2016) tried to modify the fuel by preparing a mixture of vaporized liquid gasoline, water electrolysis gas (WEG) and air to control the HCCI combustion process. The results showed a significant improvement in fuel economy and engine performance. Due to the faster reaction rate along with higher heating potential of the prepared mixture, this method allowed them to successfully handle the disadvantages of lean burn method adopted in an HCCI combustion. Song and Song (2015) analyzed the performance and knock-resistance characteristics of a HCCI engine by using various blends of methane and hydrogen as fuel. Adding hydrogen enhanced knock resistance and resulted a slightly improvement in engine efficiency, torque output and exhaust emissions. Also, due to lower combustion rates with lower and retarded peak pressure, operation range and ignition capabilities of simulated HCCI engine was expanded.

Utilizing natural gas, polyoxymethylene dimethyl ethers (PODE), diethyl ether ethanol, dimethyl ether (DME), ethanol, methanol, butanol, hydrogen and biodiesels are some example subjects of researches that have done (Kawano et al., 2004; Shibata et al., 2004; Jun and Iida, 2004; Zheng et al., 2004; Zhang et al., 2006; Xie et al., 2006; Hashimoto, 2007; Kanoto et al., 2007; Li et al., 2007a; Shibata and Urushihara, 2007; Maurya and Agarwal, 2008; Shibata and Ogawa, 2012; Mochizuki et al., 2014; Takahiro Shima, 2015; Das et al., 2015; Hou et al., 2015; Kumar and Rehman, 2016; Wang et al., 2016; Jamsran et al., 2016; Sharma and Dhar, 2016; Xie et al., 2016). By considering all results, fuels with high research octane number, low cetane number, high hydrogen to carbon ratios, low boiling temperatures and high elevated pressure auto-ignition temperatures were the most appropriate choices to use. Indeed, all of these researches demonstrated valuable information about alternative fuels usage in order to expand the HCCI operating range including lower levels of emissions.

In addition to naturally aspirated HCCI combustion, further investigations were formed by multiple researchers in respect of adding breathing capabilities to optimize the

emissions, efficiency and fuel consumption of HCCI combustion. Gharahbaghi et al. (2006) performed an investigation about the effects of equivalence ratio, valve timing and pressure ratio on the operation of two supercharged HCCI engines. First engine was a single-cylinder, supercharged with compressed air fed from the shop supply and the second one was a V6 engine which employed a mechanically coupled supercharger. Lower equivalence ratios along with excessive air flow supplied by supercharger produced a lean mixture which is favorable to HCCI operation. Although higher load operation was possible by retarded exhaust valve timing, higher levels of NO_x emission was produced through this condition. In an experimental work, a combined boosted HCCI engine (external boosting and engine turbocharger) was analyzed thermodynamically and resulted in the expansion of operation map while produced very low NO_x emissions (Kulzer et al., 2011). In a similar numerical study, Taritas et al. (2014) determined the maximum achievable load with an ethanol fueled HCCI engine that equipped with two different configurations of boosting systems including a variable valve actuation, air cooler, external EGR, internal EGR, variable geometry turbocharger and a supercharger. According to the results, in order to have a stable combustion, they suggested to use the internal EGR instead of external EGR to increase the intake charge temperature. Though both combination enhanced the engine operation range in some specific conditions, they did not cover all of conditions. Also these systems are complex and need more attempts to get the optimum configuration. On the contrary, Makkapati and Curtis (2014) formed an experimental observation in a single-cylinder HCCI engine by applying a combination of intake boosting and cooled EGR. Although their test was defined to steady state operation of engine, noticeable development was gained including operation range and fuel efficiency.

1.2.2.3 Premixed charge compression ignition (PCCI)

Premixed Lean Diesel Combustion (PREDIC) A different combustion model called PREmixed lean DIesel Combustion (PREDIC) was developed by Takeda et al. (1996), in which, fuel injected at the very earlier stage of compression stroke, almost beginning of that. They analyzed emission characteristics of PREDIC model by using two side injectors and showed notable reduction in NO_x emissions in comparison with conventional diesel engine. In later researches, Nakagome et al. (1997) demonstrated that, although PREDIC model produced low levels of NO_x emissions with HCCI-like

mixture and an auto-ignition occurred near the top dead center, combustion rate and ignition timing control was difficult, which revealed a higher fuel consumption and knock. Tsurushima et al. (2001) compared three combustion models; conventional diesel combustion, HCCI combustion and PREDIC combustion models. In view of HCCI model, fuel mixed with air in an intake manifold, while in PREDIC model, fuel was injected into the cylinder at very early stage of compression stroke. They illustrated that both PREDIC and HCCI models required high levels of EGR to complete the combustion under lower loads and control the ignition timing under higher loads. Although both models revealed low heat loss characteristics under lower loads, thermal efficiency of HCCI combustion model was higher than PREDIC combustion model. Both HCCI and PREDIC combustion models was only able to operate in low load conditions.

Modulated Kinetics (MK)

A new combustion concept which called modulated kinetics (MK) has been developed by Kimura et al. (1999). They illustrate that MK concept can be considered as a low temperature premixed combustion strategy which results simultaneously reduction in soot and NO_x emissions, which are most important issues for diesel engines. They attained this aim with decreasing the combustion temperature by applying high levels of exhaust gas recirculation (EGR) to reduce the concentration of oxygen, extended the ignition delay in order to have an adequate mixing time, retarded fuel injection timing corresponding to the extended ignition delay and high swirl ratios engendered to restrain the formation of HC in a single cylinder test engine. Additionally, MK concepts is capable of using in high loads.

In a later study, Kimura et al. (2001) expanded the MK combustion operating range by using a multi cylinder test engine. They analyzed the effect of combining a low compression ratio, EGR cooling and high injection pressure and found that this combination could make ignition delay longer than injection duration. Moreover, they showed that the engine could run near the stoichiometric condition, since the ignition delay is longer than injection duration, as a result of favorable mixture preparation, PM formation could be prevented. Further investigations by Ogawa et al. (2000) discovered that, the higher swirl ratios retarded the start of injection timing and

improve the fuel economy of MK concept by reducing cooling losses.

Premixed Charge Compression Ignition (PCCI)

Premixed charge compression ignition (PCCI) concept seems to be a promising way of achieving low emissions with expanding operating range of HCCI combustion. PCCI combustion is a generalization of HCCI combustion with a premixed combustion of a highly diluted or lean mixture, whereas the combustion process is primarily controlled by the chemical kinetics. Although PCCI combustion is also controlled by chemical kinetics, it exhibits the equivalence ratio gradients which could affect the combustion process. Also, injection timing of PCCI combustion can be relatively retarded than for HCCI combustion and as a result prevents intense wall wetting and fuel impinging, which is one of major problems of HCCI combustion.

Actually, PCCI combustion is a hybrid of HCCI and conventional diesel combustion. Low levels of NO_x and soot could be achieved with PCCI combustion model in which, fuel is induced into the cylinder in various ways; port-fuel injection during the intake stroke, an early direct injection during the compression stroke or a late direct injection in vicinity of TDC. While, by considering HCCI combustion, in order to have a homogeneous air-fuel mixture before auto-ignition, fuel is injected very early during the intake stroke.

Aoyama et al. (1996) manufactured a single cylinder with port injection of gasoline in order to investigate the fuel consumption and emission characteristics of PCCI combustion method. Engine was operated stably with a fairly lean mixture and high compression ratio. According to their experiment, however spontaneous ignitions occurred at unspecific points, the PCCI engine produced notably lower NO_x emissions with a fuel consumption equal to conventional diesel engines.

Since in HCCI combustion, air-fuel mixture was injected into the cylinder at the very early stage of intake stroke and resulted the fuel adhesion to low temperature cylinder wall and oil dilution which reduced combustion efficiency and drastically increased HC emissions, Okude et al. (2004) employed PCCI combustion concept in single-cylinder engine to eliminate the mentioned problem. They found valuable information about application of PCCI combustion by applying PCCI model individually and a

combination of PCCI combustion and diffusion combustion during one cycle under high-load condition where the application of PCCI was not possible due to the knock. Obtained results revealed that, low levels of NO_x and soot could be gained by using PCCI method which was realized by adding high rates of cooled EGR and injecting fuel in the vicinity of top dead center. Retarded fuel injection timing prevented fuel adhesion to the cylinder wall and decreased the over-rich regions which caused a reduction in soot emissions. Moreover, high levels of cooled EGR decreased combustion temperature which caused reduction in NO_x emissions. They found that a smaller injector nozzle hole and higher injection pressure could develop the PCCI operating range and significantly reduced the soot emissions. Also, split-PCCI (PCCI with diffusion) combustion reduced NO_x and soot emissions while suppressing combustion noise at high loads.

Since high levels of EGR are required in PCCI combustion strategy, many researchers investigated the effect of EGR rates on PCCI combustion characteristics. Boyarski and Reitz (2006) accomplished an experimental study and determined the desirable configuration of intake pressure, start of injection timing and EGR rates in a light-duty early injection PCCI diesel engine. High EGR rates suppressed the combustion noise. Although a remarkable reduction in NO_x and soot emissions was obtained, fuel economy was deteriorated and higher HC and CO emissions were observed. Hardy and Reitz (2006) prepared an experimental study and checked the effects of high EGR rates and various equivalence ratios on a single-cylinder heavy duty diesel engine which operated in PCCI mode. They found that, higher EGR rates increased mixing time and reduced soot emissions. In a similar study,D'Ambrosio and Ferrari (2015) checked the impacts of EGR on a late premixed charge compression ignition engine performance, which equipped with an optimized pilot-main double injection strategy. Accordingly, under low load conditions with higher levels of EGR, ignition timing was retarded, also NO_x and soot emissions were decreased. However, under high loads due to the higher combustion rates, ignition timing delay was not affected by EGR rates and NO_x and soot emissions showed a trade-off behavior with increasing EGR. Shen et al. (2013b) analyzed the influence of EGR and intake pressure (boost) on PCCI combustion of three different fuel. They figured out that, in case of gasoline and diesel, higher EGR rates or lower intake pressure, increased ignition delay and reduced combustion duration. Also, with a lower values of intake pressure, a large portion of

heat release occurred after TDC and peak pressure rise was decreased. By considering ethanol as fuel, due to the high auto-ignition temperature of ethanol, ignition timing was delayed and resulted a quite premixed combustion. compared to gasoline and diesel cases, combustion duration was shorter and less EGR rates was required.

In two different studies that were done by Boot et al. (2009a,b), they tried to optimize an early direct injection PCCI combustion by varying EGR rates, intake temperature, intake pressure, injection timing, injection pressure, fuel temperature and utilizing external uncooled EGR. The main aim of these researches was investigation of the effects of mentioned parameters on engine performance, emissions and specifically on wall wetting issue, which is responsible for the bulk of the HC emissions. Although, except fuel injection pressure, other parameters showed a reduction in measured wall-wetting, both soot and HC emissions were higher than conventional diesel combustion. Also, in all cases NO_x emissions were reduced drastically without a penalty in fuel consumption. Similar results were obtained in a detailed study that was developed by Kiplimo et al. (2012). In addition to EGR effects, they discovered the impacts of spray impingement and injection parameters on combustion characteristics and exhaust emissions of a single cylinder PCCI diesel engine. Lower soot, HC and NO_x were produced by applying higher injection pressure, however CO emissions remained at the same levels of lower injection pressure. Although, low levels of NO_x and soot emissions were achieved by using high EGR amounts, due to the fuel impingement, too lean mixture and bulk quenching, HC and CO emissions were increased. Also, two optimum spray targeting spot were identified with and without EGR introducing. Lower soot, CO and HC with higher NO_x emissions were produced in absence of EGR, while, lower NO_x and soot emissions were gained by intruding EGR.

Fuel injection strategies play a significant role in exhaust emissions, combustion performance and expanding operating range of PCCI combustion. Different fuel injection strategies including single or multiple injection methods were employed by numerous researchers. By considering single injection strategy, fuel is injected into the cylinder via port fuel injection during the intake stroke, an early direct injection during the compression stroke, or a late direct injection in vicinity of TDC. Jung et al. (2011) investigated the influence of various injection timing, injection angle and number of nozzle holes in three types of combustion models. Fuel was injected near

the TDC for conventional diesel combustion, early in compression stroke for HCCI combustion and late in compression stroke in case of PCCI combustion. Different configurations of injectors were applied and obtained results illustrated that, in view of PCCI combustion, maximum pressure rise rate was higher and combustion duration was very shorter than other combustions. Injector with a narrow injection angle produced higher indicated mean effective pressure (IMEP) compared to the default injector which had wider injection angle. The reason was that large amount of fuel could participate in the combustion while injected fuel could be direct toward the piston bowl. Although, injector with lower number of nozzle holes produced higher IMEP, low levels of HC and CO emissions were gained by using the injector with higher number of nozzle holes, due to the better air utilization. Moreover, number of nozzle holes did not make any differences in the maximum pressure rise rate of PCCI combustion, however, that was higher for the injector with narrow injection angle compared to the default injector. The positive effect of narrow spray cone angle on NO_x and soot emissions of a PCCI combustion was also explored by Lechner et al. (2005), however there was a slight increase in fuel consumption. Single injection strategy was also the subject of a study that was done by Liu et al. (2015). They applied a single injection including early injection and late injection strategies in a 6-cylinder turbocharged PCCI diesel engine. According to the results, a two-stage heat release and a higher premixed combustion proportion than the conventional combustion was achieved with both early and late injection strategies. There was a simultaneously reduction in NO_x and soot emissions with both strategies, however, mixing controlled combustion and higher HC emissions was observed in the late injection strategy. Observations illustrated that, NO_x was extensively formed in the downstream of the spray, while soot was formed near the cylinder wall in the fuel-rich regions.

Beside cooled EGR, multiple injection strategy is also used to control the combustion phasing of PCCI combustion and reduce its peak pressure rise. Lu et al. (2011) found that by using high EGR rates, combustion rate was reduced and the start of ignition was delayed under high load condition for a PCCI combustion. Furthermore, there was not considerable differences in mixture formation, emissions and thermal efficiency of PCCI combustion under low load for both single and multi-injection strategies. Under higher loads, higher soot, CO and HC were produced by using single injection, while these emissions were decreased when multi-injection was applied.

They confirmed that, since engine load could be extended, mixture preparation was developed, indicated thermal efficiency was increased and CO and soot emissions were noticeably decreased by using multi-injection, it is more advantageous to use this strategy at high loads comparing with single injection. In order to prepare an optimal mixture, two injection pulses with different injection pressures, called adaptive injection strategy, were employed by Kokjohn and Reitz (2009). By using a variable pressure pulse injection system in this research, the first injection with a low injection pressure was utilized early in compression stroke to minimize the fuel-wall impingement and the second injection with a high injection pressure was applied near the TDC to elevate air entrainment and droplet scattering. They found that, injection duration and injection pressure of first pulse had a great influence in fuel impinging and increased injection duration resulted a small delay in combustion phasing and reduced peak pressure rise. However, there was a reduction in HC, CO and soot emissions, NO_x emissions and peak pressure rise rate of all cases were increased. They controlled this issue by applying more EGR and developed an optimal solution.

Kim et al. (2012) investigated an optimal injection condition for a PCCI diesel engine. They considered various injection parameters such as injection angle, injection duration and time of injection for three injection methods; single injection, early-main type split injection and early multiple injection. Besides higher IMEP and low soot emissions, more homogenous mixture with decreasing of spray penetration and increasing of fuel evaporation rate, were achieved by using early multiple injection method. By considering split injection, combustion and emission characteristics were fairly affected by both injection timing and injected fuel ratio of the early and main injection. An optimum injection timing and injected mass ratio was developed for split injection where the main injection was after TDC. Park and Bae (2013) compared single and double post injection effects on diesel PCCI combustion. At the first step they applied a late single injection without EGR and obtained results revealed lower NO_x emissions and longer ignition delay than conventional diesel engine. However, combustion efficiency, HC and CO emissions were deteriorated. At the second step, they fixed the main injection timing corresponding to first step and utilized single and double post injection along with EGR. Injected fuel rate was varied for both strategy and in all conditions, HC and CO emissions were reduced drastically compared to single main injection. The reason was that, combustion by post injections assisted to

combust unburned species. However, since combustion by post injection was occurred under high ambient pressure and temperature, higher NO_x emissions was produced. Because of shortened spray penetration by split of post injection, double post injection seemed to be more impressive in case of unburnt species reduction. In respect of increasing PCCI combustion operating range, various methods such as; spray targeting, direct injection, pilot injection and split injection were also discussed in multiple studies (Lee and Reitz, 2006; Kondo and Nakagawa, 2012; Torregrosa et al., 2013; Cheng et al., 2013; Tanov et al., 2014; Wang et al., 2014; Yin et al., 2015; Asad et al., 2016; Zhang et al., 2016; Najafabadi et al., 2016).

Bao et al. (2014) implemented a detailed study to discover the desirable injection strategy for PCCI combustion. Two injection strategies (single and double injection) including injection timing, injection pressure, pilot-main interval and injected fuel ratio were employed to investigate their variation effects on PCCI combustion performance. They compared single and multiple injection methods and gained valuable information. Desired PCCI combustion could be achieved by using early and late injection timing and optimized double injection strategy. by reason of they presented a capability of combustion phasing control, low exhaust emissions, very low combustion noise and high thermal efficiency. While single injection with high levels of EGR had longer ignition delay, in order to control the main combustion in multi-injection strategy, pilot-main interval and pilot injected fuel mass were changed. In comparison with single injection strategy, lower cylinder pressure, lower peak pressure rise rate and very low NO_x emissions were produced by applying multi-injection strategy. the study that was done by Wang et al. (2015) is in good agreement with pervious researches.

Spray-bowl interaction and intake valve timing were discussed in some researches. Diwakar and Singh (2009) implemented a computational study to investigate the effects of injector spray cone angles, start of injection timing and piston bowl shapes on PCCI combustion characteristics. According to the results, optimum combination of start of injection timing and spray cone angle in respect of producing lower engine-out emissions depended on the level of reentrancy and radius of curvature of the piston bowl near the bowl-lip. Similar study was formed by Cao et al. (2009). They checked the influence of injection timing and different combustion chamber design such as; open bowl, vertical side wall bowl and re-entry bowl, on combustion characteristics and exhaust emissions of a PCCI combustion. In order to expand the operating range of

PCCI combustion, Jia et al. (2015) studied the effects of late intake valve closing. They realized that low NO_x and soot emissions coupled with low fuel consumption could be attained by utilizing high levels of EGR, boosted intake pressure, optimized injection timing and retarded intake valve close timing. In a supplementary investigation, two different configurations of conventional actuators including; multi-pulse fuel injectors, an EGR valve and variable geometry turbo-charging, and a flexible intake valve closure modulation which dictated the effective compression ratio were used to improve the PCCI combustion performance (Kulkarni et al., 2009). Early fuel injection with a reduction in effective compression ratio and medium levels of EGR resulted a well-timed PCCI combustion with low NO_x emissions and good fuel economy.

In addition to injection strategies, a large number of studies indicated the alternative fuels usage and fuel composition effects on operating range of PCCI combustion. Masuda and Chen (2009); Ogawa et al. (2010); Shen et al. (2013a); Mancaruso and Vaglieco (2013); Bakker et al. (2014); Saravanan et al. (2015) discovered the effects of using ethanol and ethanol-blend fuels on PCCI combustion performance. Since adding ethanol leaded to low cetane number, the ignition delay was increased and combustion rate was decreased. So, due to the longer ignition delay air-fuel mixture was improved and resulted slightly higher brake thermal efficiency and a reduction in soot emissions. Various types of biodiesel, n-butanol and blends of them were applied by Northrop et al. (2009); Veltman et al. (2009); Valentino et al. (2012); Cheng et al. (2014). According to their study, biodiesel blended fuels produced lower soot emissions, while NO_x emissions was increased in some case. Additionally, higher resistance of n-butanol blends to auto-ignition made it possible to have a proper mixture which caused an improvement in soot and NO_x emissions. Tsujimura et al. (2008); Hildingsson et al. (2010); Valentino et al. (2011); Dijkstra et al. (2011); Leermakers et al. (2011); Dumitrescu et al. (2012) studied the impacts of fuel auto-ignition characteristics, fuel volatility and fuel properties on PCCI combustion. To summarize, obtained results illustrated that fuels with higher resistance to auto-ignition increased ignition delay, so mixing period could be extended. Also, if two fuels introduced same combustion phasing and ignition delay under a given condition, their emission characteristics were also matched. Furthermore, cetane number which also known as fuel reactivity rate was the most important fuel property that affecting the PCCI combustion. less reactive fuels or fuels with low cetane number had better brake

specific fuel consumption due to the optimized combustion phasing and shorter combustion duration. Due to the longer ignition delay of low cetane number fuels, air and fuel were mixed properly and formed very low levels of soot emissions. although HC and CO emissions were primarily affected by combustion phasing, slightly higher levels of these emissions were produced by low cetane number fuels. In case of fuels that contains oxygen, due the carbon decomposition, it had positive effects on soot emissions. so as a consequence, utilizing fuels which contain oxygen and has low cetane number seems to be an interesting way to enhance the applicability of PCCI combustion engines.

2. COMPUTATIONAL METHOD FOR ENGINE SIMULATION

2.1 Introduction

The present chapter is intended to presenting an overview of the CFD workflow that pursued for simulation of the in-cylinder physical and chemical processes controlling engine performance and emission characteristics. The workflow description together with the CFD solver and modeling details which are revealed in the present chapter are based on the commercial AVL FIRE® CFD code. First, a basic introduction of the overall CFD methodology, including the pre and post-processing tools and the flow solver is provided. Then the models which are implemented for simulation of turbulence, spray formation/propagation, ignition and combustion as well as pollutant formation are pronounced.

Computational Fluid Dynamics (CFD) provides a detailed description of the fluid flow and transport phenomena occurring in the system, employing simplified kinetic mechanisms in order to develop current high computational effort. In another words, CFD is the analysis of systems involving fluid flow, heat transfer and associated phenomena such as chemical reactions by means of computer-based simulation. CFD codes are structured around the numerical algorithms that can solve fluid flow problems. By using CFD, partial differential equations which indicate conservation laws for mass, momentum and energy, are replaced by a set of solvable algebraic equations. Noticeable advantages of CFD make it a promising way to realize flow patterns that are difficult, expensive or impossible to study using experimental techniques. Although the results of a CFD simulation are not completely reliable, significantly reduces requirements for expensive and time consuming experimental tests.

Indeed, in parallel with advanced combustion concepts and alternative fuel usage, 3D CFD simulation of in-cylinder spray formation/propagation, combustion and pollutant formation processes is receiving increasing attention during engine and combustion

system development. Nowadays, CFD has been successfully defined for the calculation of fluid flow, mixture formation and combustion in internal combustion engines as a supplementary tool to in-cylinder pressure analysis, combustion diagnostics and optical mixture formation.

2.2 CFD Simulation Methodology Using AVL FIRE®

The commercially available AVL FIRE® CFD package includes sophisticated user interface to input problem parameters and to comment the simulation results. The CFD simulation of internal combustion engine can be divided into three main stages;

- pre-processing
- solver
- post-processing

All tools which are needed to cover the mentioned tasks to successfully perform an IC-engine CFD calculation are available through a fully interactive graphical user interface.
For meshing of the moving IC engine geometries AVL FIRE® offers proper tools and methods which are applicable to all types of SI and CI engines. The related solver technology is capable of handling turbulent multi-phase reactive flows on moving (compressing/expanding) computational meshes and the related post-processing capabilities are essential for solution monitoring and results analysis.

2.2.1 Pre-processing

Pre-processing consists of the input of a flow problem to a CFD program by means of an operator-friendly interface and the subsequent transformation of this input into a suitable form for use by the solver. The pre-processing stage involves:

- The computational domain: definition of the geometry of the region of interest.
- Grid generation: the subdivision of the domain into a number of smaller and non-overlapping sub-domains(a grid of cells or control volumes).
- Selection of the physical and chemical phenomena that need to be modelled.

- Definition of fluid properties.
- Specification of appropriate boundary conditions at cells which coincide with or touch the domain boundary.

In brief, first the generation of the computational meshes that required to cover the fluid domain over the crank-angle interval of interest, then the characterization of the initial and boundary conditions of the flow solver settings and specification of the physical and chemical models assumed to simulate the in-cylinder processes.

2.2.2 Flow solver and solution algorithm

The AVL FIRE® CFD code solves the general conservation equations of mass, momentum and enthalpy plus additional transport equations for turbulence related quantities, conservation of chemical species and additional scalar quantities such as mixture fraction, reaction progress variable and flame surface density. The solution method is based on a fully conservative finite volume approach. All dependent variables for momentum, pressure, density, turbulent kinetic energy, dissipation rate and scalar quantities (such as chemical species) are evaluated at the centers of the computational cells (control volumes) (Demirdzic et al., 1993). The numerical algorithm consists of the following steps:

- Integration of the governing equations of fluid flow over all the finite control volumes of the domain
- Discretization: conversion of the resulting integral equations into a system of algebraic equations
- Solution of the algebraic equations by an iterative method

The first step, the control volume integration, distinguishes the finite volume method from all other CFD techniques. The finite volume approach in the CFD rests on general conservation principles for properties describing the behavior of a matter when it interacts with its surrounding. The resulting statements express the conservation of relevant properties for each finite size cell. The conservation of a general flow variable ϕ (enthalpy as an example) within a finite control volume can be expressed as a balance

between the various processes tending to increase or decrease it. So:

$$\left[\begin{array}{c}\text{Rate of change of } \phi \text{ in the control volume with respect to time}\end{array}\right] = \left[\begin{array}{c}\text{Net rate of increase of } \phi \text{ due to the convection in to the control volume}\end{array}\right] + \left[\begin{array}{c}\text{Net rate of increase of } \phi \text{ due to the diffusion in to the control volume}\end{array}\right] + \left[\begin{array}{c}\text{Net rate of creation of } \phi \text{ inside the control volume}\end{array}\right]$$

The AVL FIRE® CFD code contains suitable discretization techniques for the treatment of the transport phenomena, convection (transport due to fluid flow), diffusion (transport due to variations of ϕ from point to point) and the source terms (associated with the creation or destruction of ϕ) as well as the rate of change with respect to time. In this regard, a second-order midpoint rule is used for integral approximation and a second order linear approximation for any value at the cell-face. The diffusion term is incorporated into the surface integral source after employment of the spatial interpolation practice. Also various differencing schemes are available for discretization of the convection term. Moreover, the rate of change is discretized by using implicit schemes, namely an Euler implicit scheme and a three time level implicit scheme of second order accuracy. There are no straightforward guidelines for making these choices since they are problem dependent.

The overall solution procedure is iterative and is based on the Semi-Implicit Method for Pressure-Linked Equations algorithm (SIMPLE) applicable to turbulent flows at all speeds (Patankar and Spalding, 1972). The principal difficulty in solving the momentum equations for incompressible flows lies in the determination of the pressure. As illustrated in Figure 2.1, in the iterative SIMPLE-like algorithms, the discrete form of the continuity equation is converted into an equation for the pressure correction. The pressure-corrections are then used to update the pressure and velocity fields so that the velocity components obtained from the solution of momentum equations satisfy the continuity equation.

At each iteration, at each cell, a new value for variable ϕ in cell P can then be calculated from that equation. The change of variable ϕ values from the previous (outer) iteration (ϕ^{k-1}) to the next iteration (ϕ^{k}) is limited in order to ensure the convergence of the solution procedure. The limitation or under-relaxation is done implicitly, as presented by Patankar (1980):

$$\phi_P^k = \phi_P^{k-1} + U(\phi_P^{new,predicted} - \phi_P^{k-1}) \tag{2.1}$$

Where U is the under-relaxation factor with values between 0 and 1. The implicit implementation of the above relaxation formula leads to the modified algebraic equations.

The iterative process is repeated until the change in the variable from one iteration to the next becomes so small that the solution can be considered converged, referred to the residual. At convergence, all discrete conservation equations are obeyed in all cells to a specified tolerance, the solution no longer changes with additional iterations, and finally mass, momentum, energy and scalar balances are obtained. Residuals measure imbalance or error in conservation equations. It is common to require the residuals to be on the order of 10^{-3} to 10^{-5} or less for convergence.

For solving the large sets of linear equation systems deriving from the discretization of the governing equations, AVL FIRE® adopts efficient preconditioned conjugate gradient methods. The symmetric gradient method is employed for solving equations with symmetric matrix and the bi-conjugate method is adopted for equations with asymmetric matrix. Both methods are used with either incomplete Cholesky or Jacoby preconditioning technique.

As explained, the underlying physical phenomena are non-linear and also coupled with more than one dependent variable features in each equation, so an iterative solution approach is required. There are two approaches; the coupled (simultaneous) and segregated (sequential). In the first one, all equations are part of the single $M \times N$ system while in the second, segregated approach, each equation for the considered variable is decoupled by treating other variables as known. This leads to a sub-set of M linear algebraic equations for each dependent variable. Having much smaller storage requirements, the segregated SIMPLE approach is adopted in the AVL FIRE® CFD Solver. The segregated SIMPLE algorithm gives a method of calculating pressure and velocities. The method is iterative, and when other scalars are coupled to the momentum equations the calculation needs to be done sequentially. The sequence of operations in a CFD procedure which employs the SIMPLE algorithm is given in Figure 2.1.

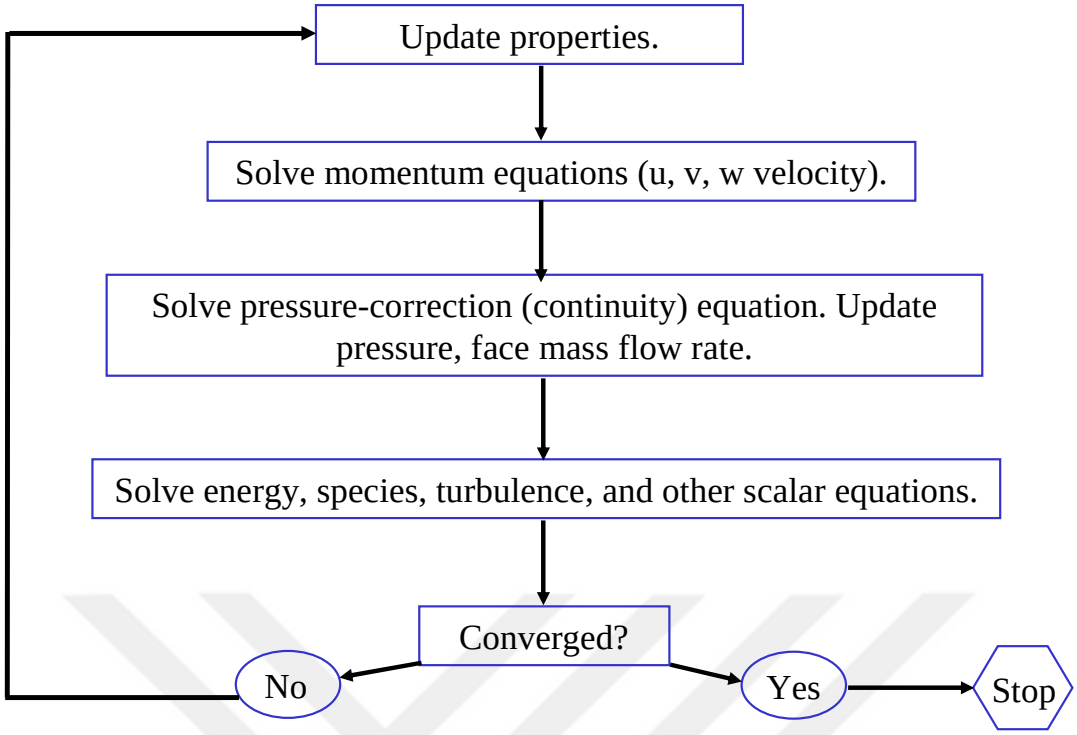


Figure 2.1 : Segregated SIMPLE solution procedure for Pressure-Based solver (Versteeg and Malalasekera, 2007).

Meeting the requirements of different fields of application, AVL FIRE® simulations may be set up in steady or transient (unsteady) mode. Various initial and boundary conditions are available to match the setup of any simulation to the real flow problem. Depending on applications of internal combustion engine, the solver is capable of handling computational models including moving boundaries.

2.2.3 Post-processing

The AVL FIRE® post-processor offers numerous functions enabling detailed online job monitoring, results visualization and analysis. These include:

- Domain geometry and grid display
- Vector plots
- Line and shaded contour plots
- 2D and 3D surface plots
- Particle tracking

- View manipulation (translation, rotation and scaling)
- Color postscript output
- Generation of animation for dynamic result display

During the simulation, the post-processor allows monitoring of the convergence behavior and the results development by visualizing the residuals of the differential equations as well as selected results as graphs in 2D diagrams. The post-processor enables the generation of 2D and 3D cuts for visualization of scalar and vector quantities as iso-lines, iso-values and iso-surfaces, where the vector quantities can be also displayed as vector plots. Additionally, the display of streamlines and particle tracing is possible.

In order to analyze the results, the post-processor offers the possibility of operations on 3D result data, macro and formula capabilities and import of selected test-bed data. For the purpose of result presentation, the post-processor also offers shading, blending and texturing options, manipulation of object lighting, manipulation of color assignments, inserting of text and pre-defined text variables, generation of colored plots in various formats and generation of animations.

Performing the computation itself requires operator skills of a different kind. Specification of the domain geometry and grid design are the main tasks at the input stage and subsequently the user needs to obtain a successful simulation result. These two aspects characterize such a result are convergence and grid independence.

2.3 Computational Meshes

Mesh generation is often the most decisive and strongly limiting factor in CFD calculation accuracy. A good computation mesh should be wall-adapted, sufficiently fine and problem-adapted, so that all flow structures such as flames can be well resolved. In practice, these requirements can often not be fulfilled completely satisfactorily. Another problem is mesh movement, while only a few CFD codes exist which provide for the functionality of a mesh movement, as it is an important factor in the treatment of in-cylinder problems (moving valves and piston). In the case of stationary meshes, the situation is less critical and the meshes can usually be exchanged. The surface-based flow resolution represents a compromise between

high-quality mesh and complexity of mesh generation, which is currently being introduced in various commercial software packages such as AVL FIRE® .

The pre-processor of AVL FIRE® offers interesting meshing tools for the generation of boundary fitted computational grids to represent the complex IC engine geometries including moving parts such as piston and intake/exhaust valves. The flexible automated meshing environment applies advanced hybrid grid generation techniques which enable fast, reliable and accurate meshing of the complex 3D domains. In order to generate the set of meshes required to cover the complete IC engine cycle, a baseline computational mesh, that is usually generated for the piston and valve positions at TDC, is automatically adapted to reflect the geometrical conditions for the crank-angle interval of interest. In order to meet the demands concerning accuracy and reliability of the numerical results, the quality of the computational grids has to actualize certain requirements.

The possibility of starting from user-defined geometry sub-domains enables the efficient meshing of complex geometries by simultaneously maintaining a high grid quality. Topology, cell orientation and mesh resolution in critical areas such as small gaps can be easily controlled by the user. Adopting arbitrary and conform interfaces, the relevant geometry can easily be split into different domains, such as intake port, valve seat and combustion chamber, avoiding the mutual interaction of different parts with respect to topology and distortion due to mesh movement. Thus, the complexity of the meshing process is reduced to meshing of simple parts which can easily be exchanged for performing parametric studies related to geometrical and valve lift and timing variations.

In order to further reduction in the complexity of the mesh generation process and consequently maximize ease-of-use and minimize meshing times, AVL FIRE® also supports a fully automated grid generation approach. The automatically generated computational grids consist of mainly hexahedral elements with a few tetrahedrons, prisms and pyramids in the vicinity of local refinement areas. The boundary layers consist of hexahedral elements and prisms only. Sophisticated grid refinement techniques and algorithms for automatic resolution of geometrical details provide maximum flexibility for all relevant grid generation tasks.

Mesh movement in AVL FIRE® is based upon interpolation between two grids of identical topology and number of elements set up at two different positions of

the moving elements, typically at different piston or valve positions. Thus it is possible to virtually generate grids for any position of the moving geometry between the extreme positions represented by the original two grids, enabling the expansion and compression of the computational grid according to different predefined or user-defined displacement functions. At some point during expansion and compression of the mesh, the cell aspect ratio or other mesh quality criteria may exceed permitted values. For that reason, a procedure called rezones is performed, which ensures an optimum cell density and quality over the entire crank-angle interval under consideration. The rezoning method can be applied to arbitrarily complex geometries with an arbitrary number of moving boundaries. Since the computational grid is generated for one representative surface model, artificially assembled valve and piston positions are allowed. Extreme positions such as TDC, BDC and maximum valve lift are detected automatically and respective grids are generated without requiring additional user input.

Additionally, due to the often symmetric arrangement of IC engine injector and piston bowl configurations the analysis and optimization of the spray injection and combustion processes is usually done by simulating an engine segment model only. The flow domain under investigation is then limited to the combustion chamber part around one single fuel spray applying cyclically symmetric boundary conditions for the crank-angle interval from inlet valve closure (IVC) to exhaust valve opening (EVO). In this case the computational grid generation can be based on parameterized 2D curves, describing the combustion chamber and optionally the injector geometry. Based on this input, the generation of the grids required to cover the simulation period between intake valve closing and exhaust valve opening, is performed automatically within AVL FIRE® Engine Simulation Environment Diesel (ESE Diesel) tool. The meshing process also takes into account the generation of a piston position independent mesh topology for the spray domain, a defined number and thickness of boundary layers and matching of the compression ratio without requiring user interaction.

The only way to eliminate errors due to coarseness of a grid is to perform a grid dependence study, which is a procedure of successive refinement of an initially coarse grid until certain key results do not change. Then the simulation is grid

independent. A systematic search for grid-independent results forms an essential part of all high-quality CFD studies.

2.4 Basic Fluid Mechanical Equations

The fluid will be regarded as a continuum. For the analysis of fluid flows at macroscopic length scales, the molecular structure of matter and molecular motions may be ignored. The behaviour of the fluid is described in terms of macroscopic properties, such as velocity, pressure, density and temperature, and their space and time derivatives.

2.4.1 Conservation equations

In the following, the basic equations of fluid mechanics are briefly restated. The governing equations of fluid flow represent mathematical statements of the conservation laws of physics:

- The mass of a fluid is conserved.
- The rate of change of momentum equals the sum of the forces on a fluid particle (Newton's second law).
- The rate of change of energy is equal to the sum of the rate of heat addition to and the rate of work done on a fluid particle (first law of thermodynamics).

It should be mentioned, this section presents the epitome of conservation equations. In order to gain more information about intermediate mathematical operations and derivations in detail see (Wendt, 2008).

2.4.1.1 Mass conservation (continuity equation)

The first step in the derivation of the mass conservation equation is to write down a mass balance for the fluid element:

$$\begin{bmatrix} \text{Rate of increase} \\ \text{of mass in fluid} \\ \text{element} \end{bmatrix} = \begin{bmatrix} \text{Net rate of flow} \\ \text{of mass into fluid} \\ \text{element} \end{bmatrix}$$

The rate of increase of mass in the fluid element is

$$\frac{\partial}{\partial t}(\rho \delta x \delta y \delta z) = \frac{\partial \rho}{\partial t} \delta x \delta y \delta z \, . \tag{2.2}$$

It is needed to account for the mass flow rate across a face of the element, which is given by the product of density, area and the velocity component normal to the face. Figure 2.2 illustrates the net rate of flow of mass into the element across its boundaries.

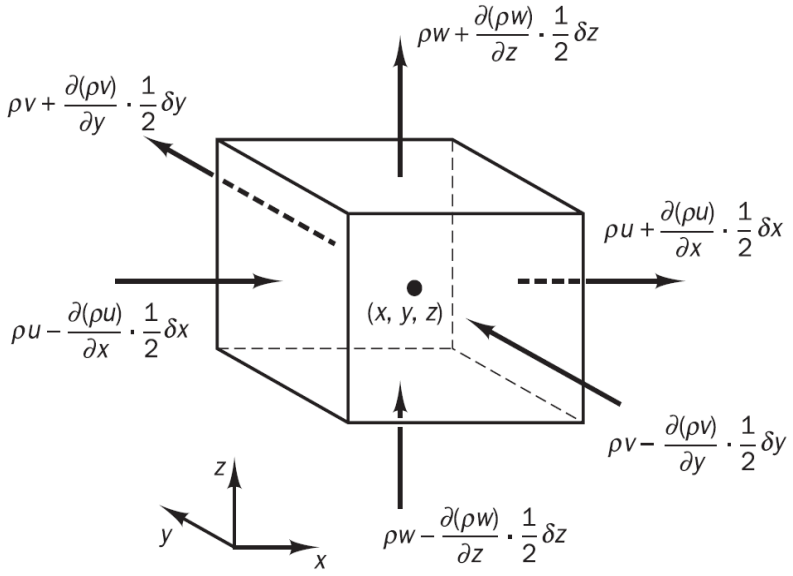


Figure 2.2 : Rate of mass flows into the fluid element (Versteeg and Malalasekera, 2007).

Flows which are directed into the element produce an increase of mass in the element and get a positive sign and those flows that are leaving the element are given a negative sign. Finally, all terms of the resulting mass balance are arranged on the left hand side of the equals sign and the expression is divided by the element volume $\delta x \delta y \delta z$. This yields

$$\frac{\partial \rho}{\partial t} + \left[\frac{\partial(\rho u)}{\partial x} + \frac{\partial(\rho v)}{\partial y} + \frac{\partial(\rho w)}{\partial z} \right] = \frac{\partial \rho}{\partial t} + \nabla \cdot (\rho \mathbf{u}) = 0 \tag{2.3}$$

Where **u** is the vector velocity in cartesian space and is given by

$$\mathbf{u} = u\vec{i} + v\vec{j} + w\vec{k}$$

Equation (2.3) is the unsteady, three-dimensional mass conservation (continuity equation) at a point in a compressible fluid. The first term on the left hand side is the rate of change in time of the density (mass per unit volume). The second term describes the net flow of mass out of the element across its boundaries and is called the convective term.

The momentum and energy conservation laws make statements regarding changes of properties of a fluid particle. This is termed the Lagrangian approach. Each property

of such a particle is a function of the position (x,y,z) of the particle and time t. By assuming that the value of a property per unit mass is denoted by ϕ, the total or substantive derivative of ϕ with respect to time following a fluid particle is

$$\frac{D\phi}{Dt} = \frac{\partial \phi}{\partial t} + \frac{\partial \phi}{\partial x}\frac{dx}{dt} + \frac{\partial \phi}{\partial y}\frac{dy}{dt} + \frac{\partial \phi}{\partial z}\frac{dz}{dt} \tag{2.4}$$

A fluid particle follows the flow, so $dx/dt = u$, $dy/dt = v$ and $dz/dt = w$. Thus the substantive derivative of ϕ is given by

$$\frac{D\phi}{Dt} = \frac{\partial \phi}{\partial t} + u\frac{\partial \phi}{\partial x} + v\frac{\partial \phi}{\partial y} + w\frac{\partial \phi}{\partial z} = \frac{\partial \phi}{\partial t} + \mathbf{u}\cdot\nabla\phi \tag{2.5}$$

Where $\frac{D\phi}{Dt}$ defines rate of change of property ϕ per unit mass.

Although, it is possible to develop numerical methods for fluid flow calculations based on the Lagrangian approach by tracking the motion and computing the rates of change of conserved properties ϕ for collections of fluid particles. It is more common to develop equations for collections of fluid elements making up a region fixed in space. This is termed the Eulerian approach.

In case of the mass conservation equation, the rate of change of property ϕ per unit volume for a fluid particle is given by the product of $\frac{D\phi}{Dt}$ and density ρ, hence

$$\rho\frac{D\phi}{Dt} = \rho\left[\frac{\partial \phi}{\partial t} + \mathbf{u}\cdot\nabla\phi\right] \tag{2.6}$$

The most useful forms of the conservation laws for fluid flow computation are achieved with changes of a flow property for a fluid element that is stationary in space.

As mentioned before, Eq.(2.3) indicates the sum of the rate of change of density in time and the convective term in the mass conservation for a fluid element. The generalization of terms of Eq.(2.3) for an arbitrary conserved property is

$$\frac{\partial(\rho\phi)}{\partial t} + \nabla\cdot(\rho\phi\mathbf{u}) \tag{2.7}$$

Which expresses the rate of change in time of ϕ per unit volume plus the net flow of ϕ out of the fluid element per unit volume. In longhand notation

$$\frac{\partial(\rho\phi)}{\partial t} + \nabla\cdot(\rho\phi\mathbf{u}) = \rho\left[\frac{\partial \phi}{\partial t} + \mathbf{u}\cdot\nabla\phi\right] + \phi\left[\frac{\partial \rho}{\partial t} + \nabla\cdot(\rho\mathbf{u})\right] = \rho\frac{D\phi}{Dt} \tag{2.8}$$

Where the term $\phi\left[\frac{\partial\rho}{\partial t}+\nabla\cdot(\rho\mathbf{u})\right]$ is equal to zero by virtue of mass conservation (Eq.(2.3)), finally

$$\rho\frac{D\phi}{Dt}=\frac{\partial(\rho\phi)}{\partial t}+\nabla\cdot(\rho\phi\mathbf{u})=\rho\left[\frac{\partial\phi}{\partial t}+\mathbf{u}\cdot\nabla\phi\right] \tag{2.9}$$

Eq. (2.9) derives the relationship between the equations for a fluid particle that is moving with the flow (Lagrangian) and a fluid element that is stationary in space (Eulerian), that states in words

$$\begin{bmatrix}\text{Rate of increase}\\ \text{of } \phi \text{ for a fluid}\\ \text{particle}\end{bmatrix}=\begin{bmatrix}\text{Rate of increase}\\ \text{of } \phi \text{ of fluid}\\ \text{element}\end{bmatrix}+\begin{bmatrix}\text{Net rate of flow}\\ \text{of } \phi \text{ out of fluid}\\ \text{element}\end{bmatrix}$$

For an incompressible fluid (liquid) the density ρ is constant and Eq.(2.3) becomes

$$\frac{\partial u}{\partial x}+\frac{\partial v}{\partial y}+\frac{\partial w}{\partial z}=\nabla\cdot\mathbf{u}=0 \tag{2.10}$$

2.4.1.2 Momentum equation

Newton's second law states that the rate of change of momentum of a fluid particle equals the sum of the forces on the particle:

$$\begin{bmatrix}\text{Rate of increase}\\ \text{of momentum of}\\ \text{fluid particle}\end{bmatrix}=\begin{bmatrix}\text{Sum of forces on}\\ \text{fluid particle}\end{bmatrix}$$

There are two types of forces on fluid particles:

- Surface forces: act directly on the surface of the fluid element.
  - pressure forces
  - viscous forces
- Body forces: act directly on volumetric mass of the fluid element.
  - gravity force
  - centrifugal force
  - Coriolis force
  - electromagnetic force

The state of stress of a fluid element is defined in terms of nine stress components shown in Figure 2.3. The pressure, a normal stress, is denoted by τ_{ii}. Viscous stresses or shear stresses are denoted by τ_{ij}. The suffices i and j in τ_{ij} indicate that the stress component acts in the j-direction on a surface normal to the i-direction. By considering

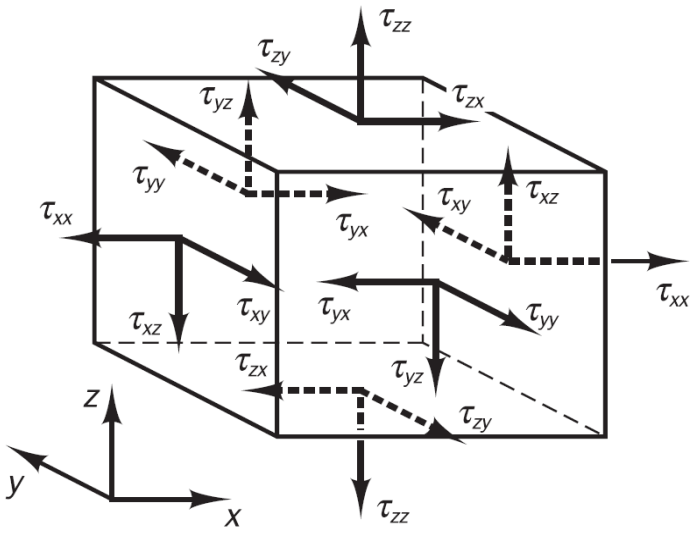


Figure 2.3 : Stress components on three faces of fluid element (Versteeg and Malalasekera, 2007).

Eq.(2.9), with $\phi = \mathbf{u}$ and assuming the fluid to be Newtonian, eventually the complete momentum equation (Navier–Stokes equation) in conservation form is expressed as

$$\rho\frac{Du}{Dt} = \frac{\partial(\rho u)}{\partial t} + \nabla\cdot(\rho u\mathbf{u}) = -\frac{\partial p}{\partial x} + \frac{\partial}{\partial x}\left(\lambda(\nabla\cdot\mathbf{u}) + 2\mu\frac{\partial u}{\partial x}\right) + \frac{\partial}{\partial y}\left[\mu\left(\frac{\partial v}{\partial x} + \frac{\partial u}{\partial y}\right)\right] + \frac{\partial}{\partial z}\left[\mu\left(\frac{\partial u}{\partial z} + \frac{\partial w}{\partial x}\right)\right] + \rho f_x \tag{2.11a}$$

$$\rho\frac{Dv}{Dt} = \frac{\partial(\rho v)}{\partial t} + \nabla\cdot(\rho v\mathbf{u}) = -\frac{\partial p}{\partial y} + \frac{\partial}{\partial x}\left[\mu\left(\frac{\partial v}{\partial x} + \frac{\partial u}{\partial y}\right)\right] + \frac{\partial}{\partial y}\left(\lambda(\nabla\cdot\mathbf{u}) + 2\mu\frac{\partial v}{\partial y}\right) + \frac{\partial}{\partial z}\left[\mu\left(\frac{\partial w}{\partial y} + \frac{\partial v}{\partial z}\right)\right] + \rho f_y \tag{2.11b}$$

$$\rho\frac{Dw}{Dt} = \frac{\partial(\rho w)}{\partial t} + \nabla\cdot(\rho w\mathbf{u}) = -\frac{\partial p}{\partial z} + \frac{\partial}{\partial x}\left[\mu\left(\frac{\partial u}{\partial z} + \frac{\partial w}{\partial x}\right)\right] + \frac{\partial}{\partial y}\left[\mu\left(\frac{\partial w}{\partial y} + \frac{\partial v}{\partial z}\right)\right] + \frac{\partial}{\partial z}\left(\lambda(\nabla\cdot\mathbf{u}) + 2\mu\frac{\partial w}{\partial z}\right) + \rho f_z \tag{2.11c}$$

Where μ is the molecular viscosity coefficient, λ is the bulk viscosity coefficient and

f_i is the body force per unit mass. If the weight of fluid is the only body force, f_i can replaced with the gravity (g). Also Stokes made the hypothesis that

$$\lambda = -\frac{2}{3}\mu \tag{2.12}$$

So far the general compressible case is considered, where ρ is variable as a function of location and time. For the case of incompressible flow (liquids), where ρ is constant, the continuity and Navier–Stokes equations are simplified. Typical engine 3D-flows like cylinder flows are necessarily compressible, but this compressibility is weak, that in fact the properties of the incompressible equations are valid.

2.4.1.3 Energy equation

The energy equation is derived from the first law of thermodynamics, which states that the rate of change of energy of a fluid particle is equal to the rate of heat addition to the fluid particle plus the rate of work done on the particle:

$$\begin{bmatrix} \text{Rate of increase} \\ \text{of energy of fluid} \\ \text{particle} \end{bmatrix} = \begin{bmatrix} \text{Net rate of heat} \\ \text{added to fluid} \\ \text{particle} \end{bmatrix} + \begin{bmatrix} \text{Net rate of work} \\ \text{done on fluid} \\ \text{particle} \end{bmatrix}$$

The total energy of a moving fluid per unit mass is the sum of its internal energy per unit mass and its kinetic energy per unit mass. By considering the terms on the right hand side, the rate of work done on the fluid particle in the element by a surface force is equal to the product of the force and velocity component in the direction of the force. The net rate of heat transfer to the fluid particle is resulted from volumetric heating such as absorption and heat transfer across the surface due to temperature gradients (thermal conduction).

As before with $\phi = E$, an equation for the rate of increase of energy of a fluid particle per unit volume is derived, which is given by

$$\rho \frac{DE}{Dt} \tag{2.13}$$

The total energy E is

$$E = e + \frac{1}{2}\left(u^2 + v^2 + w^2\right) \tag{2.14}$$

where e is the internal energy per unit mass and the second term is the kinetic energy per unit mass.

Here the final form of energy equation is presented. For more information about intermediate mathematical operations and equations of each term in detail see (Wendt, 2008).

$$\rho\frac{DE}{Dt}=\frac{\partial(\rho E)}{\partial t}+\nabla\cdot(\rho E\mathbf{u})=\rho\dot{q}+\frac{\partial}{\partial x}\left(k\frac{\partial T}{\partial x}\right)+\frac{\partial}{\partial y}\left(k\frac{\partial T}{\partial y}\right)$$
$$+\frac{\partial}{\partial z}\left(k\frac{\partial T}{\partial z}\right)-\frac{\partial(up)}{\partial x}-\frac{\partial(vp)}{\partial y}-\frac{\partial(wp)}{\partial z}+\frac{\partial(u\tau_{xx})}{\partial x}+\frac{\partial(u\tau_{yx})}{\partial y}+\frac{\partial(u\tau_{zx})}{\partial z} \quad (2.15)$$
$$+\frac{\partial(v\tau_{xy})}{\partial x}+\frac{\partial(v\tau_{yy})}{\partial y}+\frac{\partial(v\tau_{zy})}{\partial z}+\frac{\partial(w\tau_{xz})}{\partial x}+\frac{\partial(w\tau_{yz})}{\partial y}+\frac{\partial(w\tau_{zz})}{\partial z}+\rho f_i\cdot\mathbf{u}\ .$$

Where $\dot{q}$ is the heat transferred per unit time per unit area by thermal conduction, k is the thermal conductivity and $\rho f_i\cdot\mathbf{u}=\rho\left(uf_x+vf_y+wf_z\right)$.
Eq.(2.15) is the conservation form of energy equation, written in terms of total energy. There are alternative forms of the energy equation and the equation can be written in terms of enthalpy h or total enthalpy $\left[h+\frac{1}{2}\left(u^2+v^2+w^2\right)\right]$.

2.4.1.4 Species transport

The Species Transport Module provides the necessary transport equations for gas and liquid phase chemical species in the computational domain. Several options are available for the calculation of the physical properties of the chemical species and the mixture of gases and liquids.
Depending on the application, AVL FIRE® offers two main options;

- general species transport model
- standard species transport model

In current study, standard species transport model is used. In order to reduce the number of equations to be solved, dimensionless quantities are introduced to represent the reactive system (Simple Chemical Reacting System (SCRS) (Spalding, 2013)). The SCRS involves a reaction between two reactants(fuel and oxidizer) and the reaction may proceed by more than one step.

$$Fuel+Oxidizer\rightarrow Product$$

Fuel mass fraction is defined as:

$$y_{\text{fu}} = \frac{m_{\text{fu},u}}{m_{tot}} \tag{2.16}$$

Where $m_{\text{fu},u}$ is the mass of unburned fuel and m_{tot} is the total mass of mixture.

The mixture fraction is defined as the sum of the unburned fuel mass $m_{\text{fu},u}$ and the mass of fuel in the burnt phase $m_{\text{fu},b}$, divided by the total mixture mass m_{tot} :

$$\text{f} = \frac{m_{\text{fu},u} + m_{\text{fu,b}}}{m_{tot}} \tag{2.17}$$

The amount of EGR is defined by introducing the residual gas mass fraction:

$$g = \frac{m_{rg}}{m_{oxid}} \tag{2.18}$$

Where m_{rg} is the residual gas mass and m_{oxid} is the mass of oxidizer. EGR changes the fluid from originally pure air to a mixture of air and residual gas, thus the oxidizer mass is defined as

$$m_{oxid} = m_{air} + m_{rg} \tag{2.19}$$

It should be mentioned, mass fraction of EGR is not related to the total mass in the system and just explains the amount of residual gas within the oxidizer.

The solution of transport equations for the density weighted mean quantities with $\phi = Y$, where Y denotes the mass fraction;

$$\left[\begin{array}{c}\text{Rate of increase}\\ \text{of Y of fluid}\\ \text{element}\end{array}\right] + \left[\begin{array}{c}\text{Net rate of flow}\\ \text{of Y out of fluid}\\ \text{element}\end{array}\right] = \left[\begin{array}{c}\text{Rate of increase}\\ \text{of Y due to}\\ \text{diffusion}\end{array}\right] + \left[\begin{array}{c}\text{Rate of}\\ \text{increase of Y}\\ \text{due to sources}\end{array}\right]$$

Hence

$$\rho\frac{DY}{Dt} = \frac{\partial(\rho Y)}{\partial t} + \nabla\cdot(\rho Y\mathbf{u}) = \rho\left[\frac{\partial Y}{\partial t} + \mathbf{u}\cdot\nabla Y\right] = -\nabla\cdot J + \rho\dot{r} \tag{2.20}$$

Where $\dot{r}$ is the reaction rate and from Fick's law J is defined as:

For laminar flows

$$J_i = -\rho D_i \nabla Y_i \tag{2.21}$$

And for turbulent flows

$$J_i = -\left(\rho D_i + \frac{\mu_t}{Sc_t}\right)\nabla Y_i \tag{2.22}$$

Here D_i is the diffusion coefficient for species i in the mixture, μ_t is turbulent viscosity and Sc_t is the turbulent Schmidt number with a default setting of 0.7.

By considering Eq.(2.20), the term of J is the diffusive mass flux and the second term $\rho\dot{r}$ represents the rate of creation by the mass addition to the continuous phase from dispersed phase (due to vaporization of liquid droplets) and any user-defined sources. The determination of the mean reaction rate $\rho\dot{r}$ of Eq.(2.20) is the primary objective of combustion modeling.

2.4.2 Equations of state

The motion of a fluid in three dimensions is described by a system of five partial differential equations: mass conservation (2.3), x, y and z-momentum equations ((2.11)) and energy equation (2.15) in terms of seven unknown flow-field variables. Among the unknowns, there are four thermodynamic variables: ρ, p, e and T. Relationships between the thermodynamic variables can be obtained through the assumption of thermodynamic equilibrium. The fluid velocities may be large, but they are usually small enough that, even though properties of a fluid particle change rapidly from place to place, the fluid can thermodynamically adjust itself to new conditions so quickly that the changes are effectively instantaneous. Thus the fluid always remains in thermodynamic equilibrium. Equations of state relate the other variables to the two state variables. If ρ and T are used as state variables, we have state equations for pressure p and specific internal energy e.

$$p = p(\rho, T) \qquad \text{and} \qquad e = e(\rho, T) \tag{2.23}$$

For a perfect gas:

$$p = \rho RT \qquad and \qquad e = c_v T \tag{2.24}$$

Where R is the specific gas constant and c_v is the specific heat at constant volume.
The assumption of thermodynamic equilibrium eliminates all but the two thermodynamic state variables. In the flow of compressible fluids, the equations of state provide the linkage between the energy equation on the one hand and mass conservation and momentum equations on the other hand. This linkage arises through the possibility of density variations as a result of pressure and temperature variations in the flow field.
Liquids and gases flowing at low speeds behave as incompressible fluids. Without density variations there is no linkage between the energy equation and the mass conservation and momentum equations. The flow field can often be solved by considering mass conservation and momentum equations only. The energy equation

only needs to be solved alongside the others if the problem involves heat transfer. All current CFD codes use the equations of state for ideal gases.

2.5 Turbulence

The speed of flame front propagation depends heavily on the flow condition of the surrounding gas. Laminar (low Reynolds number, low flow velocity) and turbulent flows (high Reynolds number, high local flow velocity) are two major forms of fluid flow. In case of laminar flow, fluid layers move in parallel to each other with no disruption between the layers in the direction of flow. Mixing and transport of the reaction partners take place relatively slowly via molecular diffusion processes and shear stress depends only on the viscosity of the fluid and independent of the density While in a turbulent flow field, different streams of fluid form eddies and unpredictable currents in a different direction than the overall direction of flow and fluid layers cross each other. Moreover, mixing and transport of the reaction partners are facilitated by turbulent eddies within the flow and shear stress depends on the density of the fluid. (Heywood, 1988).

Most IC engine related fluid flow problems are turbulent flows. Hence, as a basis for precisely simulating the real flows, accurately modeling the phenomenon of turbulence is very important. This is in particular necessary, since turbulence not only determines the details of the fluid flow itself, but also strongly influences the physical and chemical processes taking place during mixture formation and combustion. For instance, in IC engines the turbulent kinetic energy is a major influencing factor on the propagation and evaporation of liquid fuel spray droplets and the subsequent combustion of the air-fuel mixture.

2.5.1 Turbulence modeling

To simulate the turbulent flows numerically, there are three primary methods.

- Reynolds-Averaged Navier-stokes (RANS) models
- Large Eddy simulation (LES)
- Direct Numerical simulation (DNS)

However, among three available approaches DNS is the most accurate one and all turbulent flows can be simulated by numerically solving the full Navier-Stokes equations and no modeling is required, this approach is the most computationally expensive way in high Reynolds flows. The DNS grids are very fine and resolves the whole spectrum of scales, therefore this method requires enormous computational resources for highly turbulent flows. In case of RANS models, all turbulent length scales are modeled for mean flow and the governing equations can be time-averaged or ensemble-averaged with time-dependent boundary conditions to remove the small scales and resulting in a modified set of equations that are computationally less expensive to solve. LES technique, which consists of resolving governing equations for energy containing large scales and modeling the smaller scales, lies between these two approach. Although, the modified equations contain additional unknown variables and turbulence models are needed to determine these variables in terms of known quantities and to achieve closure, RANS models are widely used in engineering applications.
In general, the RANS based turbulence models are divided into zero, one and two equation models according to the number of the equations that they solve to obtain the turbulent viscosity. The zero-equation models also called algebraic models are calculated directly from the flow variables. There are several two-equation models, which are based on solving differential equations. Three of the most popular and widely used models are the k-ε model of Jones and Launder (1972), the k-ω model of Wilcox (1998) and the SST model of Menter (1994) which blends the k-ε model in the outer region and k-ω model in the near wall region.
AVL FIRE® provides various turbulence models and some of RANS based models are listed as following:

- RANS based models
  - One equation models
    - Spalart-Allmaras model
  - Two equation models
    - Standard k-ε model
    - Renormalization-group (RNG) k-ε model
    - Realizable k-ε model

    - Standard k-ω model
    - Shear-Stress Transport (SST) k-ω model
- Seven equation model
    - Reynolds Stress Model (RSM)

Unfortunately, no single turbulence model is universally accepted as being superior for all cases of problems and the choice of turbulence model depends on considerations such as the level of required accuracy, the available computational resources and the time available for the simulation. In order to choose the most appropriate model, understanding the capabilities and limitations of various options is necessary.

2.5.2 k-ε model

The k-ε model is the most widely used turbulence model, particularly for industrial computations and has been implemented into most CFD codes. It is numerically robust and has been tested in a broad variety of flows including heat transfer, combustion and two-phase flows. It is generally accepted that the k-ε model usually yields reasonably realistic predictions of major mean-flow features in most situations. It is particularly recommended for a quick preliminary estimation of the flow field or in situations where modeling other physical phenomena such as chemical reactions, combustion, radiation, multi-phase interactions brings in uncertainties that outweigh those inherent in the k-ε turbulence model. The standard k-ε(Launder and Spalding, 1974) model consists of the transport equations for the turbulent kinetic energy k and for turbulent dissipation rate ε. The model transport equation for k is derived from the exact equation, while the model transport equation for ε is obtained using physical reasoning and has little resemblance to its mathematically exact counterpart.

k and ε are used to define velocity scale ϑ and length scale l representative of the large-scale turbulence as follows:

$$\vartheta = k^{1/2} \qquad , \qquad l = \frac{k^{3/2}}{\varepsilon} \tag{2.25}$$

The turbulent or eddy viscosity is specified by applying dimensional analysis as follows:

$$\mu_t = \rho C_\mu \frac{k^2}{\varepsilon} \tag{2.26}$$

Where C_μ is a dimensionless constant.

The standard k-ε model uses the following transport equations for k and ε:

$$\rho\frac{Dk}{Dt} = \frac{\partial(\rho k)}{\partial t} + \nabla\cdot(\rho k\mathbf{u}) = \nabla\cdot\left[\left(\frac{\mu_t}{Pr_k}\right)\nabla k\right] + 2\mu_t S_{ij}\cdot S_{ij} - \rho\varepsilon + S_k \tag{2.27}$$

$$\rho\frac{D\varepsilon}{Dt} = \frac{\partial(\rho\varepsilon)}{\partial t} + \nabla\cdot(\rho\varepsilon\mathbf{u}) = \nabla\cdot\left[\left(\frac{\mu_t}{Pr_\varepsilon}\right)\nabla\varepsilon\right] + C_{1\varepsilon}\frac{\varepsilon}{k}2\mu_t S_{ij}\cdot S_{ij} - C_{2\varepsilon}\rho\frac{\varepsilon^2}{k} + S_\varepsilon \tag{2.28}$$

Where, $C_{1\varepsilon}$ and $C_{2\varepsilon}$ are constants and given in Table 2.1. Pr_k and Pr_ε are the turbulent Prandlt numbers for k and ε ,respectively. S_k and S_ε are user defined source terms. The shear tensor S_{ij} is defined as

$$S_{ij} = \frac{1}{2}\left(\frac{\partial u_j}{\partial x_i} + \frac{\partial u_i}{\partial x_j}\right). \tag{2.29}$$

With the help of k and ε, the diffusion constants for the additional turbulent diffusion terms can be calculated in the transport equations.

The model constants have the following default values which have been determined from experiments:

Table 2.1 : Coefficients of standard k–ε-model.

Model	C_μ	$C_{1\varepsilon}$	$C_{2\varepsilon}$	Pr_k	Pr_ε
Standard	0.09	1.44	1.92	1.0	1.3

Production and destruction of turbulent kinetic energy are always closely linked. Dissipation rate ε is large where production of k is large. The model equation(2.28) for ε assumes that its production and destruction terms are proportional to the production and destruction terms of the k-equation(2.27). Adoption of such forms ensures that ε increases rapidly if k increases rapidly and that it decreases sufficiently fast to avoid (non-physical) negative values of turbulent kinetic energy if k decreases. Constants $C_{1\varepsilon}$ and $C_{2\varepsilon}$ allow for the correct proportionality between the terms in the k and εequations. In current study, standard k-ε model is used for modeling the turbulence.

2.6 Combustion Models

Modeling the combustion chemistry and the turbulence/chemistry interaction during hydrocarbon oxidation is the major challenge in simulating turbulent reacting flows. The chemical kinetic reactions of typical hydrocarbon fuels involve hundreds of intermediate species and their reaction paths usually comprise of several hundred up to several thousand of reaction steps. Neither are the reaction details and the related rate coefficients of relevant hydrocarbon fuels known in sufficient detail nor would it be possible to account for the entire set of reactions within an engineering environment due to excessively high computational demands. The intimate coupling between the chemistry and the flow field quantities results from the high non-linearity of the chemical reaction rates under the presence of local stochastic fluctuations of the flow and composition fields. The common practice adopts an averaging procedure replacing the instantaneous flow field quantities by its mean and fluctuating components. Mathematically this results in the appearance of terms in the conservation equations which contain statistical correlations of fluctuating components that have to be expressed based upon known mean flow quantities. A large variety of models of various levels of complexity and sophistication have been proposed in the last decades in order to appropriately model the complex hydrocarbon auto-ignition and combustion chemistry and the mean rate of reaction in the relevant conservation equations. Depending on the specific IC-engine combustion system and the underlying combustion regimes, tailored models are required in order to cover the relevant physical and chemical processes to be considered. In the following, an overview of the models adopted in in this study for calculation of ignition and combustion processes in spark-ignition and compression-ignition engine configurations is provided.

2.6.1 SI combustion

The premixed flame propagation characteristic during SI-engine combustion is mainly determined by the in-cylinder turbulent flow, the local mixture composition distribution and the in-cylinder pressure and temperature conditions in the unburned charge ahead of the flame. The local turbulent flame speed itself is governed by the fuel specific laminar flame velocity and by the turbulent fluctuations of the flow field, resulting in wrinkling of the flame.

2.6.1.1 Coherent flame model (flame surface density model)

The Coherent Flame Model (CFM) which is developed by Richard et al. (2007); also called the flame surface density model, provides an improved physical description. In it, turbulence does not directly accelerate the flame, but wrinkles it more strongly. However, a more strongly wrinkled flame burns faster.

For this purpose, an additional transport equation is solved for the flame surface density Σ (flame surface per volume unit), or instead, for the specific flame surface $\sigma = {}^{\Sigma}/_{\rho}$. This equation exists in the various versions, see (Poinsot and Veynante, 2005). One typical variant reads

$$\rho\left(\frac{\partial}{\partial t}+v_i\frac{\partial}{\partial x_i}\right)\sigma-\frac{\partial}{\partial x_i}\left[\rho D_t\frac{\partial\sigma}{\partial x}\right]=\alpha_F\frac{\varepsilon}{k}\rho\sigma-\beta_F\frac{s_l}{c\,(1-c)}\,(\rho\sigma)^2 \quad , \tag{2.30}$$

where

$$D_t=c_\mu\frac{k^2}{\varepsilon}\ , \tag{2.31}$$

and α_F and β_F contain, besides model constants, functional dependencies on the turbulent and chemical time and length scales. The first term on the right side describes the flame surface production from turbulence, the second term represents a sink caused by burn-out. In addition, another transport equation must be solved for the progress variable

$$\rho\left(\frac{\partial}{\partial t}+v_i\frac{\partial}{\partial x_i}\right)c-\frac{\partial}{\partial x_i}\left(\rho D_t\frac{\partial}{\partial x_i}c\right)=\rho_u s_l\rho\sigma\ . \tag{2.32}$$

According to Gülder (1984),the laminar burning velocity is given as

$$s_l=W\Phi^\eta\exp\left(-\xi\,(\Phi-\Phi^*)^2\right)\left[\frac{T_u}{T_{ref}}\right]^\alpha\left[\frac{p}{p_{ref}}\right]^\beta \quad . \tag{2.33}$$

where T_u is the mixture temperature in the unburned part and $\Phi = {}^1/_\lambda$ is the fuel-air ratio. The following parameters are also used:

Table 2.2 : Parameters used in laminar burning velocity Eq.(2.33).

$W[m/sec]$	η	ξ	α	β	T_{ref}	p_{ref}	Φ^*
0.47	-0.33	4.48	1.56	-0.22	300	1	1.04

If an equilibrium between flame surface production and destruction exists in Eq.(2.30), then:

$$(\rho\sigma)_{eq} s_l = \frac{\alpha_F}{\beta_F}\frac{\varepsilon}{k} c(1-c) \quad . \tag{2.34}$$

In the case of flame surface density models, the flame front is again well-described by a solitary wave (this time in the σ and c-field), with a well-defined propagation speed and well-defined c and σ profiles. The c field goes thereby from 0 (in front of the flame) to 1 (behind the flame), while σ starts at zero before the flame, increases to a maximum value in the flame, in order then to fall again to zero towards the rear flame front. To calculate the propagation speed of a planar flame front, determining the propagation speed of the flame forefront; for this, Eq.(2.30) and Eq.(2.32) have to be linearized in σ and c, where $\rho = \rho_u$. The equations thus obtained read

$$\begin{aligned} \rho_u\left(\frac{\partial}{\partial t} + v\frac{\partial}{\partial x}\right)\sigma - \rho_u D_t \frac{\partial^2\sigma}{\partial x^2} &= \alpha_F \frac{\varepsilon}{k}\rho_u\sigma - \beta_F s_l (\rho_u)^2 \left(\frac{\sigma}{c}\right)\sigma \quad , \\ \rho_u\left(\frac{\partial}{\partial t} + v\frac{\partial}{\partial x}\right)c - \rho_u D_t \frac{\partial^2 c}{\partial x} &= (\rho_u)^2 s_l \left(\frac{\sigma}{c}\right) c \quad . \end{aligned} \tag{2.35}$$

One recognizes that a stationary solution with $\sigma/c = const$.exists

$$\begin{aligned} c(x,t) &= c_0 \exp\left(-\omega\left(x-(v+s_t)t\right)\right) \quad , \\ \sigma(x,t) &= \sigma_0 \exp\left(-\omega\left(x-(v+s_t)t\right)\right) \quad . \end{aligned} \tag{2.36}$$

Insertion into Eq.(2.35) provides

$$\begin{aligned} \omega s_t - D_t\omega^2 &= \alpha_F\frac{\varepsilon}{k} - \beta_F s_l \rho_u \frac{\sigma_0}{c_0} \quad , \\ \omega s_t - D_t\omega^2 &= s_l\rho_u\frac{\sigma_0}{c_0} \quad , \end{aligned} \tag{2.37}$$

which finally leads to

$$\omega = \frac{s_t \pm \sqrt{s_t^2 - 4D_t \frac{\alpha_F}{\beta_F + 1} \frac{\varepsilon}{k}}}{2D_t} \quad . \tag{2.38}$$

According to the KPP theorem, the propagation speed follows

$$s_t = 2\sqrt{D_t \frac{\alpha_F}{\beta_F + 1} \frac{\varepsilon}{k}} \quad . \tag{2.39}$$

Depending on the concrete formulation of the initial Eq. (2.30), this calculation may have a somewhat different outcome.

2.6.1.2 Extended coherent flame models (ECFM)

The ECFM has been mainly developed in order to describe combustion in DI-SI engines. This model is fully coupled to the spray model and enables stratified combustion modeling including EGR effects and NO formation. The model relies on a conditional unburned/burnt description of the thermochemical properties of the gas. The ECFM contains all the features of the CFM.

This class of models is based on SI engine CFM models describing a flame front combustion. There is an averaging between auto-ignition (very fast reaction kinetics) and diffusion combustion, but not between flame front propagation and diffusion combustion. Typically, several zones are introduced locally:

- Air zone; unmixed
- Fuel zone; unmixed
- Mixed zone; (air + residual gas) + fuel + combustion product

For turbulent combustion phenomena, the ECFM model leads to the calculation of the mean fuel reaction rate. Hence, this model uses a 2-step chemistry mechanism for the fuel conversion like:

$$\mathrm{C}_n\mathrm{H}_m\mathrm{O}_k + \left(n + \frac{m}{4} - \frac{k}{2}\right)\mathrm{O}_2 \rightarrow n\,\mathrm{CO}_2 + \frac{m}{2}\,\mathrm{H}_2\mathrm{O} \tag{2.40}$$

$$\mathrm{C}_n\mathrm{H}_m\mathrm{O}_k + \left(\frac{n}{2} - \frac{k}{2}\right)\mathrm{O}_2 \rightarrow n\,\mathrm{CO} + \frac{m}{2}\,\mathrm{H}_2 \tag{2.41}$$

in order to consider CO and H_2 formation in near stoichiometric and fuel rich conditions, while for fuel lean conditions their formation is neglected. In the above formula n, m and k represent the number of carbon, hydrogen and oxygen atoms of the considered fuel.

The reaction rate for reaction (2.40) is calculated by:

$$\omega_{\mathrm{fu},1} = \omega_L \gamma \tag{2.42}$$

with γ as a function depending on the equivalence ratio ϕ, number of carbon and hydrogen atoms, respectively, and for the second fuel consumption reaction (2.41):

$$\omega_{\mathrm{fu},2} = \omega_L (1-\gamma) \tag{2.43}$$

where ω_L is mean laminar fuel consumption rate per unit surface along the flame front and the mean turbulent reaction rate is computed as the product of the flame surface density σ and the laminar burning velocity S_L via;

$$\overline{\rho \dot{r}_{\mathrm{fu}}} = -\omega_L \Sigma \tag{2.44}$$

where

$$\omega_L = \rho_{\mathrm{fu,fr}} S_L \quad \text{with} \quad \rho_{\mathrm{fu,fr}} = \rho_{\mathrm{fr}} y_{\mathrm{fu,fr}} \tag{2.45}$$

In this equation, $\rho_{\mathrm{fu,fr}}$ is the partial fuel density of the fresh gas, ρ_{fr} the density of the fresh gas and $y_{\mathrm{fu,fr}}$ is the fuel mass fraction in the fresh gas.

The individual reaction rates of each species i participating in the 2-step reaction mechanism can be expressed by:

$$\omega_i = \sum_{r=1}^{2} \upsilon_{i,r} \omega_{\mathrm{fu},r} \tag{2.46}$$

with $\upsilon_{i,r}$ as the stoichiometric coefficients of species i in the reaction r, while for the reactants these coefficients are negative and for the products positive, respectively.

Therefore the mean turbulent fuel reaction rate is computed as the product of the flame surface density σ and the laminar burning velocity S_L via:

$$\overline{\rho \dot{r}_{\mathrm{fu}}} = -\Sigma \sum_{r=1}^{2} \upsilon_{i,r} \omega_{\mathrm{fu},r} \cong -\Sigma \omega_L = \begin{cases} \gamma & \text{for rection(2.40)} \\ (1-\gamma) & \text{for rection(2.41)} \end{cases} \tag{2.47}$$

It is obvious that the extended CFM can be closed if the local properties of the burnt and unburned gases are known. Hence, in each computational cell two concentrations have to be calculated: a concentration in the unburned gases and a concentration in the burnt gases, respectively. Hence two additional transport equations have to be introduced, one for the unburned fuel mass fraction and one for the unburned oxygen mass fraction. In case of spray applications a source term S_{evap} for the unburned fuel mass fraction has to be added. Using these two additional equations and the hypothesis of local homogeneity and isotropy each mass fraction can be determined. Below the two transport equations are given:

$$\frac{\partial}{\partial t}\left(\rho y_{\mathrm{fu,fr}}\right)+\frac{\partial}{\partial x_j}\left(\rho U_j y_{\mathrm{fu,fr}}\right)-\frac{\partial}{\partial x_j}\left(\frac{\mu_{\mathrm{eff}}}{\sigma_i}\frac{\partial y_{\mathrm{fu,fr}}}{\partial x_j}\right)=S_{evap} \tag{2.48}$$

$$\frac{\partial}{\partial t}\left(\rho y_{\mathrm{O_2,fr}}\right)+\frac{\partial}{\partial x_j}\left(\rho U_j y_{\mathrm{O_2,fr}}\right)-\frac{\partial}{\partial x_j}\left(\frac{\mu_{\mathrm{eff}}}{\sigma_i}\frac{\partial y_{\mathrm{O_2,fr}}}{\partial x_j}\right)=0 \tag{2.49}$$

Additionally, a transport equation for the unburned gas enthalpy is also introduced as shown below:

$$\frac{\partial}{\partial t}\left(\rho \mathrm{h_{fr}}\right)+\frac{\partial}{\partial x_j}\left(\rho U_j \mathrm{h_{fr}}\right)-\frac{\partial}{\partial x_j}\left(\frac{\mu_{\mathrm{eff}}}{\sigma_i}\frac{\partial \mathrm{h_{fr}}}{\partial x_j}\right)=\rho\varepsilon+\frac{\rho}{\rho_{\mathrm{fr}}}\frac{\partial p}{\partial t}+\mathrm{h}_{evap} \tag{2.50}$$

with a source term h_{evap} in case of evaporation of the liquid fuel. Using the unburned enthalpy and unburned gas composition, the local unburned gas temperature can be calculated.

It is supposed that the unburned gas phase consists of 5 main unburned species, namely fuel, oxygen, molecular nitrogen, carbon dioxide and water, while for the burnt gas phase it is assumed that no fuel remains any more since due to the high temperature region the fuel molecules decompose. The burnt gas is composed of 11 species, such as the atomic and molecular oxygen, nitrogen and hydrogen (O, O_2, N, N_2, H, H_2), carbon monoxide and dioxide, water, OH and NO. Using $y_{\mathrm{fu,fr}}$ and $y_{\mathrm{O_2,fr}}$ as mass fractions of the fresh fuel and oxygen tracer, the richness ϕ_{fr} of the fresh gas can be immediately obtained as the ratio of those properties like:

$$\phi_{\mathrm{fr}}=\alpha_{\mathrm{fu}}\frac{y_{\mathrm{fu,fr}}}{y_{\mathrm{O_2,fr}}} \tag{2.51}$$

where α_{fu} is a constant stoichiometric function of the considered fuel.

The fresh gas nitrogen mass fraction can be easily obtained as sum of all nitrogen containing mass fractions. In case of residual gas consideration, the remaining gas in the fresh gas phase is considered to be CO_2 and H_2O, respectively. The CO_2 mass fraction in the unburned gas phase is obtained as function of all carbon containing species while the fresh gas H_2O mass fraction depends on all hydrogen containing species and the fuel mass fractions, respectively.

The remaining quantity to be determined is the composition of the burnt gas phase. Due to the assumption that no fuel exists any more in the burnt phase, the knowledge of the mass fractions in the unburned phase leads directly to the mass fractions of the burnt gas. Hence, the composition of the burnt gas can be re-constructed using the Favre-averaged progress variable c as described previously. If y_i is the mean Favre-averaged mass fraction of species i, the burnt mass fraction (index b) is calculated via:

$$y_{i,b} = \frac{y_i - (1-c)\, y_{i,\mathrm{fr}}}{c} \tag{2.52}$$

2.6.2 CI combustion

For calculating the combustion process in diesel engines the combustion model (ECFM-3Z) adopted in AVL FIRE® distinguishes between the three major regimes relevant during compression-ignition combustion, namely auto-ignition, premixed flame and non-premixed diffusion combustion. The auto-ignition pre-reactions are calculated within the premixed charge of fuel and air, with the ignition delay governed by the local temperature, pressure, fuel/air equivalence ratio and the amount of residual gas. Local auto-ignition is followed by premixed combustion in the fuel/air/residual gas charge formed during the time period between start-of-injection and auto-ignition onset. The third regime is the one of diffusion combustion where the reaction takes place in a thin zone which separates fuel and oxidizer. In the adopted model it is assumed that the chemical time in the reaction zone is much smaller than the time needed for the diffusion process. Therefore, the rate of reaction during diffusion combustion is determined entirely by the intermixing of fuel and oxidizer. The amount

of mixing is computed with a characteristic time-scale obtained from the solution of the adopted turbulence model (Colin and Benkenida, 2004).

2.6.2.1 ECFM-3Z model

The existing ECFM model is devoted to gasoline combustion. The ECFM-3Z (three-zone extended coherent flame model) was developed by the GSM consortium (Groupement Scientifque Moteurs) specifically for diesel combustion. This is a combustion model based on a flame surface density transport equation and a mixing model that can describe inhomogeneous turbulent premixed and diffusion combustion. The model relies on the ECFM combustion model, previously described and implemented in AVL FIRE® and on a three areas mixing description. Further it is coupled with an improved burnt gas chemistry description compared to ECFM. Up to now the ECFM-3Z combustion model was only applicable for auto-ignition cases, although the code is prepared to handle for both ignition procedures, auto-ignition and spark ignition. Now the gasoline engine ECFM combustion model can also be activated via the ECFM-3Z mode using all the attractive features such as the general species treatment or separate CO/CO_2 oxidation reaction mechanism.

For prediction of the auto-ignition delay tabulated ignition data are used which are stored in look-up tables that are available in AVL FIRE® for different fuels, generated based upon chemical kinetic calculations adopting complex reaction schemes. The tabulated values are stored as functions of the parameters pressure, temperature, fuel/air equivalence ratio and residual gas content. The range of these parameters has been chosen in a way to be able to cover the relevant in-cylinder pressure, temperature and charge-mixture composition conditions prior to combustion. For the actual determination of the auto-ignition delay time in the CFD simulation, a transport equation for an auto-ignition indicator species is solved with the formation rate derived from the tabulated values. Once the local value of the indicator species attains a certain threshold value, auto-ignition is initiated. Fuel consumption is then controlled by a characteristic chemical time-scale which ensures rapid combustion after auto-ignition (Colin et al., 2005).

The hydrocarbon oxidation process during high temperature combustion is separated into three major reaction steps. First the fuel is partly oxidized to CO and to CO_2, followed by CO oxidation, and finally a post-flame equilibrium chemistry approach

is applied which results in the final species concentrations. The above described combustion reactions cover the relevant range of mixture composition from lean to rich and the different levels of residual gas content. In addition to the amount of heat that is released within the flame the procedure provides all relevant information about CO and radical species which are important for the subsequent calculation of the pollutants.

2.6.2.2 Eddy breakup model

The simplest method of modeling a turbulent diffusion flame is the so-called "eddy breakup model". It describes decay and formation processes that run with the turbulent breakup time

$$\tau_t \propto \frac{k}{\varepsilon} \tag{2.53}$$

A heat release is calculated corresponding to the conversion rate. To describe diesel combustion, the combustion progress must still be modeled. The most well-known and used method for this is the mixing time-scale model (Patterson and Reitz, 1998). In which, from the turbulent and a chemical time scale(τ_t and τ_{chem}), an effective time scale τ_{eff} is formed, with which the combustion processes proceed

$$\tau_{eff} = \tau_{chem} + f\tau_t, \quad f = \frac{1-\exp(-r)}{1-\exp(-1)}, \quad \tau_{chem} \ll \tau_t = c_\mu \frac{k}{\varepsilon} \ , \tag{2.54}$$

whereby r designates the mass fraction of all reaction products. At the start of the reaction, $f = 0$, i.e. the effective time scale corresponds to the (small) chemical time scale, the reaction progresses very quickly, and a "premixed peak" occurs. With the increase in reaction products, f increases (to 1 maximally), and now $\tau_{eff} \approx f \cdot \tau_t$ is valid, i.e. we now have a diffusion combustion. The mixing timescale model uses seven species N_2, O_2, fuel, H_2O, CO_2, CO and H_2. From a given distribution of concentration $(c^*_{(k)}, k = 1...7)$, the corresponding equilibrium distribution $(c^*_{(k)}, k = 1...7)$ is calculated. We assume that every species tends towards local equilibrium with the time scale τ_{eff}

$$\rho\left(\frac{\partial}{\partial t} + v_i\frac{\partial}{\partial x_i}\right)c_k - \frac{\partial}{\partial x_i}\left(D_t\rho\frac{\partial}{\partial x_i}c_k\right) = \rho\frac{c^*_{(k)} - c_k}{\tau_{eff}} \ . \tag{2.55}$$

The chemical equilibrium code for the mixing time-scale model works with two

lambda regimes. The limit between both of these regimes is given by the air-fuel ratio at which the fuel can be completely converted with the existing oxygen to CO and H_2. In the "rich" regime, the lambda values of which are lower than this limiting value, the equilibrium is determined such that the total available oxygen is utilized to create CO and H_2 from the fuel. In addition however, unburned fuel remains. In the "lean" regime, the lambda values of which are higher than the limiting value, we assume that no fuel remains. Besides the non-reactive N_2, five reactive species thus still remain, H_2O, H_2, O_2, CO and CO_2. Their equilibrium concentration is calculated by means of three elemental mass fraction conservation equations (for C, O and H) as well as two relations, which follow from the law of mass action

$$\frac{[CO_2]}{[CO][O_2]^{0.5}} = K_C(p,T) \ , \tag{2.56a}$$

$$\frac{[H_2O]}{[H_2][O_2]^{0.5}} = K_H(p,T) \ . \tag{2.56b}$$

From these five equations, we obtain a polynomial of fourth order, which can be solved analytically with the corresponding solution formula. Corresponding to the reaction rates of the species, a source term for the enthalpy equation is determined by means of their specific reaction enthalpy $h_{(k)}$

$$q = \rho \sum_k h_{(k)} \dot{c}_{(k)} \ . \tag{2.57}$$

With this seven-species method, local conditions can be very well prescribed, even in the rich area. Both in the modeling of reaction-kinetic influences and in turbulence interaction, the mixing time-scale model is however still very simple. Nevertheless, one can already analyze basic dependencies and mechanisms of diesel engine combustion with this modeling approach.
instead of seven species, we can also work with fewer, the minimum being three:

- Oxidants (air + recirculated residual gas)
- Fuel
- Combustion products

These three species are of a formal nature.

2.7 Multiphase Spray Module

This section describes the theory and equations of the AVL FIRE® Spray module. Spray simulations involve multi-phase flow phenomena and as such require the numerical solution of conservation equations for the gas and the liquid phase simultaneously. With respect to the liquid phase, practically all spray calculations are based on a statistical method referred to as the Discrete Droplet Method (DDM) (Dukowicz, 1980). This operates by solving ordinary differential equations for the trajectory, momentum, heat and mass transfer of single droplets, each being a member of a group of identical non-interacting droplets termed a parcel. Thus one member of the group represents the behavior of the complete parcel.

Droplet parcels are introduced in the flow domain with initial conditions of position, size, velocity, temperature and number of particles in the parcel. AVL FIRE® supports the introduction of droplets, emerging from a nozzle as a spray and entering the flow domain through the inlet areas as a gas/liquid mixture. The atomization process of sprays is accounted for with distinctive submodels. The droplet-gas momentum exchange, turbulent dispersion, evaporation of droplets, secondary break-up, droplet collision and droplet-wall interaction are covered with a comprehensive set of models which allow the usage of the module for many different flow regimes. The vapor of evaporating droplets is used as a source term of an additional transport equation for the vapor void fraction in Eulerian formulation. Solid particles can be calculated with the DDM approach by switching off particular models, e.g. the evaporation model.

The droplets are tracked in a Lagrangian way through the computational grid used for solving the gas phase partial differential equations. Full two-way coupling (interaction) between the gas and liquid phases is taken into account. In situations of negligible influence of the dispersed phase on the continuous one, the gas phase flow can be simulated in advance and the droplet simulation can be performed afterwards.

The typical application of the spray module is performed within a transient simulation of the gas phase flow. In this case the spray parcel introduction and parcels integration is done between two gas phase time steps.

2.7.1 Basic equations

The differential equations for the trajectory and velocity of a particle/droplet parcel are as follows:

2.7.1.1 Momentum

$$m_d \frac{\mathrm{d}u_{id}}{\mathrm{d}t} = F_{idr} + F_{ig} + F_{ip} + F_{ivm} + F_{ib}. \tag{2.58}$$

where F_{idr} is the drag force and given by:

$$F_{idr} = D_P \cdot \mathrm{u}_{irel} \tag{2.59}$$

D_P is the drag function, defined as:

$$D_P = \frac{1}{2}\rho_g A_d C_D |u_{rel}|. \tag{2.60}$$

C_D is the drag coefficient which generally is a function of the droplet Reynolds number Re_d and A_d is the cross-sectional area of the particle. From the various formulations in literature for the drag coefficient of a single sphere, FIRE uses the following formulation from Sch:

$$C_D = \begin{cases} \frac{24}{\mathrm{Re}_d C_P}\left(1 + 0.15\mathrm{Re}_d^{0.687}\right) & \mathrm{Re}_d < 10^3 \\ 0.44/C_P & \mathrm{Re}_d \geq 10^3. \end{cases} \tag{2.61}$$

The particle Reynolds Number is shown in the following equation where μ_g is the domain fluid viscosity.

$$\mathrm{Re}_d = \frac{\rho_g |u_{rel}| D_d}{\mu_g}. \tag{2.62}$$

When calculating the drag on small particles the Cunningham correction factor C_P based on Knudsen number Kn reduces the drag coefficient (Cunningham, 1910; Frolov, June 2011).

$$C_P = 1 + Kn_P\left(2.492 + 0.84e^{\frac{-1.74}{Kn_P}}\right) \qquad \text{with} \qquad Kn = \frac{\lambda}{D_d}. \tag{2.63}$$

The mean free path length λ in gaseous phase can be calculated as

$$\lambda = \frac{K_b T_g}{\sqrt{2}\pi l_g^2 p_g} \tag{2.64}$$

With mean molecule diameter in gas phase d_g=2.8e-10 m.

By considering the terms of Eq.(2.58), F_{ig} is a force including the effects of gravity and buoyancy

$$F_{ig} = V_P \cdot (\rho_P - \rho_g)\, g_i. \tag{2.65}$$

and F_{ip} is the pressure force, given by

$$F_{ip} = V_P.\nabla p \ . \tag{2.66}$$

F_{ivm} is the virtual mass force taking into account acceleration / deceleration of the medium surrounding the drops, particles or bubbles. This is treated by increased inertia of the Lagrangian parcels (half mass of displaced fluid is added). The additional force term finally reads as follows

$$\overrightarrow{F}_a = -\frac{1}{2} m_f \left(\frac{d\overrightarrow{v}}{dt} - \frac{D\overrightarrow{u}}{Dt} \right) \ . \tag{2.67}$$

with m_f denoting mass of displaced fluid, $\overrightarrow{v}$ parcel velocity and $\overrightarrow{u}$ ambient flow velocity.

F_{ib} summarizes other external forces called virtual mass force, magnetic or electrostatic forces, Magnus force or others. Provision is made for insertion by the user. The forces taken into account by default are the drag force F_{idr} and the gravitational force F_{ig} (the latter only if the gravitational force is activated for the domain flow too). Comparing the magnitude of all forces, the drag force is the only relevant force for fuel spray injection and combustion computation. Therefore, inserting above forces and relations into Eq.(2.58) and dividing it by the particle mass m_d the equation for the particle acceleration as used by default is:

$$\frac{\mathrm{d}u_{id}}{\mathrm{d}t} = \frac{3}{4} C_D \frac{\rho_g}{\rho_d} \frac{1}{D_d} |u_g - u_d| \left(u_{ig} - u_{id}\right) + \left(1 - \frac{\rho_g}{\rho_d}\right) g_i \ . \tag{2.68}$$

which can be integrated to get the particle velocity and from this the instantaneous particle position vector can be determined by integrating:

$$\frac{\mathrm{d}x_{id}}{\mathrm{d}t} = u_{id} \ . \tag{2.69}$$

2.7.2 Submodels

2.7.2.1 Evaporation

Several models are available for droplet heat-up and evaporation. Heat and mass transfer coefficients are set-up according to the model physics, but for fine tuning and matching with experimental data, two adjustment parameters (E_1, E_2) for the heat and mass transfer coefficients are provided for each model. In the second part of this study Dukowicz model which is described below, is used for modeling the droplet evaporation.

Heat and Mass Transfer Analogy (Dukowicz evaporation model) :
The heat and mass transfer processes are described by a model originally derived by Dukowicz (1979). Essentially it is based on the following assumptions:

- Spherical symmetry
- Quasi steady gas-film around the droplet
- Uniform droplet temperature along the drop diameter
- Uniform physical properties of the surrounding fluid
- Liquid – Vapor thermal equilibrium on the droplet surface

With the assumption of uniform droplet temperature, the rate of droplet temperature change is determined by the energy balance equation, which states that the energy conducted to the droplet either heats up the droplet or supplies heat for vaporization.

$$m_d c_{pd} \frac{\mathrm{d}T_d}{\mathrm{d}t} = L \frac{\mathrm{d}m_d}{\mathrm{d}t} + \dot{Q} \tag{2.70}$$

The convective heat flux $\dot{Q}$ supplied from the gas to the droplet surface is

$$\dot{Q} = \alpha A_s \left(T_\infty - T_s\right) \tag{2.71}$$

where α is the convective heat transfer coefficient through the film surrounding the droplet in the absence of mass-transfer and A_s is the droplet surface area.
In the evaporation model of Dukowicz, it is considered that the droplet is evaporating in a non-condensable gas. So it uses a two-component system in the gas phase, composed

of the vapor and the non-condensable gas, even though each component may consist of a mixture of different species.

Introducing the local surface heat flux $(\dot{q}_s)$ and the vapor mass flux $\left(\dot{\mathrm{f}}_{v,s}\right)$ with the assumption of uniformity of droplet surface conditions, the governing equation for the mass flux is written as

$$\frac{\mathrm{d}m_d}{\mathrm{d}t} = \dot{Q}\frac{\dot{\mathrm{f}}_{v,s}}{\dot{q}_s} \tag{2.72}$$

and then the droplet energy equation can be expressed as:

$$m_d c_{pd}\frac{\mathrm{d}T_d}{\mathrm{d}t} = \dot{Q}\left(1 + L\frac{\dot{\mathrm{f}}_{v,s}}{\dot{q}_s}\right) . \tag{2.73}$$

Eq.(2.72) defines the droplet mass change and Eq.(2.73) defines the transient droplet diameter and the droplet temperature. The ratio of the vapor mass flux to the surface heat flux can be re-expressed as follows

$$\frac{\dot{\mathrm{f}}_{v,s}}{\dot{q}_s} = \frac{\rho\beta}{k}\left(\frac{1}{1-Y_{v,s}}\right)\frac{\nabla_s Y_v}{\nabla_s T} . \tag{2.74}$$

The ratio $\frac{\nabla_s Y_v}{\nabla_s T}$ in Eq.(2.74) is determined by an analogy consideration based on the similarity of the heat and mass transfer differential equations and boundary conditions and results as:

$$\frac{\nabla_s Y_v}{\nabla_s T} = \frac{c_p}{Le\left[\frac{h_\infty - h_s}{Y_{v,\infty} - Y_{v,s}} - h_{v,s} + h_{g,s}\right]} . \tag{2.75}$$

where the Lewis number (Le) is defined as

$$Le = \frac{\rho c_p D}{\lambda}.$$

With the assumption that the Lewis number is unity (Le=1), the flux ratio in its final form can be written as:

$$\frac{\dot{\mathrm{f}}_{v,s}}{\dot{q}_s} = \frac{-B_y}{h_\infty - h_s - \left(h_{v,s} - h_{g,s}\right)\left(Y_{v,\infty} - Y_{v,s}\right)} \tag{2.76}$$

where B_y is the mass transfer number and is defined as

$$B_y = \frac{Y_{v,s} - Y_{v,\infty}}{1 - Y_{v,s}} \tag{2.77}$$

With the convective heat transfer coefficient in Eq.(2.71) replaced by the Nusselt number (Nu), the convective heat flux $\left(\dot{Q}\right)$ supplied from the gas to the droplet surface

is

$$\dot{Q} = D_d \pi \lambda \mathrm{Nu} \left(T_\infty - T_s\right) \quad . \tag{2.78}$$

For spherical droplets the heat flux $\left(\dot{Q}\right)$ can be obtained from heat transfer coefficient correlations.

The Nusselt number (Nu) is obtained from the following correlation proposed by Ranz and Marshall (1952) for single droplets and confirmed to apply to certain types of sprays by Bose and Pei (1964).

$$\mathrm{Nu} = 2 + 0.6 \mathrm{Re}_d^{1/2} \mathrm{Pr}^{1/3} \quad . \tag{2.79}$$

Here, the Reynolds (Re) and Prandtl (Pr) numbers are evaluated from the usual expressions. The reference temperature for evaluating transport properties like vapor viscosity, specific heat, thermal conductivity etc. is the average temperature between the local domain fluid temperature and the droplet surface temperature

$$\overline{T} = \frac{T_\infty + T_s}{2} \quad . \tag{2.80}$$

2.7.2.2 Break-up model

The following gives an overview of the currently applied break-up model in the AVL FIRE® spray module.

Wave model :

The growth of an initial perturbation on a liquid surface is linked to its wavelength and to other physical and dynamic parameters of the injected fuel and the domain fluid (Liu et al., 1993). There are two break-up regimes, one for high velocities and one for low velocity Rayleigh type break-up. For the first case the size of the product droplets is set equal to the wavelength of the fastest growing or most probable unstable surface wave. Rayleigh type break-up produces droplets that are larger than the original parent drops.

If a rate approach for the radius reduction of the parent drops in the Wave model is applied

$$\frac{dr}{dt} = -\frac{\left(r - r_{stable}\right)}{\tau_a} \tag{2.81}$$

Where τ_a is the break-up time of the model, which can be calculated as:

$$\tau_a = \frac{3.726 \cdot C_2 \cdot r}{\Lambda \cdot \Omega} \tag{2.82}$$

The constant C_2 corrects the characteristic break-up time and varies from one injector to another. r_{stable} is the droplet radius of the product droplet, which is proportional to the wavelength Λ of the fastest growing wave on the liquid surface.

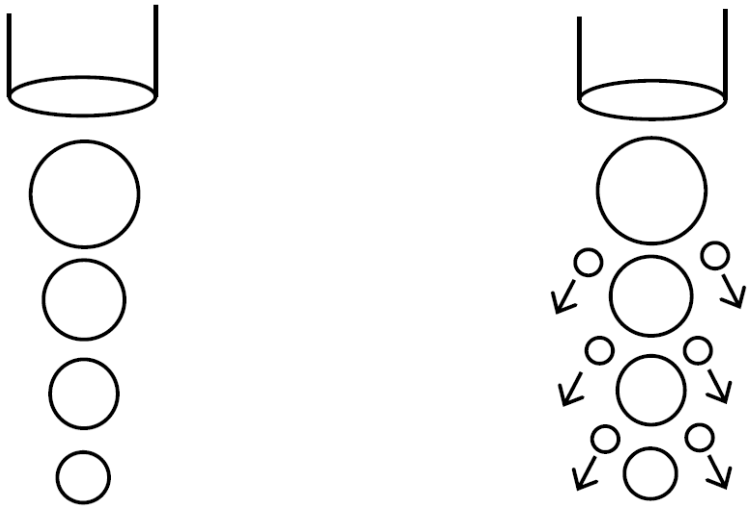
$$r_{stable} = C_1 \cdot \Lambda \quad . \tag{2.83}$$

The recommended default value of C_1 taken from the original paper of Reitz is 0.61. The wave length Λ and wave growth rate Ω depend on the local flow properties.

$$\Lambda = 9.02 \cdot r \cdot \frac{\left(1 + 0.45 \cdot \mathrm{Oh}^{0.5}\right)\left(1 + 0.4 \cdot \mathrm{T}^{0.7}\right)}{\left(1 + 0.87 \cdot \mathrm{We}_g^{1.67}\right)^{0.6}} \quad . \tag{2.84}$$

$$\Omega = \left(\frac{\rho_g r^3}{\sigma}\right)^{-0.5} \cdot \frac{0.34 + 0.38 \cdot \mathrm{We}_g^{1.5}}{(1 + \mathrm{Oh})\left(1 + 1.4 \cdot \mathrm{T}^{0.6}\right)} \quad . \tag{2.85}$$

Entering Reynolds (Re) and Ohnesorge number (Oh) as well as $\mathrm{T} = \mathrm{Oh} \cdot \mathrm{We}^{0.5}$.
As shown in Figure 2.4, if the standard WAVE model with blob injection where the initial droplets have the diameter of the nozzle orifice is used for the simulation, that only gives big droplets in the region close to the nozzle which hardly evaporate. The effect is too less vapor in the vicinity of the nozzle which is not physical. This is due to the fact that the droplets are still very large at the beginning and therefore hardly evaporate.



Standard wave model Wave model + Child

Figure 2.4 : Different WAVE break-up models (AVL, 2013).

There is an approaches to produce some vapor close to the nozzle by applying the child droplets breakup model which strips off mass from the initial large droplets and generates a number of smaller droplets in the near nozzle region (Figure 2.4). These smaller droplets are vaporized more rapidly. The constants which are used in wave breakup model are described as below;

C1 : This constant usually does not vary.

C2 : This constant adjusts breakup to different nozzle types and varies between 5 and 60. C2 influences the characteristic breakup time and hence breakup length and may vary from one injector to another. A smaller value of C2 decreases breakup time (breakup length) and usually decreases penetration length.

C3 : It should usually be set to 1 to take liquid viscosity of the fuel into account. A value of zero will calculate breakup assuming an inviscid liquid.

C4 : It controls the number of parcels that will be initialized and can be varied in a wide range from 0.1 to 0.5 without influencing the amount of shed mass too much where the lower the value the more new parcels. If C4 is too low (close to zero) too many child droplet parcels will be created and the droplet array suffers from overflow.

C5 : This constant gives control over the mass in the parcels and ranges from 0.01 to 0.3 where the lower the value the less mass will be put into the child droplet parcel. Higher values of C5 lead to an increase of vapor in the vicinity of the nozzle. The penetration of the liquid and the vapor is hardly influenced by this variation.

2.7.2.3 Turbulence dispersion model

As particles pass through the flow it is assumed that they interact with the individual turbulent eddies. Each interaction deflects the particle as dictated by the instantaneous velocity of the turbulent eddy and the particle inertia. These additional turbulence effects on the spray particles cannot be resolved by the flow field in detail so a turbulent dispersion model is used.

The particle trajectory is determined similar to a random walk computation until the particle passes out of the region under consideration. The instantaneous gas velocity within a turbulent eddy is obtained from the mean domain fluid velocity u_{ig} and the turbulence kinetic energy k. Both are known from the solution of the gas phase equations. The interaction time of a particle with the individual eddies is estimated from two criteria, the turbulent eddy life time and the time required for a particle

to cross the eddy. In current study, the Enable model is implemented for turbulence dispersion in spray module.

Enable model :

In the stochastic dispersion method employed by Gosman and Loannides (1983), the effects of turbulence on the spray particles are modeled by adding a fluctuating velocity u_{ig}.

Assuming isotropic turbulence the components of the particle fluctuating velocity u_i' is determined randomly from a Gaussian distribution with standard deviation $\sigma = \sqrt{2k/3}$ where k is the turbulence kinetic energy of the gas at the particle location.

$$u_i' = \left(\frac{2}{3}k\right)^{1/2} \cdot \mathrm{sign}\left(2\mathrm{Rn}_i - 1\right) \cdot \mathrm{erf}^{-1}\left(2\mathrm{Rn}_i - 1\right) \tag{2.86}$$

Rn_i is a random number in the range from $[0 < \mathrm{Rn}_i < 1]$ for each vector component and erf^{-1} is the inverse Gauss function.

The fluctuation velocity u_i' is chosen as a piecewise constant function of time and is updated when the turbulence correlation time t_{turb} has passed. The turbulence correlation time t_{turb} is the minimum of the eddy break-up time and the time for the particle to traverse an eddy, and is given by

$$t_{turb} = \min\left(C_\tau \frac{k}{\varepsilon}\ ,\ C_1 \frac{k^{3/2}}{\varepsilon} \frac{1}{|u_g + u' - u_d}\right) \tag{2.87}$$

where $C_\tau = 1$ and $C_1 = 0.16432$ are model constants.

The case that the computational time step δt is larger than the turbulence correlation time t_{turb}, the spray integration time step is reduced to t_{turb}.

2.7.2.4 Spray-wall interaction

Wall interaction of liquid droplets can play a major role for diesel and gasoline engines. Especially for small bore diesel engines the distance between the injector and the bowl can be very small, so that large parts of the fuel are not yet evaporated or atomised when they hit the wall. This influences the combustion process and consequently the production of emissions, as an incomplete combustion in the vicinity of the wall will result in high HC emissions and soot particles.

The behavior of a droplet at wall interaction depends on several parameters like droplet velocity, diameter, droplet properties, wall surface roughness and wall temperature. At

very low inlet velocities the droplet sticks to the wall or to the wall film. When the inlet velocity increases a vapor or gas boundary layer is trapped underneath the droplet and causes the liquid to rebound. During the rebound parts of the kinetic energy are dissipated and the outgoing normal velocity is usually lower than the incoming normal velocity. A further increase of the velocity leads either to the spread or the splash regime. In the spread regime the complete liquid spreads along the wall with hardly any normal velocity. In the splash regime a part of the liquid remains near the surface and the rest of it is reflected and broken up into secondary droplets.

Walljet1 :

This model in principle is based on the spray/wall impingement model of Naber and Reitz (1988). The concept is that under engine conditions a vapor cushion is formed under the droplets and that they rebound or slide along the walls. This model does not take into account the wallfilm physics. This allows spray/wall impingement calculations to be performed without using the wallfilm module, which is sufficient in a variety of practical applications where the wallfilm physics do not play an essential role within the wall interaction process.

In the currently implemented model it is assumed that a droplet which hits the wall suffers one of the two consequences, namely rebound or reflection in the manner of a liquid jet, depending on the Weber number. The transition criterion between these two regimes is described by a critical Weber number which is taken to be $We_{cr} = 80$.

For the jet regime, when the Weber number is bigger than a predefined value ($We_{cr} = 80$), it is assumed that an incident drop is reflected in the manner similar to how a liquid jet would behave (Naber and Reitz, 1988). The droplet reflection velocity in this respect is calculated with the assumption that the magnitude is unchanged, but only the reflection direction varies. The tangential direction of the reflected droplets may turn on the surface plane by the angle ψ varying from $-180 < \psi < 180$. The circumferential angle ψ is determined by a probability distribution function, derived assuming a two-dimensional potential flow jet conserving mass and momentum (Naber and Reitz, 1988):

$$\psi = -\frac{\pi}{k} \ln \left[1 - p \left(1 - e^{-k} \right) \right] \tag{2.88}$$

The random number p varies within 0 and 1; the parameter k is calculated from

$$\sin\alpha = \left(\frac{e^K+1}{e^k-1}\right)\frac{1}{1+\left(\frac{\pi}{k}\right)^2} \tag{2.89}$$

The droplet diameter after the impingement in both regimes is calculated as a function of Weber number currently distinguishing between the following Weber number criteria (Jiro et al., 1994). The reflection angle may vary within $0 < \beta < 5$ degrees.

$$\begin{cases} \mathrm{We} < 50 & d_1 = d_0 \\ 50 \leq \mathrm{We} \leq 300 & d_1 = d_0 \cdot \mathrm{f}(\mathrm{We}_{\perp,in}) \\ \mathrm{We} > 300 & d_1 = 0.2 d_0 \ . \end{cases} \tag{2.90}$$

2.8 Ignition Model

Five different ignition models are available for the CFM combustion models. Two models of increasing complexity are available for the initiation of combustion by a spark plug when using ECFM: Arc and Kernel Tracking Ignition Model(AKTIM) and the spherical delay model.

2.8.1 Spherical model

In this study, spherical model is chosen as the ignition model for SI engine simulation. This ignition model can be used for all CFM models (mainly recommended). In this model a spherical flame kernel is released using the spark position, ignition time, flame kernel radius and spark duration with the flame surface density specified in the AVL FIRE® Workflow manager. The flame surface density is kept constant in all ignition cells within the flame kernel radius over the spark duration. After end of ignition the flame surface density must be self-sustaining for a propagating combustion.

2.9 Pollutant Model

This section provides a brief overview of the applied models for calculation of NO and soot formation. The presented models are applicable to both CI and SI engines and can be combined with the available ignition and combustion models which described in the previous section. As a result of the application of the NO and soot formation models, details of the local interaction of mixture formation, combustion and pollutant formation are obtained. Based on the temperature and species composition distributions in different sections across the combustion chamber

the governing processes can be easily interpreted. The impact of combustion system parameter variations on the details of the soot and NO formation mechanisms can be assessed on a local space and time resolved basis. The extraction of global pollutant formation data then serves as the basis for further assessment of the combustion system behavior under parameter variations. This enables the individual study of, for example, the influence of start of injection and injection pressure on NO and soot formation trends.

The AVL FIRE® emission module enables the calculation of pollutants (mainly nitrogen oxide and soot) in engines and other combustion devices. The overall NO formation can be calculated with six different models which are based on the extended Zeldovich mechanism or a combination of other different NO formation mechanisms. Four models are available for the determination of the soot formation and oxidation. One uses tabulated values from extended chemistry calculations, one determines the soot formation and oxidation by a reduced chemical reaction scheme and the other two are based on empirical formulations.

All models can be combined with all combustion models. If there are no other special needs, it is recommended to use the 'Extended Zeldovich' model for NO formation and the 'Kinetic' model for soot formation in engine applications.

2.9.1 NO model

In general, the nitric oxide formation stems from three principal sources:

- Thermal NO which is formed due to the dissociation of the molecular air-nitrogen (Bowman, 1975; Hanson and Salimian, 1984; Polifke, 1995).
- Prompt NO (Fenimore NO) formed by the "attack" of hydrocarbon fragments on the air-nitrogen (Bowman, 1975; Görner, 1991).
- NO formed from nitrogen containing components in the fuel

Fuel-NO formation can principally be neglected during the combustion process in internal combustion engines. Prompt NO formation can also principally be neglected since this process plays no dominant role in comparison to the thermal NO formation (< 5 [%] of NO is produced via this path) (Görner, 1991; Polifke, 1995; Zeldovich et al., 1947). NO is formed in both the flame front and post-flame gases.

In engines, the cylinder pressure rises during the combustion process, so earlier burnt gases are compressed to a higher temperature level as they have immediately after their combustion. Hence, the thermal NO formation in the burnt gases always dominates in comparison to the NO formed in the flame front and represents the main source of the nitric oxide in engines whose reaction paths are effective at high temperatures (> 1800 [K]). The reaction mechanism can be expressed in terms of the so-called extended Zeldovich mechanism:

$$N_2 + O \underset{k_{1b}}{\overset{k_{1f}}{\leftrightarrow}} NO + N \tag{2.91}$$

$$N + O_2 \underset{k_{2b}}{\overset{k_{2f}}{\leftrightarrow}} NO + O \tag{2.92}$$

$$N + OH \underset{k_{3b}}{\overset{k_{3f}}{\leftrightarrow}} NO + H \tag{2.93}$$

The first reaction represents the rate limiting step in comparison to the other reactions. A very high activation energy (or temperature) is necessary to decompose the stable triple-bond of the molecular air-nitrogen. Accordingly, this reaction is significantly fast at high temperatures (hence thermal). In principal, it can be seen that the thermal nitric oxide formation is mainly determined by only five chemical species (O, H, OH, N and O_2) but not by the fuel being used. In order to obtain the required concentrations of the radicals, a complex reaction mechanism must be used in order to determine NO concentration. In the literature different possibilities are suggested to represent the rate law for NO (Heywood, 1988; Bogensperger, 1996). Complex kinetic mechanisms are applicable only for simple flame computations (e.g. one-dimensional, laminar, etc.). For real turbulent flame calculations, their use is impractical due to the complexity of the interacting processes (turbulence, radiation, heat transfer, etc.) which must be considered to obtain realistic results. Therefore, simplified approaches must be used for complex applications, whereby essential information is not lost due to the reduction procedure (Maas and Pope, 1992; Lam, 1994). This reduction is based on the partial equilibrium assumption of the considered elementary reactions using the extended Zeldovich mechanism describing the thermal nitrous oxide formation.

The first two reactions (2.91) and (2.92) were originally proposed by Zeldovich et al. (1947), and extended later by including the third reaction (2.93). It was observed later that the nitrogen atoms released at reaction (2.92) are oxidized to nitric oxide mainly

by hydrogen radicals at near-stoichiometric conditions and in fuel-rich mixtures. The third reaction (2.93) is usually negligible except in fuel rich flames. The reaction mechanism [(2.91), (2.92) and (2.93)] is known as the extended Zeldovich mechanism that considers the effect of oxygen, nitrogen and hydrogen radicals on NO formation. It is very important to point out that all three chemical reactions that represent the Zeldovich mechanism exhibit strong temperature dependency.

The temporal change of NO concentration (or net rate of NO formation) via reactions is given by:

$$\frac{\partial c_{NO}}{dt} = k_{1f} c_{\mathrm{O}} c_{\mathrm{N_2}} + k_{2f} c_{\mathrm{N}} c_{\mathrm{O_2}} + k_{3f} c_{\mathrm{N}} c_{\mathrm{OH}} - k_{1b} c_{\mathrm{NO}} c_{\mathrm{N}} - k_{2b} c_{\mathrm{NO}} c_{\mathrm{O}} - k_{3b} c_{\mathrm{NO}} c_{\mathrm{H}} \quad (2.94)$$

considering forward and backward directions where the concentrations c are given in $[{}^{mol}/_{cm^3}]$.

The thermal NO reactions are highly dependent on temperature, residence time and atomic oxygen concentration. The first reaction (2.91) has a very high activation energy and it is usually accepted as being the rate-limiting step of the thermal NO formation. Due to the high activation energy required to split the strong N_2 triple bond, the rate of formation of NO is significant only at high temperatures (greater than 1800 K). All the required radicals for this NO formation model are calculated based on the equilibrium approach (5 different equations) known and used in the ECFM combustion model, where conditional approaches are used in order to determine burned species mass fractions based on mean and fresh gas species mass fractions and the reaction progress variable, respectively.

2.9.2 Soot model

Under high temperature and fuel rich conditions, as typically found in diesel combustion, hydrocarbon fuels exhibit a strong tendency to form carbonaceous particles - soot. Usually, under engine running conditions, most of the soot formed in the early stages of the combustion process is depleted due to oxidation. This takes place in oxygen rich areas of the combustion chamber later in the engine cycle. In diesel engines, it is the amount and completeness of the soot oxidation process that actually determines the engine particle emission characteristics. The formation of

particulate involves a large number of different chemical and physical processes, like the formation and growth of large aromatic hydrocarbons, their subsequent conversion to particles, the coagulation of primary particles, and the growth of solid soot particles due to the accumulation of gaseous components (Bockhorn et al., 1985). The soot particle formation process is characterized by a gaseous-solid conversion, whereby the solid phase does not exhibit a uniform chemical and physical topology.

It is evident that the formation of soot, the conversion of hydrocarbon rich, aliphatic compounds involving only a relatively small number of carbon atoms into an agglomerate comprising millions of them, is the result of a highly complex chemical process involving hundreds of reactions and as many intermediate and radical species. Particle oxidation mainly occurs due to the attack of atomic oxygen onto the carbonaceous particles under high temperature conditions. In spite of the high complexity of the underlying processes, the individual reactions contributing to the soot formation and oxidation rates can be related to known flame parameters, such as fuel mass fraction, partial pressure of oxygen, flame temperature and/or turbulent mixing intensity.

A number of different sub-models have been proposed in the past in order to capture the individual aspects of relevant contribution of nucleation, particle growth and oxidation to the soot emission level in engines (Magnussen and Hjertager, 1977; Nagle and Constable, 1962; Tatschl et al., 1995; Tesner et al., 1971). These sub-models are based upon different simplifying assumptions concerning the relative contributions of the individual chemical and physical processes to the overall net formation rate.

The soot formation model currently implemented in AVL FIRE® is based upon a combination of suitably extended and adapted joint chemical/physical rate expressions for the representation of the processes of particle nucleation, surface growth and oxidation.

Under ideal conditions, the combustion of hydrocarbon fuels forms CO_2 and H_2O. The necessary amount of oxygen is the stoichiometric oxygen requirement $O_{2,st}$ calculated from the following equation:

$$C_nH_mO_k + \left(n + \frac{m}{4} - \frac{k}{2}\right) O_2 \rightarrow n\, CO_2 + \frac{m}{2}\, H_2O \tag{2.95}$$

The real amount of oxygen, available for the combustion, is expressed by the air access ratio $\lambda = {}^{O_2}/_{O_{2,st}}$ or by the equivalence ratio ϕ:

$$\Phi = \frac{1}{\lambda} = \frac{O_{2,st}}{O_2} \tag{2.96}$$

For conditions at equivalence ratios $\Phi > 1$, there is a big potential for soot formation. Soot formation is controlled by the chemistry in laminar diffusion flames. The soot concentration is a function of the local species concentration and temperature, and independent of the residence time.

The Kinetic Soot Model :

The basis of this model is a detailed chemical reaction scheme for the calculation of soot formation and oxidation. It combines the mechanisms of formation of polyaromatic hydrocarbons, polyynes, two mechanisms of soot precursor formation due to condensation of polyaromatic and polyyne molecules, soot particle growth by the reactions of HACA mechanism and polyyne molecule addition, the mechanism of acetylene pyrolysis and pure carbon cluster formation, as well as the reactions of hydrocarbon (*n*-heptane) oxidation (Agafonov et al., 2002; Appel et al., 2000; Krestinin, 2000; Wang and Frenklach, 1997). The complete detailed kinetic scheme of the soot formation process incorporates 1850 gas-phase reactions 186 species and 100 heterogeneous reactions with participation of four ensembles of micro-heterogeneous particles of different types. The current model contains a reduced number of species and reactions and has been developed in order to provide a computationally efficient kinetic overall soot model. The model can describe the behavior of soot formation and oxidation for different fuel classes. Exact reactions constants have been implemented for methane, propane, ethanol, *n*-heptane and tetradecane. If the fuel which has been specified by the user does not exactly match one of these species, AVL FIRE® decides automatically the best parameter set to be used. The reduced reaction mechanism which is applied in the model e.g. for tetradecane is shown below:

$$
\begin{aligned}
&C_{14}H_{30} + 7\,O_2 = 14\,CO + 15\,H_2 \\
&H_2 + H_2 + O_2 = H_2O + H_2O \\
&CO + CO + O_2 = CO_2 + CO_2 \\
&CO + H_2O = CO_2 + H_2 \\
&C_{14}H_{30} + C_{14}H_{30} = 28\,C + 30\,H_2 \\
&C + C + O_2 = CO + CO \\
&C + H_2O = CO + H_2
\end{aligned}
\tag{2.97}
$$

The reaction parameters for the main soot formation reaction are changing due to the local equivalence ratio. The soot is oxidized due to the presence of oxygen and also due to water. This model is employed in current study .

3. COMPARATIVE STUDY; VALIDATION, PARAMETRIC STUDY AND MODIFICATION TO NATURAL GAS FUELED HCCI ENGINE

In this chapter, first a validation study is presented and the simulated SI engine is validated with available experimental data for three different engine speeds; 1500[rpm], 1660[rpm] and 1800[rpm], under engine load (p_{me}) of 3 [bar] and then a comprehensive parametric study of individual influences of exhaust gas recirculation, equivalence ratio and spark timing on the performance and exhaust emissions of the simulated gasoline engine is carried out at a fixed engine speed of 1500 [rpm].

Commercially available AVL FIRE® CFD code is used to perform the simulations. Boundary fitted computational grids are generated by Engine Simulation Environment Diesel (ESE Diesel) tool, then in-cylinder processes are simulated via Workflow Manager tool. The validation results prove the code's ability to evaluate performance and emission characteristics of this engine.

In order to carry on the study, additional simulations are done by applying the natural gas (methane) as an alternative fuel and the performance and emission characteristics of CNG engine are compared with those of validated gasoline engine.

Since the primary focus of this research is the examination of different combustion strategies for reducing NO_x and soot emissions along with engine performance improvement, in addition to conventional natural gas fueled SI engine, a low temperature combustion strategy known as Homogeneous Charge Compression Ignition (HCCI) is developed by using the natural gas as fuel.

In order to achieve the most appropriate model which adequately predicts the combustion process and accurately evaluates the performance and emission characteristics of this engine, more than 80 simulations are done by varying the boundary conditions, combustion models, turbulence models, ignition models and spark timing. Finally, proper models and values are selected and three simulations (Case-30, Case-35 and Case-44) are chosen and verified in this section. Since the adopted models are the same for all cases which are revealed in the following, these cases only differ in initial condition and spark timing that are based on corresponding

experimental data of each case. Applied initial conditions and spark timings for each case are illustrated in relevant sections.

3.1 Experimental Data

According to Kutlar (1998) and Doğru (2013) the test engine is constructed on the basis of a four-stroke compression ignition engine, Lombardini 3LD450. After some constructional modifications, this engine is redesigned as a spark-ignition engine for the combustion of gasoline . In this regard, the engine is equipped with a new fuel supply system and an ignition installation. As a result of modifications, the shape of combustion chamber and piston bowl have been changed and the compression ratio is reduced from 17.5 to 9.1. Figure 3.1 shows the original and adjusted piston geometries. The specifications of a single-cylinder Lombardini 3LD450 engine , which is modified by Kutlar (1998) and Doğru (2013) are listed in Table 3.1. However, the experimental results are collected for various combinations of engine speeds and loads(p_{me}), due to the mechanical limits, only engine operation under part loads and low engine speeds have been examined. Experimental data are summarized in Table 3.2 and additional diagrams which are obtained from experimental results, are used in the corresponding sections.

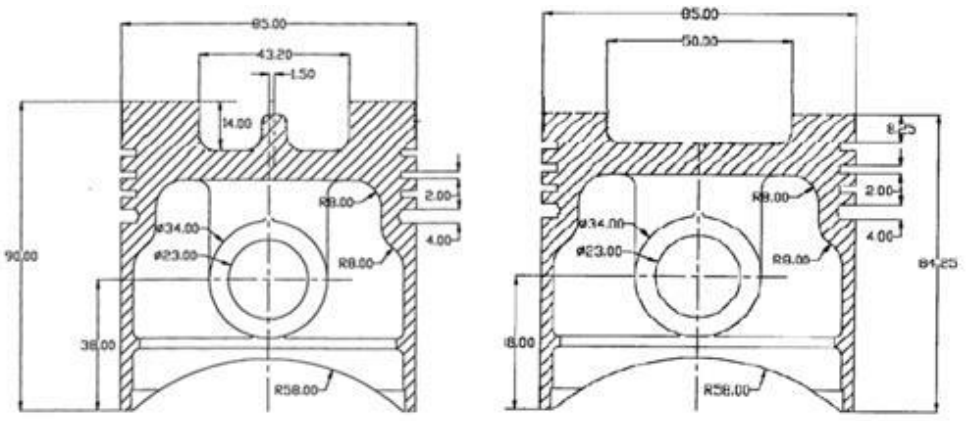


Figure 3.1 : Original piston (left) and modified piston (right) geometries (Doğru, 2013).

Table 3.1 : Modified test engine specifications (Doğru, 2013).

Engine type	Four stroke , spark ignition
Fuel	gasoline
Number of cylinders	1
Bore [mm]	85
Stroke [mm]	80
Displacement [cm^3]	454
Compression ratio	9.1:1 (originally 17.5:1)
Connecting rod length [mm]	145
Intake valve opening	16 [CAD] BTDC
Intake valve closing	40 [CAD] ABDC
Exhaust valve opening	40 [CAD] BBDC
Exhaust valve closing	16 [CAD] ATDC

Table 3.2 : Experimental data (Doğru, 2013).

No.	N [rpm]	p_{me} [bar]	F [Kg]	Mm [N.M]	N_e [kW]	$\dot{m}_f$ [Kg/h]	sfc [g/kWh]	ID [CAD]	SA [CAD]	t_{inj} [ms]	λ_{ex}	$\left(\frac{A}{F}\right)_{ex}$	$\dot{m}_{air}$ [Kg/h]	CO [vol%]	CO_2 [vol%]	O_2 [vol%]	UHC [ppm]	CH_4 [ppm]	NO_x [ppm]
1	1202	1,00	0,380	3,63	0,46	0,482	1055	4	24	1,25	0,99	14,38	6,931	0,17	13,79	1,73	2618	250	288
2	1352	0,98	0,370	3,53	0,50	0,464	927	4	32	1,50	0,99	14,40	6,682	0,75	14,19	0,73	3491	320	243
3	1504	1,00	0,380	3,63	0,57	0,522	913	5	33	1,60	0,98	14,27	7,449	0,88	14,24	0,51	2916	338	394
4	1654	1,03	0,390	3,72	0,65	0,584	905	7	34	1,75	0,98	14,26	8,328	0,96	14,15	0,57	2924	358	417
5	1804	1,00	0,380	3,63	0,69	0,644	939	9	34	1,65	0,99	14,48	9,325	1,09	14,12	0,61	2719	371	365
6	1202	2,01	0,760	7,26	0,91	0,536	587	5	21	2,40	1,00	14,56	7,804	0,58	13,85	1,16	5337	294	529
7	1351	2,01	0,760	7,26	1,03	0,580	565	7	22	2,25	1,00	14,50	8,410	0,66	14,02	0,86	3787	290	521
8	1500	2,01	0,760	7,26	1,14	0,643	564	8	24	2,30	1,00	14,55	9,356	0,62	14,07	0,84	3253	289	582
9	1655	2,04	0,770	7,35	1,27	0,715	561	9	25	2,55	1,00	14,52	10,382	0,61	14,12	0,81	3314	299	1022
10	1805	2,01	0,760	7,26	1,37	0,797	581	10	27	2,50	1,00	14,60	11,636	0,58	14,12	0,85	3059	288	841
11	1200	3,01	1,140	10,89	1,37	0,672	491	11	16	3,40	0,99	14,38	9,663	0,57	14,18	0,74	4474	276	590
12	1352	3,01	1,140	10,89	1,54	0,746	484	12	18	3,40	0,99	14,40	10,742	0,66	14,13	0,74	3953	296	752
13	1501	3,00	1,135	10,84	1,70	0,813	477	12	20	3,40	1,00	14,65	11,910	0,39	14,21	0,87	3360	284	817
14	1660	3,08	1,165	11,13	1,92	0,913	475	13	21	3,70	1,00	14,52	13,257	0,51	14,21	0,75	3370	310	1131
15	1806	2,96	1,120	10,70	2,03	0,965	477	14	22	3,25	1,00	14,67	14,157	0,41	14,13	0,94	3618	295	772

No.	N [rpm]	p_{me} [bar]	T_{in} [C]	P_{in} [mbar]	T_{ex}[C]	P_{ex} [mbar]	$T_{wat,in}$ [C]	$T_{wat,out}$ [C]	T_{Oil} [C]	P_{Oil} [mbar]	T_{atm} [C]	P_{atm} [mbar]	N_{em} [%]	$P_{mi,net}$	η_m	Isfc [g/kwh]	$\frac{P_{pump}}{P_{gross}}$	η_v	
1	1202	1,00	52,8	775	551,2	0,9	69,03	65,72	60,2	2,33	25,9	1015	43,2	1,44	69,4	733	25,5	0,358	
2	1352	0,98	51,3	663	490,1	0,88	68,51	63,37	60,6	2,82	26,8	1015	43,8	1,7	57,7	534	26,72	0,308	
3	1504	1,00	49,5	724	556,5	0,91	65,53	60,51	62,9	3,16	26,9	1015	44,6	1,72	58,1	531	24,80	0,308	
4	1654	1,03	48,3	727	558,6	0,80	65,62	60,36	64,3	3,39	26,9	1015	45,4	1,87	55,1	498	23,04	0,314	
5	1804	1,00	47,7	682	578,0	0,81	64,86	59,51	67,5	3,44	26,9	1015	45,4	1,76	56,8	534	24,89	0,322	
6	1202	2,01	50,4	855	469	2,39	65,66	63,32	59,2	2,39	26,4	1014	47,2	2,64	76,1	447	16,72	0,404	
7	1351	2,01	50,1	847	506,8	2,85	67,33	64,34	59,9	2,85	26,5	1015	47,7	2,61	77,0	435	17,92	0,387	
8	1500	2,01	48,9	873	546,2	3,16	66,57	63,18	62,7	3,16	26,4	1015	47,5	2,62	76,7	433	17,90	0,388	
9	1655	2,04	47,5	878	558,3	3,26	66,42	62,90	63,4	3,26	26,5	1015	47,4	2,9	70,3	395	15,7	0,390	
10	1805	2,01	44,9	886	610,1	3,43	65,82	62,30	68,2	3,43	26,5	1015	47,5	2,88	69,8	405	15,79	0,401	
11	1200	3,01	42,4	932	536,6	1,02	65,83	62,73	62,4	2,19	26,6	1015	48,0	3,64	82,7	406	11,65	0,501	
12	1352	3,01	41,6	935	585,3	1,18	65,23	61,60	63,3	2,60	26,6	1015	47,9	3,68	81,8	396	12,17	0,494	
13	1501	3,00	41,2	940	624,4	1,13	65,65	61,74	64,5	3,01	26,6	1015	47,6	3,68	81,5	389	13,0	0,494	
14	1660	3,08	41,6	936	645,5	1,31	65,62	61,49	65,0	3,33	26,6	1015	47,4	3,92	78,6	373	11,1	0,500	
15	1806	2,96	42,4	937	640,6	1,30	65,70	61,82	67,6	3,48	26,7	1015	47,6	3,74	79,1	378	11,79	0,487	

3.2 Pre-Processing Of Simulation

3.2.1 Meshing

Due to the often symmetric arrangement of IC-engine piston bowl configurations, the analysis and optimization of the combustion processes is usually done by simulating an engine segment model only. The prepared numerical grids are sector meshes that only consider one of the total sectors of cylinder geometry, wherein each sector included one of the injector nozzle holes. The solution method is based on a fully conservative finite volume approach. All dependent variables for momentum, pressure, density, turbulent kinetic energy, dissipation rate, and scalar quantities, such as e.g. chemical species, are evaluated at the centers of the computational cells.

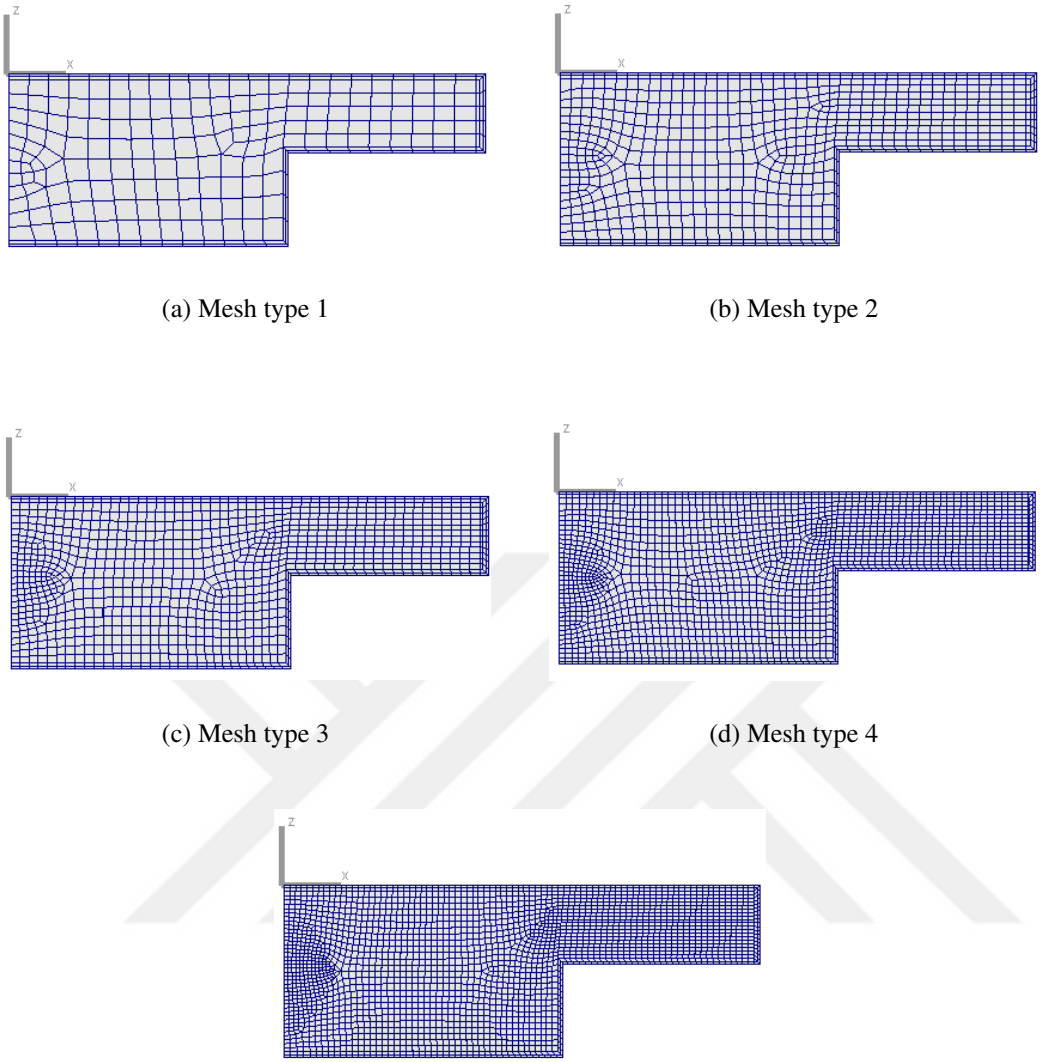
However, the piston was modeled by the dynamic mesh tools, in some places such as valves, unstructured grids were applied. Indeed, AVL FIRE® gives major attention to the numerical accuracy of the algorithm due to the use of unstructured grids. Based on simulation condition, the generation of the grids is required to cover the simulation period between intake valve closing (IVC) and exhaust valve opening (EVO).

In this step, general engine parameters and combustion chamber geometries which are given in Table 3.1, are imported into ESE Diesel tool. Furthermore, number of boundary layers, its thickness and also the desired average cell size which are listed in Table 3.3, are specified. To understand the grid sensitivity of multi-dimensional

Table 3.3 : Computational grids specification used for sector mesh generation.

	Mesh type 1	Mesh type 2	Mesh type 3	Mesh type 4	Mesh type 5
Average cell size [mm]	1.7	1	0.8	0.6	0.5
Number of boundary layers	2	2	2	2	2
Thickness of boundary layer [mm]	0.25	0.25	0.25	0.25	0.25
Maximum number of cells	12,280	16,872	33,364	56,596	77,732

engine CFD, five different grid resolutions which are shown in Figure 3.2 and listed in Table 3.3 are used in this study. As illustrated in Figure 3.3, it is found for the cell size of smaller than 0.6 [mm](mesh type4), the results are grid independent and increase in the number of grids does not change the values of calculated parameters,



(a) Mesh type 1

(b) Mesh type 2

(c) Mesh type 3

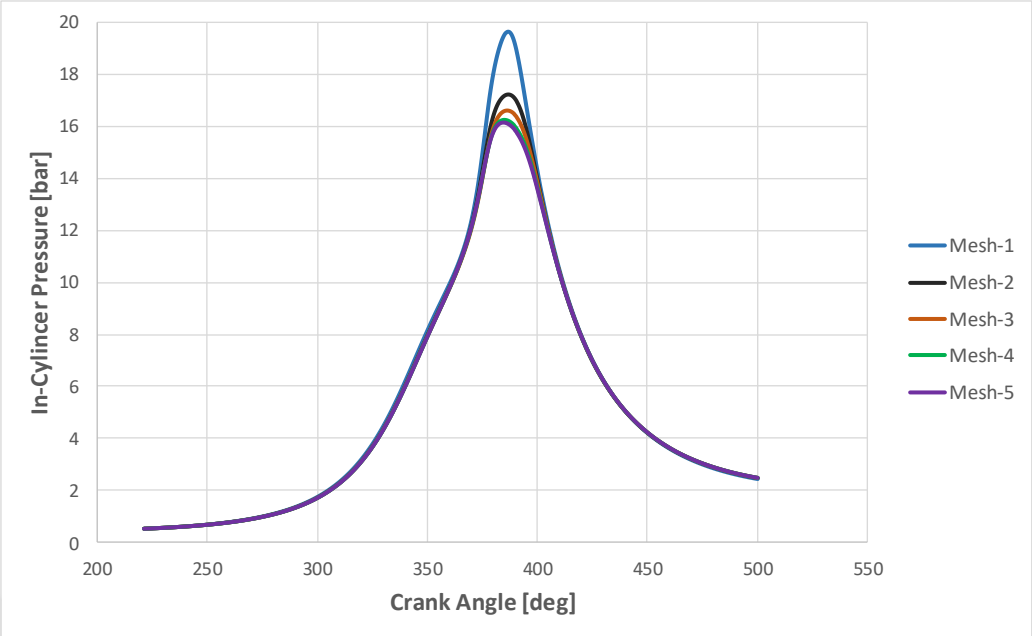
(d) Mesh type 4

(e) Mesh type 5

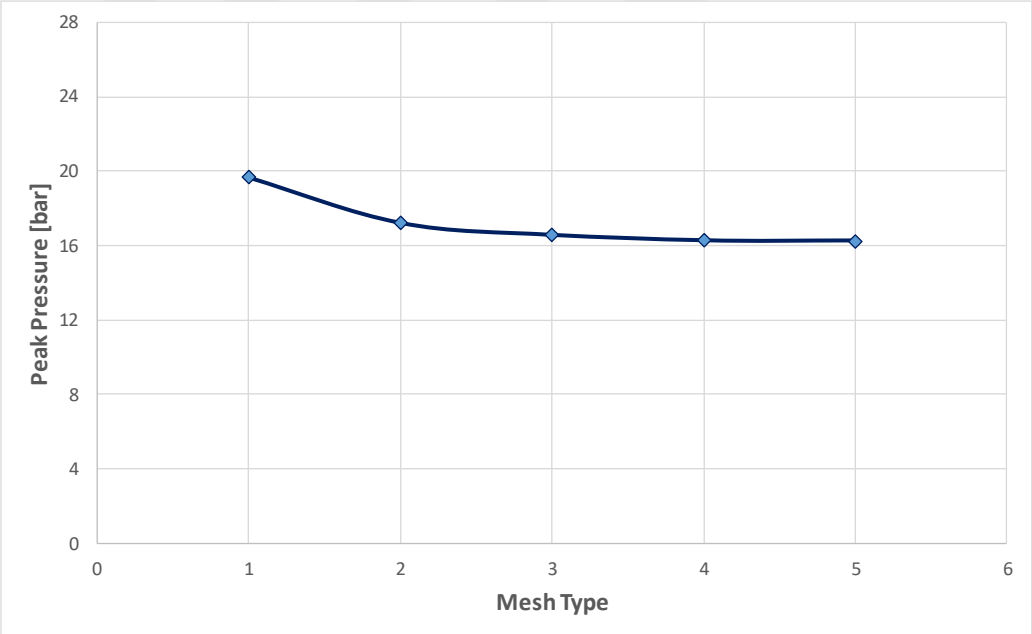
Figure 3.2 : Grid resolutions.

while the calculation time is increased significantly, so a reasonable cell size which is equal to 0.6 [mm](mesh type4), is specified. The chosen mesh type represented a compromise between computational time and accuracy, but is found to give adequately grid independent results. The adopted computational grid contains a maximum of 56,596 cells.

Although port fuel injection (PFI) is applied in this study, in order to generate sector meshes, injector geometry parameters such as number of nozzle holes are also introduced in this step. Considering that combustion strategy development using CFD is typically done using sector meshes, it is of interest to conduct the spray and mixing validation on these sector meshes, an injector with a five nozzle holes is adopted and



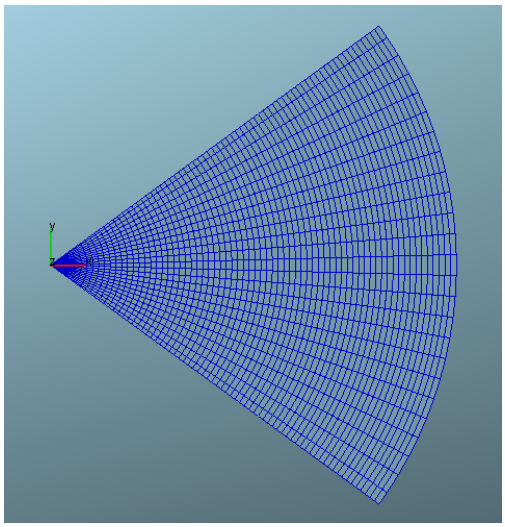
(a) In-cylinder pressure via various mesh types



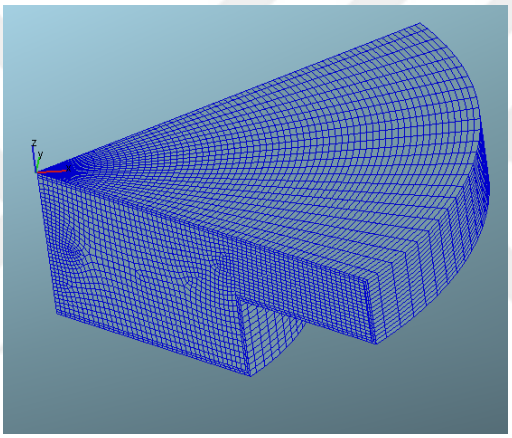
(b) Peak pressure gradient

Figure 3.3 : Effects of grid resolutions on in-cylinder pressure.

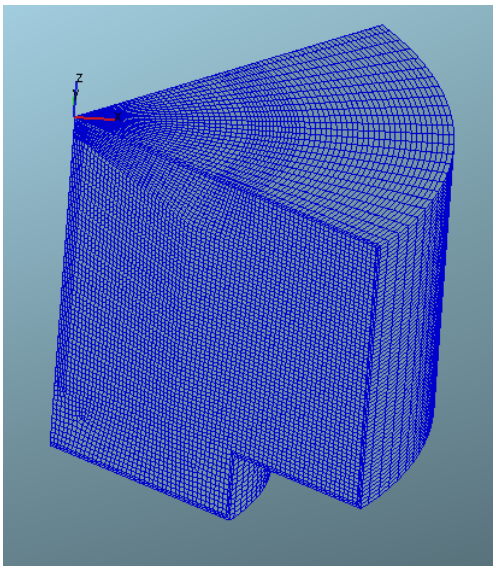
as a consequence 1/5th (72°) sector of the cylinder geometry is utilized in all engine combustion simulations. Figure 3.4 shows the sector mesh, which is generated by Engine Simulation Environment Diesel (ESE Diesel) tool via AVL FIRE® to model the combustion chamber.



(a) Top view of sector mesh



(b) Sector mesh at TDC



(c) Sector mesh at BDC

Figure 3.4 : Generated 3D sector mesh used in SI engine simulations (72° sector).

Finally, before the start of simulation the generated mesh is automatically checked via mesh quality checker, to ensure that the simulation will run without any problem. Calculated compression ratio through the mesh generating accurately matches with experimental compression ratio (9.1:1).

3.2.2 Operating mode

The flow domain under investigation is limited to the combustion chamber part around one single fuel spray applying cyclically symmetric boundary conditions for the crank-angle interval from inlet valve closure to exhaust valve opening. The combustion chamber of engine is considered as a closed thermodynamic system and the calculations are carried out from the intake valve closing (IVC) at 220°[CA] to exhaust valve opening (EVO) at 500°[CA], which are summarized in Table 3.1. In order to obtain accurate simulation results, the operating interval is divided into different crank angle steps which are given in table 3.4. In favor of gaining authentic results of ignition timing and phasing of heat release, very small steps are applied between 300°[CA] and 400°[CA]. According to the experimental data, which are

Table 3.4 : Time discretization .

Crank angle interval	Delta α
220 - 300	1
300 - 400	0.2
400 - 500	1

summarized in Table 3.2, different operating conditions such as e.g.various engine speeds and various engine loads, have been checked during the test. However, due to the mechanical limits, only engine operation under part loads and low engine speeds have been examined. In current study, by considering the cycle-to-cycle variation, input data of engine operation under $P_{me} = 3$[bar] is selected, since this operating condition showed less cycle-to cycle variation and more stable operation. Three different engine speed, 1200 [rpm], 1500 [rpm] and 1800 [rpm], under this load by considering related experimental data are utilized to achieve more reliable simulation results. Apart from the validation, for the sake of further investigations about the effects of EGR ratio, equivalence ratio and spark advance on combustion and emissions

characteristics of model, engine speed is fixed to 1500 [rpm] and all simulations are done by using this speed and corresponding input data.

3.2.3 Boundary conditions

In this step, cyclically symmetric boundary condition for the crank-angle interval is adopted to the radius surface along the center axis of the segment mesh. For the segment simulations, periodic inlet and outlet boundary conditions are used for the faces in polar direction, where mass, momentum and energy could translate from one side of the sector to the other side. Considering the experimental data, thermal boundary condition is set to the wall, where the temperature of the walls, including cylinder head, cylinder wall and piston crown, is fixed and considered as isothermal. The wall temperatures including cylinder liner, cylinder head and piston, are based on experimental experiences and depend on the operating point (load and speed). Moreover, cylinder wall and cylinder head have velocity components of zero and are modelled as a stationary wall, while piston crown is a moveable boundary and the situation of movement follows from mesh movement. The surface roughness of all surfaces is set to zero. Table 3.5 illustrates the utilized boundary conditions for engine simulation.

Table 3.5 : Utilized boundary conditions.

Name of BC	Type of BC	
Axis	Symmetric	
Segment (sector)	Periodic inlet/outlet	
Cylinder head	Thermal BC with fixed temperatures	$430°[K]$
Cylinder wall (liner)		$410°[K]$
Piston crown		$450°[K]$

Figure 3.5 schematically depicts the utilized boundary conditions for SI engine simulations.

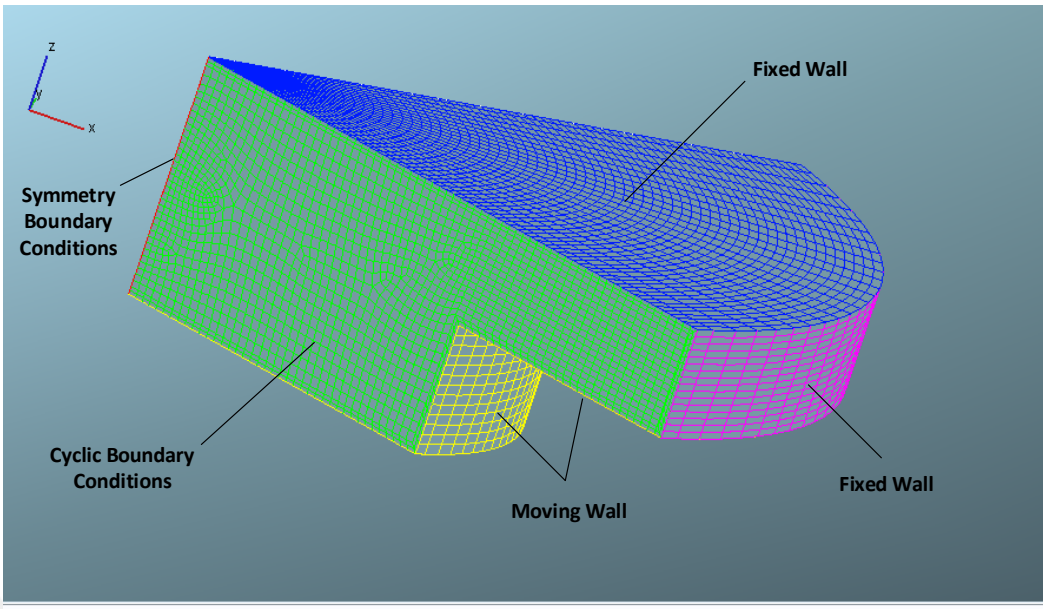


Figure 3.5 : Boundary conditions (schematic).

3.2.4 Initial conditions

As mentioned before, the combustion chamber is considered as a closed thermodynamic system and the governing equations for unsteady, compressible, turbulent flow and thermal fields are solved from IVC at 220°*CA* to EVO at 500°*CA*. However, the experimental study is done for entire system including intake and exhaust strokes, this model analyzes the engine in a closed cycle through compression, combustion and expansion processes of the engine cycle. Thus, initial values for temperature and pressure are chosen corresponding to the IVC point of the experimental data. The selected values are quite the same as the values of experiment. It should be mentioned, the air properties are considered as ideal gas.

Fuel type and the amount of inducted fuel is also specified in this step. The composition of gasolines varies widely, depending on the crude oils used, the refinery processes and the product specifications. Gasoline is a complex mixture of over 500 hydrocarbons that may have between 5 to 12 carbons. In this study, gasoline with a composition of C_8H_{17} is chosen. Considering the experiment, fuel is injected into the combustion chamber via manifold, so the fuel spray module is deactivated in the solver GUI of the FIRE Workflow Manager. In the second chapter, where the simulation is based on the direct injection and the fuel is injected directly into the cylinder during the compression stroke, this module is activated. Since, the intake stroke and the fuel injection precess

during this stroke is neglected, the presence of fuel could be assumed at the point of simulation start or IVC point. It can be done by setting a value to the equivalence ratio in initial condition. In another words, specifying a value for equivalence ratio in initial conditions means that, there is a homogeneous mixture of air and fuel at the point of start. Either the fuel induced from manifold i.e. port fuel injection(PFI) or injected directly during the intake stroke, at the point of IVC the fuel are present. According to the experimental data from Table 3.2, it can be seen air-fuel ratio equal to 1 is applied, so for the initial condition of simulation, equivalence ratio is also set to 1. Thus, we have a stoichiometric homogeneous mixture of air and fuel in the combustion chamber. Another parameter that should be specified in this step is the amount of EGR. For this purpose, two inputs are required; EGR mass fraction and EGR composition. EGR composition defines the amount of oxygen in the residual gas via a number between 0 and 1. The input EGR composition describes the equivalence ratio of the combustion process where the residual gases have been formed and therefore determines the amount of oxygen in EGR. No fuel is allowed in EGR which means that EGR composition always has to take values between 0 (pure air – full oxygen left in EGR) and 1 (stoichiometric combustion – no oxygen left in EGR). If an equivalence ratio is given then AVL FIRE® first calculates the composition of the oxidizer and after this, the correct amount of fuel is determined for the present oxygen concentration. This order of calculation is necessary because the EGR can contain oxygen which also has to be taken into account when the equivalence ratio is calculated. As described, a stoichiometric mixture is formed and a stoichiometric combustion is analyzed, so EGR composition is set to 1 which means there is no oxygen left in EGR. The second input is EGR mass fraction, which is described as initial mass fraction of residual gas and explained in section 2.4.1.4.

In the current study, it is assumed that the mass fraction of EGR has a value of 0.1 and EGR composition is equal to 1, thus the amount of stock EGR in combustion chamber is equal to 10% for the baseline simulations. In the following sections, various amounts of EGR are adopted and the influence of different EGR ratios on combustion and emissions is analyzed.

Due to the lack of experimental information about the inlet velocities, reasonable values are set to turbulence kinetic energy and turbulence length scale by considering various literatures.

Finally, laminar flame speed determination method was selected. The laminar flame speed information required in the coherent flame modeling approach is obtained from detailed chemical kinetic calculations and tabulation of the laminar flame speed data as a function of temperature, pressure, equivalence ratio and residual gas content (Bogensperger et al., 2008). In case of choosing database, tabulated values are available. These are considered to be more accurate than the empirical relations and are available for numerous fuels and for fuels which are not on this list, AVL FIRE® automatically chooses the most relevant table. Specified initial conditions for baseline simulations are summarized in Table 3.6.

Table 3.6 : Initial conditions of baseline simulations.

	Case-44	Case-30	Case-35
Engine speed [rpm]	1500	1660	1800
Pressure [bar]	0.536	0.549	0.538
Temperature [K]	360	375	380
Fuel type	Gasoline		
Equivalence ratio	1		
Mass fraction of EGR	0.1		
EGR composition	1		
Turbulence kinetic energy $[m^2/s^2]$	8		
Turbulence length scale [m]	0.003		
Laminar flame speed	Database		

3.2.5 Solver control

As described in section 2.2.2, the CFD code AVL FIRE® solves the general conservation equations of mass, momentum and enthalpy plus additional transport equations for turbulence related quantities and for conservation of chemical species and depending on the physical and chemical sub-models, employs additional scalar quantities, such as mixture fraction, reaction progress variable and flame surface density. The solution method is based on a fully conservative finite volume approach. The overall solution procedure is iterative and is based on the Semi-Implicit Method for Pressure-Linked Equations algorithm (SIMPLE) applicable to turbulent flows at all

speeds.

For solving the large sets of linear equation systems evolving from the discretization of the governing equations, AVL FIRE® adopts efficient preconditioned conjugate gradient methods. In current study, maximum iteration of 50 is set for discrete linear equations and a value of 100 is adopted for maximum iterations of convergence criteria per crank angle. The normalized residuals are set on the order of 10^{-3} to achieve convergence.

3.2.6 Turbulence model

The standard compressible k-ε turbulence model which was explained in section 2.5.2, with hybrid wall function is used for calculations and simulating the turbulent flow within the combustion chamber. In the analysis a combined 'two layered' and 'low Reynolds number' hybrid wall boundary condition is used. The need for using a small value for y^+ was eliminated by the use of hybrid wall boundary conditions, which creates very fine mesh near the walls. By using the expression of asymptotic valid for $0.1 < y^+ < 100$ or by combining the low and high Reynolds number expression for chemical species, thermal energy, shear stresses wall fluxes. The y^+ independency was achieved with providing all necessary boundary conditions for a wide range of near-wall mesh densities. The variable values on the wall and at the near wall cells are calculated by using hybrid wall functions.

3.2.7 Combustion model

For modeling the SI engine combustion, the extended coherent flame modeling approach (ECFM) is adopted in the solver. The model is based upon solving a transport equation for the flame surface density with source terms accounting for flame production due to wrinkling of the flame by turbulence effects and for flame surface annihilation due to chemical reaction. The actual version of the coherent flame model implemented in AVL FIRE® fully accounts for equivalence ratio and residual gas inhomogeneities on the flame propagation characteristics. Thus, this model can be used for all types (premixed and non-premixed) of gasoline and gas engine applications.

3.2.8 Ignition

For modeling the spark ignition, spherical model is used ,since this ignition model can be used for all CFM models. In this model a spherical flame kernel is released using the spark position, ignition time, flame kernel radius and spark duration with the flame surface density specified in the FIRE Workflow Manager. The flame surface density is kept constant in the ignition cells over the spark duration. Required values which were applied in the solver for the baseline simulation are listed in Table 3.7. where;

Table 3.7 : Required inputs for spherical ignition model

	Case-44	Case-30	Case-35
Spark timing (spark advance)	30°CA BTDC	31°CA BTDC	32°CA BTDC
Spark location	set to zero (center of cylinder head)		
Flame kernel radius size [m]	0.003		
Ignition duration [s]	0.0003		
Initial flame surface density [1/m]	300		
Stretch factor	1.6		

Flame surface density is a problem specific model constant(recommended value 100 – 500 [1/m]). This value influences the ignition delay. The higher the initial value the shorter the ignition delay.

Stretch factor is a problem specific model constant (recommended value 1.0 - 4.0). An increase of the stretch factor leads to an intensification of the production of the flame surface density and hence in a shorter and faster combustion phase.

By applying the experimental values of spark timing in simulations, start of combustion was retarded and in-cylinder peak pressure occurred far from the TDC (35-45° ATDC). Therefore, a modified spark timing was calculated by implementing some simulations and comparing start of combustion, combustion duration, in-cylinder pressure and heat release rate diagrams of simulation with experimental diagrams of them. For instance in case of baseline operating condition for this study where the engine speed is equal to 1500 [rpm], according to the experimental data which is summarized in Table 3.2, the adopted value for spark advance was 20° BTDC, while the calculated value for adjusted

spark advance is 30° BTDC. The effects of different spark timing are investigated in the following section.

3.2.9 Pollutant model

The AVL FIRE® emission module enables the calculation of pollutants (mainly nitrogen oxide and soot) in engines and other combustion devices. The Extended Zeldovich model was used for NO formation and the Kinetic model was utilized for soot formation.

3.2.10 Summary

Eventually, all taken values and adopted submodels during the pre-processing of SI engine simulation for engine speed of 1500 [rpm], as an exemplar, are shown in Table 3.8.

Table 3.8 : SI engine baseline simulation set-up.

Specification of computational mesh			
Mesh type		ESE Diesel- hexahedral dominated mesh	
Total number of cells		56,596	
Solver run mode			
Run mode	Time step	Interval	Delta-alpha
		220-300	1
		300-400	0.2
		400-500	1
Start time [deg]		220	
End time [deg]		500	
Engine speed [1/min]		1500	
Fluid properties			
Fluid properties of		Air	
Density		Ideal gas	
Turbulent Prandtl No.		0.9	
Turbulent Schmidt No.		0.9	
Initial conditions			
Pressure [bar]		0.536	

Table 3.8 (cont.): SI engine baseline simulation set-up.

Temperature [K]			360
Density [kg/m^3]			0 (calculated automatically)
Turb. kin. energy [m^2/s^2]			8
Turb. length scale [m]			0.003
Turb. diss. rate [m^2/s^3]			1239.35
Velocity u [m/s]			0
Velocity v [m/s]			0
Velocity w [m/s]			0
Scalar			0
Initialization mode			Uniform
1-Equation turbulence model .			Off
Reinitialization			Off
Smoothing			Off
Multi-component			No
Type of hydrocarbon fuel			Gasoline (C_8H_{17})
EGR mass fraction			0.1
EGR composition			1
Laminar flame speed			Database
Equivalence ratio			1
Lower heating value [J/kg]			0 (calculated automatically)
Heat of formation [kJ/kmol			0 (calculated automatically)
Boundary conditions			
Selection	BND_Piston		
Wall	Movement	Mesh movement	
	Thermal	Temperature [k]	450
	Roughness	Off	
	Slip wall	Off	
Selection	BND_Axis		
	Symmetry		
Selection	BND_Head		
Wall	Movement	Velocity	
	Thermal	Temperature [k]	430
	Roughness	Off	
	Slip wall	Off	

Table 3.8 (cont.): SI engine baseline simulation set-up.

Selection	BND_Liner		
Wall	Movement	Velocity	
	Thermal	Temperature [k]	410
	Roughness	Off	
	Slip wall	Off	
Selection	BND_Segment_1		
Inlet/Outlet	Periodic		
	Boundary connection	Boundary_connection1	
	Pressure drop	Off	
Comments on Solver setting			
Discretization			
	Calculation of boundary values		
	Exportable		On
	Calculation of derivatives		
	Least Sq. Fit		On
Simple/Simpleec/Piso/Simple-H	Simple		
Active equations			
	Momentum & continuity		Yes
	Turbulence model		k-epsilon
	Energy equation		Yes
	Total/static enthalpy		Total enthalpy
	Compressibility		Compressible
	Wall treatment		Hybrid wall function
	Heat transfer Wall model		Standard wall Function
Convergence criteria			
	Type	Min. iteration	Max. iteration
Momentum	GSTB	0	50
Continuity	AMG	0	50
Turbulence	GSTB	0	50
Energy	GSTB	0	50
Scalar	GSTB	0	50
Linear solver			
	Max. number of iteration		100
	Min. number of iteration		10
	Normalized residuals		On

Table 3.8 (cont.): SI engine baseline simulation set-up.

Comments on Module setting - Species transport	
Standard / General	Standard
Comments on Module setting - Combustion	
Combustion models	
Combustion models	Coherent Flame Model - ECFM
Spark ignition	On
Ignition models	
Spark ignition model	Spherical model
Initial flame kernel shape	Spherical
Automatic model parameters	Off
Initial flame surface density [1/m]	300
Stretch factor	1.6
Spark timing [deg]	330
Flame kernel size [m]	0.003
Ignition duration [s]	0.0003
Auto-ignition	Off
Comments on Module setting - Emission	
NO_x models	
Model	Extended Zeldovich
Soot models	
Model	Kinetic model

3.3 Simulation Results And Validation

In order to assess the accuracy and reliability of the CFD simulations, it is critical to perform validation studies over various engine operating conditions. Simulation-based design of engines requires predictive capabilities, where results do not need to be tuned for each operating condition. This requires the models adopted to simulate their respective physical and chemical processes, to be reliable under a wide range of conditions. Analyzing the results of experimental study, it should be mentioned that

the results of indication of IC engines, in particular, the results of the thermal processes analysis which taking place in the cylinder are subject to some error, resulting from the measurement accuracy and hence the uncertainty of the results.

In current study, in order to confirm the validation of the numerical simulation and predictive accuracy of model, in-cylinder pressure, heat release rate, specific fuel consumption, brake mean effective pressure and emissions predictions were compared with the measured experimental results at three different engine speeds of 1500[rpm], 1660 [rpm] and 1800[rpm]. Then the model was applied to the prediction of combustion process for different EGR ratios, equivalence ratios, spark advances and using methane as alternative fuel at the engine speed of 1500[rpm]. The combustion prediction includes cylinder pressure, heat release rate, mean effective pressure, specific fuel consumption and exhaust emissions, thus the combustion process could be analyzed in detail.

3.3.1 In-cylinder pressure comparison

In order to provide a proper data basis for model validation, cylinder pressure predictions are performed for the relevant speed/load points of the investigated engine. The initial pressure for all cases is based on the experiment but carefully adjusted and iterated to obtain better results. Comparison of simulated and experimental in-cylinder pressure at engine speeds of 1500[rpm], 1660 [rpm] and 1800 [rpm] are shown in Figures 3.6, 3.7 and 3.8, respectively. It can be seen from the figures that the predicted in-cylinder pressure are in very good agreement with the measured experimental in-cylinder pressure. The deviation in some points during the combustion is attributed to assumption of fixed wall temperatures instead of mapping to save computational time. Moreover, cyclic variations in experimental results is another possible factor that could have contributed on these negligible differences. The peak pressure discrepancy between experiment and computation is even less than 0.6 %, which demonstrated the predictive capabilities of the adopted models. Peak cylinder pressure values and related crank angles are presented in Table 3.9.

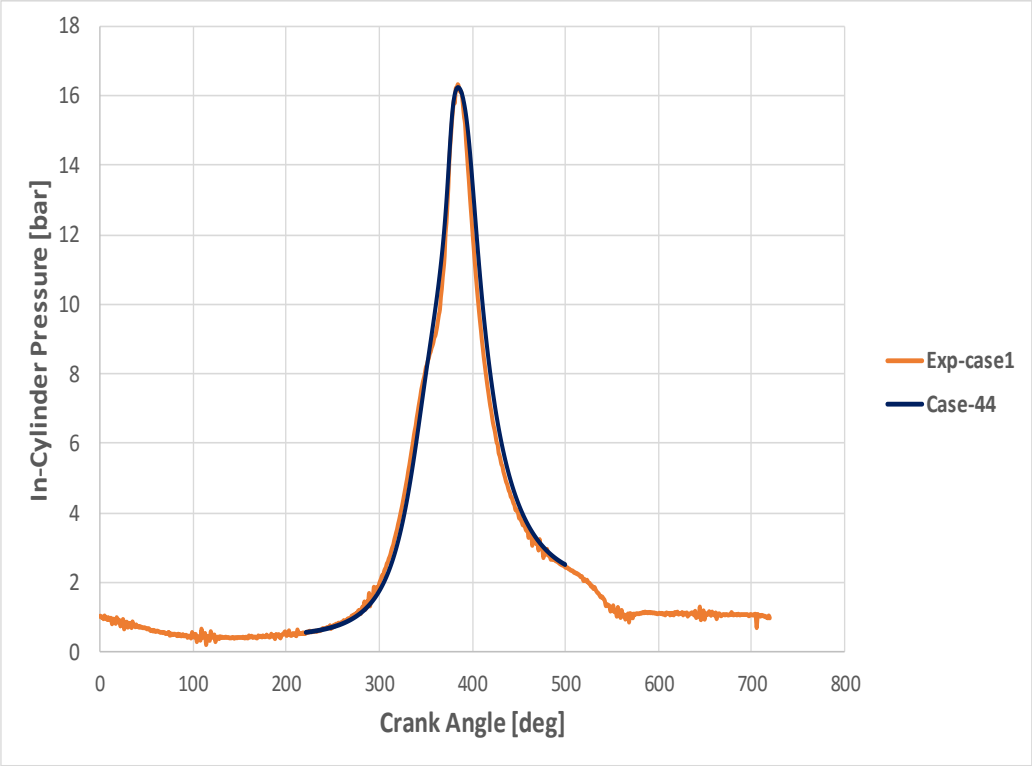


Figure 3.6 : In-cylinder pressure comparison between experimental and simulation results @1500[rpm].

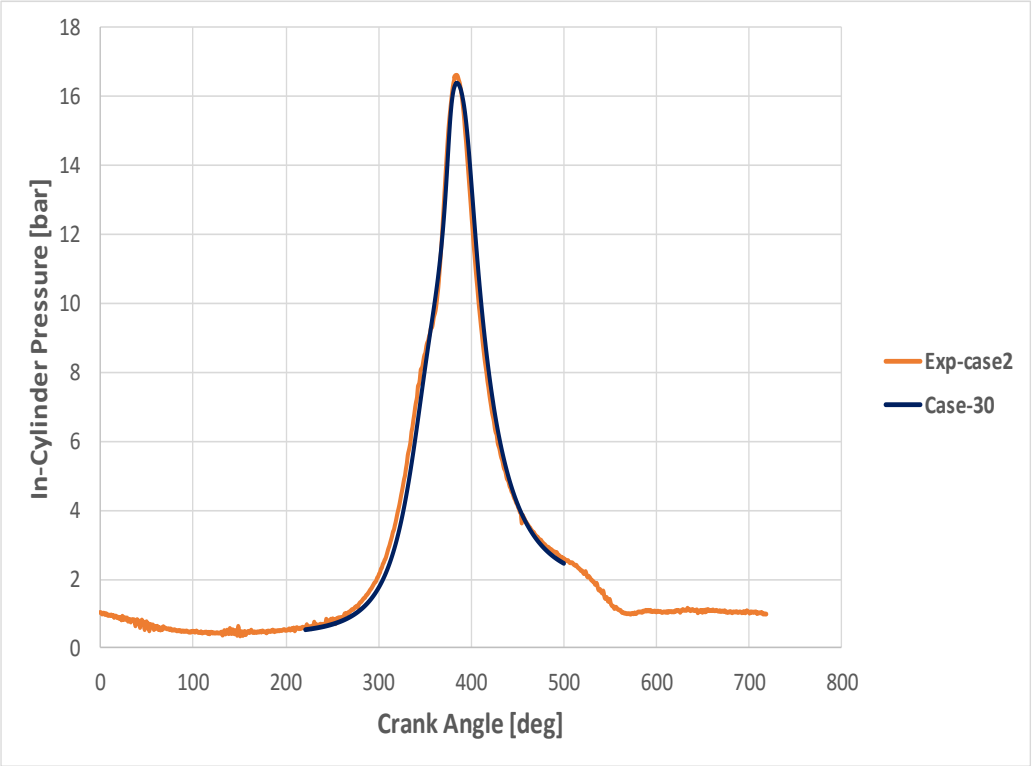


Figure 3.7 : In-cylinder pressure comparison between experimental and simulation results @1660[rpm].

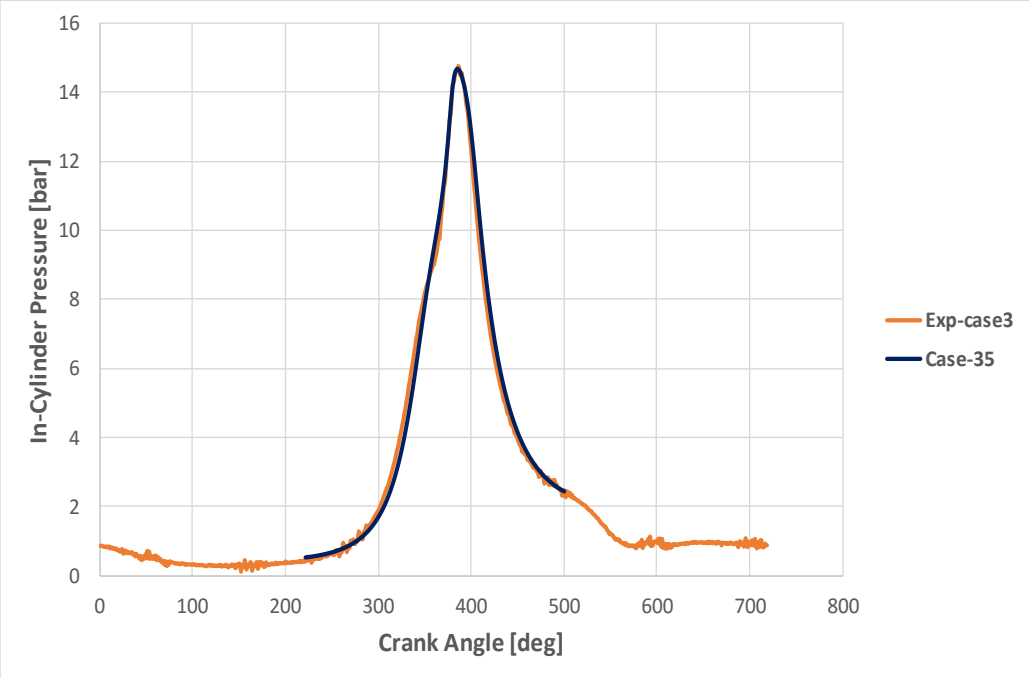


Figure 3.8 : In-cylinder pressure comparison between experimental and simulation results @1800[rpm].

Table 3.9 : Experimental and simulated peak cylinder pressures and related crank angles.

Engine speed [rpm]	Case	Peak pressure [bar]	@ CAD	dP [%]	dθ [deg]
1500	Exp-case1	16.33	384	0.1%	0
	Case-44	16.31	384		
1660	Exp-case-2	16.60	385	0.6%	0.4
	Case-30	16.50	384.6		
1800	Exp-case-3	14.73	386	0.3%	0.2
	Case-35	14.68	385.8		

3.3.2 Rate of heat release comparison

Rate of heat release represents the combustion-caused energy release per degree crank angle. Comparison of simulated and experimental heat release rate for all cases are shown in Figures 3.9, 3.10 and 3.11. The figures demonstrates that the timing of the heat release initiation and the timing of the peak heat release rate and peak value of the heat release rate are in good agreement with those of measured experimental heat release rate.

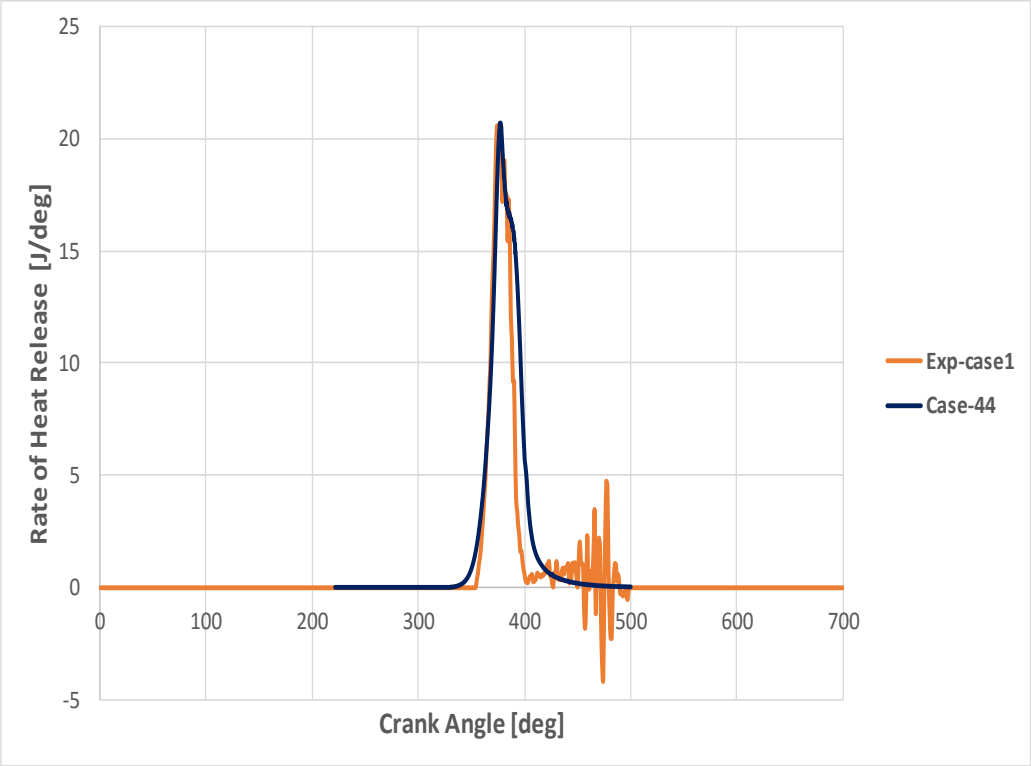


Figure 3.9 : Heat release rate comparison between experimental and simulation results @1500[rpm].

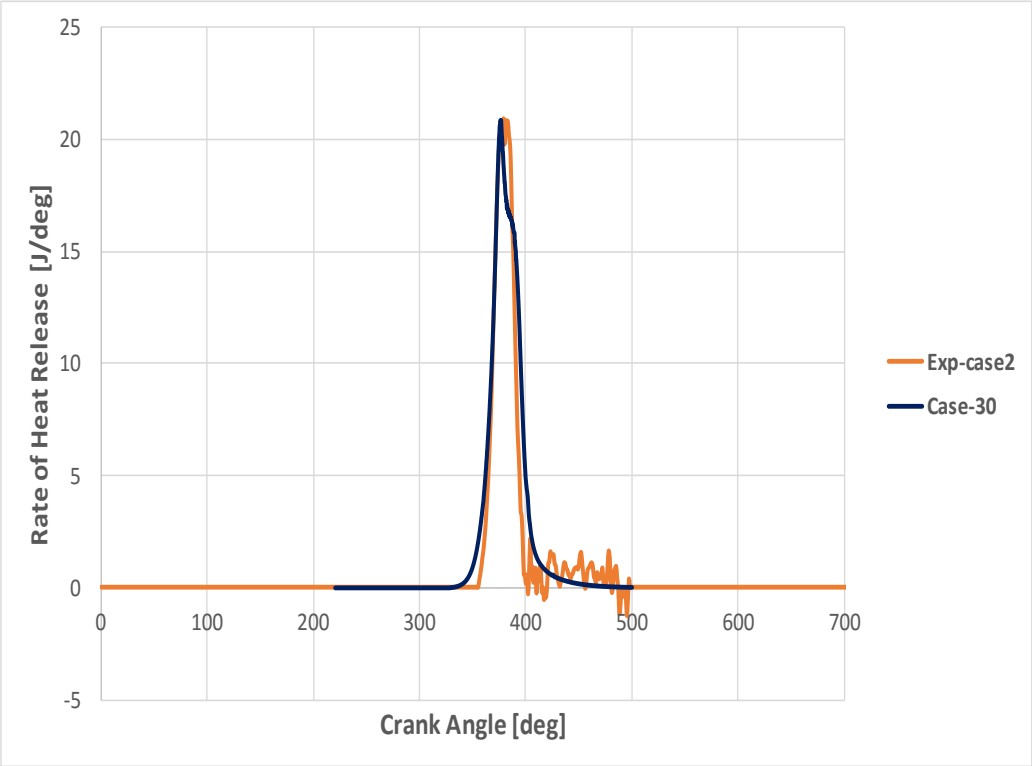


Figure 3.10 : Heat release rate comparison between experimental and simulation results @1660[rpm].

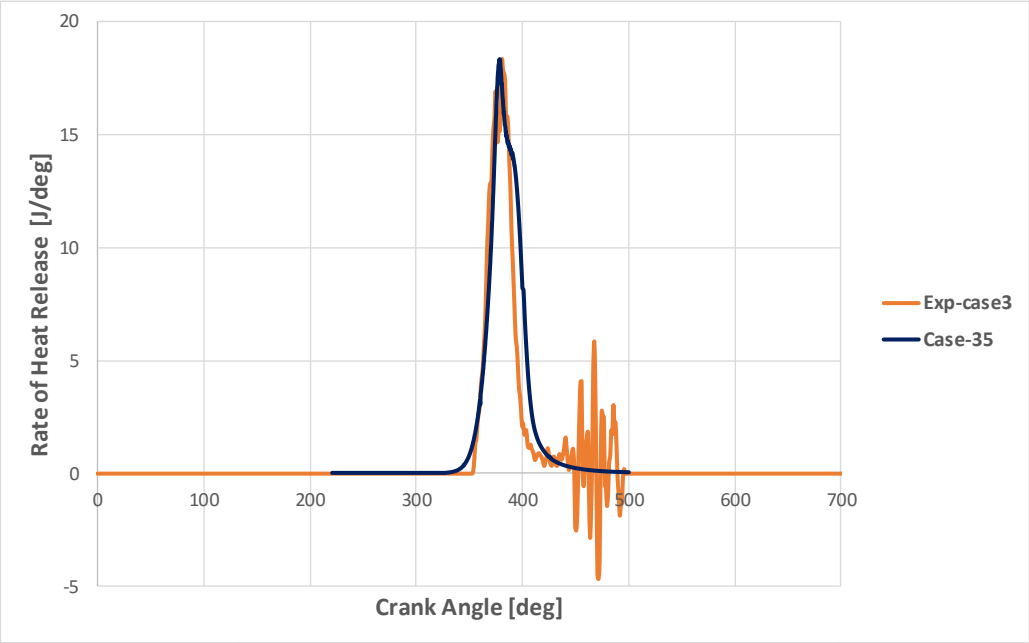


Figure 3.11 : Heat release rate comparison between experimental and simulation results @1800[rpm].

Furthermore, in order to compare the start of combustion (SOC) and combustion duration, comparison of simulated and experimental accumulated heat release for all cases are presented in Figures 3.12, 3.13 and 3.14, respectively.

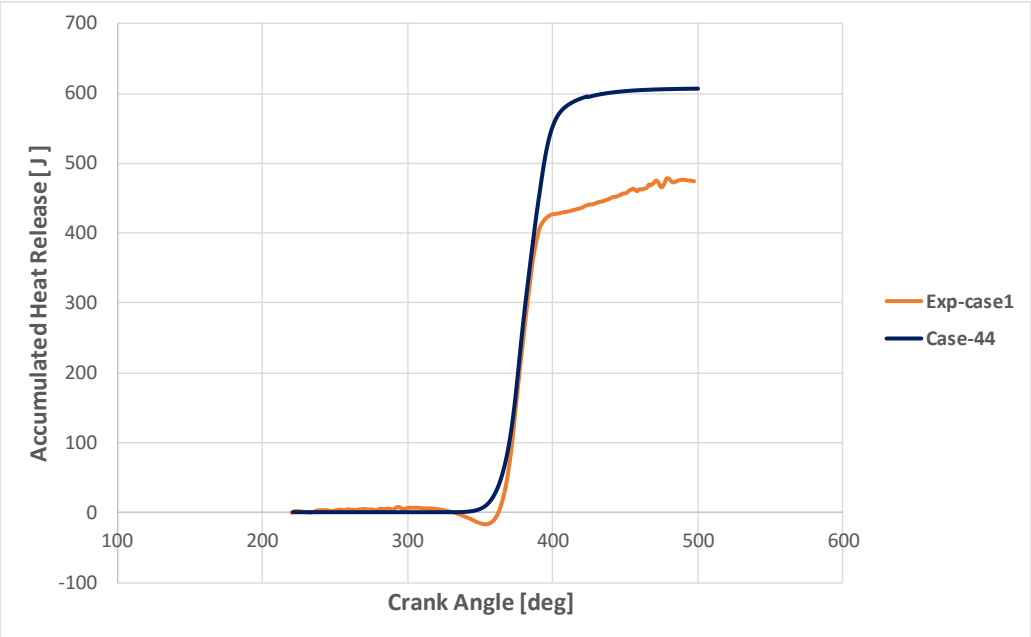


Figure 3.12 : Accumulated heat release comparison between experimental and simulation results @1500[rpm].

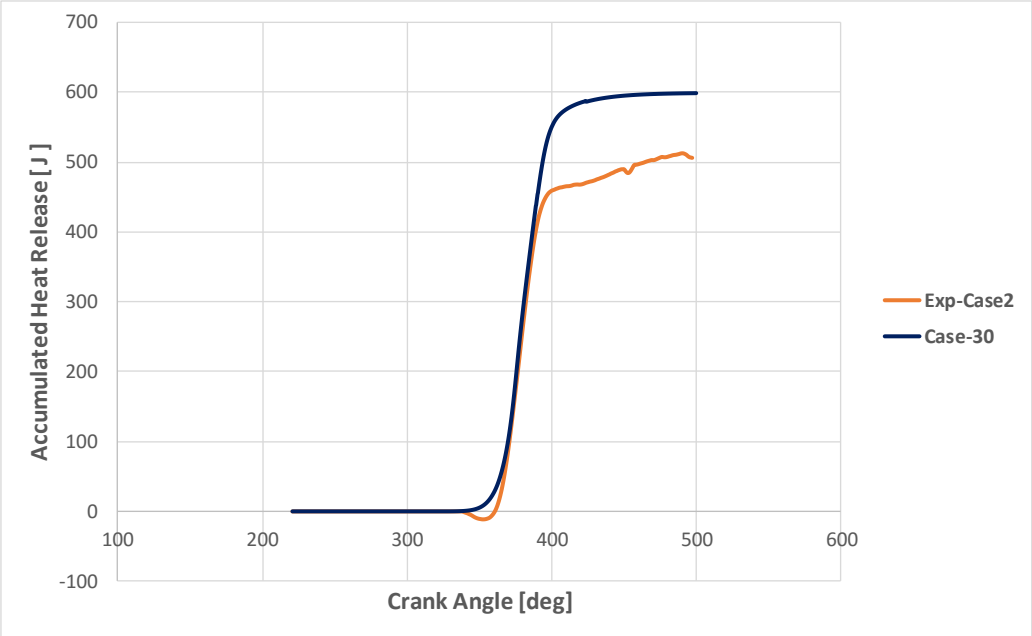


Figure 3.13 : Accumulated heat release comparison between experimental and simulation results @1660[rpm].

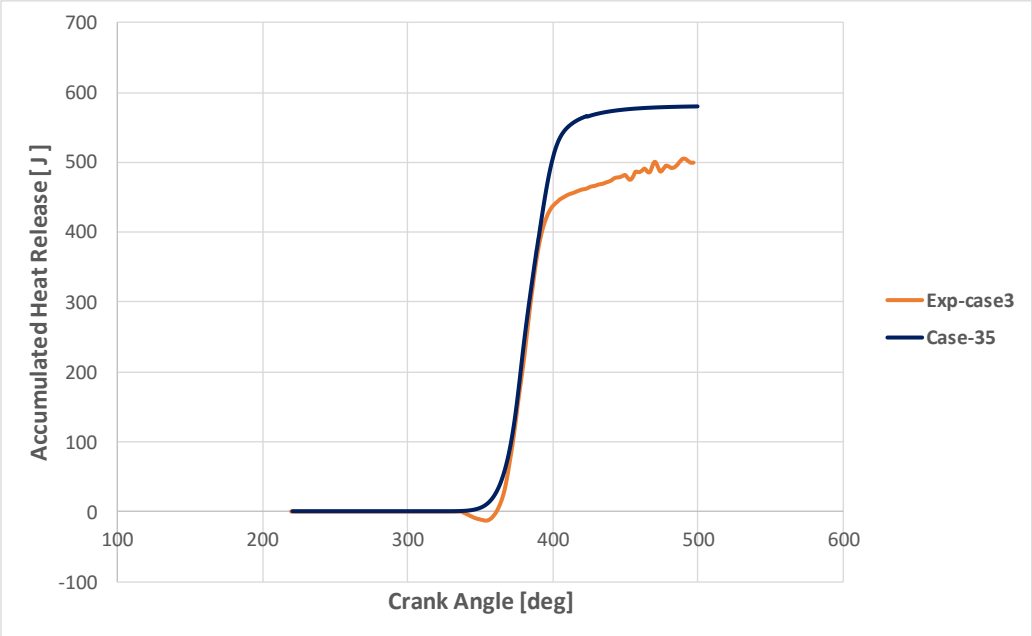


Figure 3.14 : Accumulated heat release comparison between experimental and simulation results @1800[rpm].

The accumulative heat release is the integration of the heat release rate derivative over the relevant crank angle rotation, in another words integral representation of the heat release rate between combustion start and end, reaches at the end point the energy chemically bound in the fuel multiplied by the degree of conversion. Start

of combustion (SOC) was defined as the point when 10% of the accumulative heat release had occurred and end of combustion was defined as the point for 90% of accumulative heat release. Moreover, the time between start of combustion and end of combustion is designated as combustion duration.

The energy balance is an essential quantity in judging the quality of the heat release rate evaluation. It is produced from the quotient of the energy quantity determined by the heat release rate evaluation and the maximum energy quantity released by the fuel. So;

$$EB = \frac{\int_{\varphi_{SOC}}^{\varphi_{EOC}} \frac{dQ_f}{d\varphi}}{m_f LHV - Q_{ub}} = \frac{\int_{\varphi_{SOC}}^{\varphi_{EOC}} \frac{dQ_f}{d\varphi}}{m_f LHV \eta_{com}} \tag{3.1}$$

where; LHV is the lower heating value of fuel, Q_{ub} is the energy of unburned gas, η_{com} is the combustion efficiency and described as;

$$\eta_{com} = 1 - \frac{Q_{ub}}{m_f LHV} \tag{3.2}$$

The heat release rate is thereby integrated over the entire combustion duration and represents the numerator of the quotient of the energy balance. The maximum released energy quantity, the denominator, can be calculated from the product of the fuel injected per cycle and the lower heating value, whereby ,especially in the case of the SI engine, the energy of unburned exhaust gas components must be subtracted.

Although there is some over prediction of the accumulated heat release during the end of combustion, it can be seen from the Figures 3.12, 3.13 and 3.14 , excellent agreement between model and experiment was obtained for the start of combustion phasing and combustion duration, which are also summarized in Table 3.10. According to Eq.(3.1), the slight discrepancy in rate of heat release and accumulative heat release between model and experiment during the end of combustion could be result of lower heating value of fuel assumed in simulation, differences between components of fuel i.e. C/H ratio, used in experimental test and simulation, experimental uncertainty in the mass of injected fuel and use of sector simulation, which assumes perfect symmetrical behavior for each sector.

Table 3.10 : SOC and combustion duration of experimental and simulations.

Engine speed [rpm]	Case	Start of Combustion @CAD	Combustion Duration [CAD]	dθ [deg]
1500	Exp-case1	367	31	1
	Case-44	366	32	
1660	Exp-case-2	367	31	1
	Case-30	366	32	
1800	Exp-case-3	369	36	2
	Case-35	367	38	

In summary, one can say that for a thermodynamically correct evaluation, a high precision in pressure indication and determination of all measured quantities is necessary. If all these prerequisites are fulfilled, then it is possible to determine not only the mean effective pressure, but also the temporal release of heat release rate as a decisive requirement for an efficient simulation.

3.3.3 Engine specific output

The post-processor of AVL FIRE® offers numerous functions enabling detailed online job monitoring, results visualization and analysis. By analysing the simulation results via ESE Diesel analyser tool, valuable information about engine outputs such as e.g. brake mean effective pressure, indicated power and torque, are achieved. Analysing results are listed in Table 3.11. The mean effective pressure (p_{me}) is an important characteristic quantity for the evaluation of performance and of the technological standing of an internal combustion engine. From the definition of piston work, the indicated work per cycle is obtained as

$$W_i = \oint pdV \tag{3.3}$$

and with the definition

$$W_i = p_{mi} V_d \tag{3.4}$$

where p_{mi} is mean indicated pressure and V_d $[m^3]$ is displacement volume.
The indicated power per cylinder is related to the indicated work per cycle by

$$P_i = \frac{W_i N}{n_R} \tag{3.5}$$

Table 3.11 : Engine specific output.

	Case-44	Case-30	Case-35
Engine speed [rpm]	1500	1660	1800
Break mean effective pressure BMEP [bar]	3	3.09	2.97
Combustion Noise - A + CAV Filter [dB]	80.98	81.22	81.52
Combustion Noise - A Filter [dB]	188.65	188.74	188.15
Combustion Noise - CAV Filter [dB]	80.33	80.6	80.87
Combustion Noise [dB]	207.31	207.36	206.57
Excess air ratio [-]	1	1	1
Friction mean effective pressure FMEP [bar]	1.76	1.6	1.47
Indicated mean effective pressure IMEP [bar]	4.76	4.71	4.45
Indicated power [kW]	2.7	2.94	3.03
Indicated specific power [kW/l]	5.95	6.48	6.68
Indicated specific torque [Nm/l]	37.87	37.45	35.43
Indicated torque [Nm]	17.19	17	16.09
Mean mass [kg]	2.49E-04	2.45E-04	2.37E-04
Mechanical efficiency [-]	0.63	0.66	0.67
Total mass at start of high pressure cycle [kg]	2.53E-04	2.49E-04	2.41E-04
Volume displacement [m^3]	4.54E-04	4.54E-04	4.54E-04

where N is engine speed [1/min] and n_R is the number of crank revolutions for each power stroke per cylinder. For four-stroke cycles, n_R equals 2 and for two-stroke cycles, n_R equals 1.

Finally by taking Eq.(3.4) into the account, for indicated power

$$P_i = \frac{p_{mi} v_d N}{n_R} \tag{3.6}$$

Analogous to this, for the effective(brake) power

$$P_e = \frac{p_{me} v_d N}{n_R} \tag{3.7}$$

Also the power follows from

$$P = M 2\pi N \tag{3.8}$$

Where M [N.m] is torque and N is engine speed[1/min].

The indicated power is the total power available from the expanding of gasses in the cylinders neglecting any friction or heat loss within the system. The effective (brake) power on the other hand is the usable power delivered by the engine to the load. So an additional portion is used to overcome the friction of the bearings, pistons and other

mechanical components of the engine. All of these power requirements are grouped together and called friction power (P_f)

$$P_i = P_e + P_f \tag{3.9}$$

The ratio of the effective (brake) power delivered by the engine to the indicated power is called mechanical efficiency;

$$\eta_m = \frac{P_e}{P_i} = \frac{p_{me}}{P_{mi}} \tag{3.10}$$

With the help of analyser tool, comparison of brake mean effective pressure, effective power and effective torque between simulation and experimental results as a function of engine speed are provided and shown in Figures 3.15, 3.16 and 3.17, respectively. Experimental values are adapted from Table3.2.

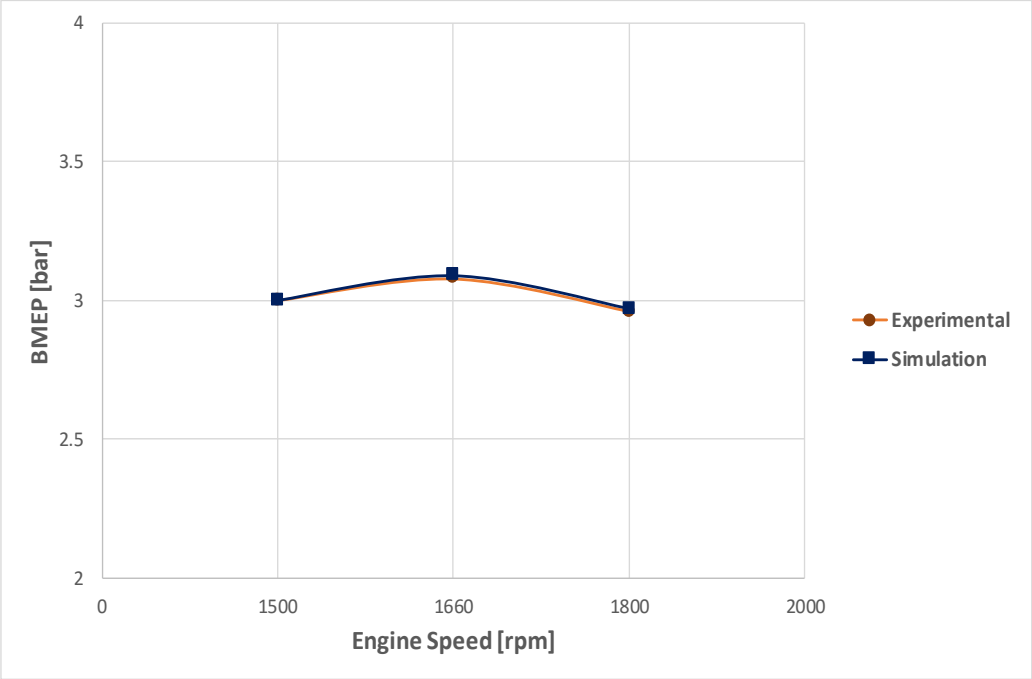


Figure 3.15 : Brake mean effective pressure comparison between experimental and simulation results.

By considering mechanical efficiency and indicated power of each case which are listed in Table3.11 and by using Eq.(3.10), the effective power is calculated and a comparison of calculated and experimental effective power as a function of engine speed is shown in Figure 3.16.

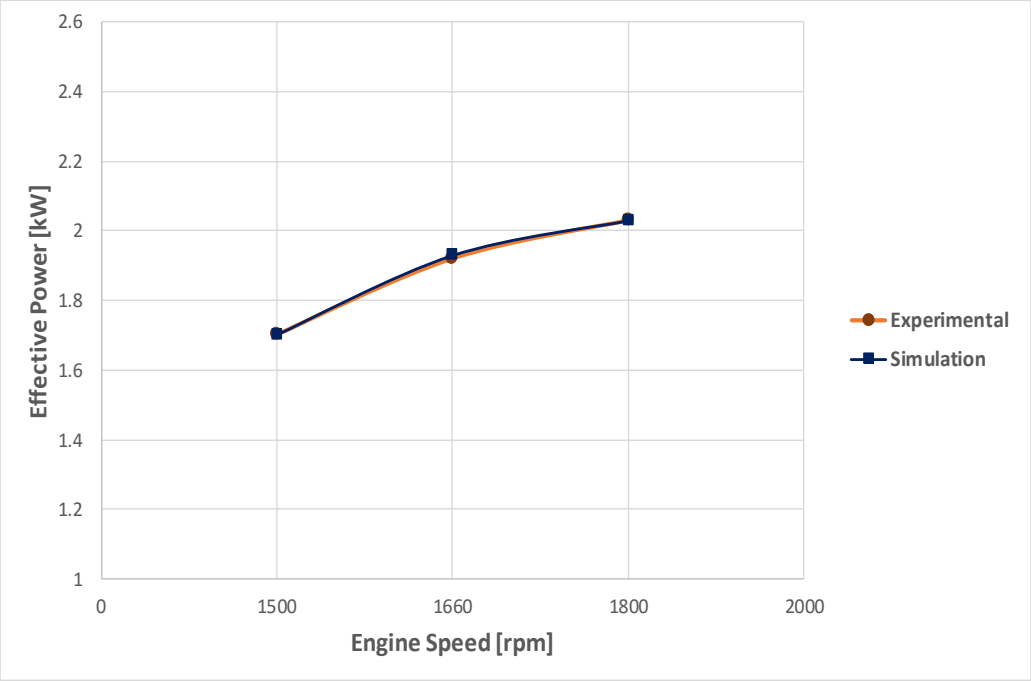


Figure 3.16 : Effective power comparison between experimental and simulation results.

A comparison of calculated and experimental effective torque as a function of engine speed is shown in Figure 3.17.

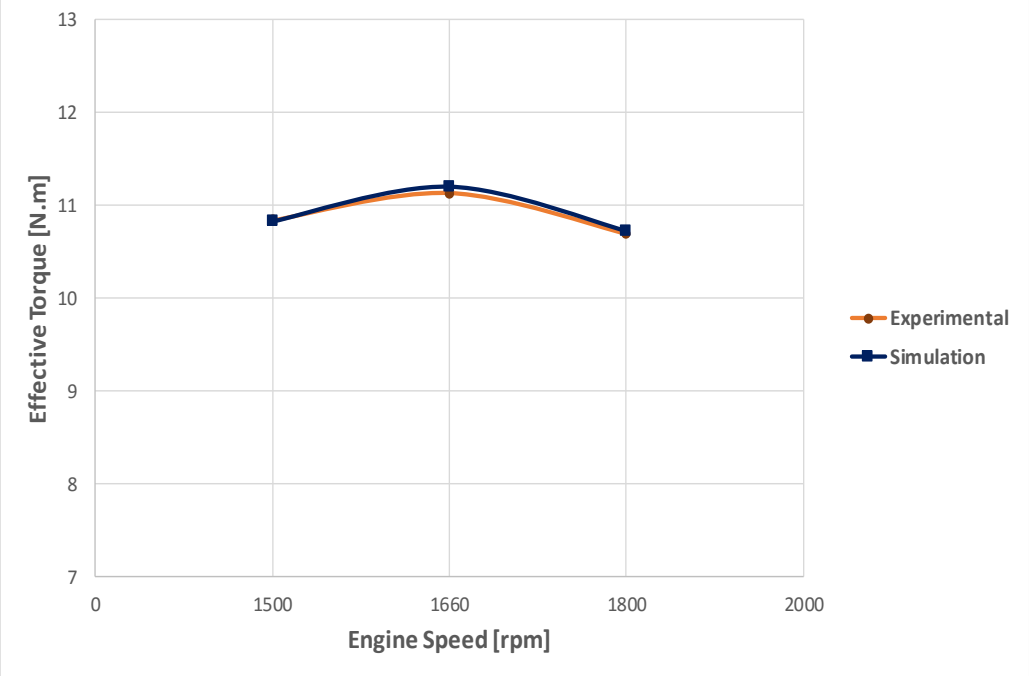


Figure 3.17 : Effective torque comparison between experimental and simulation results.

Indeed in case of engine performance characteristics, it can be seen from the presented diagrams, the simulated and experimental data matched quite well and a sufficient correlation with experimental results are achieved.

3.3.4 Specific fuel consumption comparison

Figures 3.18,3.19 and 3.20 illustrate the supplied fuel mass fraction and burnt fuel mass faction of simulations as a function of crank angle. During the simulations Burnt fuel mass fraction which could be considered as combustion efficiency equivalent (Eq.(3.2)), reached the values above 99%.

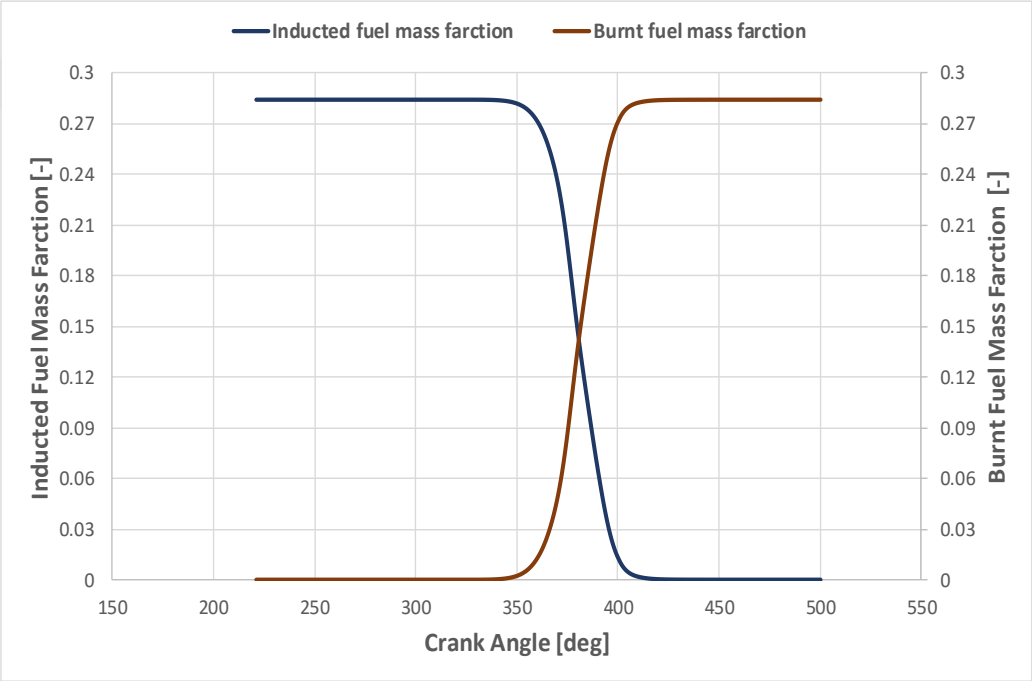


Figure 3.18 : Supplied and burnt fuel mass fraction of case-44

According to the simulation results and considering the experimental data (Table3.2), calculated and measured fuel mass flow rates ($\dot{m}_f$) are summarized in Table 3.12. The fuel consumption is measured as fuel mass flow per unit time ($\dot{m}_f$). A more useful parameter is the specific fuel consumption (sfc),which is defined as the fuel flow rate per unit power output. It measures how efficiently an engine is using the fuel supplied to produce work;

$$\text{sfc} = \frac{\dot{m}_f}{P} \tag{3.11}$$

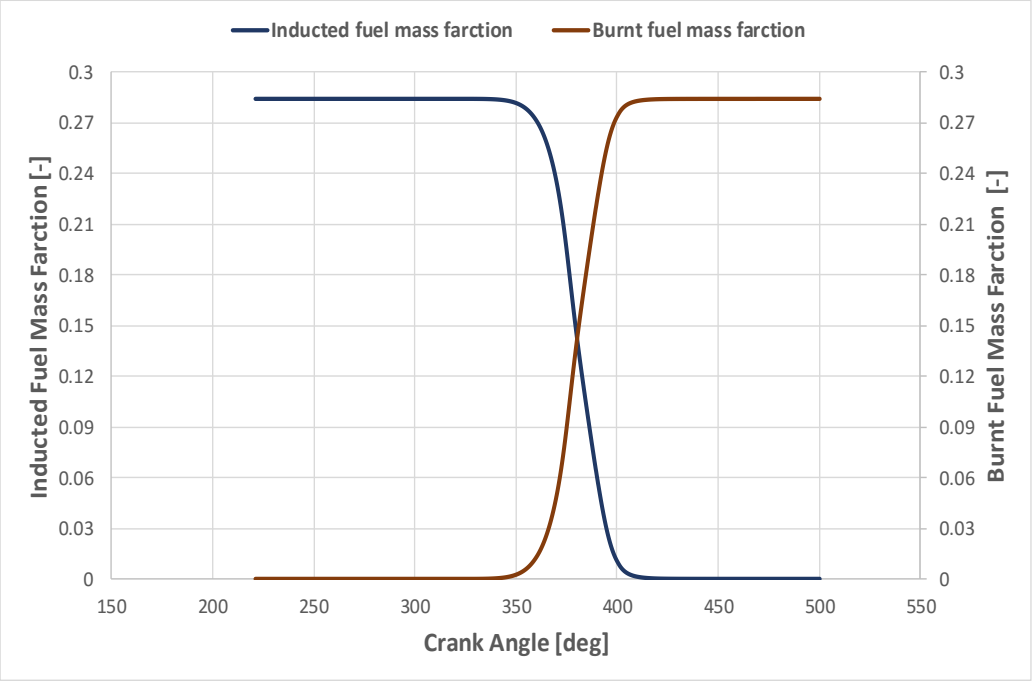


Figure 3.19 : Supplied and burnt fuel mass fraction of case-30.

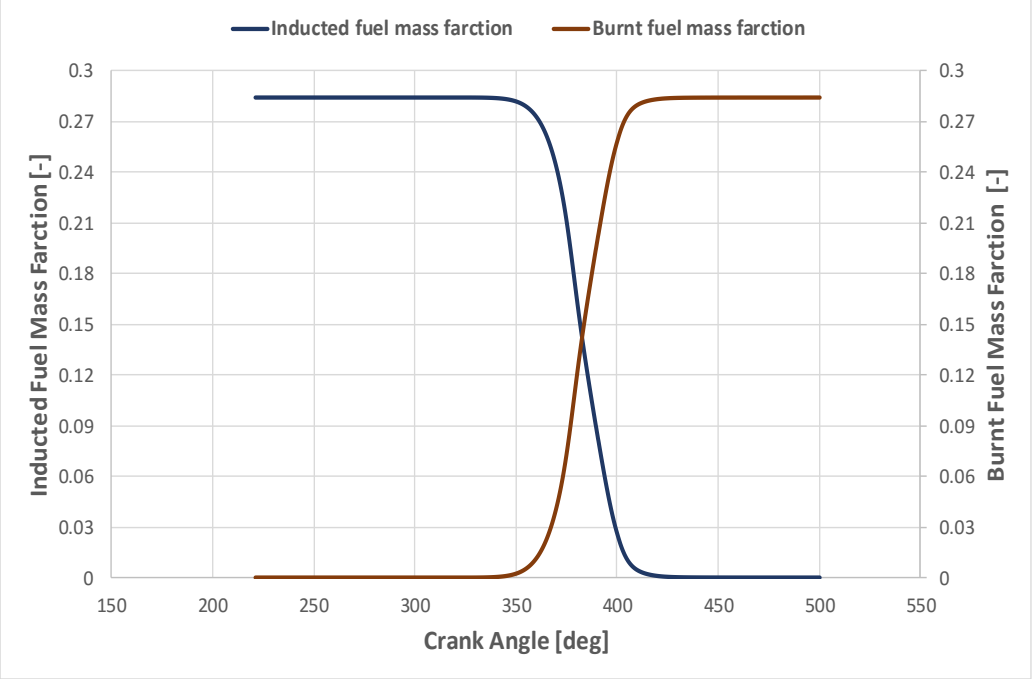


Figure 3.20 : Supplied and burnt fuel mass fraction of case-35.

Figure 3.21 compares the brake specific fuel consumption of simulations against the measurements as a function of engine speed.

Table 3.12 : Calculated and measured fuel mass flow rates.

Engine speed [rpm]	Case	$\dot{m}_f$ [kg/h]
1500	Exp-case1	0.813
	Case-44	0.649
1660	Exp-case-2	0.913
	Case-30	0.706
1800	Exp-case-3	0.965
	Case-35	0.740

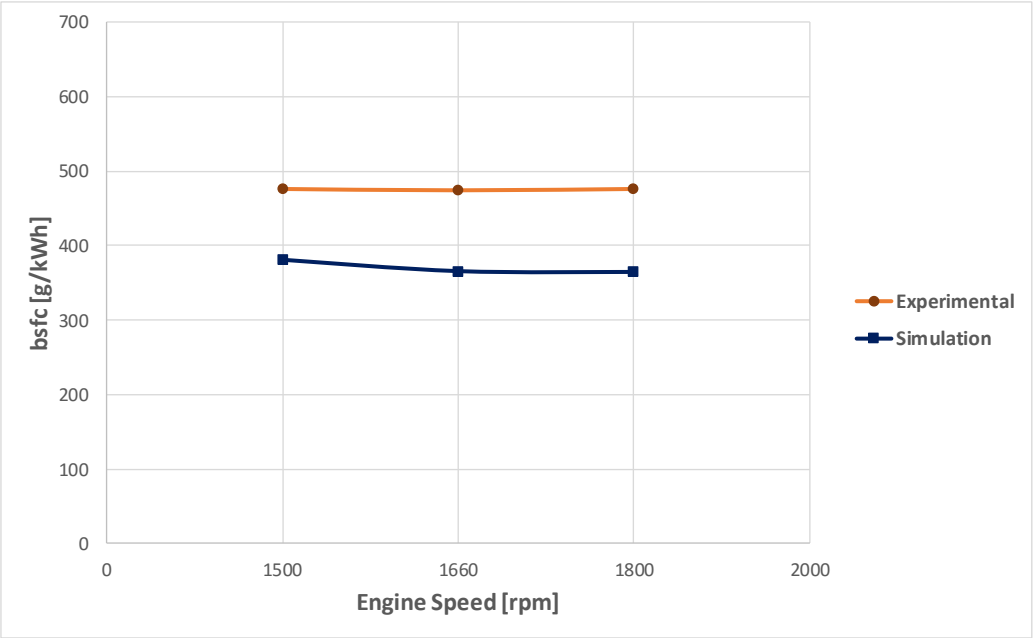


Figure 3.21 : Brake specific fuel consumption comparison between experimental and simulation results.

Some under-prediction was observed for the brake specific fuel consumption, which can be attributed to the several sources. In brief, according to Eq.(3.11), the sfc depends on fuel mass flow rate ($\dot{m}_f$) and power output (P). Since the effective power of model and experiment is matched very well, as shown in Figure 3.16, thus the only parameter that cause the differences in sfc is the fuel mass flow rate. By considering this fact, every factor that affects the amount of supplied fuel could have contributed to this observed difference. One of the most important parameters is stoichiometric air-fuel ratio which affects the amount of supplied fuel. Other important parameters such as lower heating value of the fuel, the intake air temperature and

cooling water temperature also affect the sfc of engines. By considering these factors, the discrepancy in the brake specific fuel consumption between model and experiment could be result of lower heating value of fuel assumed in simulation, differences between components of fuel (C/H ratio) used in experimental test and simulation which affect the value of stoichiometric air-fuel ratio, experimental uncertainty in the mass of injected fuel and slight differences in intake air temperature which change the amount of inducted air and as a consequence the amount of injected fuel.

3.3.5 NO_x emissions

Finally, in order to evaluate the emission characteristic of model and by considering available experimental data, a comparison of NO_x emissions between simulation and experimental results as a function of engine speed is illustrated in Figure 3.22.

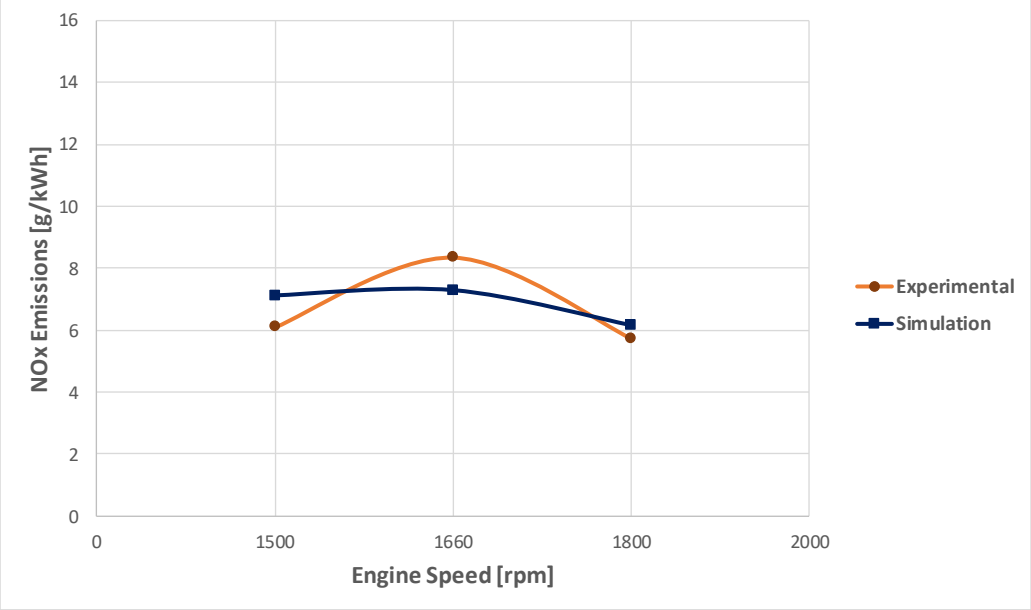


Figure 3.22 : NO_x emissions comparison between experimental and simulation results.

As it can be seen in Figure 3.22, some disagreements were observed for the amount of NO_x emissions. Hence, the thermal NO formation in the burnt gases always dominates in comparison to the NO formed in the flame front and represents the main source of the nitric oxide in engines whose reaction paths are effective at high temperatures. NO emissions form throughout the high-temperature burned gases behind the flame through chemical reactions involving nitrogen and oxygen atoms and molecules, which

do not attain chemical equilibrium. Thus, the higher the burned gas temperature, the higher the rate of NO formation. There are several additional factors which affect the formation of NO_x in the engine. The air-fuel ratio plays a major role in determining the amount of emission of NO_x , as oxides of nitrogen are formed by the reaction of nitrogen with oxygen in the combustion air. When the air-fuel ratio is greater than one which indicates that the combustion is in the lean condition, the mixture has considerably less amount of fuel and excess amount of air, it will generate higher amounts of NO_x . The firing and quenching rates also influence the rate of NO_x formation where a higher firing rate is associated with the higher peak temperatures and thus increases the NO_x emissions. On the other hand, high rates of thermal quenching result in lower peak temperatures and contribute to the reduction of NO_x emission. Therefore, the slight discrepancy in the amount of NO_x emissions between model and experiment could be result of adopted initial temperatures in simulation, lower heating value of fuel assumed in simulation, assumption of fixed wall temperatures in simulation, experimental uncertainty and measurement errors.

All in all, the model's predictive accuracy was assessed by comparing various parameters with the corresponding experimental data and indicates very good overall agreement. The created model of SI engine was successfully verified and the resulting differences are acceptable. The results of modelling allow for an analysis of engine operation both in terms of thermodynamic and flow.

3.4 Parametric Study

Based on the confidence gained from validation, the study is extended to evaluate the effect of EGR ratio, equivalence ratio and spark advance on SI engine performance and emissions. A comprehensive study of the effects of mentioned parameters with respect to the performance and exhaust emissions at a fixed engine speed of 1500 [rpm] are presented in this section.

The verified model(case-44) including grid resolution, boundary conditions and adopted submodels is used for the further investigations. In this study, the individual influence of exhaust gas recirculation, equivalence ratio and spark timing on the engine performance and emissions are investigated independently.

3.4.1 Effect of EGR

In internal combustion engines, exhaust gas recirculation is a known technique to reduce NO_x emissions. Many studies have been done on the effect of EGR which were summarized in section 1.2, but most of them have focused on compression ignition engines. In this regard, various levels of EGR 0, 5, 10, 13, 15, 18 and 20% were adopted in simulated SI engine to understand its effect on SI engine performance and emissions behavior.

3.4.1.1 In-cylinder pressure

Although introducing EGR leads to a reduction in intake oxygen concentration, as described in section 3.2.4, AVL FIRE® first calculates the composition of the oxidizer and after this, the correct amount of fuel is determined for the present oxygen concentration. This order of calculation is necessary because the EGR can contain oxygen which also has to be taken into account when the equivalence ratio is calculated. The equivalence ratio for baseline studies is set to 1.

Figure 3.23 illustrates the effect of various EGR ratios on in-cylinder pressure. As it can be seen in Figure 3.23, EGR showed a promising way of suppressing peak cylinder pressure and peak pressure rise rate. With the increase in the EGR percentage, the peak cylinder pressure and peak pressure rise rate decreased drastically. Notable distinctions concerning with the peak value and the crank angle position corresponding to the in-cylinder peak pressure are exhibited under various EGR rates. The peak pressure values and related crank angle positions for adopted amounts of EGR are summarized in Table 3.13. The peak cylinder pressure with 10% EGR rate decreased approximately by 40% and decreased by 66% with EGR rate of 18% compared with the peak cylinder pressure with 0% EGR rate. However, poor combustion is occurred by applying EGR rates higher than 18% and those cases are not preferable. According to the Figure 3.23 and Table 3.13, by increasing EGR ratio the peak pressure position is retarded and happened far from TDC, except for the EGR ratios higher than 18% which presented an unstable combustion.

Attempts to increase EGR levels for higher than 18% resulted in combustion instability and misfire. A typical problem in utilizing EGR is that if the EGR rate is too high, combustion temperature decreases so much and combustion may become very erratic.

The maximum amount of EGR is limited by requirement of the mixture to sustain a continuous flame front during the combustion process, so excessive EGR rates can cause misfire and partial burns. Therefore, the optimum EGR rate should be carefully determined to obtain a better engine performance and lower exhaust emissions.

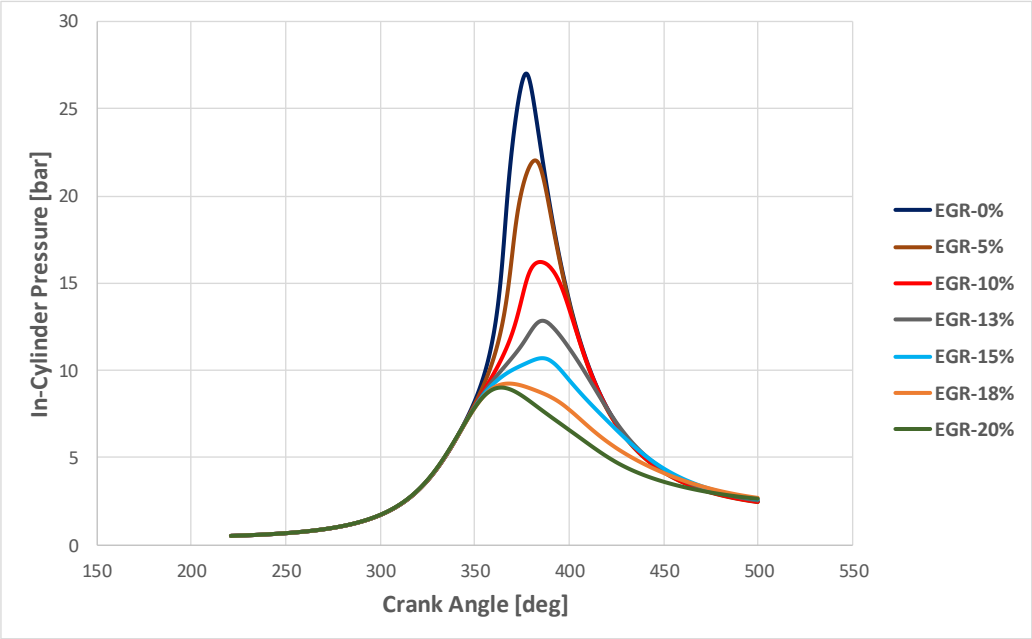


Figure 3.23 : The effect of EGR on in-cylinder pressure.

Table 3.13 : Peak cylinder pressures and related crank angles with different EGR rates.

EGR [%]	Peak pressure [bar]	@ CAD
0	27.03	377
5	22.07	382
10	16.31	384
13	12.82	385
15	10.71	385
18	9.25	368
20	8.97	364

3.4.1.2 In-cylinder mean temperature

It should be mentioned that the temperature of combustion chamber differs from one point to another at a specified crank angle step. In this regard, for each crank angle step a wide range of temperature is calculated and a mean value is offered by AVL

FIRE® as a temperature indicator for whole combustion at that moment.

Figure 3.24 shows the effect of various EGR rates on mean combustion temperature. By implementing EGR, a remarkable reduction in combustion temperature is observed, due to the EGR entering the combustion chamber and its components have higher specific heat capacities than air, thus act as a heat sink. The EGR components take up a part of the cylinder that would normally filled with a combustible air-fuel mixture and act as non-reacting species. These non-reacting species increase the specific heat capacity of mixture charge and absorb energy during the reaction and hence act to decrease the adiabatic flame temperature. As shown in figure 3.24, higher percentages of EGR introduce more exhaust gasses into the cylinder, thus more non-reacting species and lower combustion temperatures. Moreover peak combustion temperatures are retarded and occurs late in expansion stroke.

Adding EGR decreases the flame propagation speed ,and hence the combustion duration is increased and postponed to the expansion stroke. The varying trend of in-cylinder mean temperature in Figure 3.24 suggests that the applying EGR is a useful method to reduce the flame temperature for controlling NO_x formation in a SI engine. In this case, when EGR varies from 0% to 18%, the peak value of in-cylinder mean temperature decreases from 2671.5 [K] to 1851.7 [K] which means 31% reduction in peak mean temperature and also retards by 80 [CAD]. Peak value of in-cylinder temperatures and corresponding crank angles for different EGR rates are listed in Table 3.14.

As listed in Table 3.14, by increasing the percentage of EGR the peak combustion temperatures are decreased and retarded.

Table 3.14 : Peak cylinder temperatures and related crank angles with different EGR rates.

EGR [%]	Peak temperature [K]	@ CAD
0	2671.5	380
5	2531.3	387
10	2327.3	400
13	2134.8	416
15	2009.2	431
18	1851.7	460
20	1752.7	500

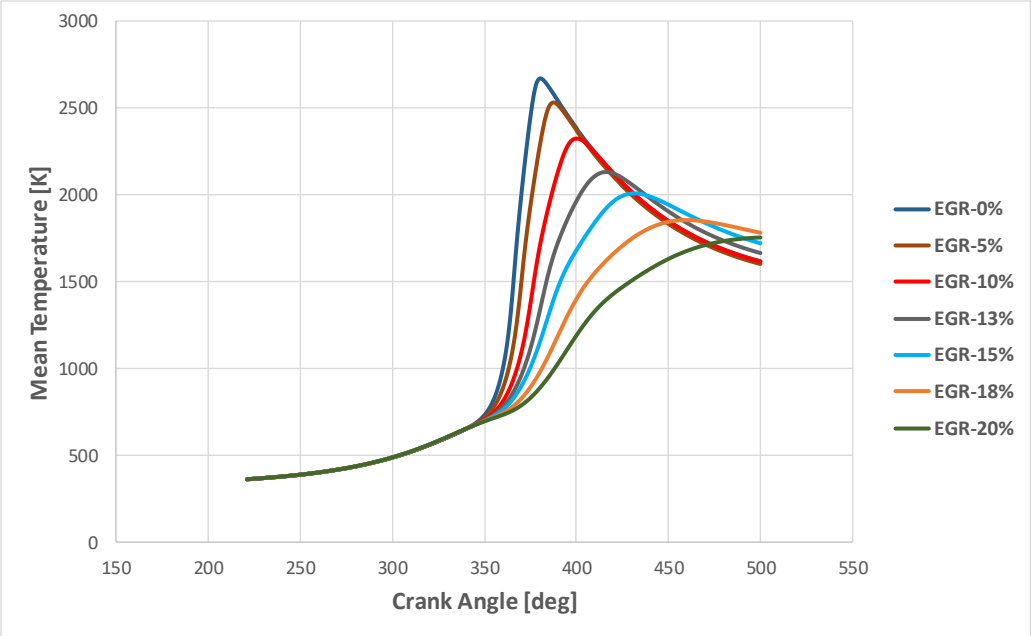


Figure 3.24 : The effect of EGR on mean temperature.

3.4.1.3 Rate of heat release and accumulated heat release

Figure 3.25 shows the heat release rate curves with different percentages of EGR. The heat release characteristics could directly exhibit the whole combustion process and evaluate combustion rationality. Observing Figure 3.25, it is found that EGR greatly affects the heat release rate. The maximum heat release rate is decreased and the corresponding crank angle position is postponed with an increase in EGR rate. By increasing EGR from 0% to 18%, maximum rate of heat release is decreased by 78%. When EGR is applied, the in-cylinder temperature and pressure reduce due to the dilution effect of EGR along with higher specific heat capacity of mixture as a consequence of added inert gas, lead to a longer ignition delay and retarded SOC, which inhibiting the heat release. In another words, by introducing EGR the flame propagation speed is decreased and hence the combustion duration is increased and moves towards the expansion stroke.

Figure 3.26 illustrates the variation of accumulated heat release with various levels of EGR. In this study, the crank angle of 10% accumulated heat release is used to evaluate the start of combustion and the interval between 10% accumulated heat release and 90% accumulated heat release is defined as the combustion duration. Calculated position of SOC and combustion durations with different EGR rates are listed in Table 3.15. It is found that, by increasing the EGR rate the mean cylinder

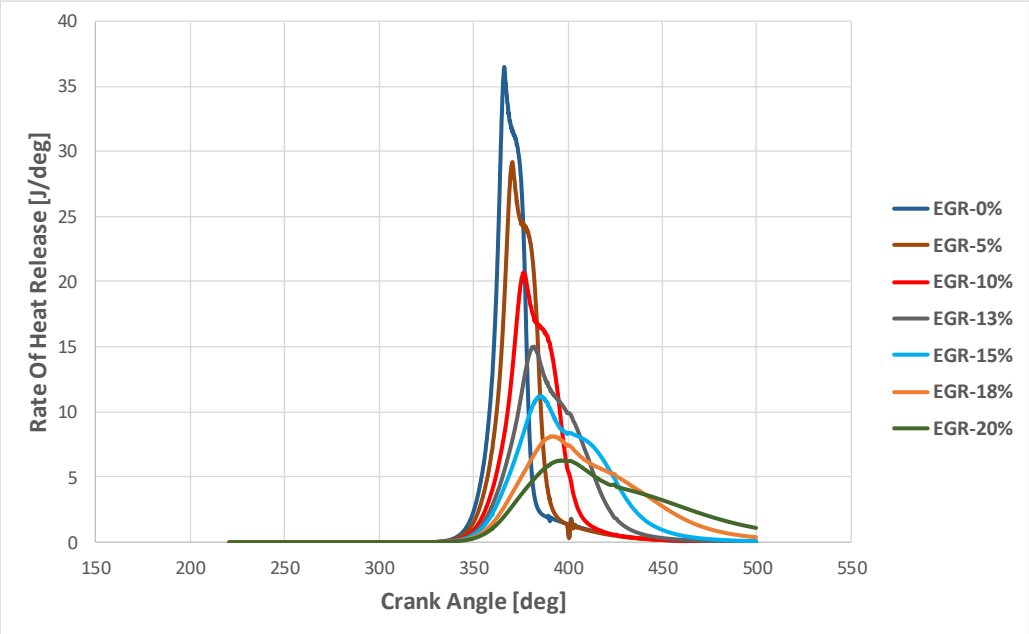


Figure 3.25 : The effect of EGR on rate of heat release.

temperature is decreased and hence worsen the mixture burning and increase the combustion duration. Thus, by applying EGR, the combustion is tended to start later in a cycle and the ignition duration or the ignition delay period, is prolonged due to a reduction in oxygen content available for combustion and decreased mean in-cylinder temperature. Consequently, the combustion is delayed and combustion duration is extended. As it can be seen in Figure 3.26 and Table 3.15, lagged SOC and longer combustion duration are obtained by increasing EGR rate.

Table 3.15 : Start of combustion position and combustion duration with different EGR rates.

EGR [%]	SOC @ [CAD]	Combustion duration [deg]
0	359	21
5	362	24
10	366	32
13	369	45
15	371	58
18	374	78
20	377	92

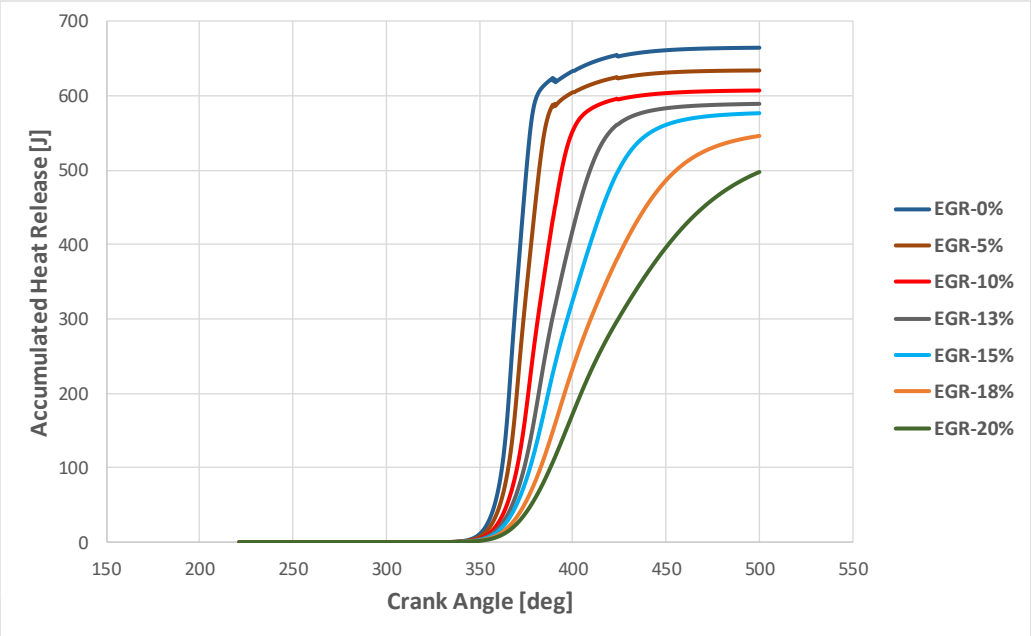


Figure 3.26 : The effect of EGR on accumulated heat release.

It is found that, when EGR increases from 0% to 18%, combustion duration is extended by 57 [CAD] and the start of combustion is retarded by about 15 [CAD]. As described, applying EGR reduces the oxygen concentration as shown in Figure 3.27. Since the equivalence ratio of combustion is set to 1, lower amount of intake oxygen leads to lower amount of inducted fuel. This reduction of fuel amount as a consequence of introducing EGR, is contributed to lower cumulative heat release, as demonstrated in Figure 3.26.

3.4.1.4 Exhaust emissions

Observing Figures 3.28 and 3.30, as EGR is introduced to the combustion, NO_x emissions reduce significantly with minimal rise in soot. Further increase in EGR lead to additional NO_x reduction but cause a significant rise in soot. It is well known that main factors affecting NO_x formation include the local temperature and the local oxygen concentration so, combination of low oxygen concentration and low in-cylinder temperature result in low levels of NO_x emission. Therefore, the efficacy of EGR can be attributed primarily to the dilution of the intake charge and the increased charge specific heat capacity.

As shown in Figure 3.27, increasing EGR reduces the intake oxygen concentration by replacing part of the intake fresh mixture with inert combustion products. The higher

heat capacity of inert gases, together with the reduced oxygen concentration results in lowered local flame temperatures during the combustion process,as shown in Figure 3.24. Consequently, combination of lower oxygen concentration in the intake air and reduced flame temperature decreases the rate of NO_x formation.

Since the peak combustion temperature and oxygen concentration are widely believed as the most significant parameters affecting NO_x production, EGR has proven to be very effective in reducing the exhaust NO_x emissions. According to the Figure 3.28, nitric oxide emissions in general decrease as EGR is increased and the simulated SI engine is able to realize a significant reduction in NO_x emissions by about 50% with 10% EGR and approximately 89% with 15% EGR, compared to operating with 0% EGR. It should be mentioned, indicated power is used to calculate the exhaust emissions.

Figure 3.29 displays the spatial distributions of NO_x and temperatures inside the cylinder at 20 [CAD] ATDC for different EGR levels. The CFD results confirmed that, as EGR increases, the oxygen concentration as well as the in-cylinder temperature decreases and hence the formation of NO_x emissions reduces.

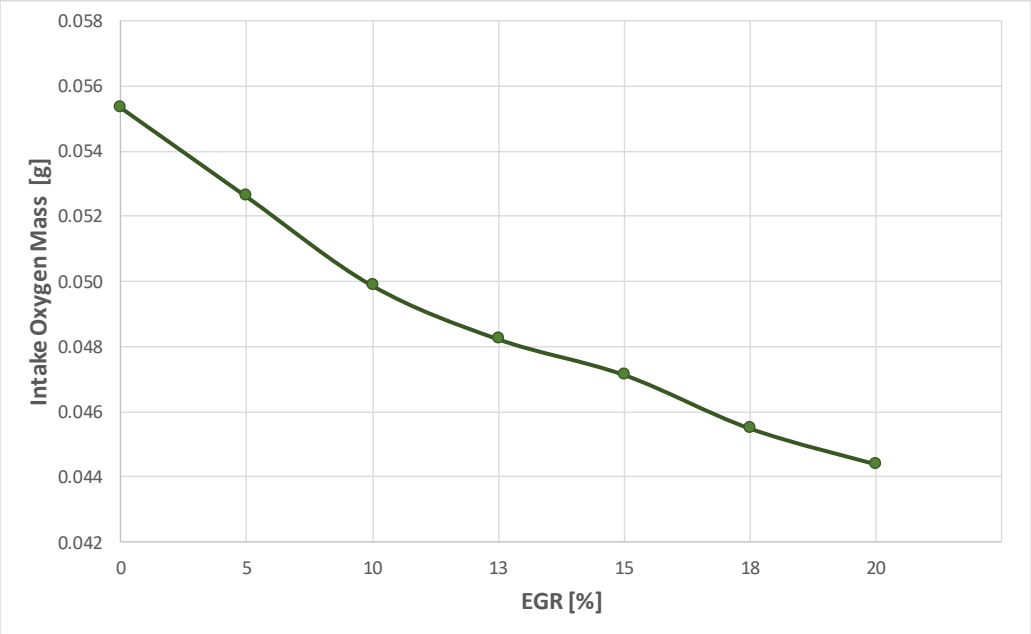


Figure 3.27 : The effect of EGR on intake oxygen.

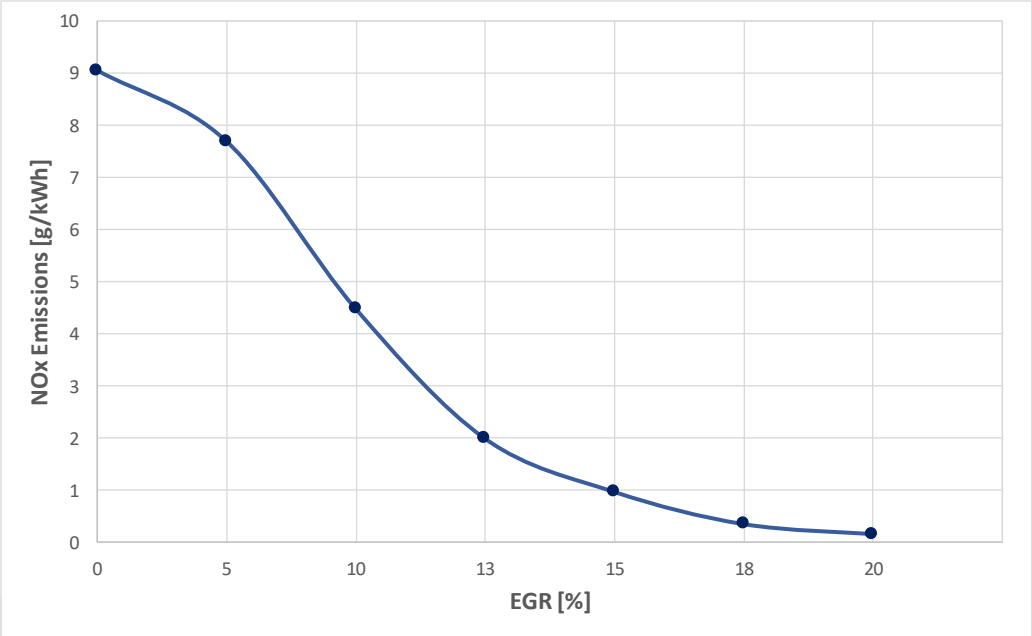


Figure 3.28 : The effect of EGR on NO_x emissions.

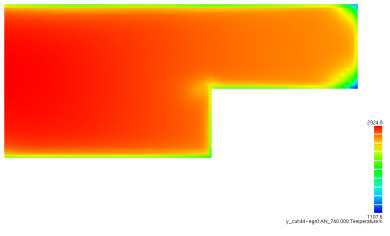
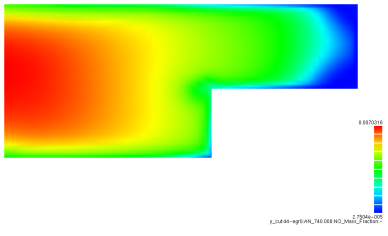
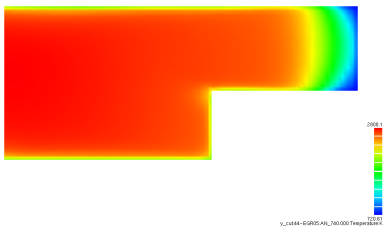
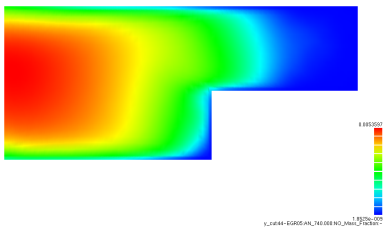
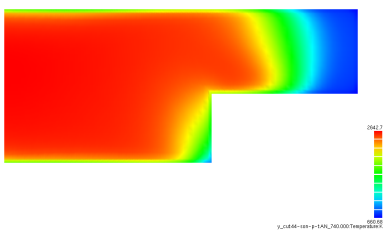
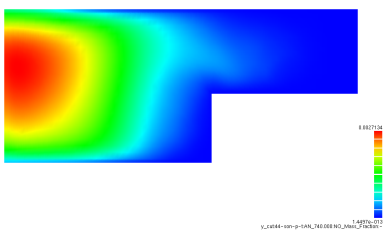
20 [CAD] ATDC		
EGR [%]	Temperature [k]	NO_x mass fraction [-]
0		
5		
10		

Figure 3.29: In-cylinder distributions of temperature and NO_x emissions with different EGR @ 20 [CAD] ATDC.

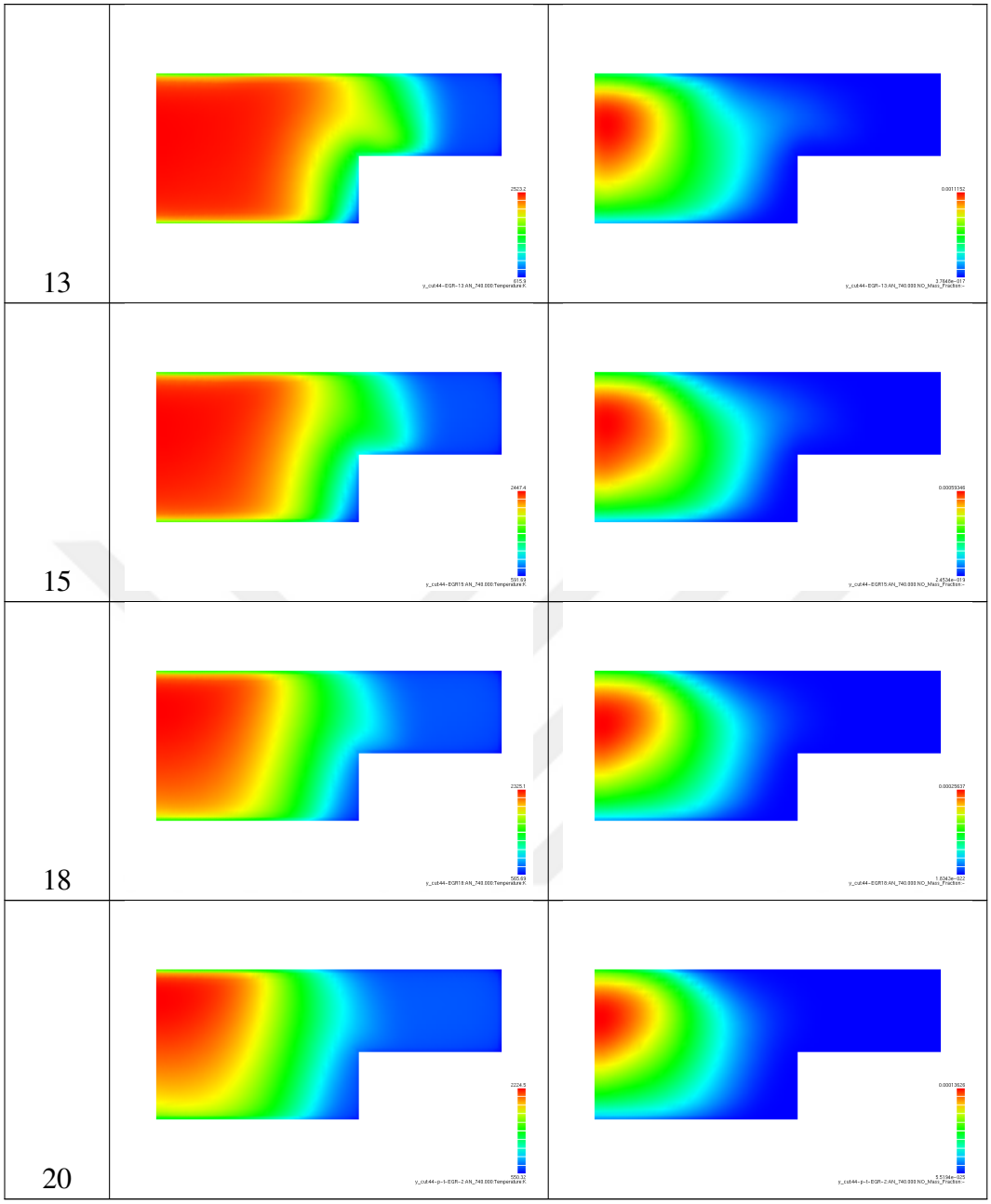


Figure 3.29 : **(Cont.)** In-cylinder distributions of temperature and NO_x emissions with different EGR @ 20 [CAD] ATDC.

Soot is primarily unburned carbon and is formed for the reason of insufficient combustion air, poor mixing and low flame temperature. Actually in comparison with CI engines, SI engines produce very low and negligible levels of the soot emissions, but for a better understanding of the effect of EGR on exhaust emission characteristics, a comparison of the engine-out soot emissions with different EGR rates are shown in Figure 3.30. By considering SI engine simulations, very low amounts of soot

emissions is produced, that is because of the premixed combustion process, since the gasoline injected via manifold, it had enough time to mix properly with air and prepare a homogenous mixture.

Although NO_x formation is reduced by utilizing high levels of EGR, there is generally a trade off with the formation of soot and it becomes apparent as combustion is becoming inherently less efficient. The soot emissions tend to increase as the EGR progressively increased. Since soot emissions are a culmination of the difference between the soot formation and soot oxidation process, the balance of these two yields the total engine-out concentration of soot. The lowered combustion temperature and lower oxygen concentration as a result of applying higher EGR rates, are thought to reduce the soot oxidation rates, thereby increasing the soot emissions.

As can be seen in Figure 3.31, as more exhaust gases get recirculated, CO emission

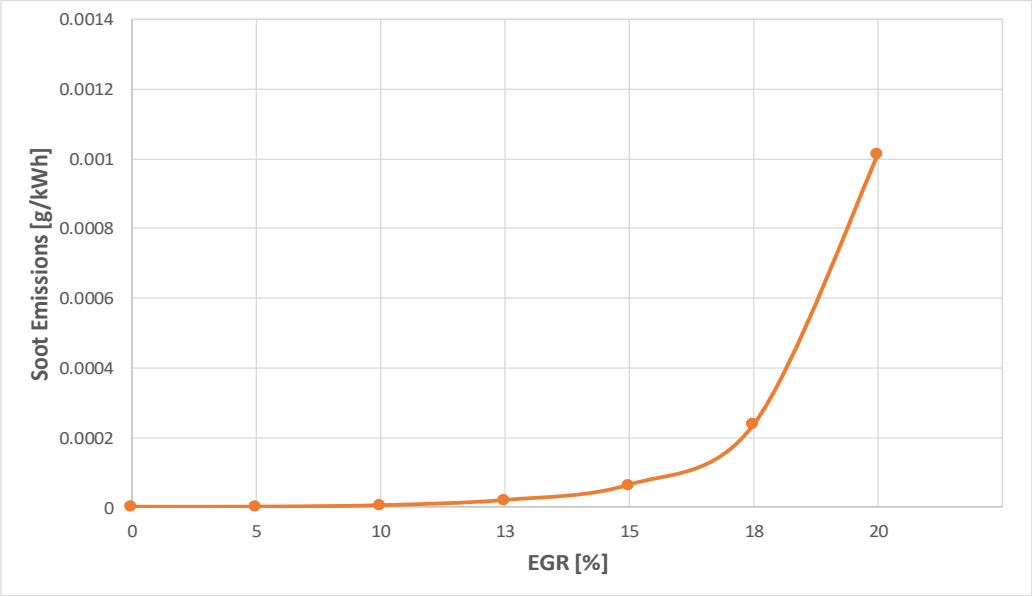


Figure 3.30 : The effect of EGR on soot emissions.

shows a slight decrease up to 13% of EGR when it hits a turnaround and starts an upward trend that in 15% turns to a substantial surge due to incomplete and inefficient combustion. Carbon monoxide is formed from fuel oxidation during combustion and is attributed to insufficient time and oxygen available for complete oxidation of CO to CO_2, and Hence by increasing exhaust gases in the combustion chamber, there would not be adequate amount of oxygen to oxidize CO and form CO_2 compounds.

Hydrocarbons or organic emissions, are the result of incomplete combustion of the hydrocarbon fuel. Although the amount of hydrocarbon emission is a useful measure

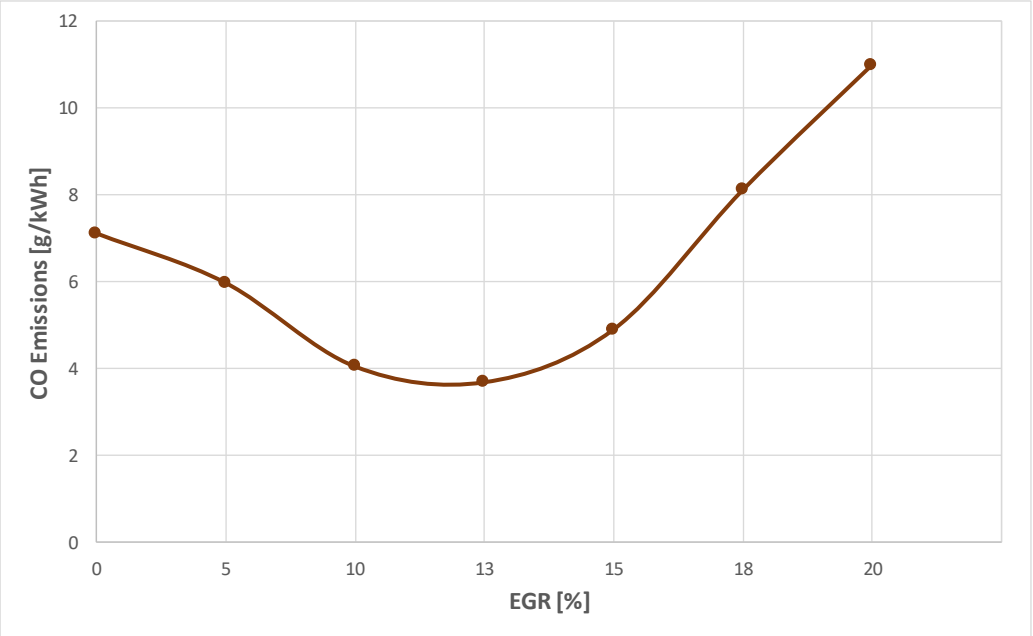


Figure 3.31 : The effect of EGR on CO emissions.

of combustion efficiency, it is not necessarily an important index of pollutant emissions (Heywood, 1988). The unburned hydrocarbon emissions exit the cylinder by being entrained in the bulk-gas flow during blowdown and at the end of the exhaust stroke as the piston pushes gas scraped off the wall out of the exhaust valve. Substantial oxidation of hydrocarbons which escape the primary combustion process by any of the above processes can occur during the expansion and exhaust. The amount of oxidation depends on the temperature and oxygen concentration time histories of these hydrocarbons as they mix with the bulk gases. As shown in Figure 3.32, Due to decrease of burning rate and oxygen concentration, HC emissions increase with increasing EGR.

3.4.1.5 Engine specific output

Figure 3.33 demonstrates that an increase in the EGR rates leads to a significant decrease in IMEP and indicated power. By increasing recycled exhaust gases, the inert components with higher specific heat capacity replaces some of the intake air, and hence, not only increases mixture specific heat capacity ,but also decreases in-cylinder trapped oxygen. This theorem also affects the flame speed and combustion phasing and slow down the combustion rate causing a low in-cylinder temperature and pressure at high levels of EGR. Since the in-cylinder pressure is decreased by increasing the

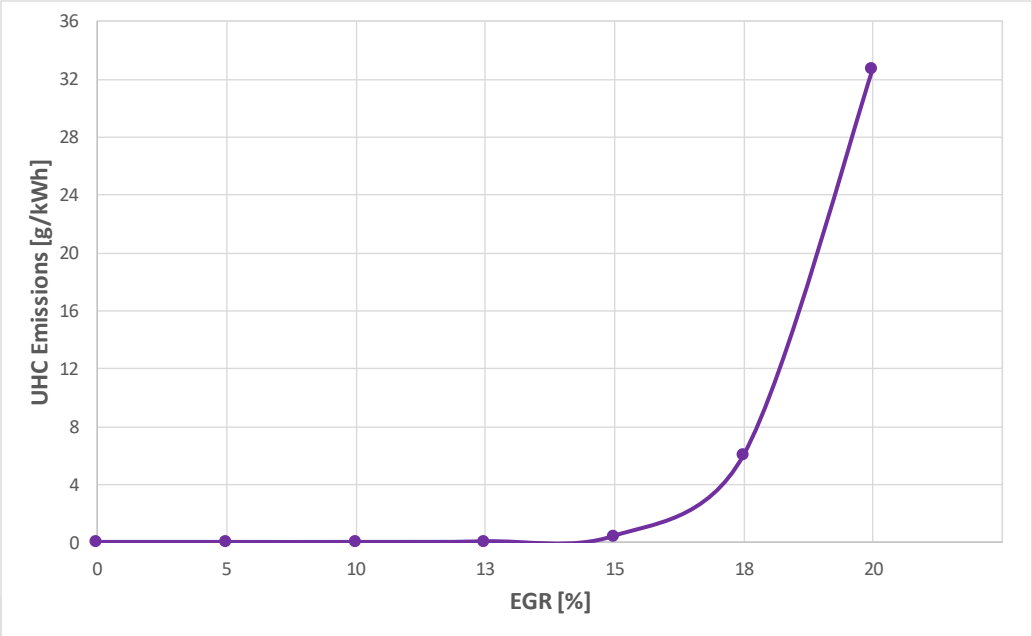


Figure 3.32 : The effect of EGR on HC emissions.

percentage of EGR (Figure 3.23), indicated mean effective pressure is also decreased (Figure 3.33). According to Eq.(3.6), decreasing in the indicated mean effective pressure results in a reduction of indicated power. The results reveal that an increase of EGR from 0% to 18%, cause a dramatic reduction of IMEP and indicated power by 44%.

ISFC is found to be largely a function of combustion phasing and an increase in EGR rate results in higher fuel consumption. This is mainly result of decreased combustion efficiency due to later phasing of combustion and longer combustion duration. As described before, introducing EGR leads to a reduction in intake oxygen concentration, however, AVL FIRE® first calculates the composition of the oxidizer and after this, the correct amount of fuel is determined for the present oxygen concentration. Therefore, to the keep the equivalence ratio equal to 1, reduced oxygen concentration required lower amount of supplied fuel. But the reduction in indicated power is drastic and non-linear, by considering Eq.(3.11), there is a bigger decline in denominator than the numerator which results in higher indicated specific fuel consumption. The ISFC increases by about 47% as the EGR increases from 0% to 18%.

By analysing the simulation results via ESE Diesel analyser tool, valuable information about engine outputs with different EGR rates are achieved. Analysing results are listed in Table 3.16.

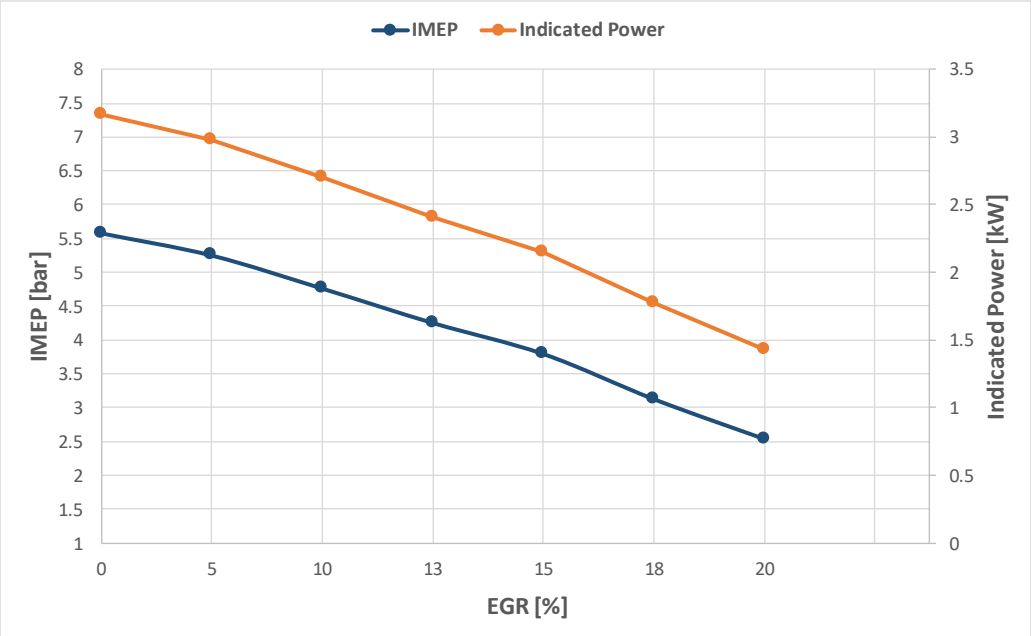


Figure 3.33 : The effect of EGR on IMEP and indicated power.

Table 3.16 : Engine specific output with different EGR rates.

EGR [%]	0	5	10	13	15	18	20
Break mean effective pressure BMEP [bar]	3.82	3.49	3	2.49	2.03	1.35	0.76
Combustion Noise - A + CAV Filter [dB]	81.51	81.06	80.98	81.24	81.56	81.87	81.62
Combustion Noise - A Filter [dB]	192.73	190.96	188.65	186.98	185.92	184.83	184.18
Combustion Noise - CAV Filter [dB]	81.58	80.7	80.33	80.51	80.81	81.1	80.84
Combustion Noise [dB]	210.59	209.26	207.31	205.65	204.46	203.14	202.38
Excess air ratio [-]	1	1	1	1	1	1	1
Friction mean effective pressure FMEP [bar]	1.76	1.76	1.76	1.76	1.76	1.76	1.76
Indicated mean effective pressure IMEP [bar]	5.58	5.25	4.76	4.25	3.79	3.12	2.53
Indicated power [kW]	3.17	2.98	2.7	2.41	2.15	1.77	1.43
Indicated specific power [kW/l]	6.98	6.57	5.95	5.32	4.74	3.89	3.16
Indicated specific torque [Nm/l]	44.41	41.8	37.87	33.84	30.16	24.8	20.1
Indicated torque [Nm]	20.16	18.98	17.19	15.36	13.69	11.26	9.13
Mean mass [kg]	2.51E-04	2.50E-04	2.49E-04	2.49E-04	2.48E-04	2.48E-04	2.47E-04
Mechanical efficiency [-]	0.68	0.66	0.63	0.59	0.53	0.43	0.3
Total mass at start of high pressure cycle [kg]	2.55E-04	2.54E-04	2.53E-04	2.53E-04	2.53E-04	2.52E-04	2.52E-04
Volume displacement [m$\hat{3}$]	4.54E-04	4.54E-04	4.54E-04	4.54E-04	4.54E-04	4.54E-04	4.54E-04

In summary, by adopting EGR, the peak values of in-cylinder pressure, mean combustion temperature and rate of heat release are decreased. Meanwhile, the crank angle positions corresponding to the maximum heat release rate, peak in-cylinder

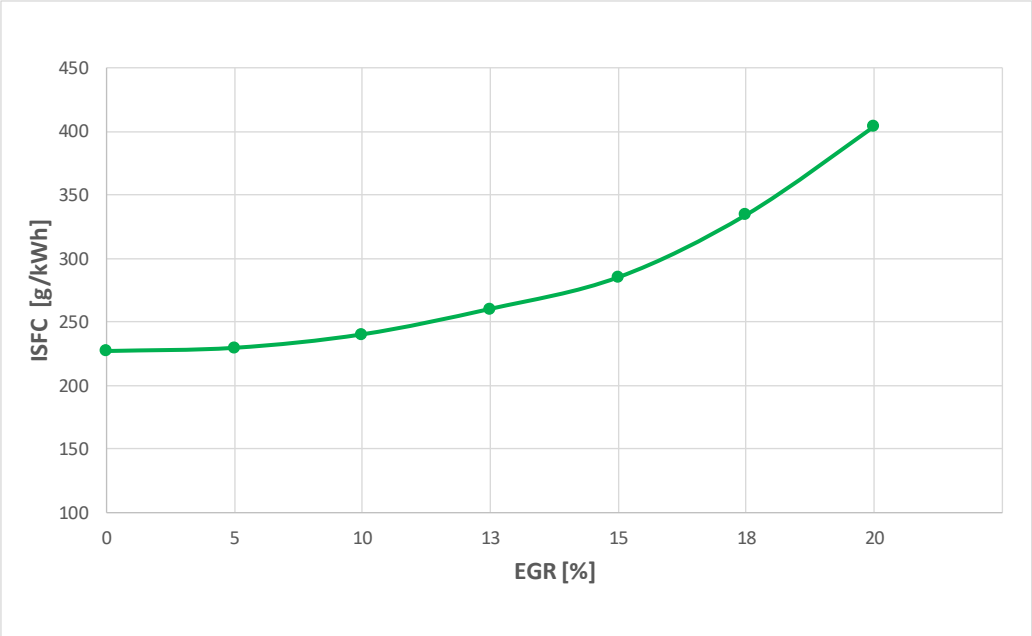


Figure 3.34 : The effect of EGR on ISFC.

pressure and peak combustion temperature postponed respectively. As higher levels of EGR are applied, indicated mean effective pressure reduces and indicated fuel consumption on the other hand increases gently. Moreover, with an increase in EGR rate, NO_x emissions decrease sharply, however for EGR rates of higher than 15% soot and CO emissions increase intensely. The results reveal that the combustion with a low level of EGR (10%) leads to a drastic reduction in NO_x emissions and a slight decrease in CO emission in parallel with a very low and negligible increase in ISFC and soot emissions. From the viewpoints of emission and performance, 10% of EGR seems to be the most desirable amount. SI engine with EGR exhibited an obvious postponed SOC and extended combustion duration. It can be attributed to that, when EGR is adopted, the cooled recycled exhaust gas increases the specific heat capacity of the mixture and decreases the oxygen content of combustion.

3.4.2 Effect of equivalence ratio

In this section the effects of equivalence ratio variations on SI engine performance and exhaust emissions are presented. Equivalence ratio (ϕ) is changed between 0.8 and 12.5 to cover the lean and rich regions. At part-load operating conditions, it is advantageous to dilute the air-fuel mixture, either with EGR or excess air. This dilution improves the fuel conversion efficiency, whereby, the expansion stroke work for a given

expansion ratio is increased as a result of the change in thermodynamic properties of the burned gases and the heat losses to the walls are reduced because the burned gas temperatures are lower.

3.4.2.1 In-cylinder pressure

Figure 3.35 shows the in-cylinder pressure with different equivalence ratios. As it can be seen, slightly rich mixture ($\phi \approx 1.1$) produces higher peak pressure and as the equivalence ratio moves leaner or richer, peak in-cylinder pressure decreases. The reason is that, by increasing the equivalence ratio the amount of inducted fuel is increased and more heat is produced. Further increase of equivalence ratio leads to the reduction of peak in-cylinder pressure due to the increasing time required to finish the excess fuel combustion besides the insufficient available air cause an incomplete combustion. On the other hand, as the mixture becomes leaner, the amount of combustible mixture and the combustion stability decrease and minimum pick pressure occurs at equivalence ratio of 0.8 due to the poor combustion quality and volumetric lower heating value of the intake mixture. The peak pressure values and related crank angle positions of different equivalence ratios are summarized in Table 3.17.

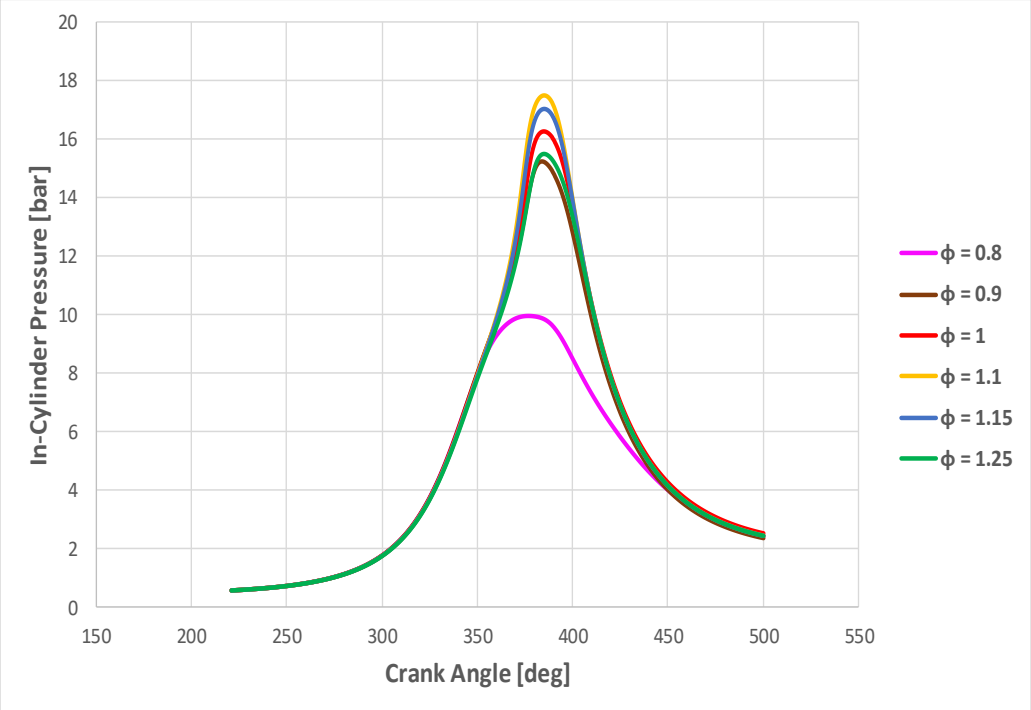


Figure 3.35 : The effect of equivalence ratio on in-cylinder pressure.

Table 3.17 : Peak cylinder pressures and related crank angles with different equivalence ratios.

ϕ [-]	Peak pressure [bar]	@ CAD
0.8	9.96	376
0.9	15.23	383
1	16.31	384
1.1	17.5	385
1.15	17.03	385
1.25	15.49	385

3.4.2.2 In-cylinder mean temperature

As the equivalence ratio is decreased below 1, the burned gas temperatures after combustion decrease which results in a reduction of the burned gas specific heats. This is because for a given volume expansion ratio, the burned gas expand through a larger temperature ratio prior to exhaust, therefore, the expansion stroke work per unit mass of fuel is increased. Additionally, as the equivalence ratio increases above 1, there is insufficient air for complete oxidation of the fuel and neutralizing the effect of decreasing burned gas temperatures which reduce the specific heat of mixture, so as a consequence, the mean combustion temperature is reduced.

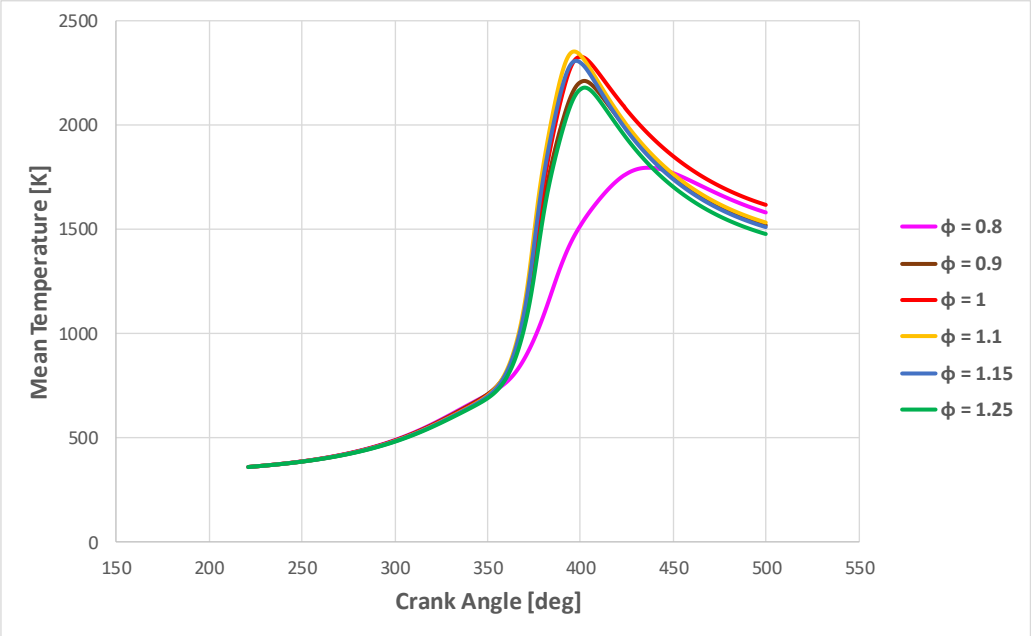


Figure 3.36 : The effect of equivalence ratio on mean temperature.

Figure 3.36 shows the effect of various equivalence ratios on mean combustion temperature. By considering mentioned reasons, minimum in-cylinder temperature is obtained with an equivalence ratio of 0.8 and the maximum temperatures occur at the start of expansion stroke of a slightly rich combustion and during the end of expansion stroke of a stoichiometric combustion. The peak value of mean in-cylinder temperatures and corresponding crank angles are listed in Table 3.18.

Table 3.18 : Peak cylinder temperatures and related crank angles with different equivalence ratios.

ϕ [-]	Peak temperature [K]	@ CAD
0.8	1792.8	437
0.9	2210.2	402
1	2327.3	400
1.1	2350.8	397
1.15	2306.2	398
1.25	2181.9	402

3.4.2.3 Rate of heat release and accumulated heat release

The effects of equivalence ratio variation on rate of heat release and accumulated heat release are shown in Figures 3.37 and 3.38, respectively. In case of lean mixture, since lower amount of fuel is supplied, the products of lean combustion have lower temperatures and less dissociation of the triatomic molecules CO_2 and H_2O. Thus the fraction of chemical energy of the fuel which is released as sensible energy near TDC is greater. Hence, a greater fraction of the fuel's energy is transferred as work to the piston during expansion and the fraction of fuel's available energy rejected to the exhaust system decreases. The maximum value of heat release rate is gained at a slightly rich combustion with an equivalence ratio of 1.1. This can be attributed to the dissociation at the high temperatures following combustion. As a result of dissociation, molecular oxygen is present in the burned gases of stoichiometric mixture, and hence some additional fuel can be added and partially burned. This increases the temperature and the number of moles of the burned gases in the cylinder.

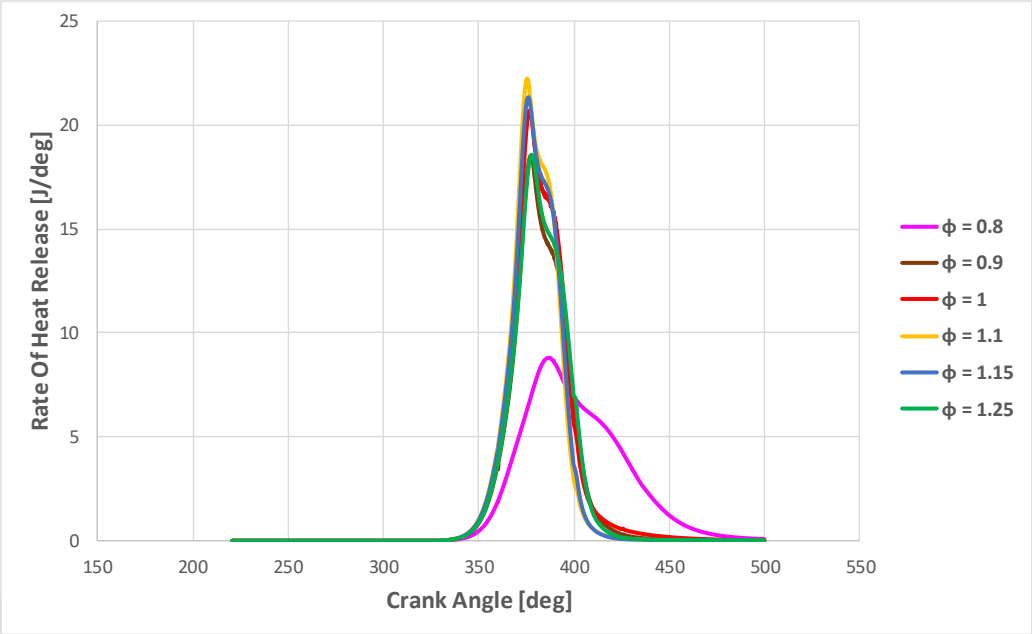


Figure 3.37 : The effect of equivalence ratio on rate of heat release.

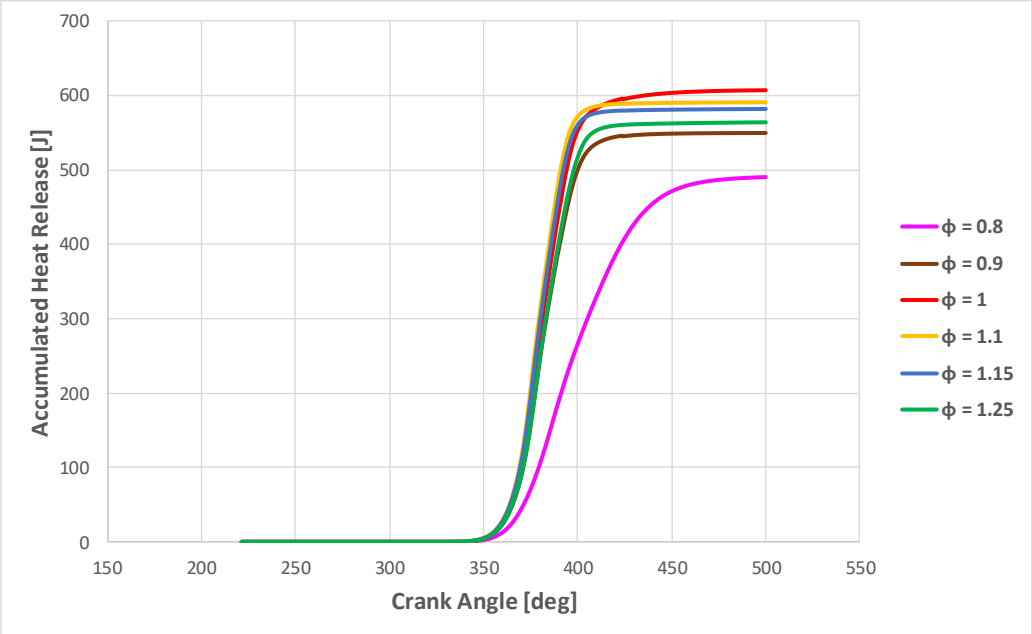


Figure 3.38 : The effect of equivalence ratio on accumulated heat release.

Calculated position of SOC and combustion durations with different equivalence ratios are listed in Table 3.19. It is found that, the combustion duration of a slightly rich mixtures, where the laminar flame speed is higher, are shorter than that of stoichiometric mixture by about 3°[CA]. Moreover, very lean mixture burns very slowly and has the longest combustion duration, since low amount of fuel is available

for combustion, the mean cylinder temperature and flame propagation speed are low in this case.

Table 3.19 : Start of combustion position and combustion duration with different equivalence ratios.

ϕ [-]	SOC [@CAD]	Combustion duration [deg]
0.8	369	65
0.9	366	33
1	366	32
1.1	365	29
1.15	365	29
1.25	366	32

3.4.2.4 Exhaust emissions

The SI engine has normally been operated with a mixture close to stoichiometric or slightly fuel rich, to ensure smooth and reliable operation. Figures 3.39, 3.41 and 3.42 show that leaner mixtures give low emissions until the combustion quality becomes poor, engine operation becomes erratic and eventually misfire occurs.

The equivalence ratio is an important parameter controlling SI engine emissions. The critical factors affecting emissions, that are governed by the equivalence ratio, are the oxygen concentration and the temperature of the burned gases. On the one hand, excess oxygen is available in the burned gases of lean combustion, and on the other hand, the maximum burned gas temperatures occur at a slightly rich combustion during the start of expansion stroke and during the end of expansion stroke and the exhaust process of a stoichiometric combustion. Figure 3.39 shows the effect of variations in equivalence ratio on NO_x emissions.

Figure 3.40 depicts the in-cylinder temperature distributions and NO_x emission concentration contours for different equivalence ratios at 20 [CAD] ATDC. As described before, the formation rate of NO_x depends on the gas temperature and oxygen concentration.

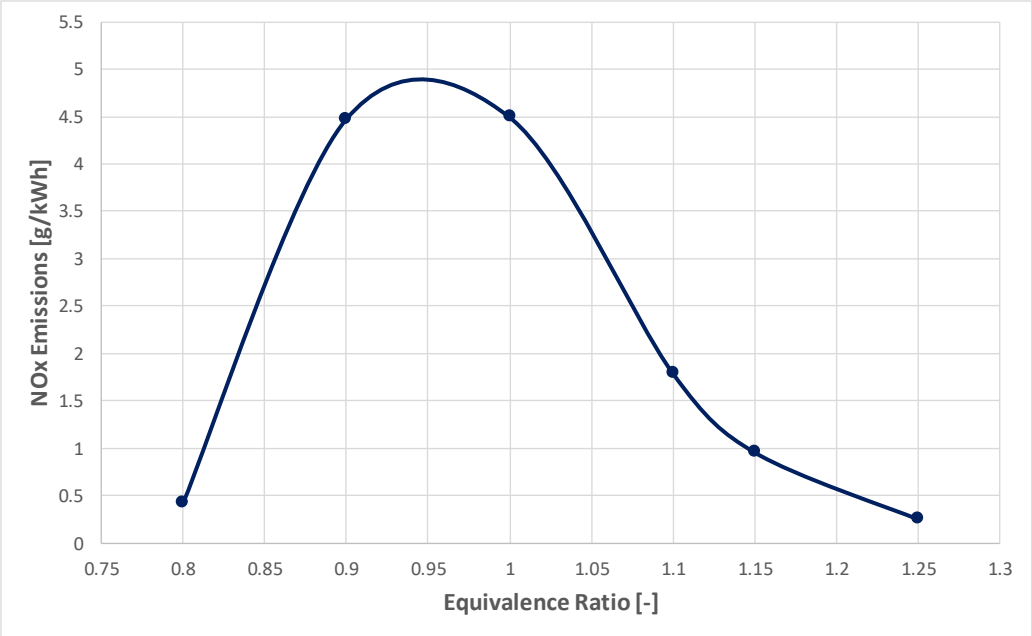


Figure 3.39 : The effect of equivalence ratio on NO_x emissions.

Observing Figures 3.40 and 3.39, however, combustion temperatures of rich mixtures are high, they have low oxygen concentrations, so produce low levels of NO_x . As the mixture is leaned out, increasing oxygen concentration initially offsets the falling gas temperatures and NO_x emissions peak at $\phi \approx 0.95$. Then, decreasing temperatures dominate and NO_x emissions decrease to low levels.

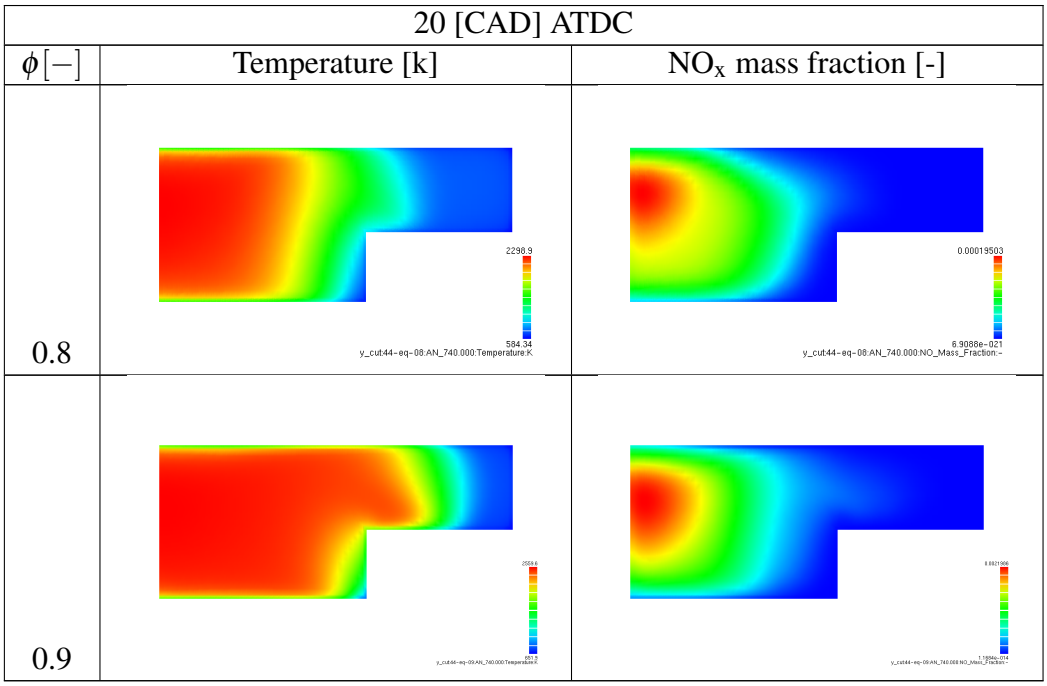


Figure 3.40: In-cylinder distributions of temperature and NO_x emissions with different equivalence ratios @ 20 [CAD] ATDC.

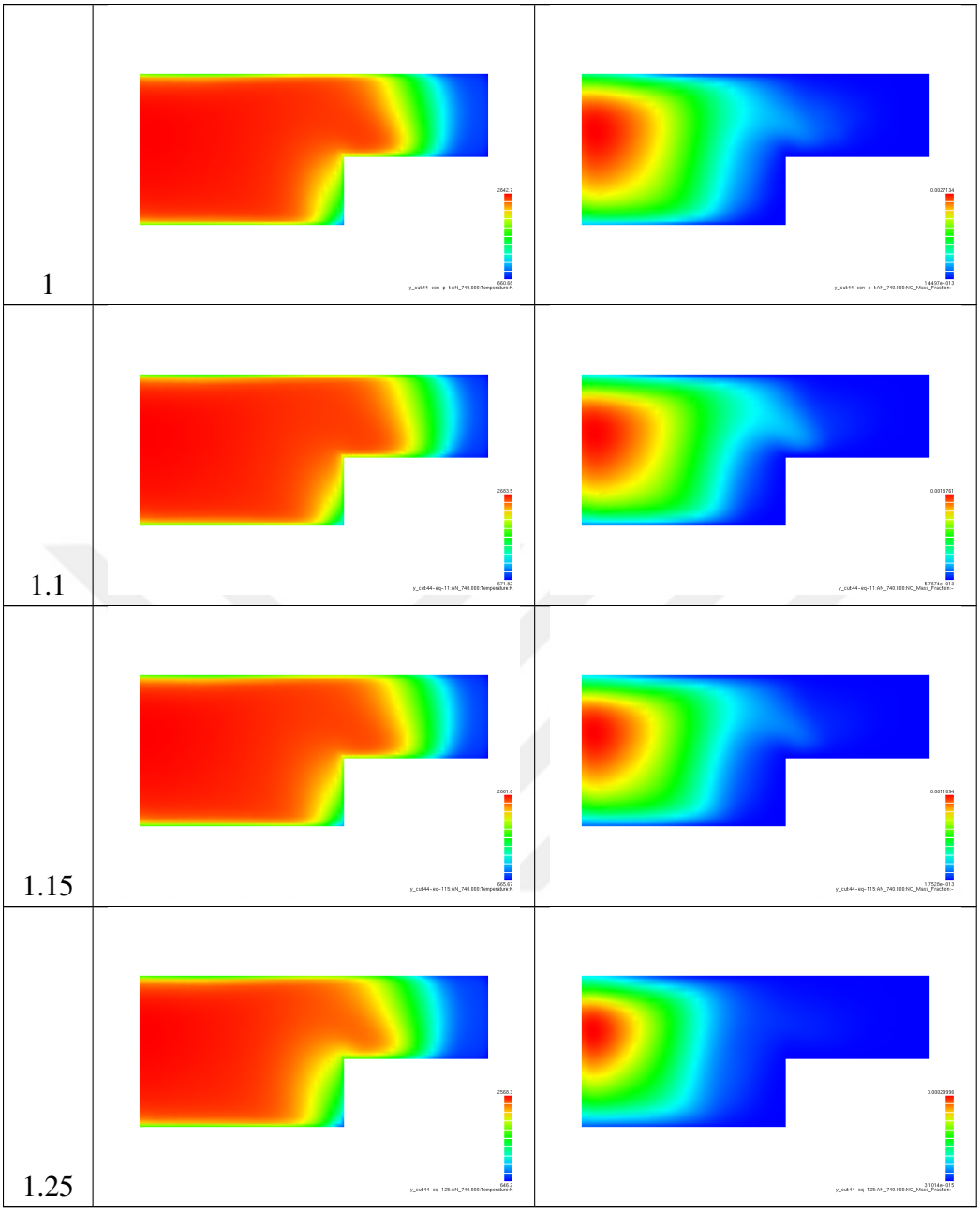


Figure 3.40 : **(Cont.)** In-cylinder distributions of temperature and NO_x emissions with different equivalence ratios @ 20 [CAD] ATDC.

In properly adjusted SI engines, soot emissions are not a significant problem, due to their low amounts. Soot is primarily unburned carbon and is formed for the reason of insufficient combustion air, poor mixing and low flame temperature. Figure 3.41 depicts that the soot emissions almost are stayed constant and in notably low levels by varying the equivalence ratio, until the mixture moves to very lean region with an equivalence ratio of 0.8, where combustion quality becomes poor, engine operation

becomes erratic and eventually misfire occurs, and hence, soot emissions increase drastically.

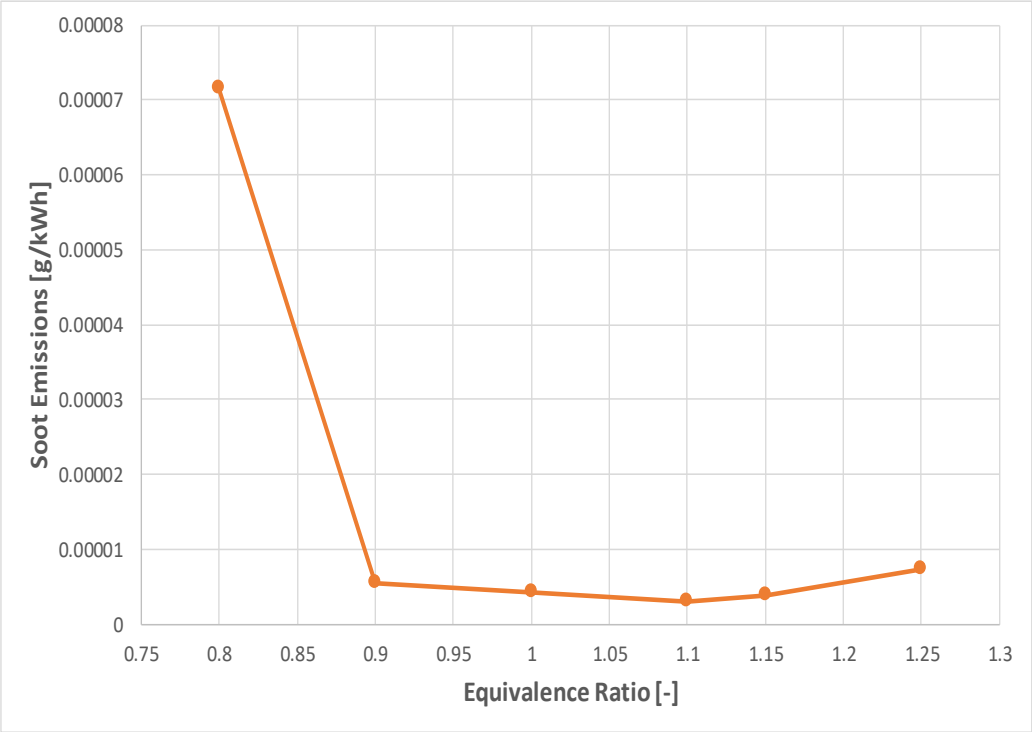


Figure 3.41 : The effect of equivalence ratio on soot emissions.

Carbon monoxide emission forms during the combustion process and is controlled primarily by the equivalence ratio. With rich air-fuel mixture, there is not sufficient oxygen to burn fully all the carbon in the fuel to form CO_2. Figure 3.42 demonstrates the CO levels in the exhaust of simulated SI engine for different equivalence ratios. As it can be seen in Figure 3.42, for rich mixtures, the amount of CO emissions is increased steadily by increasing the equivalence ratio, as the amount of excess fuel increases and there would not be adequate amount of oxygen to oxidize CO and form CO_2 compounds. For lean mixtures, CO emissions in the exhaust vary little with equivalence ratio and are in very low levels. Moreover, by moving the equivalence ratio from lean to rich there is a very small increase in the amount of CO emissions when the mixture is stoichiometric. Since SI engines often operate with a mixture close to stoichiometric at part load and fuel rich at full load, CO emissions are significant and must be controlled.

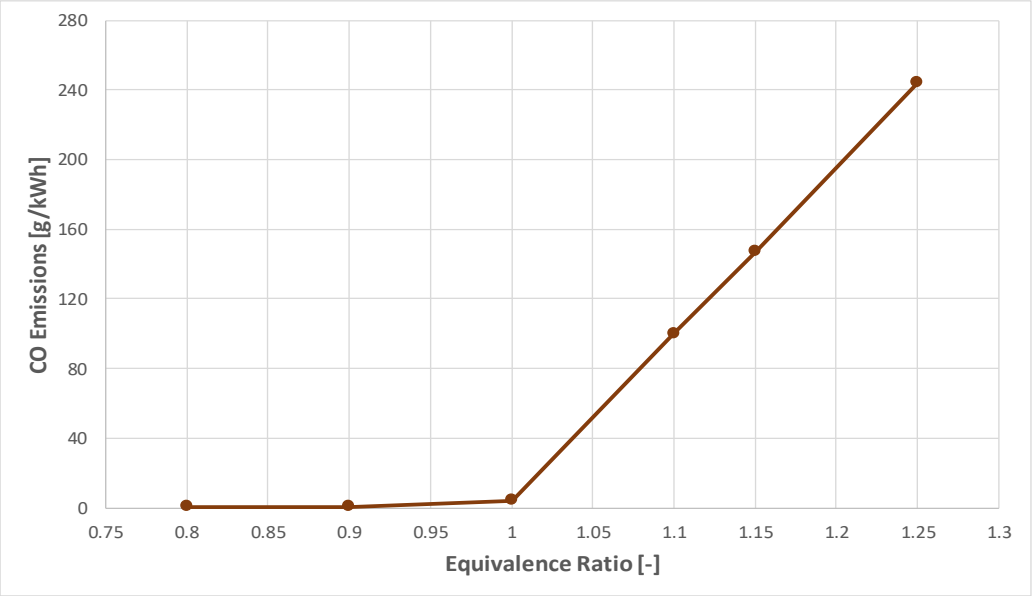


Figure 3.42 : The effect of equivalence ratio on CO emissions.

As the combustion quality deteriorates with very lean mixtures, HC emissions can rise rapidly due to incomplete combustion or misfire in a fraction of the engine's operating cycles. Figure 3.43 indicates that low amount of HC emissions are produced with various equivalence ratios except with very lean mixture, where the combustion temperature drops, the combustion quality becomes poor, engine operation becomes erratic and eventually misfire occurs, thus HC emission rises sharply.

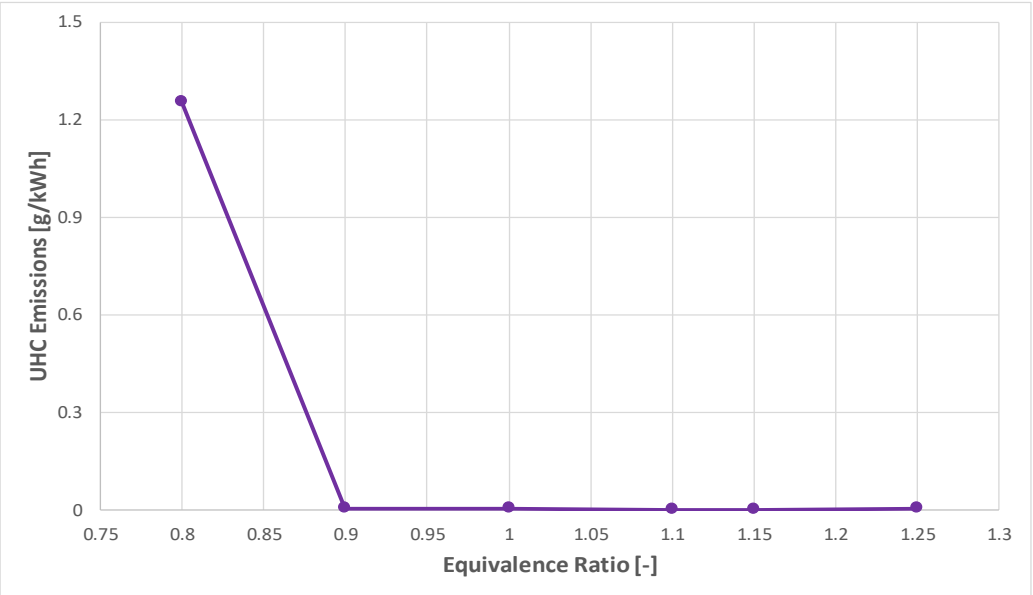


Figure 3.43 : The effect of equivalence ratio on HC emissions.

3.4.2.5 Engine specific output

The indicated mean effective pressure is increased by increasing the equivalence ratio up to 1.1. The maximum value of indicated mean effective pressure is obtained at a slightly rich combustion with an equivalence ratio of 1.1. This trend can be attributed to the dissociation at the high temperatures following combustion, molecular oxygen is present in the burned gases under stoichiometric conditions, so some additional fuel can be added and partially burned. This increases the temperature and the number of moles of the burned gases in the cylinder. These effects increase the pressure to give increased power and mean effective pressure.

Figure 3.44 illustrates that the indicated output power and IMEP increase with increasing equivalence ratio up to about $\phi \approx 1.1$, where they reach their peak value. This can be result of the fact that the ratio of the heat added by the working fluid to the heat rejected by working fluid increase with the increasing equivalence ratio. With further increase in equivalence ratio, the power output and IMEP start to decline as the equivalence ratio increases. It can be attributed to the insufficient available air and hence incomplete combustion and also the decrease in the ratio of the heat added by working fluid to the heat rejected by working fluid.

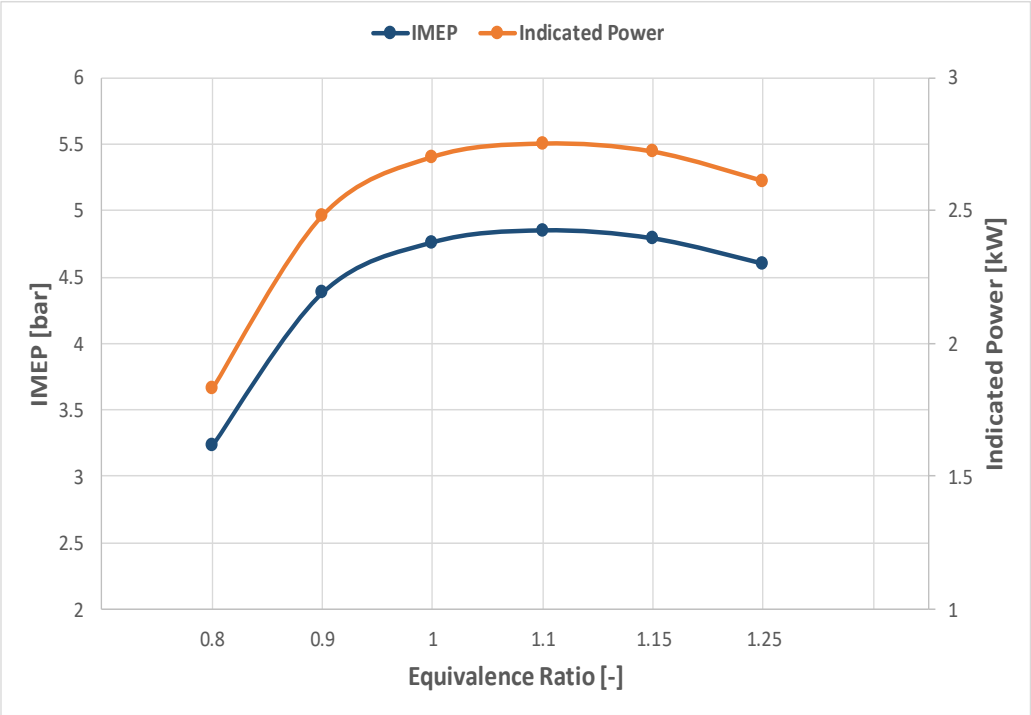


Figure 3.44 : The effect of equivalence ratio on IMEP and indicated power.

Observing Figure 3.45, it can be seen that there is a decrease in ISFC with increment of equivalence ratio from 0.8 to around 1. But further increase of equivalence ratio leads to the significant increasing of ISFC due to a reduction in combustion efficiency. From the results, the minimum ISFC is obtained when the equivalence ratio is around 1. The reason is that power output in this situation is high enough owing to complete combustion. On the other hand, ISFC would be higher in richer or leaner condition because of lower power output due to poor combustion quality and incomplete combustion. Thus the engine needs more heat consumption to maintain the same power output.

Engine fuel consumption under very lean regimes depends strongly on the engine combustion chamber design. The equivalence ratio for optimum fuel consumption at a given load depends on details of chamber design and mixture preparation quality. At all load points at a given speed, the ideal equivalence ratio is that which gives minimum specific fuel consumption at the required load (Heywood, 1988).

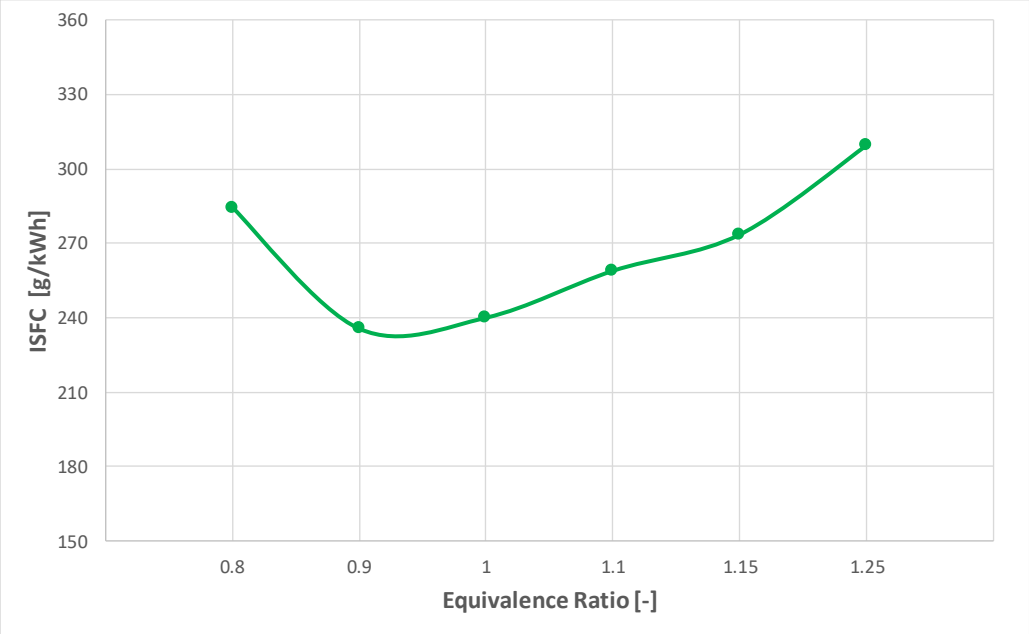


Figure 3.45 : The effect of equivalence ratio on ISFC.

Simulated engine outputs with different equivalence ratios, which are obtained by analyzing the simulation results via ESE Diesel analyser tool are summarized in Table 3.20.

Table 3.20 : Engine specific output with different equivalence ratios.

Equivalence ratio [-]	0.8	0.9	1	1.1	1.15	1.25
Break mean effective pressure BMEP [bar]	1.47	2.62	3	3.08	3.03	2.84
Combustion Noise - A + CAV Filter [dB]	80.53	80.21	80.98	80.64	80.6	80.59
Combustion Noise - A Filter [dB]	185.3	188.1	188.65	189.17	188.97	188.26
Combustion Noise - CAV Filter [dB]	79.79	79.57	80.33	80.05	79.99	79.93
Combustion Noise [dB]	203.9	206.82	207.31	207.81	207.62	206.97
Excess air ratio [-]	1.25	1.11	1	0.91	0.87	0.8
Friction mean effective pressure FMEP [bar]	1.76	1.76	1.76	1.76	1.76	1.76
Indicated mean effective pressure IMEP [bar]	3.23	4.38	4.76	4.85	4.79	4.6
Indicated power [kW]	1.83	2.48	2.7	2.75	2.72	2.61
Indicated specific power [kW/l]	4.04	5.47	5.95	6.06	5.99	5.76
Indicated specific torque [Nm/l]	25.69	34.84	37.87	38.56	38.11	36.64
Indicated torque [Nm]	11.66	15.82	17.19	17.5	17.3	16.63
Mean mass [kg]	2.47E-04	2.48E-04	2.49E-04	2.50E-04	2.51E-04	2.52E-04
Mechanical efficiency [-]	0.45	0.6	0.63	0.64	0.63	0.62
Total mass at start of high pressure cycle [kg]	2.51E-04	2.52E-04	2.53E-04	2.54E-04	2.55E-04	2.56E-04
Volume displacement [m$\hat{3}$]	4.54E-04	4.54E-04	4.54E-04	4.54E-04	4.54E-04	4.54E-04

3.4.3 Effect of spark timing

In SI engines, an electrical discharge produced between the spark plug electrodes by ignition system in order to starts the combustion process close to the end of compression stroke. The high temperature plasma kernel created by the spark develops into a self-sustaining and propagating flame front, a thin reaction sheet, where the exothermic combustion chemical reactions occur. Setting the correct ignition timing is very important, since it has significant influences on engine performance and exhaust emissions. In this section, the effects of various spark timings (90°[CA] BTDC, 55°[CA] BTDC, 49°[CA] BTDC 45°[CA] BTDC, 40°[CA] BTDC, 35°[CA] BTDC, 30°[CA] BTDC and 25°[CA] BTDC) on exhaust emissions and performance characteristics of SI engine are investigated.

3.4.3.1 Maximum brake torque

The optimum spark timing which gives maximum engine torque at fixed speed, mixture composition and flow rate is called Maximum Brake Torque (MBT) timing. This time also gives maximum brake power and minimum specific fuel consumption. So timing which is advanced or retarded from this optimum gives lower torque and higher

ISFC. Figure 3.46 illustrates the effect of spark timing variation on brake torque of simulated SI engine. Observing Figure 3.46, at given speed, as spark is advanced from an initially retarded setting, torque rises to maximum and then decreases. MBT timing also depends on engine speed and load. As speed increases, the spark must be advanced to maintain optimum timing because the duration of the combustion process in crank angle degrees increases. Moreover, as load and intake manifold pressure are decreased, the spark timing must be further advanced to maintain optimum engine performance. However, in this study, fixed engine speed of 1500 [rpm] and engine load (BMEP) equal to 3 [bar] and corresponding initial conditions, are considered for simulations. It is found that the spark timing of 311 [CAD] or 49°[CA] BTDC gives maximum brake torque and minimum ISFC, and hence can be selected as the optimum spark timing.

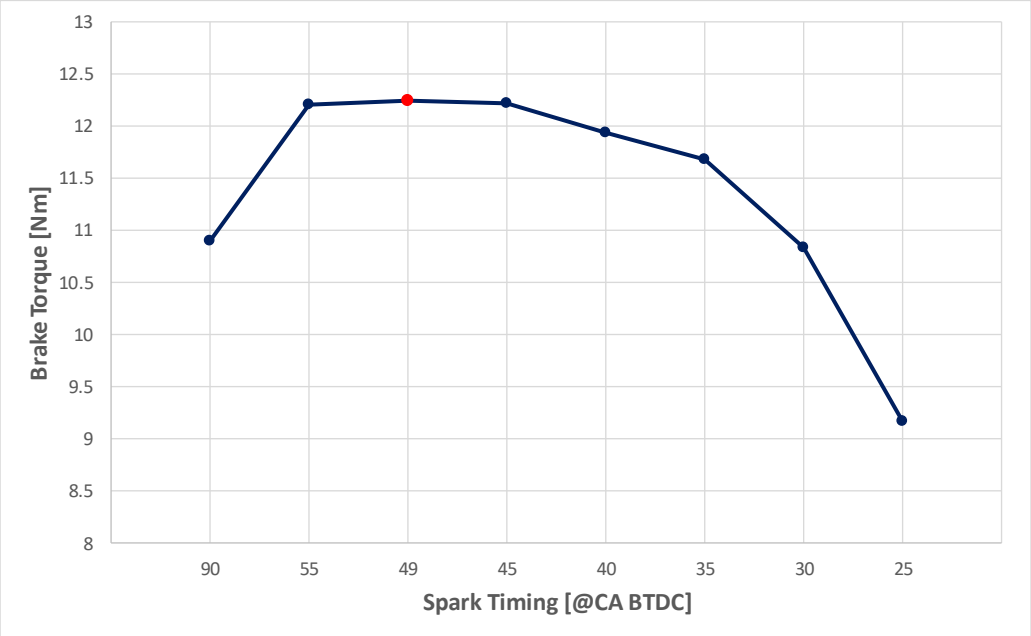


Figure 3.46 : The effect of spark timing on brake torque.

3.4.3.2 In-cylinder pressure

Figure 3.47 shows the effect of spark timing on in-cylinder pressure. If combustion starts too early in the cycle, the work which is transferred from piston to the gases in the cylinder at the end of compression stroke is too large. On the other hand, if combustion starts too late, the expansion stroke work transfer from the gas to the piston decreases. As shown in Figure 3.47, when the start of the combustion process is progressively delayed by retarding the start of spark (SOS), the expansion stroke work transfer from

the cylinder gases to the piston is decreased and the peak in-cylinder pressure occurs later in the expansion stroke and is reduced in magnitude.

By retarding the spark timing from 311 [CAD] (MBT) to 330 [CAD], the peak pressure value is decreased by about 40%. Peak pressure values and corresponding crank angles are listed in Table 3.21. However the highest peak pressure is obtained with start of spark (SOS) at 270 [CAD] or 90° [CA]BTDC, the cylinder pressure increases to undesirable levels before TDC and work is wasted in the compression stroke, therefore, this case is not preferable.

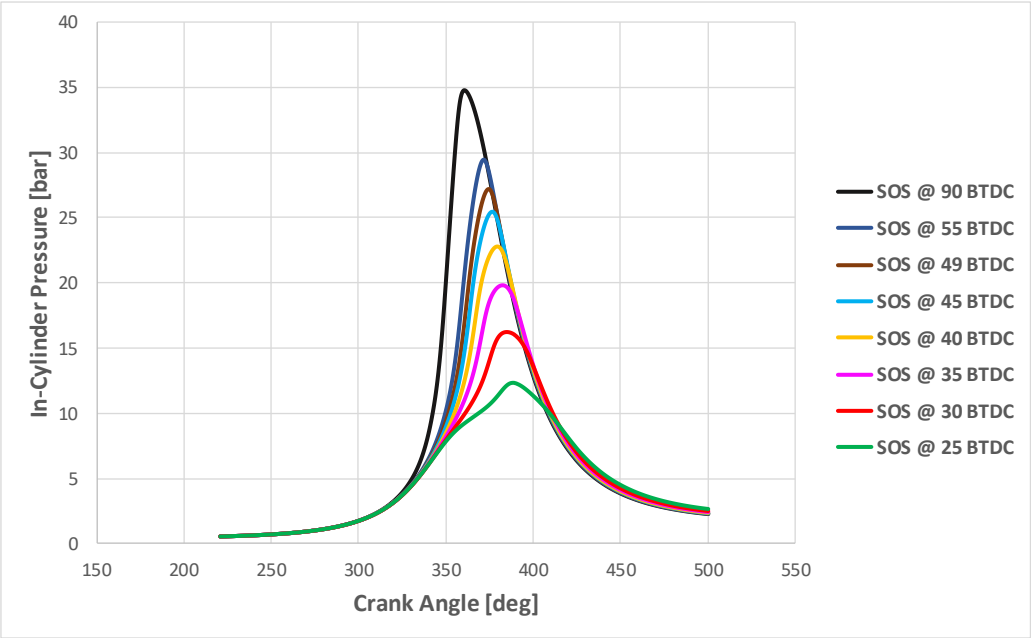


Figure 3.47 : The effect of spark timing on in-cylinder pressure.

Table 3.21 : Peak cylinder pressures and related crank angles with different spark timings.

Spark timing [CAD] BTDC	Peak pressure [bar]	@ CAD
90	34.77	360
55	29.41	371
49	27.21	374
45	25.45	376
40	22.84	379
35	19.79	382
30	16.31	384
25	12.30	388

3.4.3.3 In-cylinder mean temperature

Spark timing affects peak cylinder pressure and therefore peak combustion temperature. Figure 3.48 depicts the in-cylinder temperature with different spark timing. Observing Figure 3.48, with the increase of spark advance, larger amount of fuel is burned before TDC and combustion occurs earlier in the cycle, so in-cylinder temperature is increased at the start of expansion stroke, moreover, the burned gas expand through a larger temperature ratio prior to exhaust, and hence the combustion temperature is decreased at the end of expansion stroke. By retarding the timing on the other hand, the expansion stroke work transfer from the gas to the piston decreases, therefore the peak in-cylinder temperature is reduced. Since more fuel is burned after TDC, higher cylinder temperatures are obtained at the end of expansion stroke by retarding the spark timing.

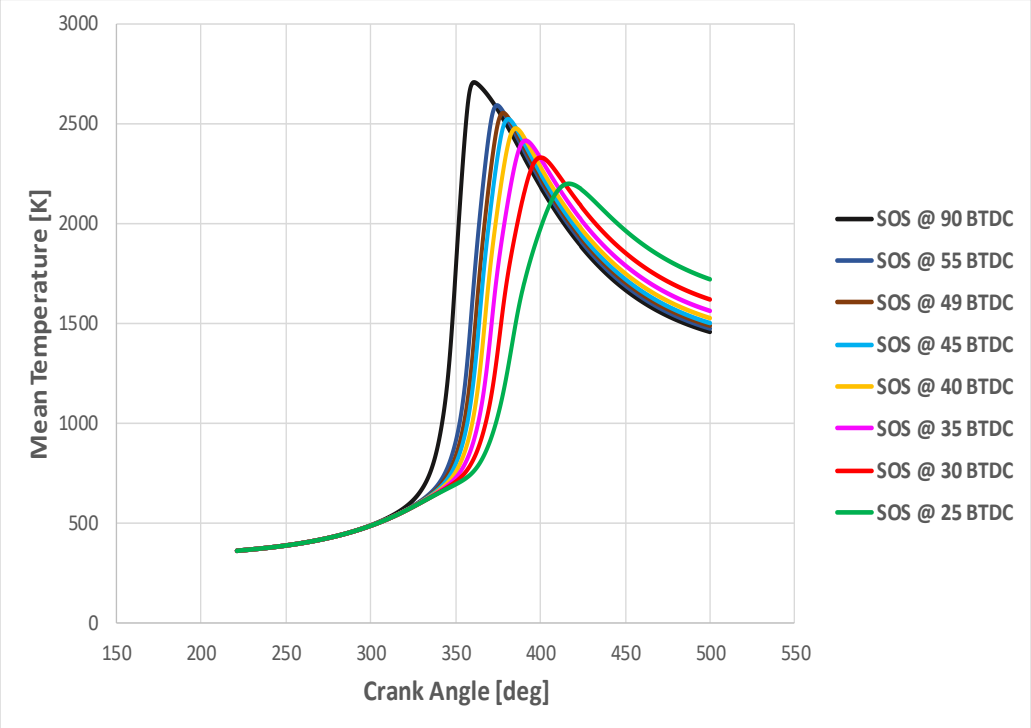


Figure 3.48 : The effect of spark timing on mean temperature.

In another words, advancing the spark timing increases the partial oxidation during the compression stroke and initiates the combustion before TDC which results in higher peak pressures, higher peak temperatures and lower exhaust temperatures. On the other hand, when the spark timing is retarded, there is less time between ignition timing and TDC to complete the chemical reaction, so large amount of fuel burns after TDC in the

expansion stroke which results incomplete combustion and an increase in the exhaust temperature. By retarding the spark timing from 49 [CAD] BTDC to 30 [CAD] BTDC, the peak cylinder temperature is decreased from 2553 [K] to 2327 [K] (9%), while the exhaust temperature is increased from 1488 [K] to 1617 [K] (9%).

3.4.3.4 Rate of heat release and accumulated heat release

Figures 3.49 and 3.50 respectively, show the heat release rate and accumulated heat release curves with different spark timing. Advancing the spark timing increases the partial oxidation during the compression stroke and initiates the combustion before TDC. As shown in Figure 3.49, at an earlier start of spark, the fuel energy is released so early before TDC which is contributed to the sharp increase in the rate of heat release and the accumulated heat release. Moreover, the maximum heat release rate is decreased and the corresponding crank angle position is postponed with retarding the spark timing. Results reveal that, by retarding the spark timing from 49 [CAD] BTDC to 30 [CAD] BTDC, maximum rate of heat release is decreased by 26% and occurred 15 [CAD] later.

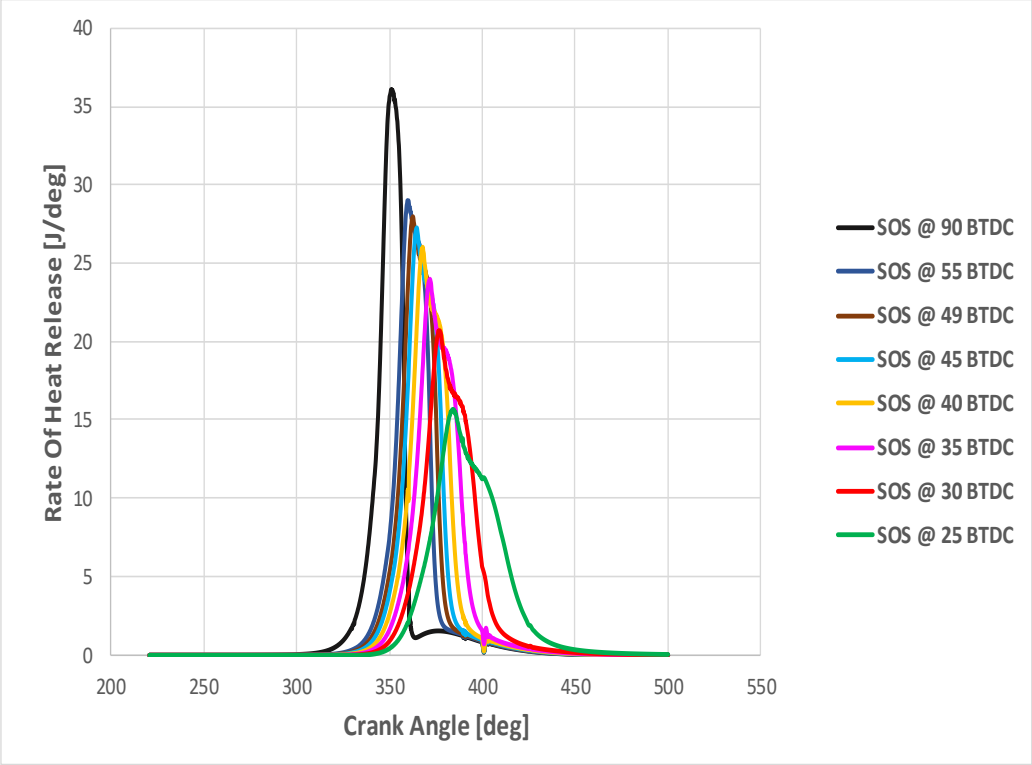


Figure 3.49 : The effect of spark timing on rate of heat release.

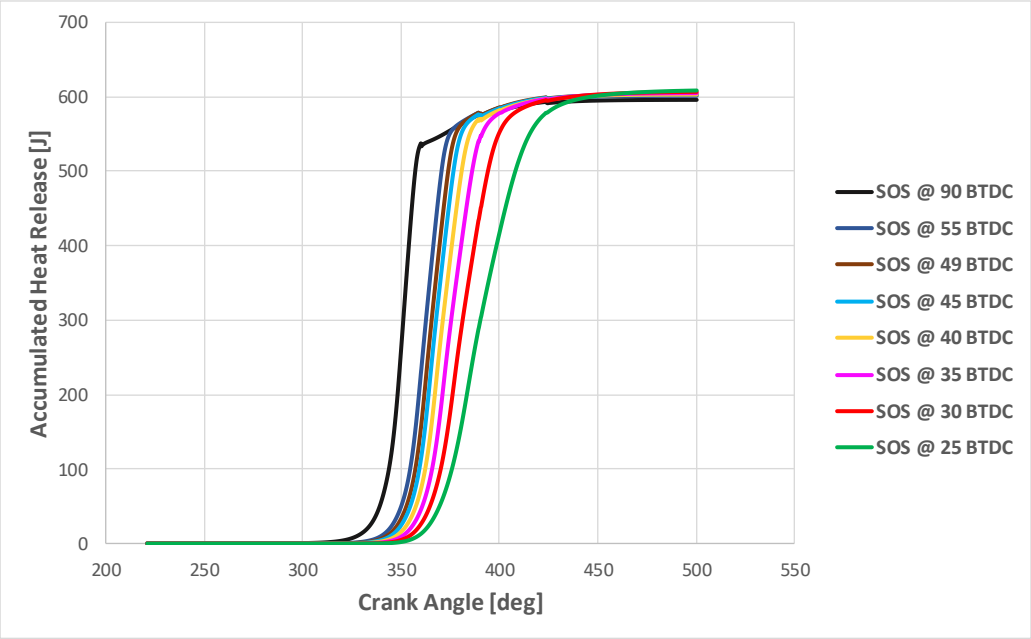


Figure 3.50 : The effect of spark timing on accumulated heat release.

As is clear from Figure 3.50, retarding the sparking timing beyond MBT time leads to increasing the combustion duration. Late ignition timing extends the combustion process longer into the expansion stroke, resulting in higher exhaust temperature. Advancing the ignition timing causes combustion to occur early in the cycle that in turn, moves the peak pressure closer to TDC and increases the temperature during the combustion process, and hence increases the burning velocity.

Table 3.22 : Start of combustion position and combustion duration with different spark timing.

Spark timing [CAD] BTDC	SOC [@CAD]	Combustion duration [deg]
90	340	21
55	351	22
49	354	22
45	356	23
40	358	26
35	362	28
30	366	32
25	371	44

Calculated position of SOC and combustion durations with different spark timing are listed in Table 3.22. As expected, an increase in burning velocity leads to reduction of the combustion duration. In comparison with retarded spark timing of 30°[CA] BTDC, it is obvious that the combustion duration of MBT timing is shorter by about 10[CAD].

3.4.3.5 Exhaust emissions

Since combustion temperature is the most important parameter for NO_x formation, spark timing significantly affects NO_x emission levels. By advancing the timing, combustion occurs earlier in the cycle and increases the peak cylinder pressure, since more fuel is burned before TDC and the peak pressure moves closer to TDC where the cylinder volume is smaller. Retarding the timing on the other hand decreases the peak cylinder pressure, because more fuel burns after TDC. Higher peak cylinder pressures result in higher peak cylinder temperatures, and hence higher formation rates of NO_x . As it can be seen in Figure 3.51, NO_x emissions steadily decrease as spark timing is retarded and moved closer to TDC. Compared with MBT spark timing, 41% reduction of NO_x is possible when spark timing is retarded and set to 30°[CA] BTDC.

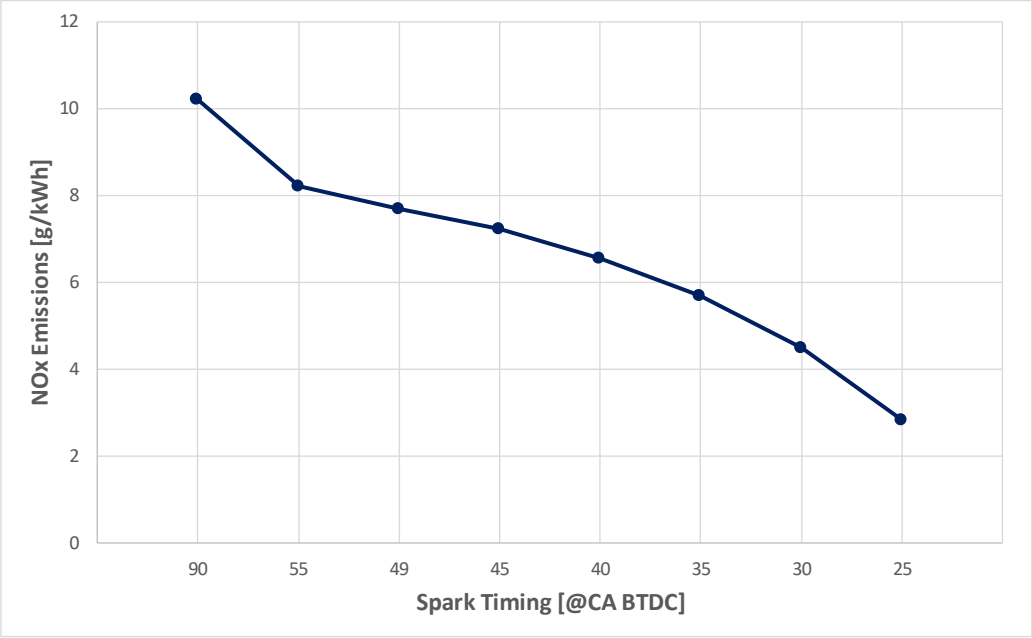


Figure 3.51 : The effect of spark timing on NO_x emissions.

Figure 3.52 illustrates the spatial distributions of temperatures and NO_x concentration inside the cylinder at 20 [CAD] ATDC for different spark timings. As it can be seen

from Figure 3.52, by retarding the spark timing, in-cylinder temperatures are decreased and hence NO_x emissions are also reduced steadily.

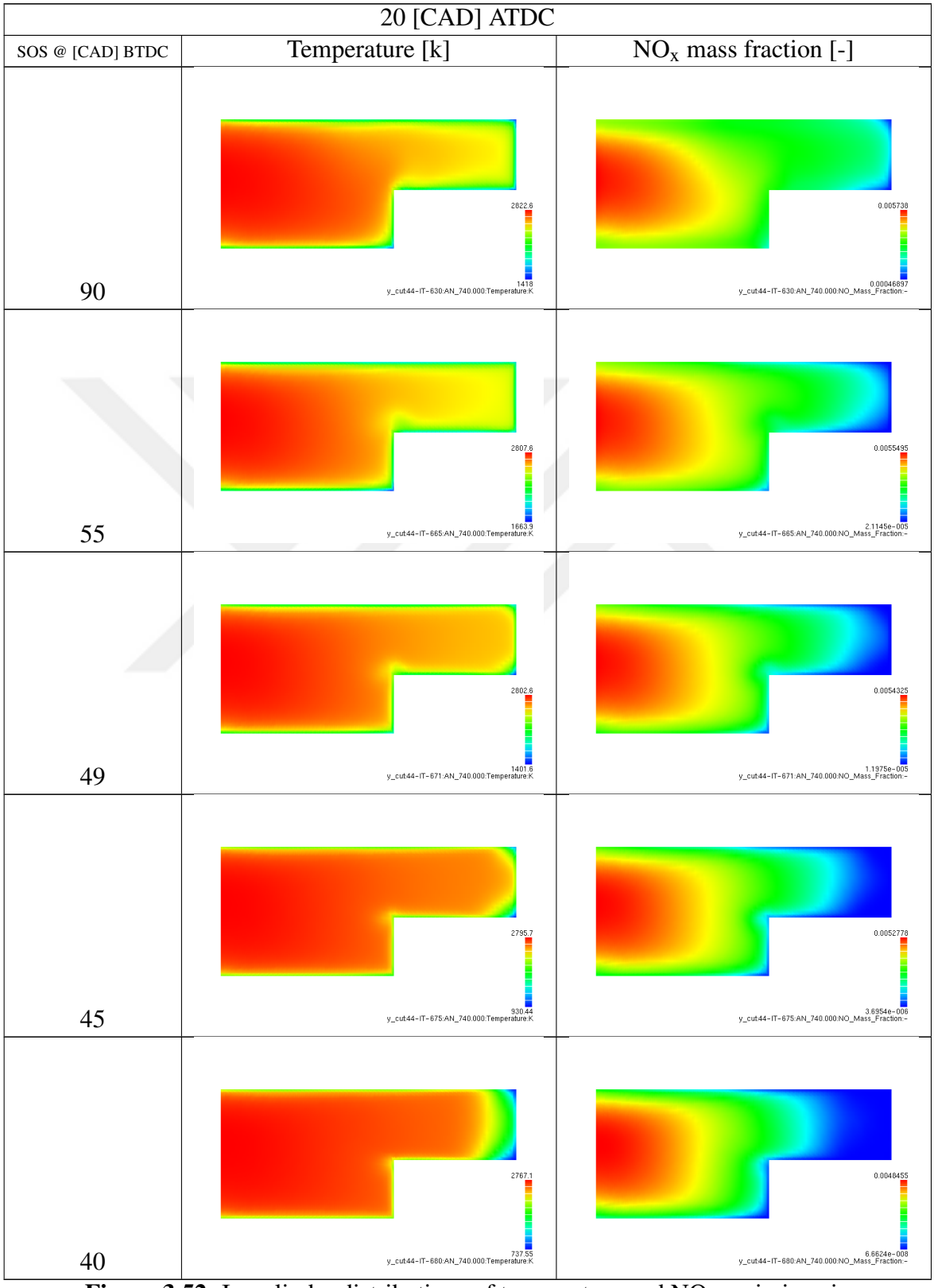


Figure 3.52: In-cylinder distributions of temperature and NO_x emissions in 20 [CAD] ATDC for different spark timings.

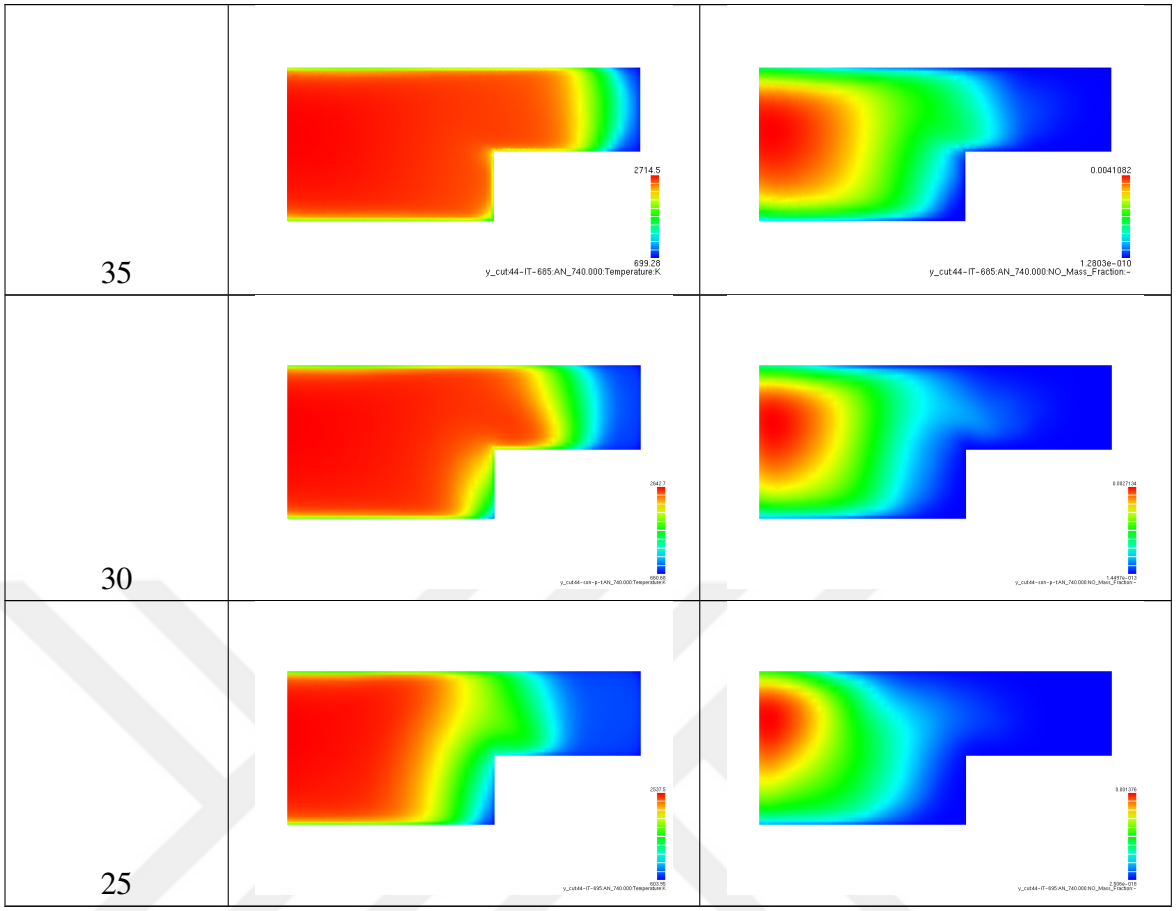


Figure 3.52 : **(Cont.)** In-cylinder distributions of temperature and NO_x emissions in 20 [CAD] ATDC for different spark timings.

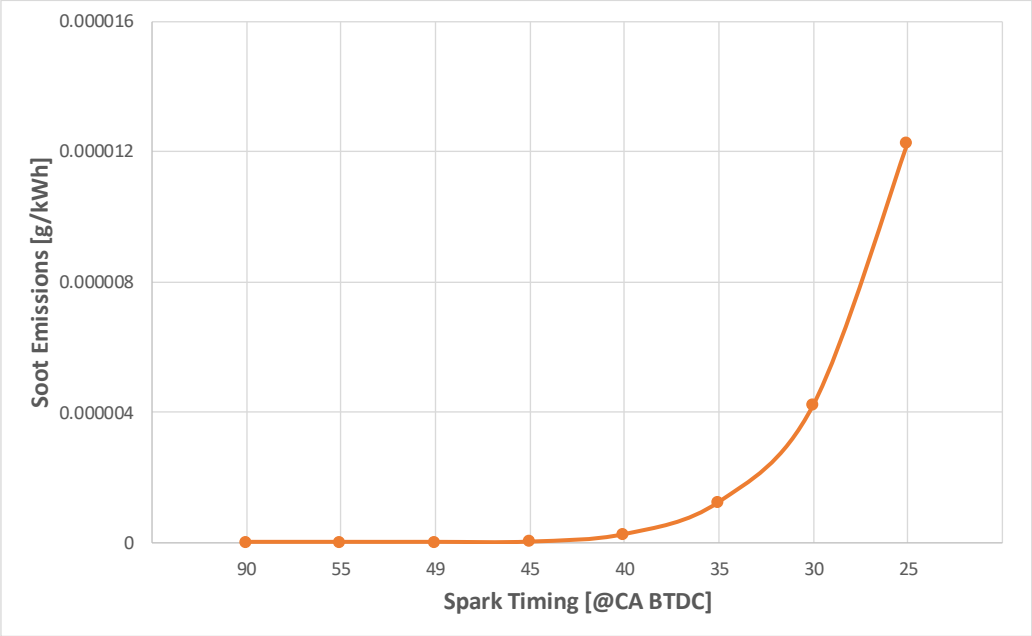


Figure 3.53 : The effect of spark timing on soot emissions.

Another cause of retarded spark timing is the expansion which occurs during the combustion and power stroke. As the piston moves away from TDC, expansion of the gases lowers both temperature and pressure within the cylinder. This slows combustion and finally quenches the flame somewhere late in the power stroke and leaves some fuel particles unreacted. Figure 3.53 depicts that the soot emissions almost are stayed constant and in notably low levels (near zero), by varying the spark timing, until the spark timing of 25°[CA] BTDC, where the combustion quality becomes poor and incomplete combustion occurs, which results in a higher level of soot emission.

CO formation is one of the principal reaction steps in the hydrocarbon combustion mechanism. Oxidation of CO to CO_2 requires relatively high temperatures. As described, exhaust temperatures are increased by retarding the spark timing which improve the oxidation reaction of CO, and hence the CO emissions are decreased. As shown in Figure 3.54, when the exhaust temperatures increase as a result of retarded spark timing, CO emissions are decreased. At the spark timing of 25°[CA] BTDC, due to incomplete combustion some amount of CO is not oxidised ,and hence higher amount of CO emission is produced.

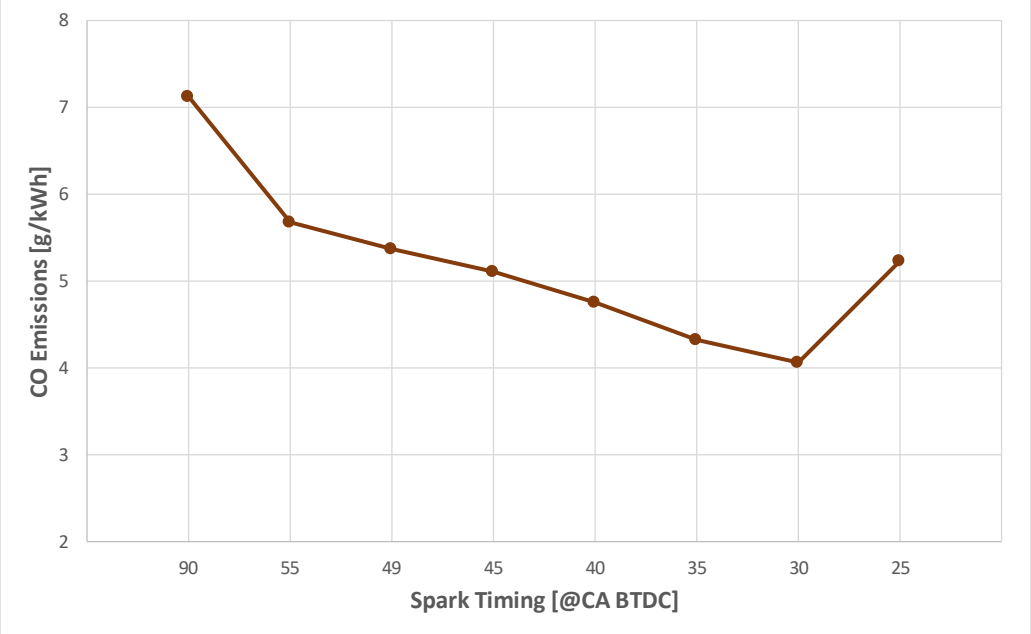


Figure 3.54 : The effect of spark timing on CO emissions.

Unburned hydrocarbon consist of fuel that is incompletely burned. Advanced timing changing the amount of oxidation in the cylinder as well as in the exhaust. As shown in Figure 3.55, advancing the spark timing increases the combustion temperature and

reduces the combustion duration, and thus promotes more complete combustion which leads to lower levels of unburned hydrocarbon emission. While retarded timing results an inefficient combustion and hence higher amount of HC emissions.

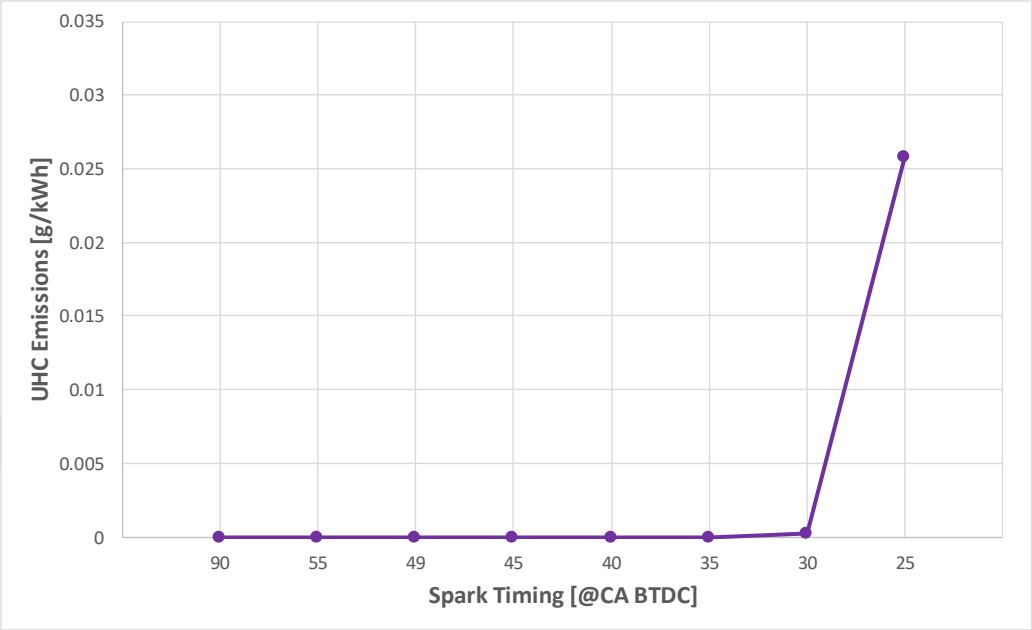


Figure 3.55 : The effect of spark timing on HC emissions.

3.4.3.6 Engine specific output

With earlier starts of combustion the peak pressures, and therefore peak temperatures in the cylinder are increased. The result of this is that the heat transfer in the cylinder also increases, leading to higher wall heat losses. Accordingly, because of the lower efficiency and reduced heat transfer losses, the exhaust gas temperature decreases with earlier start of combustion and increases at later start of combustion, since the fuel energy released very late can only make a small contribution to the work of the piston. Thus, higher power output is achieved with correct ignition timing.

Figure 3.56 show that IMEP tends to increase with increasing the spark advance till 49 °[CA] and then drop off. The indicated mean effective pressure also drops on either side of the optimum MBT. Best performance is achieved with the ignition timing of 49 °[CA] BTDC when the greatest portion of the combustion takes place near TDC. If ignition timing is not advanced enough, the piston will already be moving down when much of combustion takes place. In this case, the ability of expanding this portion of the gas through the full range is reduced and results in performance reduction. Moreover, if the spark timing is too advanced, too much of the gas will burn while

the piston is still rising, and hence the work that must be done to compress this gas will increase and results in decrease of net work and performance. Simulated engine outputs with different spark timings are summarized in Table 3.23.

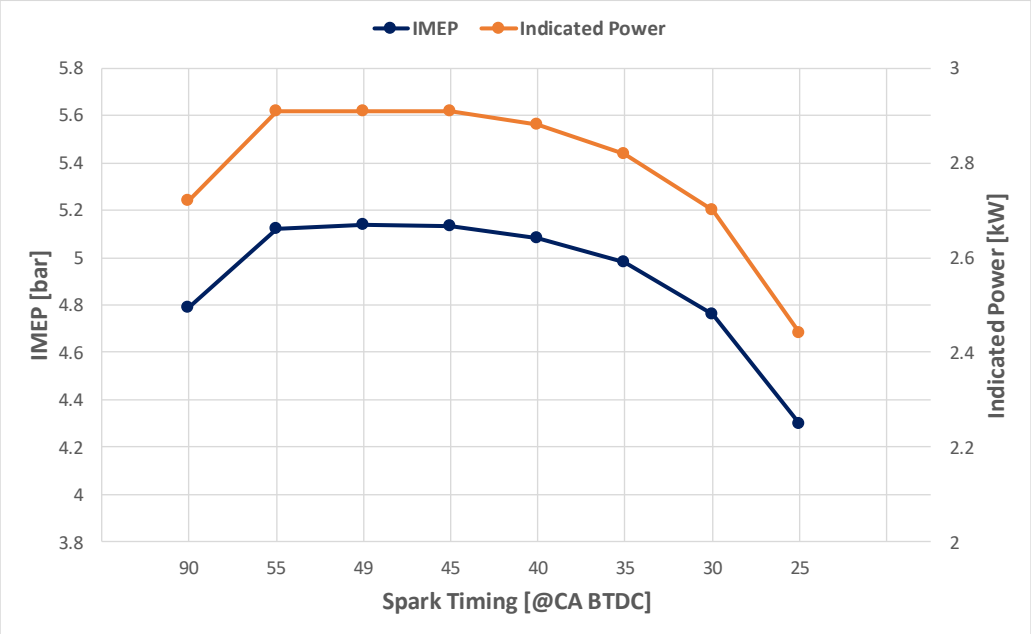


Figure 3.56 : The effect of spark timing on IMEP and indicated power.

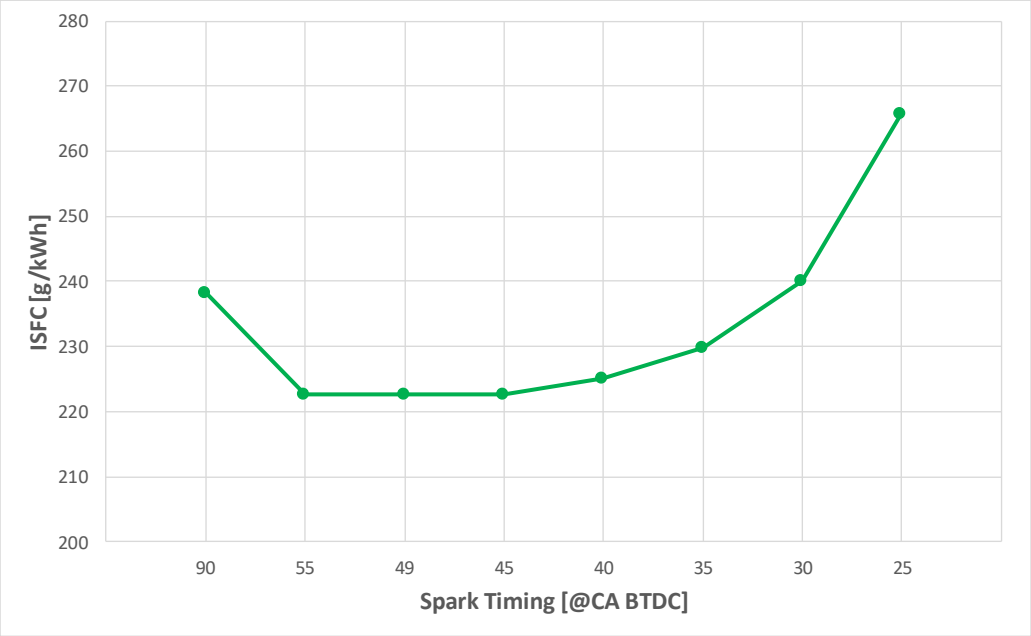


Figure 3.57 : The effect of spark timing on ISFC.

Observing Figure 3.56, one can clearly recognize that the indicated power drops with either too early or too late spark timing, and since the fuel mass for this investigation

is left constant, as shown in Figure 3.57, the indicated specific fuel consumption is increased by retarding or advancing the spark timing from MBT point. For the sake of gaining high efficiency with very low ISFC, it is possible to set the spark timing to minimum spark advance of 49 °[CA] BTDC (MBT). Advancing the ignition timing to 311 [CAD] (MBT) leads to 7.5% reduction of ISFC compared to the spark timing of 330 [CAD] (verified model).

Table 3.23 : Engine specific output with different spark timing.

Spark Timing @ [CAD] BTDC	90	55	49	45	40	35	30	25
Break mean effective pressure BMEP [bar]	3.03	3.36	3.37	3.37	3.32	3.21	3	2.54
Combustion Noise - A + CAV Filter [dB]	80.79	80.25	80.26	80.35	80.48	80.64	80.98	81.58
Combustion Noise - A Filter [dB]	195.44	193.46	192.75	192.18	191.27	190.12	188.65	186.77
Combustion Noise - CAV Filter [dB]	81.79	80.5	80.28	80.21	80.16	80.15	80.33	80.84
Combustion Noise [dB]	213.37	211.52	210.92	210.43	209.66	208.67	207.31	205.38
Excess air ratio [-]	1	1	1	1	1	1	1	1
Friction mean effective pressure FMEP [bar]	1.76	1.76	1.76	1.76	1.76	1.76	1.76	1.76
Indicated mean effective pressure IMEP [bar]	4.79	5.12	5.14	5.13	5.08	4.98	4.76	4.3
Indicated power [kW]	2.72	2.91	2.91	2.91	2.88	2.82	2.7	2.44
Indicated specific power [kW/l]	5.99	6.4	6.42	6.41	6.35	6.22	5.95	5.38
Indicated specific torque [Nm/l]	38.12	40.76	40.87	40.8	40.44	39.59	37.87	34.23
Indicated torque [Nm]	17.3	18.5	18.55	18.52	18.36	17.97	17.19	15.54
Mean mass [kg]	2.50E-04	2.50E-04	2.50E-04	2.50E-04	2.50E-04	2.49E-04	2.49E-04	2.49E-04
Mechanical efficiency [-]	0.63	0.66	0.66	0.66	0.65	0.65	0.63	0.59
Total mass at start of high pressure cycle [kg]	2.53E-04	2.53E-04	2.53E-04	2.53E-04	2.53E-04	2.53E-04	2.53E-04	2.53E-04
Volume displacement [m$\hat{3}$]	4.54E-04	4.54E-04	4.54E-04	4.54E-04	4.54E-04	4.54E-04	4.54E-04	4.54E-04

In summary, the optimum spark setting depends on the rate of flame development and propagation, the length of flame travel path across the combustion chamber, and the details of flame termination process after it reaches the wall. These depend on engine design, operation conditions and the properties of fuel, air and burned gas mixture.
Theoretically, the rate of combustion should be such that combustion duration is minimum with the high rate of pressure rise. This causes maximum pressure and maximum temperature of the cycle to occur near TDC to produce greater force acting through a long period of power stroke. If ignition is too early, the cylinder pressure will increase to undesirable levels before TDC and work will be wasted in the compression

stroke. If ignition is late, peak pressure will not occur early enough and work will be lost at the start of power stroke due to lower pressure. Therefore, engines are designed that only 50% of pressure rise is completed by the TDC, resulting in peak pressure and temperature occurring at 10-15 °[CA] ATDC, which reduces the heat loss and make engine operation smooth. Thus, the combustion has to be completed within 15°[CA] ATDC (Rajput, 2005).

In this section, optimal spark timing is predicted and the best spark timing for model is found to be earlier in the cycle than the spark timing of validated model and test engine. As illustrated in section 3.3, validated model (Case-44) has a spark timing of 330 or 30°[CA] BTDC. While further investigation shows that the performance is benefitted by more advance. An optimum spark timing ensures that the rate of combustion is maximum when the piston is close to TDC, thus making better use of power stroke.

3.5 Simulation Results By Using Natural Gas As Fuel

In this section, instead of gasoline, natural gas (methane) as an alternative fuel is used in simulations to extend the study and investigate the effect of utilizing natural gas on SI engine performance and emissions. In this work, methane (CH_4) is considered as representative of natural gas.

Gasoline fuels are used in engines with external or internal mixture formation with spark ignition. Due to the low temperatures and in-cylinder pressures, the fuel must be highly volatile for the sake of a sufficient mixture formation. As a result, only hydrocarbon compounds with short chain length are used in gasoline fuels. Only alkanes with four to eight carbon atoms and aromatics built on one benzene ring (mono-aromatics) have a notable fraction in gasoline mixture. The characteristic property of a gasoline fuel is described by its octane number. The higher octane number, the less ignitable and more knock proof.

In case of natural gas, it is a combustible gas which is used in combustion engines mainly as compressed natural gas (CNG). The main component of natural gas is methane with a percentage of above 95%(volume), along with higher alkanes and inert gases (N_2, CO_2). Because of the short chain length and molecular sizes, CNG has very high octane numbers (ranging from 120 to 130), and hence, it is suitable for using in SI engines. Moreover, SI engines can be converted to operate with CNG quite easily

by adding a second fueling system. Table 3.24 represents the properties of natural gas and gasoline.

Table 3.24 : Properties of natural gas and gasoline.

Properties	Gasoline	Natural Gas
Formula	C_8H_{17}	CH_4
Octane number	90-100	120-130
Molecular Weight	113.17	16.04
Stoichiometric (A/F)	14.9	17.2
Lower heating value [MJ/kg]	44	50
Density [kg/m^3]	750	0.72

The mesh structure, boundary and initial conditions, combustion and emission models, spark timing and engine speed are as same as the verified baseline model (case-44) and only the type of fuel is changed to natural gas. Simulation results are then compared with the verified baseline simulation (case-44) results to understand the influence of using natural gas as fuel in simulated SI engine.

As shown in section 3.4.3, the validated model (Case-44) does not operate with MBT spark timing, since it is adjusted with corresponding experimental data. According to a comparative study which is done by Evans and Blaszczyk (1997), the MBT spark timing for CNG is between 2 and 10 crank angle more advanced than that for gasoline at an equivalence ratio close to stoichiometric. Inasmuch as the operating condition is not changed for CNG engine in this study, this case also does not operate with MBT spark timing.

According to Heywood (1988), in a spark ignition engine, the presence of gaseous fuel in in the intake system reduces the air partial pressure below the mixture pressure. Additionally, $\dot{m}_f/\dot{m}_a$ only equals the engine operating fuel/air ratio if the fuel is fully vaporized. For conventional liquid fuels such as gasoline the effect of fuel vapor and hence fuel/air ratio, is small. While, for gaseous fuels the volumetric efficiency is significantly reduced by fuel vapor in the intake mixture. Also, compared to liquid fuels, larger volume of inlet air is occupied by natural gas. By using ideal gas state equation, it can be easily shown the volume occupied by natural gas is larger than that by gasoline in a stoichiometric air-fuel mixture.

The volumetric efficiency of engine η_v is defined as the ratio of actual mass flow rate of air through the engine,$\dot{m}_a$ divided by the maximum possible mass flow rate of air that the engine geometry would allow

$$\eta_v = \frac{\dot{m}_a}{\rho_{a,in} V_d k N} \tag{3.12}$$

Where, $\rho_{a,in}$ is the density of air at engine inlet, V_d is the displacement volume of engine, k is the number of power strokes per engine revolution(k=1/2 for four-stroke engine), and N is engine speed [rpm].

Volumetric efficiency gives an idea of the mass of air and fuel admitted to engine at given operation condition. According to Eq.(3.12), at the same operating conditions for CNG engine lower amount of air is induced into the cylinder and the volumetric efficiency of CNG engine is reduced by 7.3%. Moreover, by considering the stoichiometric air-fuel ratio of natural gas which is about 17.2, lower amount of intake air results in lower amount of supplied natural gas fuel to keep the air-fuel ratio of combustion equal to stoichiometric. Amount of intake air and supplied fuel at the start of cycle for both cases are summarized in Table 3.25. From Table 3.25, it can be seen that lower amount of natural gas and air are induced into the combustion chamber.

Table 3.25 : Amount of intake air and supplied fuel.

Gasoline		Natural gas	
Air [g/cycle]	Fuel [g/cycle]	Air [g/cycle]	Fuel [g/cycle]
0.2145	0.0144	0.1995	0.0116

3.5.1 Rate of heat release and accumulated heat release comparison

Figures 3.59 and 3.60 respectively, show the heat release rate and accumulated heat release of natural gas and gasoline as a function of crank angle. Mass fraction of burnt natural gas and gasoline as a function of crank angle is illustrated in Figure 3.58. As it can be seen in Figure 3.58, the combustion of natural gas starts earlier and a large fraction of natural gas is burned at the start of expansion stroke. Another important factor is the lower heating value (LHV) of fuels which is a measure of heat release during complete combustion. Since larger fraction of natural gas is burned earlier and it has a higher LHV than gasoline, the sensible energy of natural gas which is released at the start of expansion stroke is greater. These reasons can be contributed to the

sharp increase in the rate of heat release and the accumulated heat release of natural gas at the start of expansion stroke.

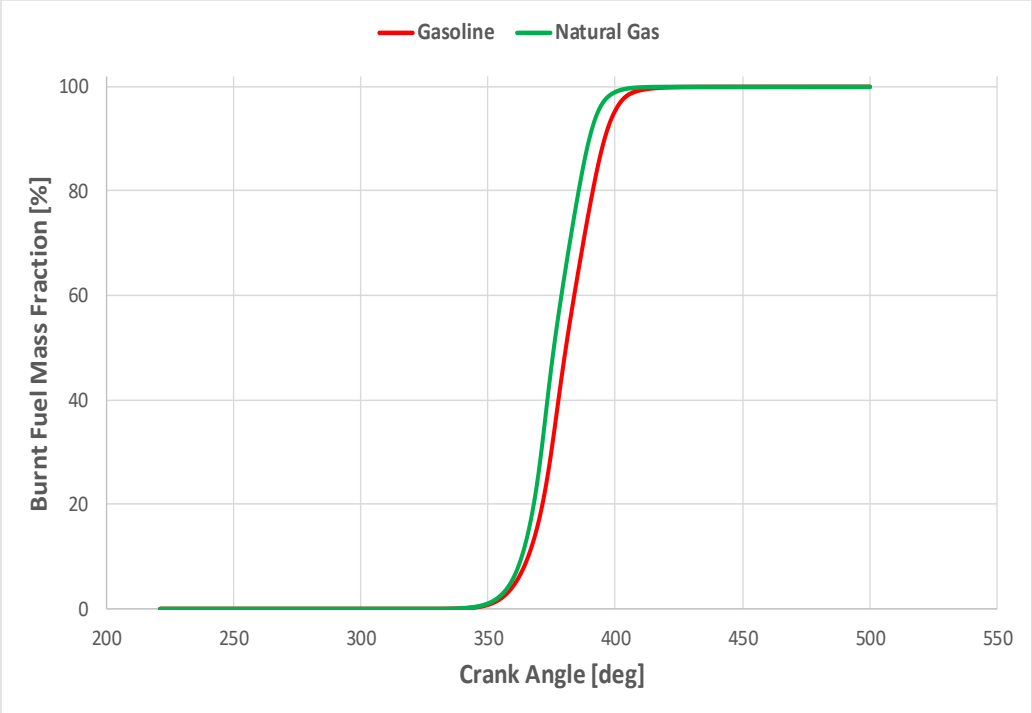


Figure 3.58 : Mass fraction of burnt gasoline and natural gas engines.

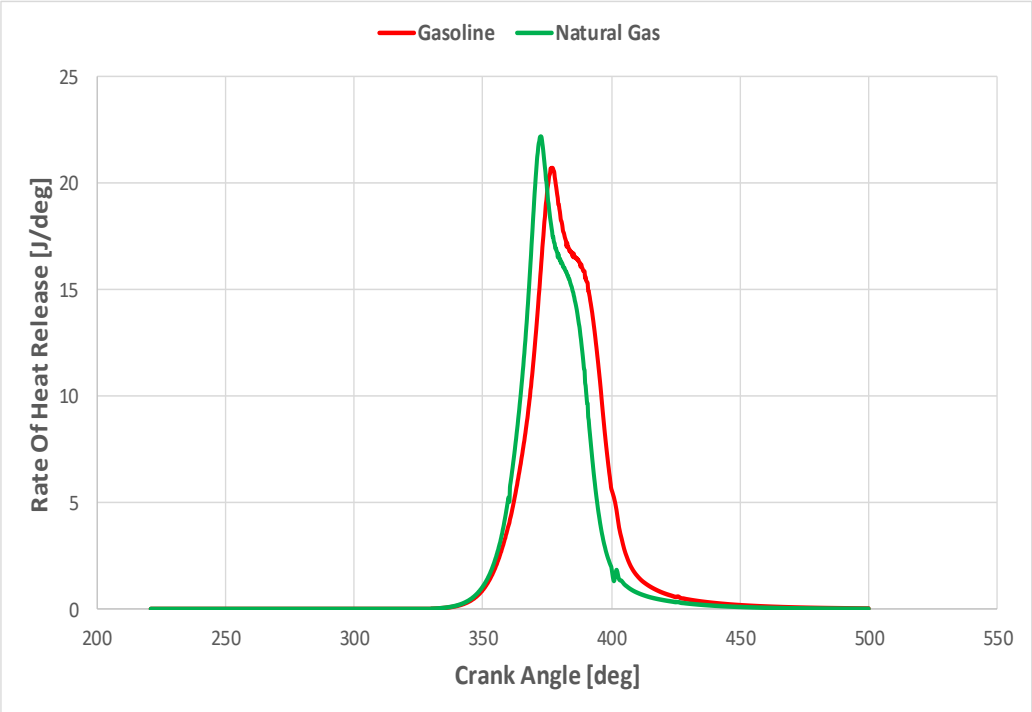


Figure 3.59 : Heat release rate of gasoline and natural gas engines.

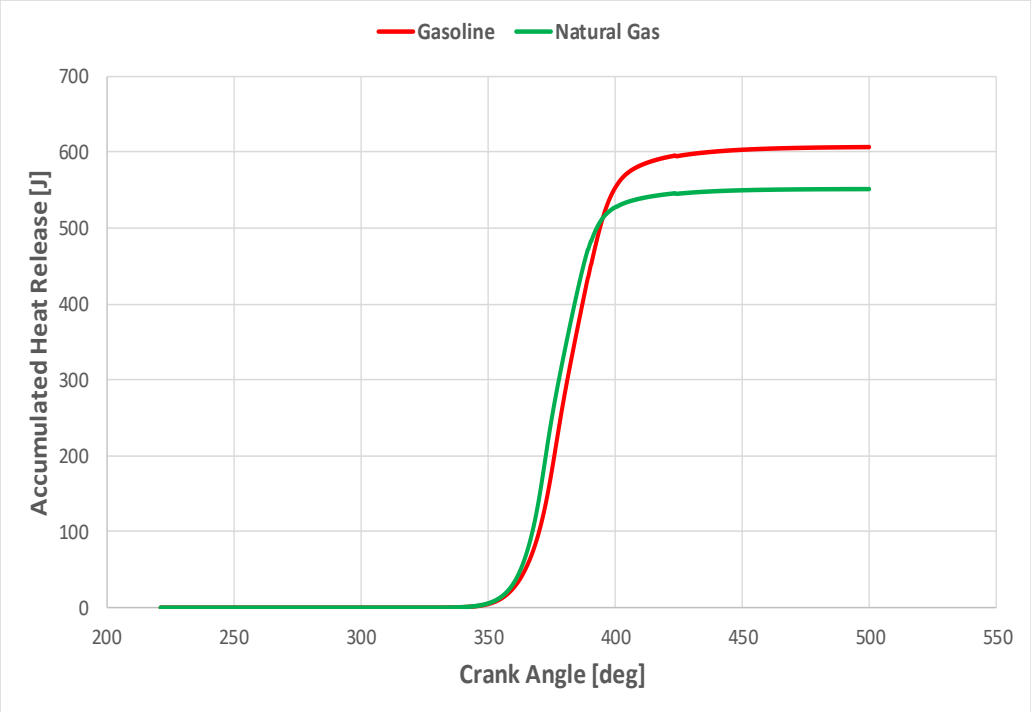


Figure 3.60 : Accumulated heat release of gasoline and natural gas engines.

However, natural gas has higher LHV than gasoline, as shown in Table 3.25 lower amount of natural gas is inducted into the combustion chamber, which results in lower total energy content of CNG-air mixture by about 50 [J]. Energy content of mixture is calculated via

$$Q_m = m_f \times LHV \tag{3.13}$$

The lower heating value of fuels and calculated energy content of mixtures are listed in Table 3.26. Higher heat release rate and accumulated heat release of gasoline at the end of expansion stroke, shown in Figures 3.59 and 3.60, can be attributed to the higher energy content of gasoline-air mixture and its retarded combustion start. Calculated position of SOC and combustion durations for both cases are listed in Table 3.27.

Table 3.26 : LHV of fuels and energy content of mixtures.

Fuel	Mass [g/cycle]	LHV [MJ/kg]	Mixture energy content [J/cycle]
Gasoline	0.0144	43.6	628
Natural gas	0.0116	50	578

Table 3.27 : Start of combustion position and combustion duration of gasoline and natural gas engines.

Fuel	SOC [@CAD]	Combustion duration [deg]
Gasoline	366	32
Natural gas	363	29

From Table 3.27 , it is obvious that the combustion of natural gas starts earlier than gasoline, near the TDC, and has shorter duration by about 3 [CAD].

3.5.2 In-cylinder mean temperature and in-cylinder pressure comparison

Comparison of in-cylinder pressures and mean temperatures of natural gas and gasoline combustion as a function of crank angle are shown in Figures 3.62 and 3.61, respectively. As described in previous section, the fraction of chemical energy of the natural gas which is released as sensible energy near TDC is greater. Hence, a greater fraction of the fuel's energy is transferred as work to the piston at start of expansion and the fraction of fuel's available energy rejected to the exhaust system decreases. This causes an intense increase in temperature and pressure of natural gas combustion at the start of expansion stroke and subsequent reduction at the rest of stroke due to expansion and quenching.

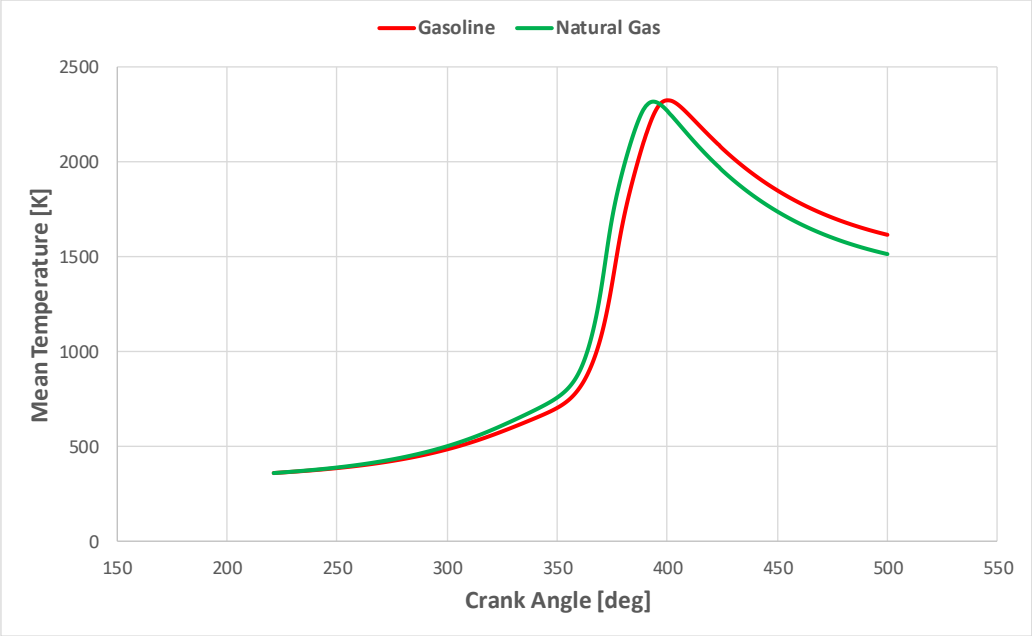


Figure 3.61 : Mean in-cylinder temperature of gasoline and natural gas engines.

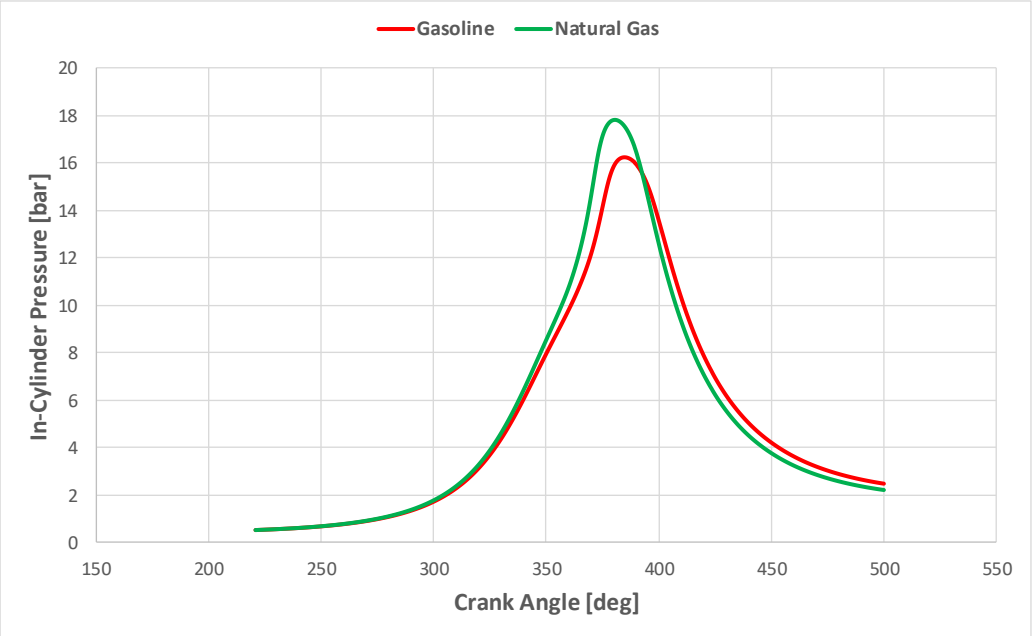


Figure 3.62 : In-cylinder pressure of gasoline and natural gas engines.

The peak pressure values of natural gas and gasoline combustion and related crank angle positions are summarized in Table 3.28.

Table 3.28 : Peak cylinder pressures and related crank angles of natural gas and gasoline combustion.

Fuel	Peak pressure [bar]	@ CAD
Gasoline	16.31	384
Natural gas	17.85	380

By using natural gas as fuel, peak pressure position is advanced by 4 [CAD] and its value is increased by about 9.4% compared to the peak in-cylinder pressure of gasoline combustion.

3.5.3 Emissions

Formation of NO_x emissions mainly depends on combustion temperature and oxygen concentration. As it can be seen in Figure 3.61, the combustion temperature of natural gas is lower than that of gasoline. Additionally, as described before and listed in Table 3.25, the amount of inlet air for CNG engine is also lower than gasoline engine. As shown in Figure 3.63, the combination of lower combustion temperature and lower

amount of intake air leads to lower NO_x formation of CNG engine.

Carbon monoxide emissions are the product of incomplete combustion. Inasmuch as the equivalence ratio of both combustion is equal to 1, there is sufficient oxygen for complete oxidation of CO to CO_2, so there are other parameters that affect the CO formation. Carbon to hydrogen ratio of fuel (C/H) is one of the most significant parameters that can affect the formation of CO. Lower C/H ratio of a fuel, decreases the amount of CO. C/H ratio of natural gas is 1:4 and smaller than that of gasoline which is 8:17 in this study. Besides having lower C/H ratio,observing Figure 3.61, the combustion temperature of natural gas is also lower than that of gasoline, which reduces the dissociation from CO_2 to CO. Therefore, by considering mentioned reasons lower amount of CO is produced by CNG engine.

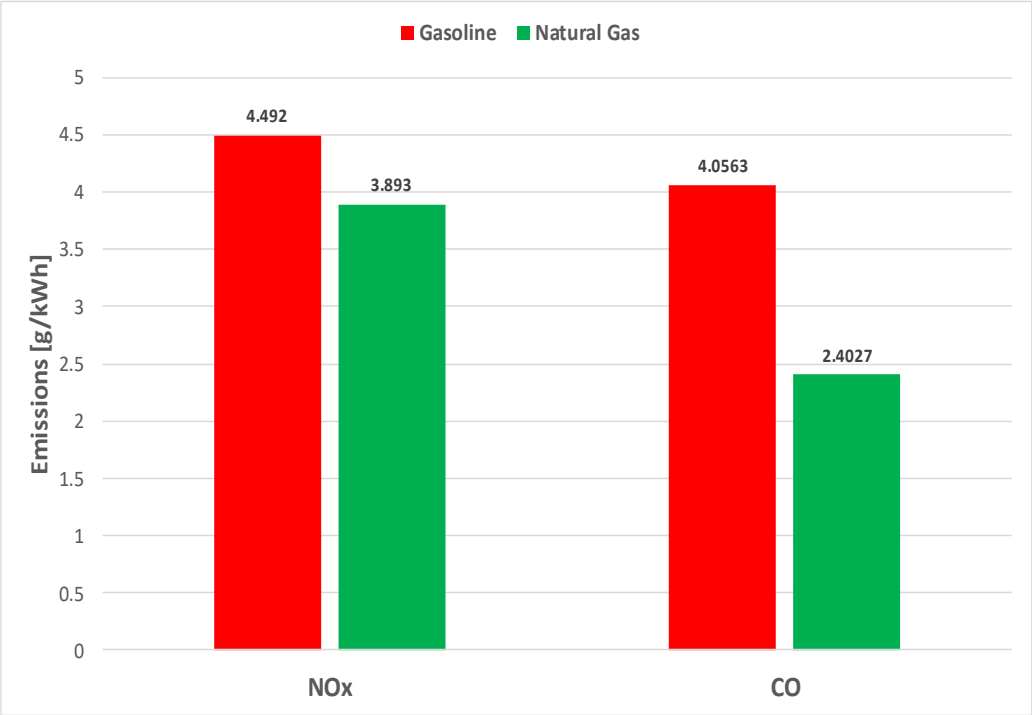


Figure 3.63 : NO_x and CO emissions of gasoline and natural gas engines.

As shown in Figure 3.63, the amount of CO emissions can be decreased by more than 40% and also NO_x reduction of 14% is possible when the engine operates on natural gas instead of gasoline.

Figure 3.64 shows the in-cylinder temperature distributions and NO_x emission

concentration contours for natural gas and gasoline fueled SI engines at different crank angles.

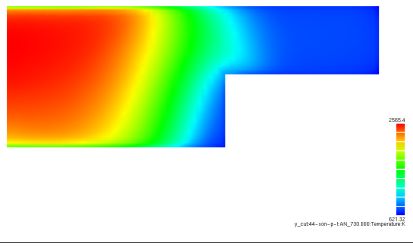
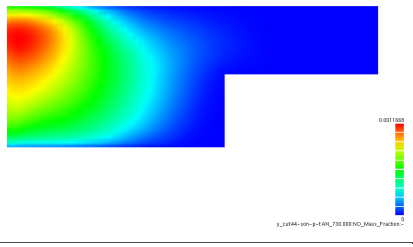
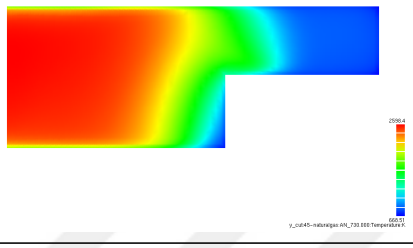
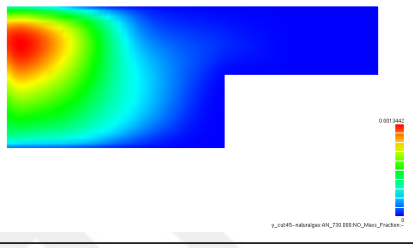
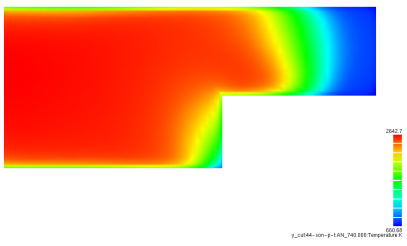
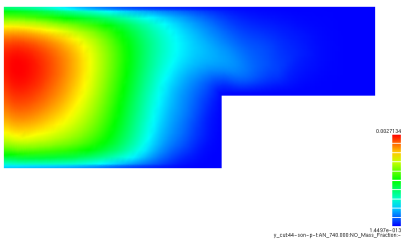
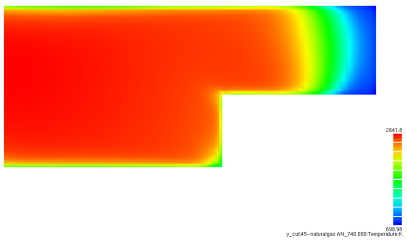
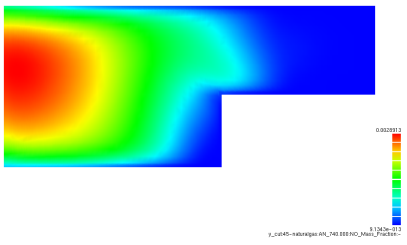
Fuel	Temperature [k]	NO_x mass fraction [-]
@ 10 [CAD] ATDC		
Gasoline		
Natural gas		
@ 20 [CAD] ATDC		
Gasoline		
Natural gas		

Figure 3.64 : In-cylinder distributions of temperature and NO_x emissions for natural gas and gasoline fueled SI engines in different crank angles.

Table 3.29 reveals that the engine-out unburned hydrocarbon emissions can also be reduced below the corresponding levels for gasoline engine, since the gaseous state

of natural gas avoids wall wetting effects on intake manifold and cylinder liner. The smaller percentage of HC emissions from oil film adsorption-desorption phenomena also contributes to reduction of natural gas engine-out HC emissions compared to those of gasoline engine. An additional feature of natural gas engines is that their main HC emission is methane and it has negligible reactivity.

Soot emissions are a culmination of the difference between the soot formation and soot oxidation process,and hence the balance of these two yields the total engine-out concentration of soot. In case of natural gas combustion, the lowered combustion temperature and lower oxygen concentration are thought to reduce the soot oxidation rates, thereby increasing the soot emissions of natural gas engine. As shown in Table 3.29, although natural gas engine produces higher soot emissions than gasoline engine, soot emission levels for both cases are remarkably low and negligible.

Table 3.29 : Soot and unburned hydrocarbon emissions of natural gas and gasoline engines.

Fuel	Soot [g/kWh]	UHC [g/kWh]
Gasoline	4.22E-06	2.22E-04
Natural gas	1.06E-03	4.71E-05

3.5.4 Engine specific output

It is observed that by using natural gas as fuel the indicated power output is reduced by about 8% compared to the gasoline fueled engine under similar conditions, as shown in Figure 3.65. This is primarily because of lower density of natural gas, which requires the induction of a large volume of natural gas in order to produce similar power levels as gasoline engine. This volume of gaseous fuel displaces a similar volume of air from entering the engine and hence, reducing the volumetric efficiency by 7.5%. Moreover, there is also a decrease in IMEP by about 8%, with the majority of the reduction coming from the lower volumetric efficiency associated with naturally aspirated natural gas engine.

Specific fuel consumption is a very important characteristic for comparing the performance of IC engines fueled with different fuels. Observing Figure 3.66, the ISFC of natural gas fueled engine is 13% lower than that of gasoline engine. The reason is that, as mentioned, stoichiometric air-fuel ratio of natural gas is about 17.2

and higher than that of gasoline which is about 14.9, and also LHV of natural gas is higher than gasoline which means lower amount of fuel is needed for the same work output (Table 3.25).

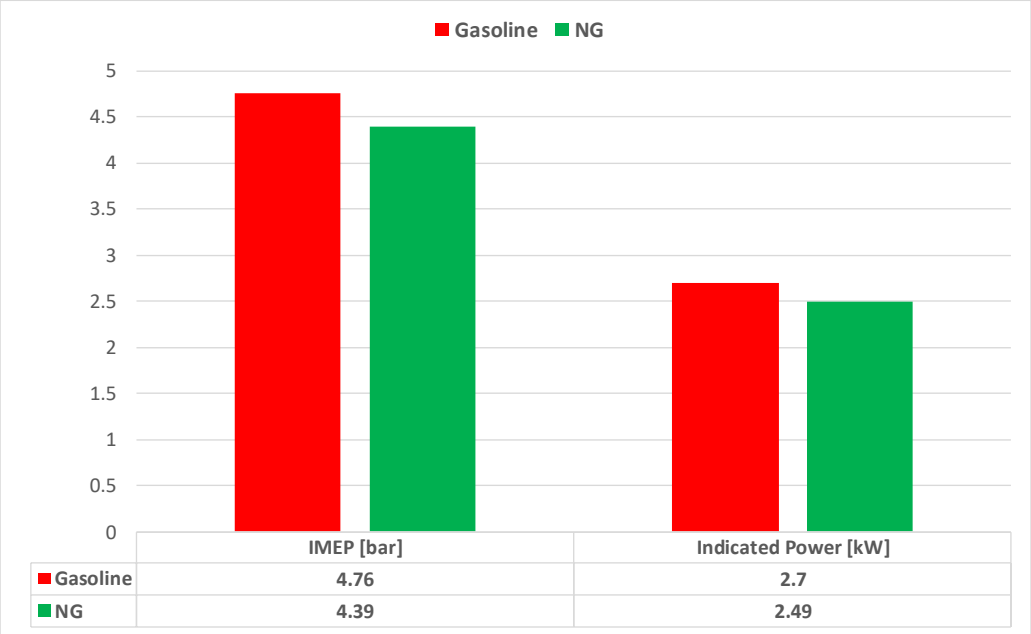


Figure 3.65 : IMEP and indicated power of gasoline and natural gas engines.

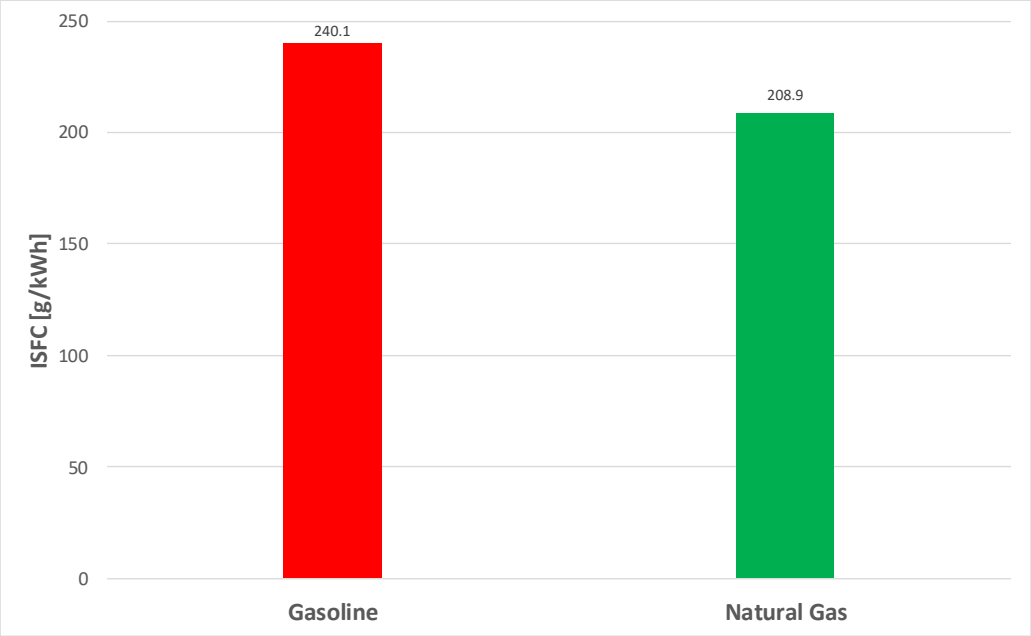


Figure 3.66 : ISFC of gasoline and natural gas engines.

Specific engine outputs for both cases which are obtained by analyzing the simulation results via ESE Diesel analyser tool are summarized in Table 3.30.

Table 3.30 : Gasoline and natural gas engine specific output.

Fuel	Gasoline	Natural Gas
Break mean effective pressure BMEP [bar]	3	2.63
Combustion Noise - A + CAV Filter [dB]	80.98	79.76
Combustion Noise - A Filter [dB]	188.65	189.29
Combustion Noise - CAV Filter [dB]	80.33	79.25
Combustion Noise [dB]	207.31	207.94
Excess air ratio [-]	1	1
Friction mean effective pressure FMEP [bar]	1.76	1.76
Indicated mean effective pressure IMEP [bar]	4.76	4.39
Indicated power [kW]	2.7	2.49
Indicated specific power [kW/l]	5.95	5.49
Indicated specific torque [Nm/l]	37.87	34.97
Indicated torque [Nm]	17.19	15.87
Mean mass [kg]	2.49E-04	2.28E-04
Mechanical efficiency [-]	0.63	0.6
Total mass at start of high pressure cycle [kg]	2.53E-04	2.32E-04
Volume displacement [m$\hat{3}$]	4.54E-04	4.54E-04

3.6 Natural Gas fueled HCCI Combustion Modeling

3.6.1 Introduction

The aim of this section is the implementation of natural gas fueled HCCI combustion strategy to improve the engine performance in parallel with decreasing the engine-out emissions.

As described in previous section, natural gas has high octane numbers ranging from 120 to 130, due to this high value of octane number, natural gas has a higher knock resistance than gasoline which enables the use of higher compression ratios. However, natural gas does not autoignite under compression ratios of conventional CI engine. For use of natural gas in CI engine, special modes of operation such as HCCI mode and dual-fueling are required.

Homogeneous Charge Compression Ignition (HCCI) is a merger of conventional diesel (stratified charge compression ignition) and gasoline (homogeneous charge spark ignition) engines. The aim of HCCI concept is to achieve a homogenous mixture of fuel and air well before the combustion event, like SI engines. This can be made possible by early injection of the fuel in the intake port or directly into the combustion chamber at the start of induction stroke and allowing sufficient time between the injection and ignition event to allow uniform mixing of air and fuel. This mixture undergoes compression and auto ignites as in CI engines. Thus it burns instantaneously throughout, without the hot flame front of SI combustion or the locally rich diffusion combustion of CI engines.

The HCCI engine does not use a spark plug system, but the mixture of air and fuel is compressed and by increasing the temperature of the mixture, the initial energy is provided for combustion. At the end of compression, the combustion initiates by the auto-ignition phenomenon and it happens simultaneously at several points in the cylinder. The lean premixed fuel and the simultaneous ignition at several points in the combustion chamber decrease the combustion temperature, which prevent the production of NO_x and decrease soot emissions. In an ideal HCCI engine, the auto ignition is done simultaneously in all points of the cylinder. This causes heat to be released suddenly (high combustion rate) and knock would happen in the engine. Hence, HCCI engines must operate with lean mixture.

Despite traditional SI and CI engines in which spark and fuel injection controls the start of combustion, respectively, and combustion rate depends on flame propagation speed or the injection duration, combustion timing of HCCI concept is controlled by chemical kinetics and intensely depends on initial condition, fuel quality and thermodynamic history experienced during the compression stroke.

Figure 3.67 shows a comparison of SI, CI and HCCI engines, where SI engines have a spark plug to initiate the combustion with a flame front propagating across the combustion chamber. CI engines have a fuel injector to inject the fuel and the combustion takes place in a compressed hot air region. HCCI engines on the other hand, have no spark plug or fuel injector and the combustion starts spontaneously in multiple locations.

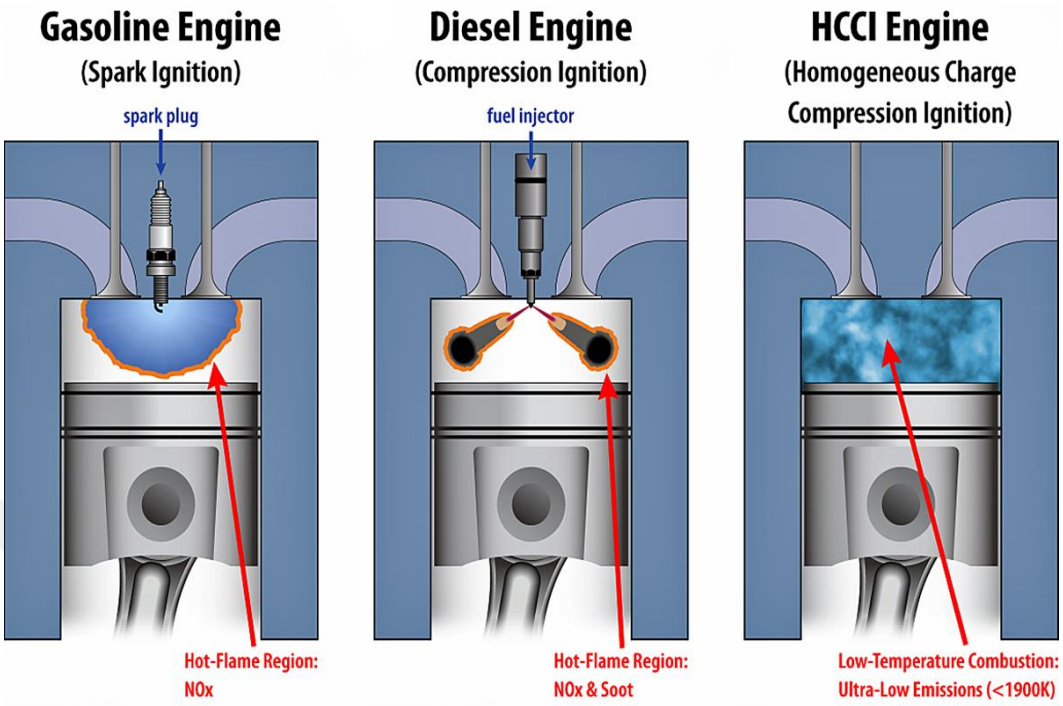


Figure 3.67 : A comparison of SI, CI and HCCI engines, adapted from (William and Charles, 2011).

By contrast to the conventional SI and CI engines, some advantages and disadvantages of HCCI engine are summarized in the following:

Advantages:

- Flexibility of HCCI engines to use various fuels
- HCCI engines produce low emissions under low and medium loads in comparison with diesel and gasoline engines. Homogenous mixture and lean burning produce lower soot emissions, additionally lower combustion temperatures result in lower levels of NO_x emissions in comparison with SI engines.
- A higher compression ratio is used, which results in a higher thermal efficiency than SI engines.
- Elimination of throttling loss in HCCI compared with SI engines, which gives higher efficiency.

Disadvantages:

- Operating range of HCCI engines bounded to low and medium load conditions, by virtue of enormously rapid pressure rise (high combustion rate) occurred in high load conditions and resultant knocking and misfire
- Ignition timing of HCCI combustion is controlled by chemical kinetics which is complicated and makes it difficult to control
- Although HCCI engines are capable of simultaneous reduction in NO_x and soot emissions, due to the early injection, low temperature and wall wetting of fuel they lead to higher HC and CO emissions.

As described in section 1.2.2.2, numerous researches have been done to expand the operating range of HCCI engines and solve the mentioned problems.

3.6.2 Pre-processing of simulation

HCCI combustion is achieved when the energy within the cylinder is greater than the activation energy required to auto ignite the fuel-air mixture. There are some typical ways to enable the use of natural gas in HCCI engines. The high autoignition temperature of natural gas which is about 1100 [K] (due to its high octane number) requires the use of high compression ratios, intake air heating or a combination of those to achieve combustion. The simplest method of creating enough pressure to auto ignite the mixture, is increasing the compression ratio of the engine. The other method is increasing the temperature of inlet air which can be done either by preheating the inlet air with a pre-heater unit or by using hot internal or external EGR to ensure the autoignition.

In this study, the compression ratio of engine is increased to achieve an engine that can operate with HCCI concept. In this regard, previously verified single-cylinder SI engine is modified by decreasing the clearance volume and eliminating the spark plug and the throttling valve. Considering the cylinder geometries, the clearance gap is the only parameter that is reduced and other engine specifications including connecting rod length, bore, stroke, shape of piston crown, and hence displaced volume of engine are not changed. The fuel supply method is not changed and natural gas is still inducted into the combustion chamber via manifold (port fuel injection). As a result

of modifications, the compression ratio is increased from 9.1 to 17.5 and the SI engine is altered to an HCCI engine. Specifications of both SI and HCCI engines are listed in Table 3.31.

Table 3.31 : Verified SI engine and modified HCCI engine specifications .

Engine type	Four stroke , SI	Four stroke , HCCI
Fuel	gasoline / natural gas	natural gas
Compression ratio	9.1:1	17.5:1
Clearance gap [mm]	7	1.98
Number of cylinders	1	
Bore [mm]	85	
Stroke [mm]	80	
Displacement [cm^3]	454	
Connecting rod length [mm]	145	
Intake valve opening	16 [CAD] BTDC	
Intake valve closing	40 [CAD] ABDC	
Exhaust valve opening	40 [CAD] BBDC	
Exhaust valve closing	16 [CAD] ATDC	

In order to generate the computational grid, general engine parameters and combustion chamber geometries which are given in Table 3.31, are imported into ESE Diesel tool. The specification of computational grid that is used for sector mesh generation are listed in Table 3.32. The adopted computational grid contains a maximum of 46,864 cells.

Table 3.32 : Computational grid specification used for sector mesh generation.

Average cell size [mm]	0.6
Number of boundary layers	2
Thickness of boundary layer [mm]	0.2
Maximum number of cells	46,864

Figures 3.68 and 3.69, respectively, depict the grid resolution and the 3D sector mesh of HCCI engine that is generated with AVL FIRE® ESE Diesel tool to simulate the combustion process from the IVC at 220°[CA] to EVO at 500°[CA] .

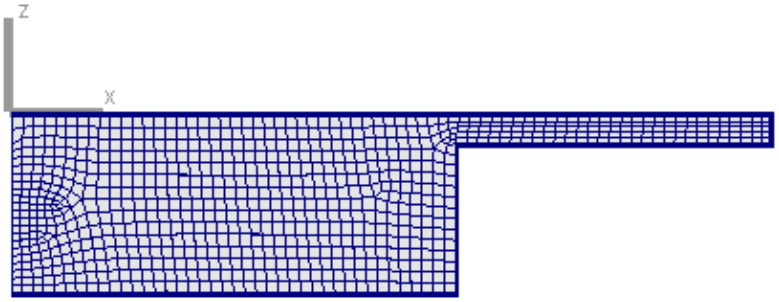


Figure 3.68 : Grid resolution.

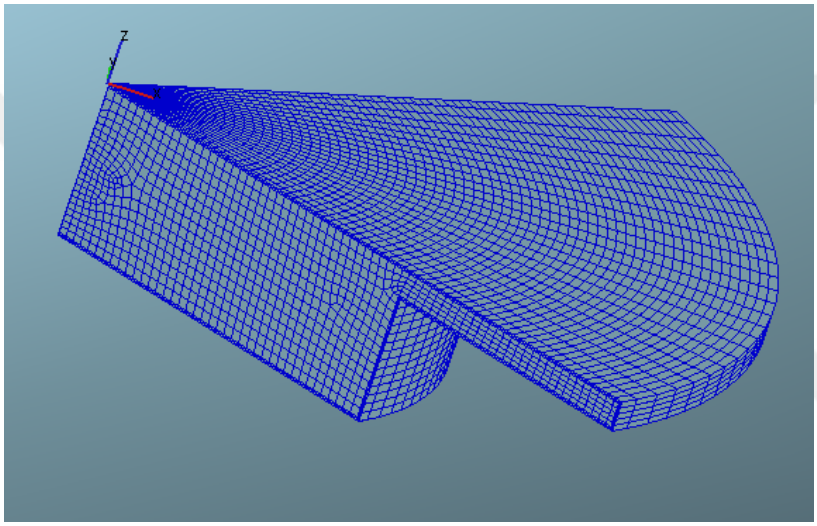


Figure 3.69 : Generated 3D sector mesh used in HCCI engine simulations (72° sector).

In order to achieve precise simulation results, the operating interval is divided into different crank angle steps which are given in table 3.33. In favor of gaining credible results of ignition timing and phasing of heat release, very small steps are applied between 300°[CA] and 400°[CA].

Table 3.33 : Time discretization .

Crank angle interval	Delta α
220 - 300	1
300 - 400	0.2
400 - 500	1

Applied boundary conditions are similar to those of verified SI engine, where the cylinder liner, cylinder head and piston bowl are considered as a wall and thermal boundary conditions with fixed temperatures are selected for them. Moreover, cylinder liner and cylinder head have velocity components of zero and are modelled as a stationary wall, while piston bowl is a moveable boundary and the situation of movement follows from mesh movement. Cyclically symmetric boundary condition is adopted to the radius surface along the center axis of the segment mesh and for the segment simulations, the faces in polar direction are considered as an interface boundary and periodic inlet and outlet boundary conditions are used. Table 3.34 illustrates the utilized boundary conditions for HCCI engine simulation.

Table 3.34 : Utilized boundary conditions for HCCI engine.

Name of BC	Type of BC	
Axis	Symmetric	
Segment (sector)	Periodic inlet/outlet	
Cylinder head	Thermal BC with fixed temperatures	$430^{\circ}[K]$
Cylinder wall (liner)		$410^{\circ}[K]$
Piston crown		$450^{\circ}[K]$

For a HCCI engine, the load can be altered by changing the amount of inducted fuel (equivalence ratio) at constant airflow or by changing the amount of exhaust gases which are introduced into the cylinder like diesel engines. In favor of performing a reasonable comparison with the simulation results of conventional natural gas and gasoline fueled SI engines, which are presented and discussed in pervious sections, firstly both gasoline and HCCI engine are considered to operate under same load (IMEP) at engine speed of 1500 [rpm]. Then the effect of equivalence ratio variations on combustion process of HCCI engine at a fixed engine speed of 1500 [rpm] is investigated. Specified initial conditions for baseline simulation of HCCI engine and verified gasoline engine are summarized in Table 3.35.

Table 3.35 : Initial conditions of HCCI engine simulation.

Initial condition	SI engine	HCCI
Engine speed [rpm]	1500	1500
Pressure [bar]	0.536	1.2
Temperature [K]	360	360
Fuel type	gasoline/natural gas	natural gas
Equivalence ratio	1	0.35
Mass fraction of EGR	0.1	
EGR composition	1	0.5
Turbulence kinetic energy [m^2/s^2]	8	
Turbulence length scale [m]	0.003	
Laminar flame speed	Database	

The overall solution procedure and employed methods for solving the general conservation equations and linear equation systems are the same as SI engine and are described in section 2.2.2. The standard compressible k-ε turbulence model which is explained in section 2.5.2, with hybrid wall function is used for calculations and simulating the turbulent flow within the combustion chamber.

In this work, the eddy breakup combustion model is used for simulation of HCCI combustion. As described in section 2.6.2, this model is based on the ideas of the eddy dissipation concept, which assumes that the mean turbulent reaction rate is determined by the intermixing of cold reactants with hot combustion products.

In order to represent ignition more realistically, a semi-empirical multi-step model, HCCI model, is applied. This model is based on shell model which is originally developed by Halstead et al. (1975) to predict knocking in SI engines and later expanded for modeling diesel ignition by Kong et al. (1995). The shell model can be seen as a mathematical equation system in which the ignition properties of complex hydrocarbons can be described. The resultant reaction scheme comprises eight reactions between five generic species. In this reaction scheme, species that play a similar role in the ignition chemistry are combined and treated as a single entity. The reaction mechanism of shell model which is used in this work for the simulation of homogeneous charge compression ignition are as the following:

- Initiation

$$RH + O_2 \xrightarrow{\omega_i} 2R^* \tag{3.14}$$

- Propagation

$$R^* \xrightarrow{\omega_p} R^* + P \tag{3.15}$$

$$R^* \xrightarrow{\omega_1} R^* + B \tag{3.16}$$

$$R^* \xrightarrow{\omega_4} R^* + Q \tag{3.17}$$

$$R^* + Q \xrightarrow{\omega_2} R^* + B \tag{3.18}$$

- Branching

$$B \xrightarrow{\omega_b} 2R^* \tag{3.19}$$

- Linear termination

$$R^* \xrightarrow{\omega_3} I \tag{3.20}$$

- Quadratic termination

$$2R^* \xrightarrow{\omega_t} I \tag{3.21}$$

Where; RH represents a hydrocarbon molecule (hydrocarbon fuel), R^* describes a hydrocarbon radical, Q is unstable intermediate species and B is branch species. P designates products of combustion (CO, CO_2 and H_2O) and I is inactive (inert) species. The Shell model includes 26 parameters that must be adjusted in order to represent a particular fuel (Theobald and Cheng, 1987).

3.6.3 Simulation results

This part not only shows the results for natural gas fueled HCCI engine but also compares them with the previously simulated gasoline and natural gas fueled SI engines. For the sake of presenting a meaningful comparison with the simulation results of conventional natural gas and gasoline fueled SI engines, which are presented and discussed in pervious sections, firstly both gasoline and HCCI engine are considered to operate under the same load (IMEP=4.76[bar]) at engine speed of 1500 [rpm].

Figure 3.70 shows the in-cylinder pressure curves as a function of crank angle for gasoline fueled SI engine (SI-Gasoline), natural gas fueled SI engine (SI-NG) and

natural gas fueled HCCI engine (HCCI-NG). In case of HCCI engine, because the compression ratio is higher and the whole charge reacts simultaneously, the heat is released in a very short time, resulting in an intense pressure rise and higher peak pressure compared to the conventional SI engines. Notable distinctions concerning with the peak pressure value and the crank angle position corresponding to the in-cylinder peak pressure are exhibited with different engines. The peak pressure values of HCCI and SI engines and related crank angle positions are summarized in Table 3.36.

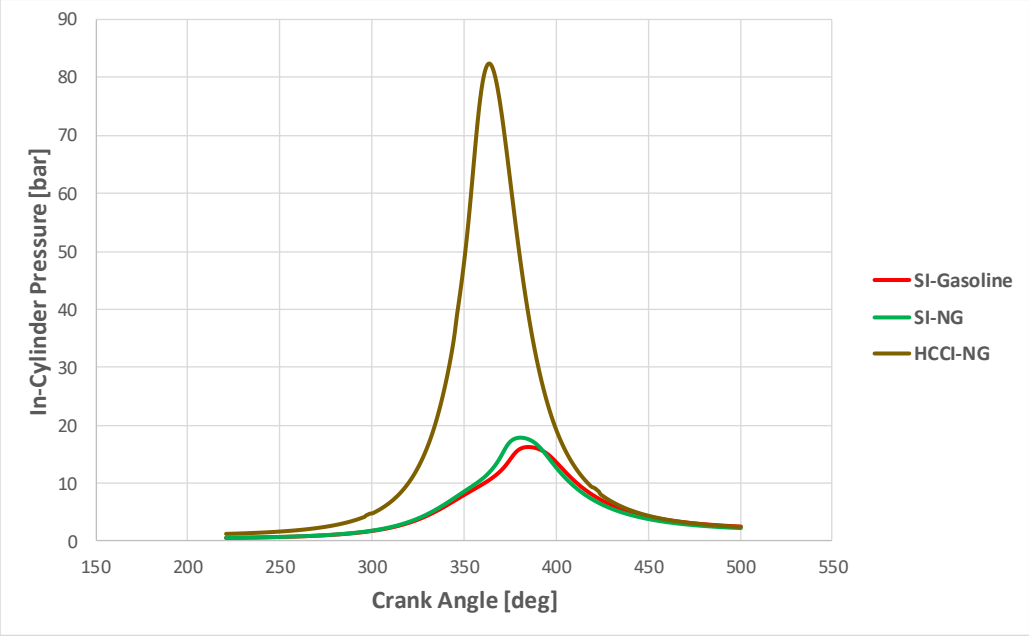


Figure 3.70 : In-cylinder pressure of SI-Gasoline, SI-NG and HCCI-NG engines.

Although both SI-Gasoline and HCCI-NG engines operate under same load (low load), considering Figure 3.70 and Table 3.36, fast combustion of HCCI causes very high and fast pressure rise and the peak pressure of HCCI combustion is four times higher than that of SI-Gasoline engine, and is approximately 3.6 times more than the peak pressure of SI-NG engine. The results reveal that the operating range of HCCI engine is bounded to moderate loads, by virtue of enormously rapid pressure rise (high combustion rate) occurred in high load conditions and resultant knock. This rapid rates of pressure rise and strong in-cylinder pressure waves can damage the engine over time and cause excessive noise.

Table 3.36 : Peak cylinder pressures and related crank angles for different engines.

Engine	Peak pressure [bar]	@ CAD
SI-gasoline	16.31	384
SI-NG	17.85	380
HCCI-NG	82.5	364

Figure 3.71 depicts the mean combustion temperatures of simulated engines as a function of crank angle. Since the SI engine operates with stoichiometric conditions, as the flame propagates within the combustion chamber, the charge mixture that burns earlier is compressed to higher temperatures after combustion. As a result, the temperature of a gas element burned just after spark discharge can reach over 2300 [K]. Inasmuch as the reactions of HCCI combustion occur simultaneously, the compression effect on the burned gases is absent. As it can be seen in Figure 3.71, as long as the HCCI engine operates with lean mixture, the overall combustion temperature is significantly reduced by the presence of excess air and the peak temperature of HCCI combustion is about 1620 [K]. The high levels of charge dilution in HCCI cause lower in-cylinder temperatures compared with SI engines, which is important in determining the emissions characteristics of HCCI engine.

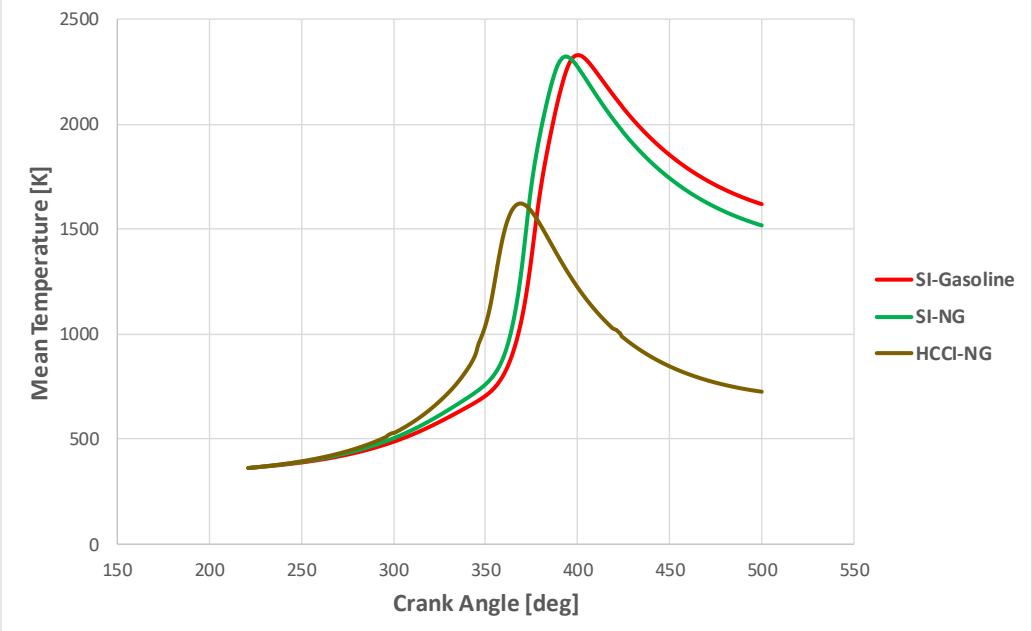


Figure 3.71 : In-cylinder mean temperature of SI-Gasoline, SI-NG and HCCI-NG engines.

Figure 3.72 demonstrates the heat release rate of simulated engines as a function of crank angle. The fuel-air mixture in the HCCI engine is generally well-mixed prior to the start of combustion. Compared to SI engines, the fuel chemistry plays more important role in determining combustion characteristics of HCCI engine. Generally in HCCI combustion, fuels with lower octane number or higher cetane number, such as diesel, display two-stage ignition, while fuels with higher octane number or gasoline-type fuels, such as natural gas, present single-stage ignition behavior (Baumgarten, 2010).

The heat release of SI engine combustion is characterized by a thin flame front which separates the cylinder into two zones. The zone behind the flame front contains combustion products and the zone that the flame front preceding, contains premixed fuel and air. Thus, the heat release is limited to the reaction zone within the flame front. While the HCCI combustion is characterized by simultaneous combustion throughout the combustion chamber allowing all of the charge mixture to participate in the heat release process (Baumgarten, 2010). In another words, compared to the SI engine, where only a small part of the total mixture is part of the flame front and takes place in combustion process at the same time, the whole charge reacts at the same time in the case of HCCI combustion. Although the local temperatures are significantly lower than that of the flame front in SI engine (Figure 3.71), the HCCI combustion releases the heat from the entire charge more rapidly and uniformly.

Observing Figure 3.72, since the whole charge is involved simultaneously in the combustion process, heat release of HCCI combustion has shorter overall duration with higher peak value than the conventional ones and the majority of heat release occurs in a very short period. The rapid release of heat from the fast burning process in HCCI is one of the basic reasons for power output limitations of HCCI engine. Excessive rates of heat release and the accompanying excessive pressure rise rates can damage the engine over time.

Combustion timing in HCCI and many LTC engines is predominantly determined by the chemical kinetics. As a result, the entire time history of temperature, pressure, composition and other factors has an effect on determining ignition timing. This complex interaction of parameters makes combustion timing more difficult to control in HCCI in comparison with SI engines (Halstead et al., 1975; Kalghatgi and Head, 2004).

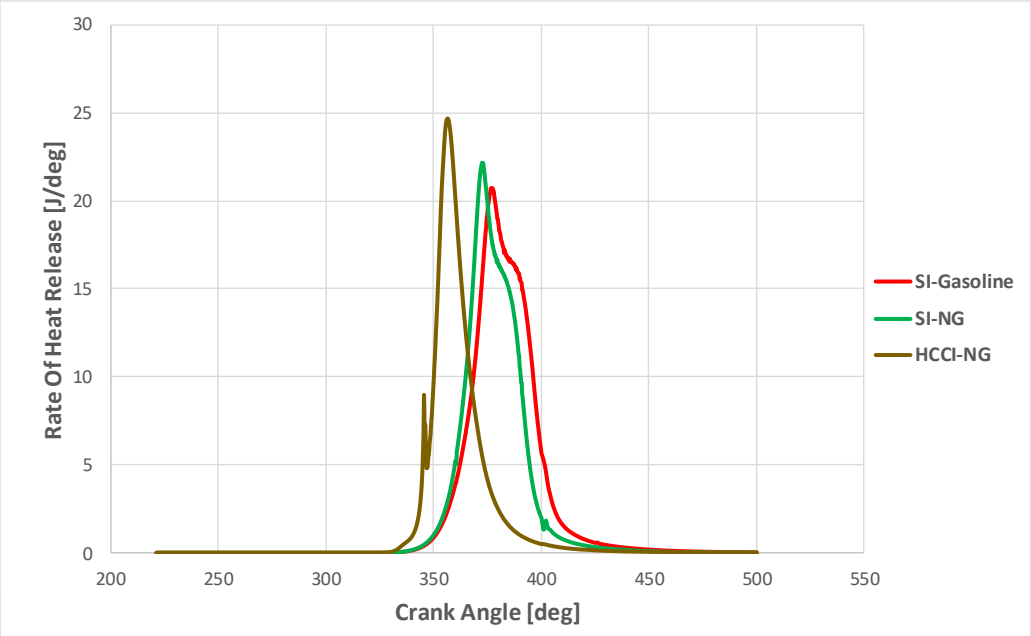


Figure 3.72 : Heat release rate of SI-Gasoline, SI-NG and HCCI-NG engines.

The HCCI engine lacks direct combustion phasing control approaches such as spark in SI engines and its ignition timing is controlled by the chemical kinetic reactions of the charge mixture during the compression stroke. In macroscopic view, it is mainly influenced by properties of fuel and the histories of in-cylinder pressure, temperature and concentration of fuel-air mixture. In this study, the crank angle of 10% accumulated heat release is used to evaluate the start of combustion and the interval between 10% accumulated heat release and 90% accumulated heat release is defined as the combustion duration. Calculated position of SOC and combustion durations for different engines are listed in Table 3.37.

Table 3.37 : Start of combustion position and combustion duration for different engines.

Engine	SOC [@CAD]	Combustion duration [deg]
HCCI-NG	349	27
SI-Gasoline	366	32
SI-NG	363	29

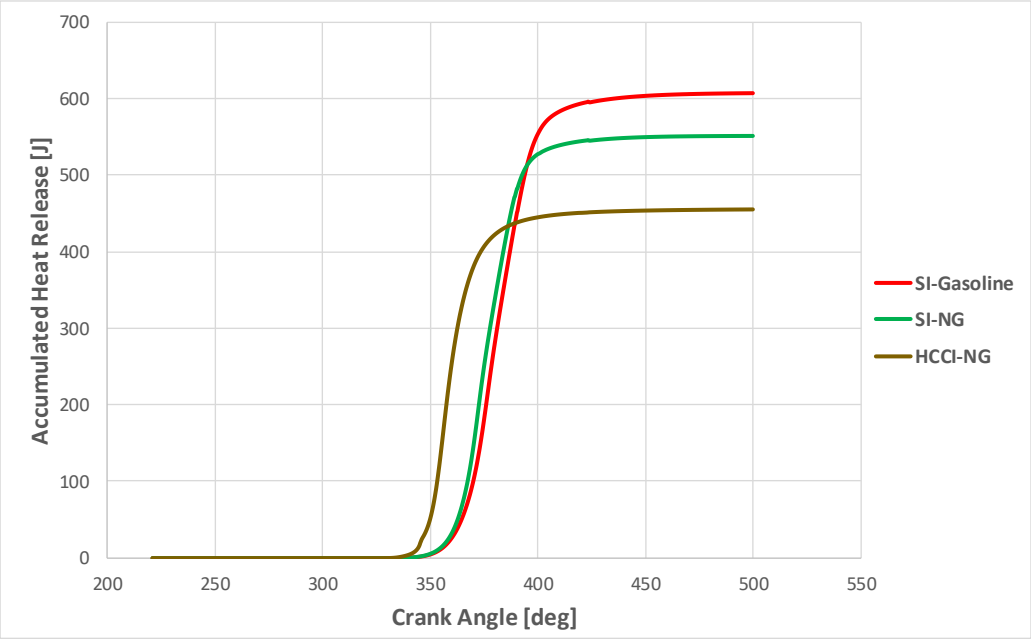
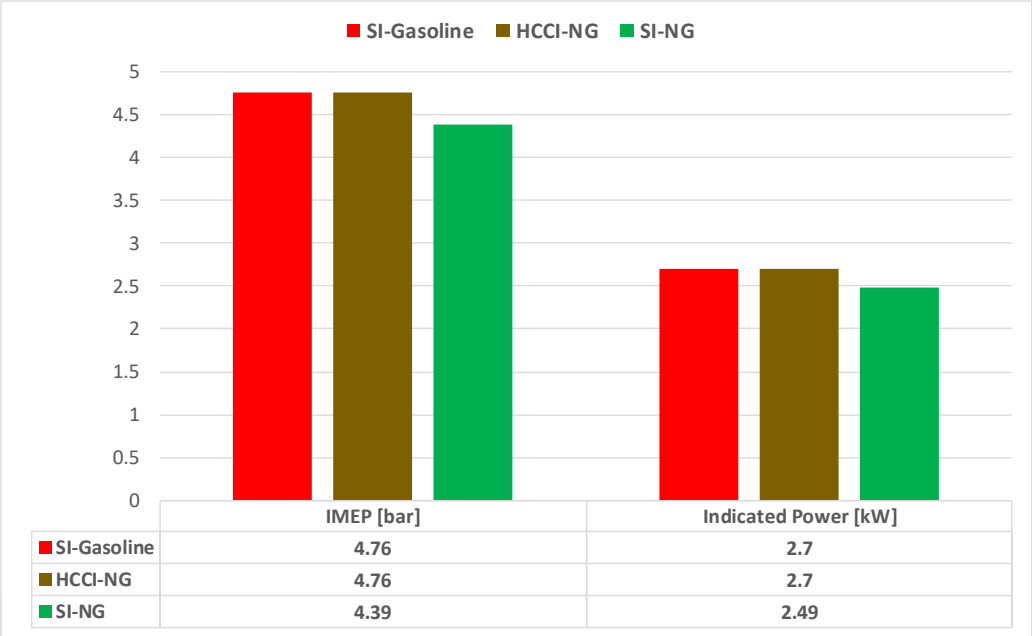


Figure 3.73 : Accumulated heat release of SI-Gasoline, SI-NG and HCCI-NG engines.

From the results, the start of HCCI combustion occurs when the in-cylinder gas temperature reaches a value of 1030 [K]. This required high temperature for autoignition of natural gas is attributed to its high octane number. As shown in Figure 3.73 and Table 3.37, HCCI-NG engine has the shortest duration of combustion among the engines. The combustion starts at 11 [CAD] BTDC and ends at 16 [CAD] ATDC, which means that a fast combustion occurs in a small volume and results in rapid pressure rise and higher peak pressure in comparison with SI engines in which, the combustion starts later and occurs in a larger volume.

As described before and shown in Figure 3.74, both SI-Gasoline and HCCI-NG are considered to operate under same load. It is observed in previous section that by using natural gas as fuel in SI engine the indicated power output and IMEP are reduced by about 8% compared to the gasoline fueled SI engine under similar initial conditions. The majority of this reduction coming from the lower volumetric efficiency associated with naturally aspirated natural gas engine.

Figure 3.75 illustrates the ISFC of simulated HCCI and SI engines. Because the HCCI engine can be run under the WOT (wide open throttle) condition even for a part load operation and the equivalence ratio varies with the load, just as it does in a diesel engine, the pumping losses are extremely lower than in an SI operation at



	IMEP [bar]	Indicated Power [kW]
SI-Gasoline	4.76	2.7
HCCI-NG	4.76	2.7
SI-NG	4.39	2.49

Figure 3.74 : IMEP and indicated power of SI-Gasoline, SI-NG and HCCI-NG engines.

low and intermediate loads. This contributes to the relatively high efficiency of HCCI combustion at the part load operation. Other advantages over SI operation are faster combustion and the reduction in heat loss due to the low combustion temperature. This higher thermal efficiency of HCCI engine is discussed in details in the following.

As it can be seen from Figure 3.75, the HCCI-NG presents the best fuel economy among the engines due to the above mentioned reasons. At part-load conditions because the HCCI engine operates with very lean mixture ($\phi = 0.355$) in absence of throttling and also delivers a power density similar to SI engine (2.7 [kW]), the ISFC of HCCI-NG engine is remarkably lower than that of SI-Gasoline and SI-NG engines. Under the condition with same engine speed of 1500 [rpm] and 4.76 [bar] of IMEP, the HCCI mode indicates the ISFC of 152.3 [g/kWh], which is approximately 37% lower than that of gasoline fueled SI engine and is lower by about 27% than the ISFC of natural gas fueled SI engine. The results prove that in comparison with SI engine, a noticeable improvement in fuel economy can be achieved by implementing the HCCI strategy.

Although SI engines use the Otto-cycle which is shown in Figure 3.76, in reality, combustion in Otto-cycle four stroke engine does not take place according to ideal cycle. The compression and expansion processes are not isentropic, since heat transfer

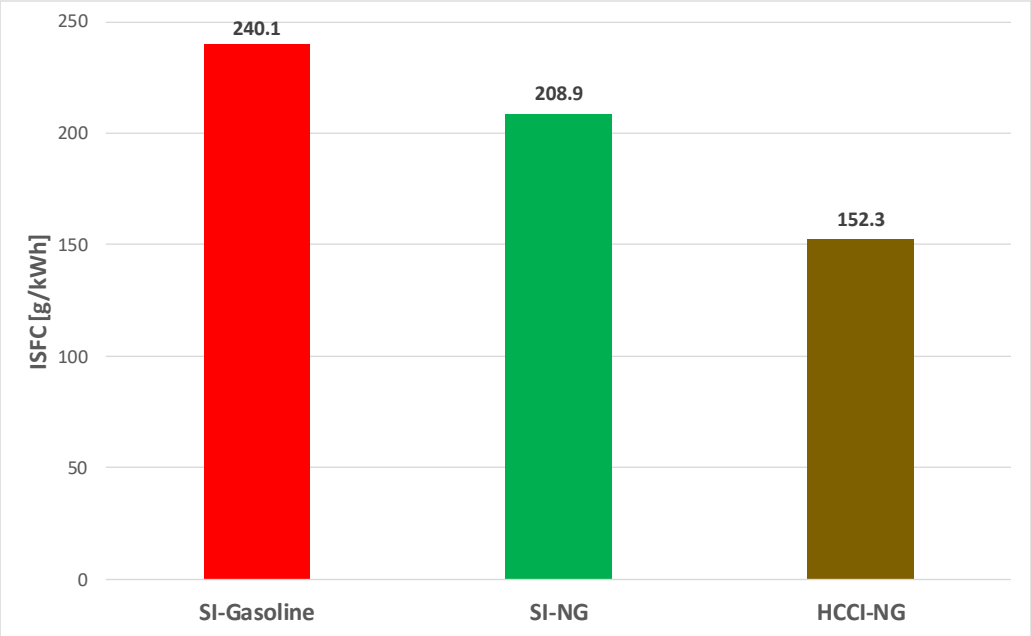


Figure 3.75 : ISFC of SI-Gasoline, SI-NG and HCCI-NG engines.

occurs through the cylinder walls, head and piston. Moreover, the combustion process does not happen as a constant volume process since a small flame kernel is created by the spark, which gradually propagates outwards the cylinder walls and during this flame propagation process the piston continues to move causing variation of the cylinder volume. Additionally, the heat rejection process is also not a constant volume process, and besides that, the ideal cycle does not capture the pumping work required for the induction and exhaust strokes. Typical compression ratios for Otto-cycle engines are between 8:1 and 12:1 for SI engines, which is equal to 9.1 in this study. This compression ratio has a noticeable effect on the thermal efficiency of Otto cycle, that is represented as:

$$\eta_{th,Otto} = 1 - \frac{1}{\mathrm{CR}^{\gamma-1}} \tag{3.22}$$

Therefore, thermal efficiency can be increased by increasing the compression ratio, CR, or the ratio of specific heats of the in-cylinder gases, γ. The ratio of specific heats is not easily subject to significant variation, hence the only practical way of increasing thermal efficiency is through higher compression ratios. However, the compression ratio is limited by the onset of knocking.

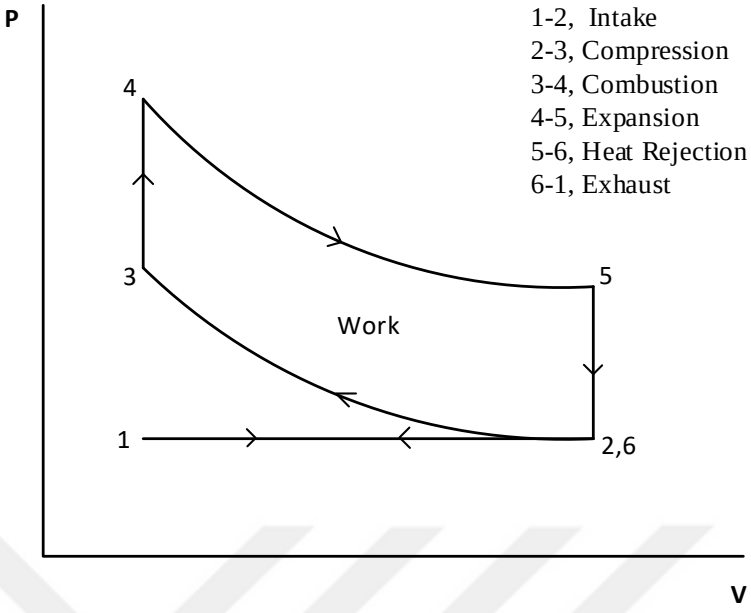


Figure 3.76 : P-V diagram of ideal Otto-cycle (NASA, 2015).

HCCI on the other hand follows a thermodynamic process that is even closer to the ideal Otto cycle than SI engines. The fundamental difference between SI and HCCI lies in the fact that the burning rate of SI engines is controlled by a gradual flame propagation process, while the burning rate of HCCI combustion is controlled by the fast chemical kinetics of an autoignition process. As a consequence, the heat addition thermodynamic process takes place under conditions that are much closer to a constant volume process.

Given that the HCCI engine can be approximated with the Otto cycle, the thermal efficiency can be estimated using the Otto cycle efficiency relationship in Eq (3.22). The higher compression ratio of HCCI engine, which is 17.5:1 in this study, compared to SI engine (9.1:1) is one reason for its ability to achieve higher thermal efficiency similar to CI engines. Another factor that contributes to the high efficiency of HCCI engine is that the intake air is not throttled for power output control. As a result, HCCI engine does not suffer from the throttling losses which affect part-load operating conditions in SI engines.

One of the most important benefits of HCCI combustion is the possibility of dramatic reduction of NO_x and soot emissions simultaneously. Nitrogen oxide emissions, NO and NO_2, are predominantly formed through the Zeldovich chemical path through the

Table 3.38 : NO_x emissions of different engines.

Engine	NO_x [g/kWh]
SI-Gasoline	4.492
SI-NG	3.893
HCCI-NG	0.0051

breakdown of the strong triple bond between nitrogen atoms in N_2. This chemical pathway has an activation temperature near 1800 [K] (Zeldovich et al., 1947).
Given that the HCCI combustion takes advantage of highly diluted charges (lean mixture), peak in-cylinder temperature remains very low in comparison to SI engines, as shown in Figure 3.71. As a result, HCCI engine produces tremendously lower levels of NO_x emissions compared to SI engines which are shown in Table 3.38. Additionally, since soot is formed in the rich regions of fuel, it is not an important concern for engines in which the fuel is well mixed prior to ignition. Especially in case of HCCI engine, in which a uniform lean mixture is combusted, extremely low levels of soot emissions, near zero, is produced.

One common tool for understanding the different operating and emissions characteristics of conventional SI, conventional diesel and HCCI engines, called $\phi-$T plot, is used in this section. Figure 3.77, shows such a plot and labels the regions for SI, diesel and HCCI combustion, along with the different regions of NO_x and soot formation. As shown in Figure, SI combustion occurs in a high temperature region near an equivalence ratio of 1, where high NO_x formation occurs. Conventional diesel combustion begins at high equivalence ratios where soot formation occurs and transitions towards high temperature combustion where NO_x formation occurs.
Figure 3.78 depicts the $\phi-$T plot of simulated HCCI-NG engine, which is prepared by ESE Diesel tool. As it can be seen in Figure 3.78, since HCCI combustion occurs at leaner equivalence ratio ($\phi = 0.355$) and where sufficient charge dilution allows for lower temperatures (peak temperature of 1620 [K]), this low temperature combustion strategy avoids the regions of high soot and NO_x formation. The operating region of HCCI-NG engine shown in this plot, is in quite well agreement with Figure 3.77.

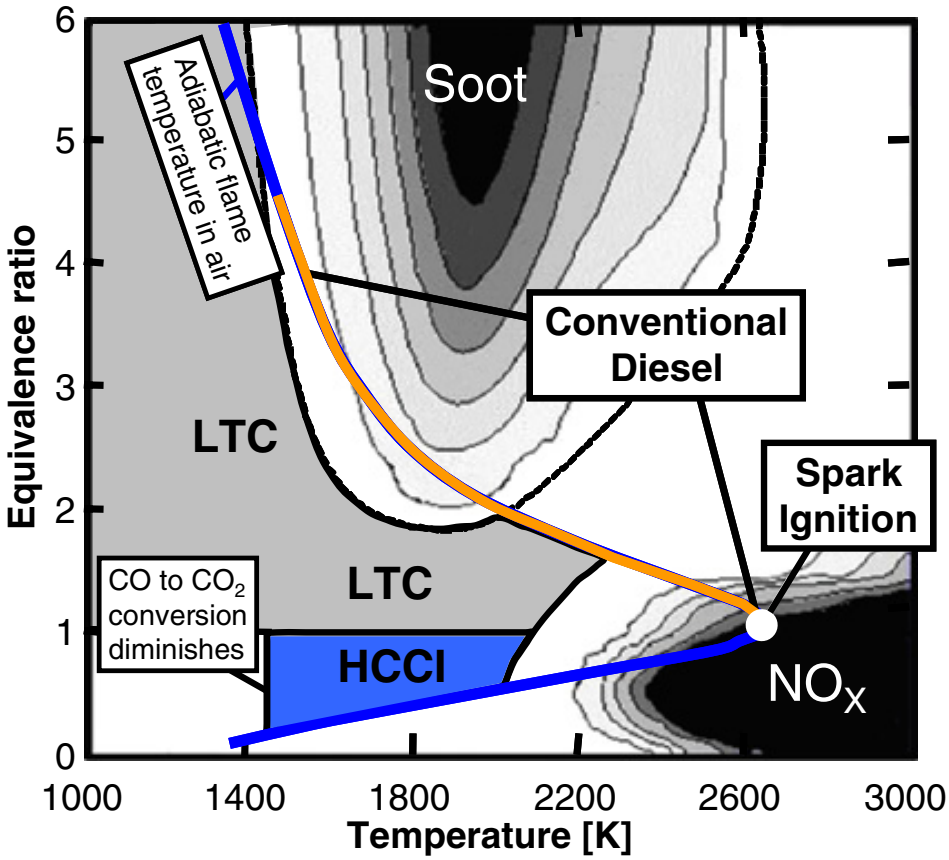


Figure 3.77 : LTC, SI, conventional CI and HCCI combustion regions on a ϕ-T map with NO_x -soot contour, adapted from (Kamimoto and Bae, 1988; Dec, 2009).

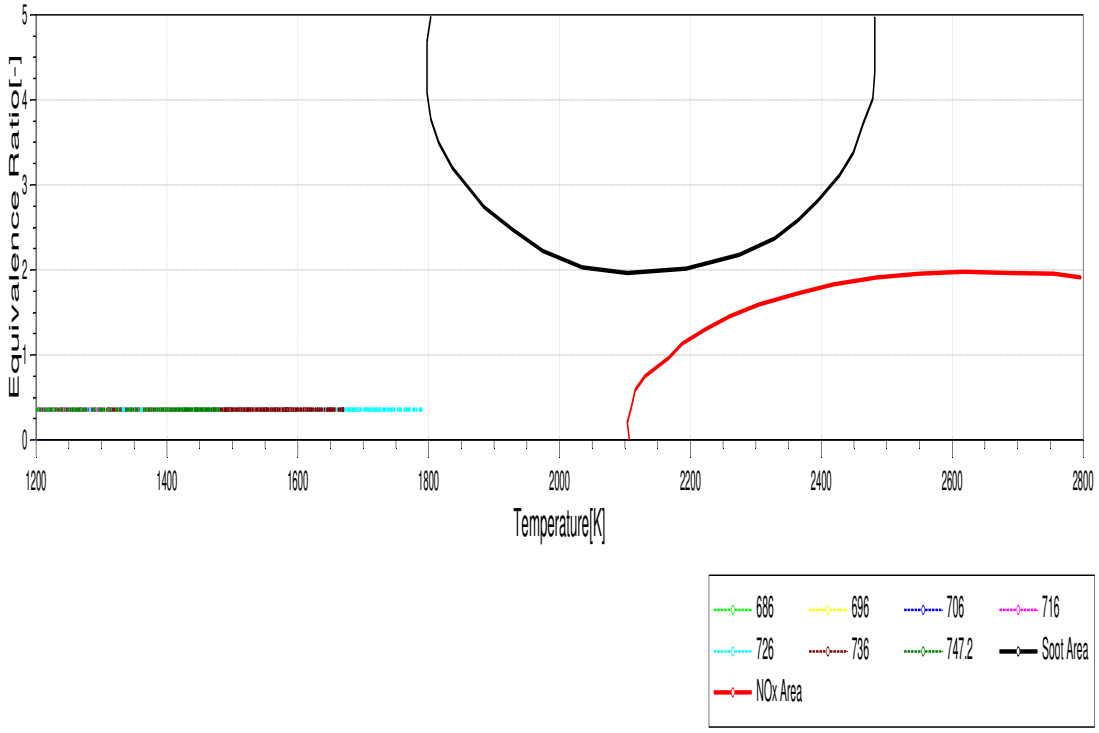


Figure 3.78 : ϕ-T plot of HCCI-NG engine.

In-cylinder temperature is a key factor in determining unburned HC emissions characteristics and lower temperatures generally cause higher emissions of unburned HC. HC emissions increase because of low combustion temperatures and corresponding incomplete oxidations. The unburned HC emissions of simulated engines are summarized in Table 3.39.

The results indicate that the unburned HC emissions of HCCI-NG engine are drastically higher than those of SI-Gasoline and SI-NG engines. As described, this increase is attributed to the burned gas temperature which is too low to consume much of fuel and results in incomplete oxidations, and hence significant increase in HC emissions compared to conventional combustion. However, these levels of HC emissions can be easily reduced by means of a common oxidation catalytic convertor.

Table 3.39 : Unburned hydrocarbon emissions of simulated engines.

Engine	UHC [g/kWh]
SI-Gasoline	2.22E-04
SI-NG	4.71E-05
HCCI-NG	0.37

Figure 3.79 shows the in-cylinder distributions of temperature and unburned equivalence ratio at different crank angles for HCCI-NG engine. As the ignition is initiated, methane is quickly consumed and release lots of heat energy which builds up the high temperature center as seen in the temperature contours. As the combustion continues, colder regions near the walls are heated by the convection with hot center regions, and the natural gas mass in those zones start to react until all of them are oxidized or temperature becomes too low to sustain the oxidation as the expansion goes on. As it can be seen from Figure 3.79, although the name HCCI indicates a homogeneous charge, there are always some thermal inhomogeneities and in many cases it is desirable to introduce some degree of charge-mixture stratification.

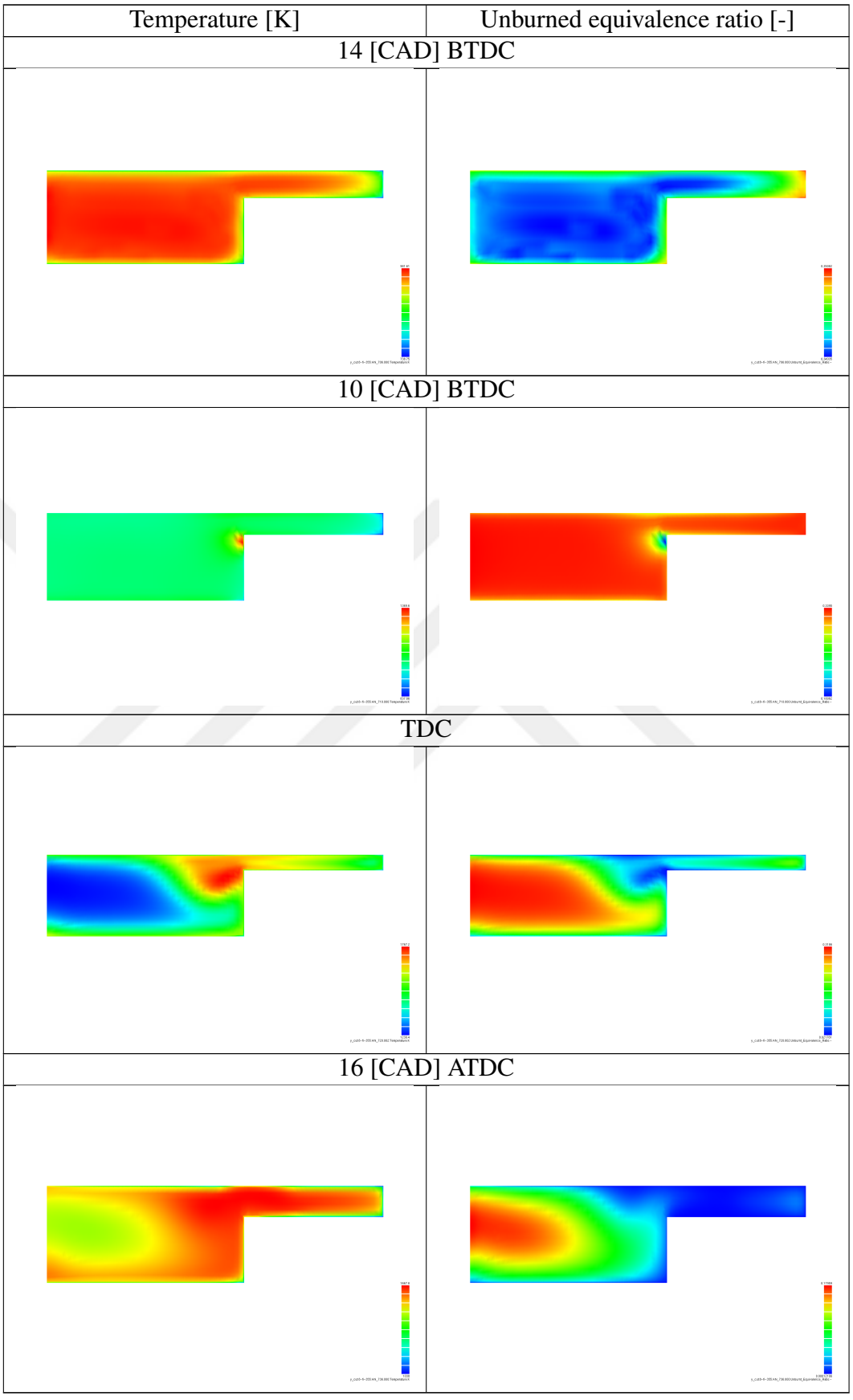


Figure 3.79 : In-cylinder distributions of temperature and unburned equivalence ratio for HCCI-NG engine.

Specific engine outputs which are obtained by analyzing the simulation results via ESE Diesel analyser tool are summarized in Table 3.40.

Table 3.40 : Specific outputs of different engines.

	SI-Gasoline	HCCI-NG	SI-NG
Break mean effective pressure BMEP [bar]	3	3	2.63
Combustion Noise - A + CAV Filter [dB]	80.98	80.07	79.76
Combustion Noise - A Filter [dB]	188.65	202.45	189.29
Combustion Noise - CAV Filter [dB]	80.33	84.21	79.25
Combustion Noise [dB]	207.31	220.58	207.94
Excess air ratio [-]	1	2.82	1
Friction mean effective pressure FMEP [bar]	1.76	1.76	1.76
Indicated mean effective pressure IMEP [bar]	4.76	4.76	4.39
Indicated power [kW]	2.7	2.7	2.49
Indicated specific power [kW/l]	5.95	5.96	5.49
Indicated specific torque [Nm/l]	37.87	37.91	34.97
Indicated torque [Nm]	17.19	17.21	15.87
Mean mass [kg]	2.49E-04	5.01E-04	2.28E-04
Mechanical efficiency [-]	0.63	0.63	0.6
Total mass at start of high pressure cycle [kg]	2.53E-04	5.01E-04	2.32E-04
Volume displacement [m$\hat{3}$]	4.54E-04	4.54E-04	4.54E-04

In summary, proper operation of an HCCI combustion engine with natural gas is difficult mainly because of the fuel resistance to auto-ignition. Natural gas combustion in HCCI combustion engines needs high initial temperatures, achieved by high levels of pre-heating or a high compression ratio. In addition, because of the high rate of heat release, the mixture has to be heavily diluted with EGR or excess air to prevent combustion knocking. As a result, natural gas HCCI combustion is more difficult to achieve in comparison to that of other liquid fuels.

In HCCI, the combustion process and the burn rate are controlled by chemical kinetics, and thus high compression ratio is used to elevate the fuel-air temperature to levels at which the chemical reactions proceed quickly enough to produce autoignition.

The high levels of charge dilution typical in HCCI also cause lower in-cylinder temperatures compared with SI or diesel engines, which is important in determining the emissions characteristics of HCCI engines. In-cylinder temperatures are typically sufficiently low to avoid significant NO_x formation and the premixed nature of HCCI allows very low soot emissions, near zero. However, the low in-cylinder temperatures also cause higher emissions of unburned hydrocarbons.

For stable combustion, the operating range of an HCCI engine is significantly narrower than that of conventional engines. Because of the nature of combustion, a mixed charge ignites across the entire combustion chamber above the high load limit, thereby increasing the pressure rising rate, noise and vibration. Below the low load limit, the ignition delay is prolonged so that misfire can occur because of the low equivalence ratio and the low exhaust gas temperature. This narrow operating range of HCCI is one of the reasons that it cannot be adapted to real engines and even if it is adapted, the engine has to operate with both HCCI and SI modes, so its fuel economy effect is significantly small.

4. SIMULATION OF LOW TEMPERATURE COMBUSTION DIESEL ENGINE

In this chapter, first a conventional single cylinder diesel engine under full load condition at engine speed of 1500[rpm] is simulated with AVL FIRE® CFD code. This engine is assumed to be the reference engine. Then a parametric study of individual influence of engine load and combined effects of exhaust gas recirculation and injected fuel mass on the performance, combustion and exhaust emissions of the simulated conventional diesel engine is carried out at a constant engine speed of 1500 [rpm]. Furthermore, in the second part of this chapter, in order to achieve the partially premixed compression ignition and lower temperature combustion of diesel engine, the effects of multiple injection strategies including first injection quantity and first injection duration on performance and exhaust emissions of diesel engine are studied. The effects of various combinations of EGR together with split injection strategy are also investigated and compared with the simulation results of single injection diesel engine.

4.1 Introduction

In compression ignition engines, air alone is inducted into the cylinder and the fuel is injected directly into the combustion chamber just before the combustion process is required to start. In contrast to SI engine, the air flow at given speed of CI engine is essentially unchanged, load control is achieved by varying the amount of injected fuel per cycle and combustion start is controlled by the start of injection. The compression ratio of CI engines is much higher than that of conventional SI engines, depending on the engine type and whether the engine is naturally aspirated or turbo-charged, is in the range of 12 to 24. However, the valve timings used are similar to those of SI engines. The combustion process of conventional diesel engine is characterized by heterogeneous mixture formation and combustion. In case of conventional CI engines, fuel is directly injected under higher pressure, usually shortly before the TDC, into the cylinder. The liquid fuel entering the combustion chamber atomizes into small

droplets, vaporizes and then mixes with air, resulting in a heterogeneous mixture of fuel and air. Combustion is initiated by an autoignition process as a result of high temperatures and pressures which are above the ignition point of fuel. In conventional diesel combustion process, usually there is a very short time available for mixture formation, therefore after a short delay period, spontaneous ignition of the nonuniform air-fuel mixture parts initiates the combustion and in-cylinder pressure increases above the nonfiring engine levels. Thus, a fast injection and an as good as possible atomization of the fuel are prerequisites for a rapid and intensive mixing of fuel and air.

The spray generated during injection can be roughly subdivided into two regions, one with a dense spray near the nozzle exit and a thin spray region further down the flow. The first decomposition of the cohesive fuel spray into ligaments and droplets is called primary spray breakup. In modern high-pressure injection systems, cavitation and turbulence are the most important mechanisms of primary spray breakup (Arcoumanis et al., 1998). Break-up of already existing droplets into smaller droplets due to aerodynamic forces caused by the relative speed between droplet and the environment is called secondary spray breakup. In addition, droplets can collide with each other and coalesce. The droplets are heated up as a result of convective heat transfer and temperature radiation of the hot chamber walls, and the fuel finally begins to evaporate. Besides the physical properties and the combustion chamber conditions (pressure, temperature), the fuel evaporation rate is determined by the size of the droplet surface formed and thus depends on primary and secondary breakup as well as the amount of air entrained into the spray.

The period of time between the start of fuel injection into the cylinder and the combustion start is called ignition delay. The physical and chemical processes occurring during this time are very complex. The essential physical processes are the atomization of fuel, vaporization and mixing of fuel vapor with air, to form a combustible mixture. The ignition delay can be controlled by means of temperature and pressure at the start of injection, which in turn depend on the intake temperature and pressure, compression ratio, start of injection and the wall temperatures. Furthermore, the ignitability of the fuel (cetane number), injection pressure, geometry of nozzle holes and in-cylinder flow significantly affect the ignition delay duration.

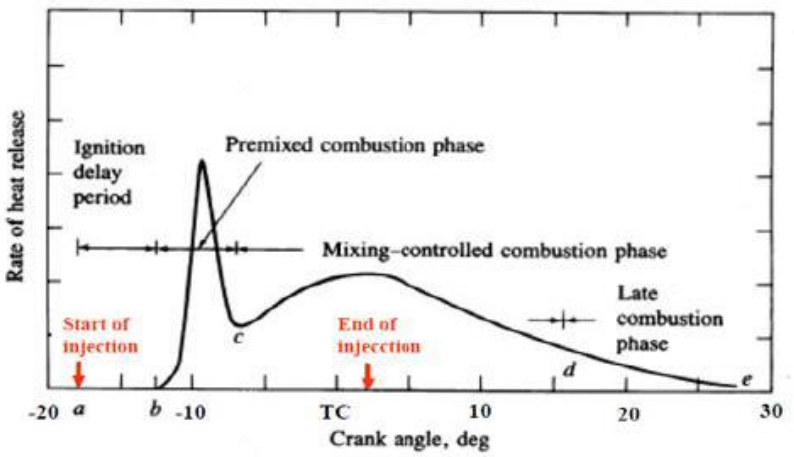


Figure 4.1 : Identifying diesel combustion phases, adapted from (Heywood, 1988).

Figure 4.1 provides a schematic representation of combustion sequence of a diesel engine with direct injection. As it can be seen, the sequence of diesel engine combustion can be subdivided into three phases.

- Phase 1: initial premixed combustion or rapid combustion phase
- Phase 2: main combustion or mixing-controlled combustion phase
- Phase 3: post-combustion or late combustion phase

The first phase occurs immediately after ignition. The fuel injected during the ignition delay mixes with air in the combustion chamber and forms a nearly homogeneous and reactive mixture. After the ignition delay, which is physically and chemically controlled, this mixture burns rapidly in a few crank angle degrees. In case of initial premixed combustion phase, the rate of heat release is controlled by the speed of the chemical reactions and amount of fuel-air mixture formed during the ignition delay. The combustion noise of diesel engines is caused by the high speed of pressure rise at the start of combustion.

In the second phase, heat release rate is primarily controlled by the turbulent mixing processes between fuel and air, therefore also called mixture-controlled combustion. Figure 4.2 shows a cross-section through a reacting diesel injection spray following the conceptual model of Dec (1997) and Flynn et al. (1999). Liquid fuel atomization,

droplet vaporization, mixing of fuel vapor with air, combustion and pollutant formation all take place simultaneously in this phase. The air ratio in the spray increases both with increasing distance to the injection nozzle as well as with the distance to the spray axis. A diffusion flame is formed around the injection spray on an iso-surface with a stoichiometric air fuel ratio. Upstream of the liquid penetration length, a rich mixture zone is formed which leads to partial oxidation of the fuel. The partially oxidized products of the rich premixed combustion and the particles formed move further downstream and are transported into the diffusion flame, where they are completely oxidized into carbon dioxide and water. The rate of heat release may reach a second peak in this phase, which is usually lower than the first peak and decreases as this phase progresses.

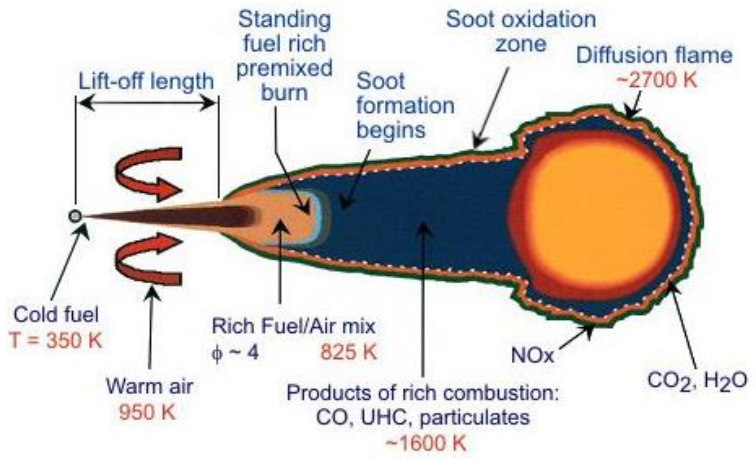


Figure 4.2 : Conceptional model of diesel combustion, (Dec, 1997; Flynn et al., 1999).

Finally, as the injection process is finished, no additional momentum is added to the spray by the injection and the flame jet structure evolves into a pocket of rich premixed products surrounded by a diffusion flame. The exact properties of this zone depend on the injection system. If the nozzle needle closes very quickly, then the last fuel parcels still have high speed, so that they have a similar combustion sequence as in main combustion. On the other hand, a slow closure of the needle leads to low speeds of the last fuel parcels with low amount of oxygen entrained and consequently increases formation of soot. The kinetics of the final combustion phase become slower as the temperature of cylinder gases decrease during expansion so again the combustion is

controlled chemically. This phase is extremely important for the oxidation of the previously formed soot particulate.

In comparison with the conventional SI engines, since the injection commences just before combustion starts, there is no knock limit as in the SI engine and hence a higher compression ratio can be used in CI engine. Consequently due to the higher compression ratios, CI engines perform higher thermal efficiencies and better fuel economy. However, these advantages come with some drawbacks such as higher noise levels, more limited engine speed, diminished start ability and higher levels of NO_x and soot emissions.

Although diesel engines are usually operated with a globally lean air-fuel ratio, direct injection leads to different mixture regions ranging from very lean through stoichiometric to very rich mixture ratios. Such stratification of mixture inescapably leads to the formation of exhaust emissions, especially soot and NO_x emissions.

In order to better understand of soot and NO_x formation regions, an equivalence ratio-temperature (ϕ-T) map was developed by Kamimoto and Bae (1988). Figure 4.3 shows such a plot and labels the regions for SI, diesel, HCCI and PCCI combustion, along with the different regions of NO_x and soot formation. It is well known that the equivalence ratio and temperature region in which NO_x is formed are different from those of soot formation. NO_x emissions are formed in high temperature regions with low equivalence ratio, while soot emission is formed in high equivalence ratio regions with specific temperature. As described, conventional diesel combustion includes regions with different equivalence ratio. A vert rich region at the spray center, a lean region in the vicinity of the spray and further down the flow and a stoichiometric region which lies between the above two regions. By considering the soot and NO_x formation regions and charge stratification of conventional diesel engine, it would be difficult to reduce the both exhaust emissions simultaneously.

For the sake of simultaneously reduction of NO_x and soot emissions, low temperature combustion strategies have been widely studied by numerous researchers(section1.2). The ϕ-T plot (local equivalence ratio versus local temperature) is a convenient way of depicting the different CI combustion concepts. These advanced combustion modes decrease the combustion temperature and over-rich regions by introducing fuel at early stages of cycle to form a near-homogenous lean mixture. This lean and uniform

mixture along with high levels of EGR lead to simultaneously reduction of soot and NO_x emissions.

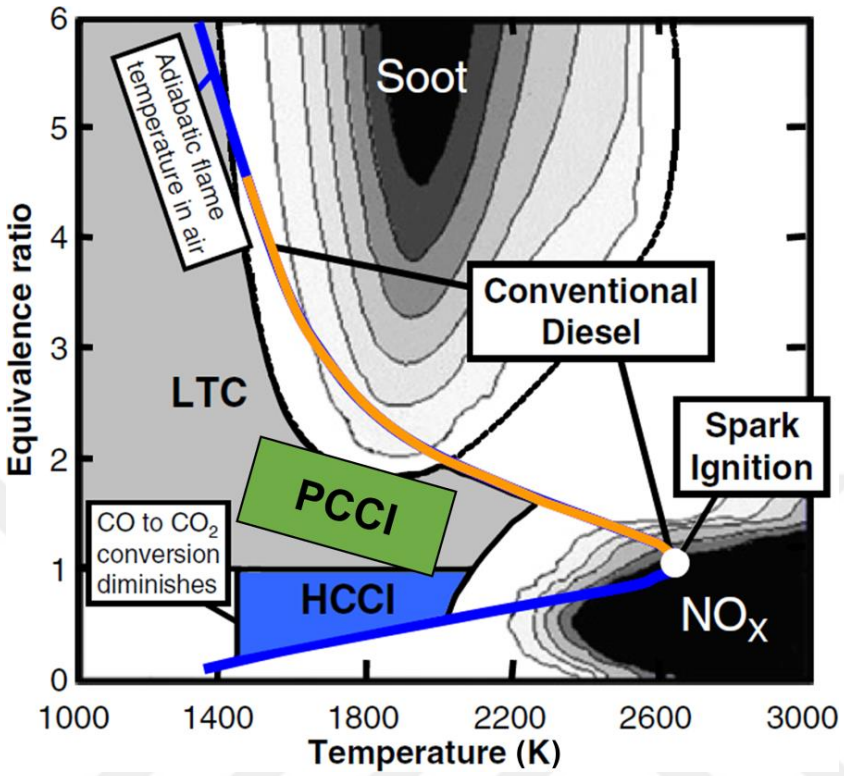


Figure 4.3 : LTC, SI and conventional CI combustion regions on a ϕ-T map with NO_x -soot contour, (Kamimoto and Bae, 1988).

4.2 Conventional DI Diesel Engine Modeling

In the following, first the pre-processing of baseline simulation including adopted computational grids, initial and boundary conditions, combustion model and spray submodels is briefly restated. Then the effects of injected fuel mass and EGR on performance and engine-out emissions of simulated diesel engine are investigated.

4.2.1 Pre-processing of simulation

In respect of generating the sector mesh, general engine parameters and combustion chamber geometries which are given in Table 4.1, are imported into ESE Diesel tool. The geometries that are used for meshing the combustion chamber and piston bowl are the same as previously employed geometries of HCCI engine (section 1.2.2.2), thus the compression ratio of diesel engine is also equal to 17.5. The number of boundary layers, its thickness and average cell size are listed in Table 4.2. The applied valve

timings are similar to those of simulated SI and HCCI engines. Based on simulation condition, the generation of the grids is required to cover the simulation period between intake valve closing (IVC) and exhaust valve opening (EVO). The combustion chamber of engine is considered as a closed thermodynamic system and the calculations are carried out from the intake valve closing (IVC) at 220°[CA] to exhaust valve opening (EVO) at 500°[CA], which are summarized in Table 4.1.

Table 4.1 : Simulated diesel engine specifications .

Engine type	Four stroke , Compression ignition
Fuel	Diesel
Number of cylinders	1
Bore [mm]	85
Stroke [mm]	80
Displacement [cm^3]	454
Compression ratio	17.5:1
Connecting rod length [mm]	145
Intake valve opening	16 [CAD] BTDC
Intake valve closing	40 [CAD] ABDC
Exhaust valve opening	40 [CAD] BBDC
Exhaust valve closing	16 [CAD] ATDC

Table 4.2 : Computational grids specification used for diesel engine sector mesh generation.

Average cell size [mm]	0.75
Number of boundary layers	2
Thickness of boundary layer [mm]	0.2
Maximum number of cells	36,904

Figures 4.4 and 4.5 respectively, depict the grid resolution and the 3D sector mesh of DI diesel engine that is generated with AVL FIRE® ESE Diesel tool to simulate the combustion process from the IVC at 220°[CA] to EVO at 500°[CA] .

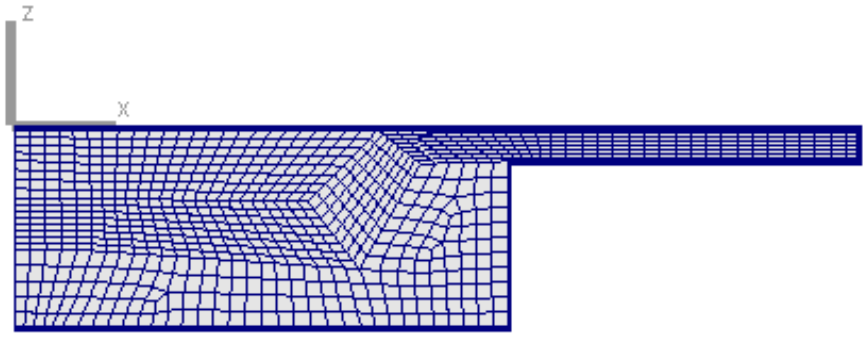


Figure 4.4 : Grid resolution.

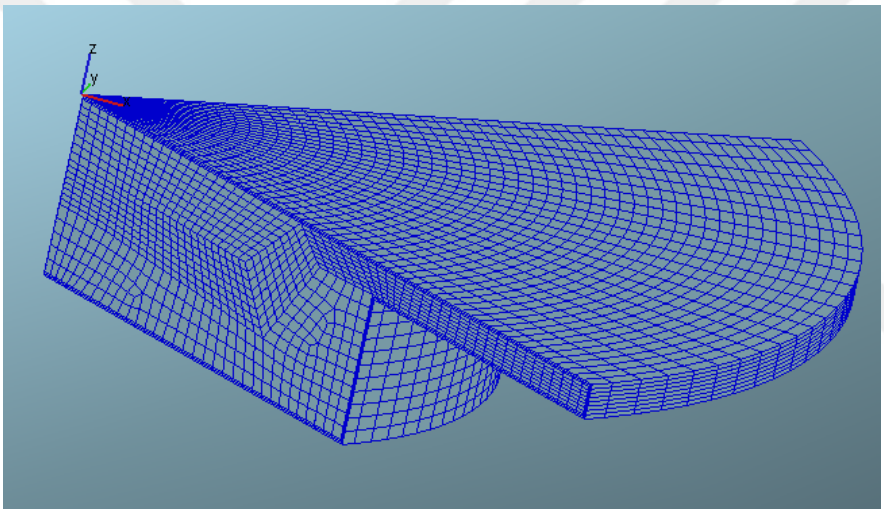


Figure 4.5 : Generated 3D sector mesh used in simulations (72° sector).

In order to obtain accurate simulation results, the operating interval is divided into different crank angle steps which are given in table 4.3. In favor of gaining authentic results of ignition timing, injection process and phasing of heat release, very small steps are applied between 290°[CA] and 440°[CA].

Table 4.3 : Time discretization .

Crank angle interval	Delta α
220 - 290	1
290 - 440	0.2
440 - 500	1

Furthermore, cyclically symmetric boundary condition for the crank-angle interval is adopted to the axis. For the segment simulations, periodic inlet and outlet boundary conditions are used, where mass, momentum and energy could translate from one side of the sector to the other side. Thermal boundary condition is set to the wall, where the temperature of the walls, including cylinder head, cylinder wall and piston crown, is fixed and considered as isothermal. The surface roughness of all surfaces is set to zero. Table 4.4 illustrates the utilized boundary conditions for diesel engine simulation.

Table 4.4 : Utilized boundary conditions for simulation of diesel engine.

Name of BC	Type of BC	
Axis	Symmetric	
Segment (sector)	Periodic inlet/outlet	
Cylinder head	Thermal BC with fixed temperatures	$520^{\circ}[K]$
Cylinder wall (liner)		$470^{\circ}[K]$
Piston crown		$570^{\circ}[K]$

However there is not any available experimental data for this engine, by considering that the engine is operated under full load condition, reasonable values for initial temperature, pressure and turbulence kinetic energy are chosen and the air properties are considered as ideal gas. Diesel with a composition of $C_{13}H_{23}$ is chosen as fuel, and since it is injected directly into the combustion chamber during the compression stroke, the initial equivalence ratio is set to zero and the spray module is activated in the solver GUI of the FIRE Workflow Manager. Another parameter that should be specified in this step is the amount of EGR. For this purpose, it is assumed that the mass fraction of EGR has a value of 0.05 and since diesel engine usually operates with lean air-fuel mixture, there is excess oxygen in exhaust gases, and hence EGR composition is set to 0.6. So the amount of stock EGR in combustion chamber is equal to 5% for the baseline simulation.

The swirl flow is a rotating flow around cylinder axis. it generates by the geometry of intake ports and by the geometry of valve seats. swirl is used in diesels to promote mixing between the inducted air charge and injected fuel. swirl is also used to speed up the combustion process increasing amount of air swirl within the cylinder are used

in direct injection diesel engines as engine size decreases and maximum engine speed increases, to achieve adequately fast fuel-air mixing rates. In this regard, it is assumed that the swirl has a value of 2500 [1/min] for all simulations. Taken initial conditions for baseline simulation of diesel engine are summarized in Table 4.5.

Table 4.5 : Initial conditions for baseline simulation of diesel engine.

Initial condition	Taken value
Pressure [bar]	1.3
Temperature [kelvin]	330
Fuel type	Diesel ($C_{13}H_{23}$)
Equivalence ratio	0
Mass fraction of EGR	0.05
EGR composition	0.6
Swirl [1/min]	2500
Turbulence kinetic energy [m^2/s^2]	10
Turbulence length scale [m]	0.004
Laminar flame speed	Database

The overall solution procedure and employed methods for solving the general conservation equations and linear equation systems are described in section 2.2.2. The standard compressible k-ε turbulence model which was explained in section 2.5.2, with hybrid wall function is used for calculations and simulating the turbulent flow within the combustion chamber.

For modeling the diesel engine combustion, the three-zone extended coherent flame modeling (ECFM-3Z) approach is adopted in the solver. As described in section 2.6.2, this combustion model is based on a flame surface density transport equation and a mixing model that can describe inhomogeneous turbulent premixed and diffusion combustion. Moreover, it is coupled with an improved burnt gas chemistry description compared to ECFM. For prediction of the auto-ignition delay, the two-stage model is employed where the auto-ignition delay time for cool flame ignition and main ignition is interpolated from tabulated values. This is the recommended choice and tabulated

ignition data are stored in look-up tables that are available in AVL FIRE® for different fuels, generated based upon chemical kinetic calculations adopting complex reaction schemes. The tabulated values are stored as functions of pressure, temperature, fuel/air equivalence ratio and residual gas content. The range of these parameters has been chosen in a way to be able to cover the relevant in-cylinder pressure, temperature and charge-mixture composition conditions prior to combustion. For the actual determination of the auto-ignition delay time in the CFD simulation, a transport equation for an auto-ignition indicator species is solved with the formation rate derived from the tabulated values. Once the local value of the indicator species attains a certain threshold value, auto-ignition is initiated. Fuel consumption is then controlled by a characteristic chemical time-scale which ensures rapid combustion after auto-ignition (Colin et al., 2005).

Since fuel is injected directly into the combustion chamber during the compression stroke, the spray module is activated. Spray modeling involve multi-phase flow phenomena and as such require the numerical solution of conservation equations for the gas and the liquid phase simultaneously. Droplet parcels are introduced in the flow domain with initial conditions of position, size, velocity, temperature and number of particles in the parcel. AVL FIRE® supports the introduction of droplets, emerging from a nozzle as a spray and entering the flow domain through the inlet areas as a gas/liquid mixture. The atomization process of sprays is accounted for with distinctive submodels. The droplet-gas momentum exchange, turbulent dispersion, evaporation of droplets and droplet-wall interaction are covered with a comprehensive set of models which allow the usage of the module for many different flow regimes. For spray modeling some general input data such as injected fuel mass and injection timing, which are listed in Table 4.6, are required. Adopted submodels for spray modeling which explained in section 2.7, are summarized in Table 4.7.

Table 4.6 : Injected fuel mass and injection timing.

General input data	
Injected fuel mass [kg/cycle]	3.40E-05
Start of injection [CAD]	355
End of injection [CAD]	375

Table 4.7 : Adopted submodels for spray modeling.

Spray Module	
	Model
Evaporation	Dukowicz
Break-up	Wave
Turbulence dispersion	Enable
Spray-wall interaction	Walljet1

The Extended Zeldovich model is used for NO formation and the Kinetic model is utilized for soot formation. Eventually, all taken values and adopted submodels during the pre-processing of diesel engine simulation are summarized in Table 4.8.

Table 4.8 : Diesel engine baseline simulation set-up.

Specification of computational mesh			
Mesh type		ESE Diesel- hexahedral dominated mesh	
Total number of cells		36,904	
Solver run mode			
Run mode	Time step	Interval	Delta-alpha
		220-300	1
		300-400	0.2
		400-500	1
Start time [deg]		220	
End time [deg]		500	
Engine speed [1/min]		1500	
Fluid properties			
Fluid properties of		Air	
Density		Ideal gas	
Turbulent Prandtl No.		0.9	
Turbulent Schmidt No.		0.9	
Initial conditions			
Pressure [bar]		1.3	
Temperature [K]		330	
Density [kg/m^3]		0 (calculated automatically)	

Table 4.8 (cont.): Diesel engine baseline simulation set-up.

Turb. kin. energy [m^2/s^2]		10	
Turb. length scale [m]		0.004	
Turb. diss. rate [m^2/s^3]		1299.04	
Velocity u [m/s]		0	
Velocity v [m/s]		0	
Velocity w [m/s]		0	
Scalar		0	
Initialization mode		Uniform	
1-Equation turbulence model .		Off	
Reinitialization		Off	
Smoothing		Off	
Multi-component		No	
Type of hydrocarbon fuel		Diesel ($C_{13}H_{23}$)	
EGR mass fraction		0.05	
EGR composition		0.6	
Laminar flame speed		Database	
Equivalence ratio		0	
Lower heating value [J/kg]		0 (calculated automatically)	
Heat of formation [kJ/kmol		0 (calculated automatically)	
Boundary conditions			
Selection	BND_Piston		
Wall	Movement	Mesh movement	
	Thermal	Temperature [k]	570
	Roughness	Off	
	Slip wall	Off	
Selection	BND_Axis		
	Symmetry		
Selection	BND_Head		
Wall	Movement	Velocity	
	Thermal	Temperature [k]	520
	Roughness	Off	
	Slip wall	Off	
Selection	BND_Liner		
Wall	Movement	Velocity	
	Thermal	Temperature [k]	470

Table 4.8 (cont.): Diesel engine baseline simulation set-up.

Selection	BND_Segment_1		
Inlet/Outlet	Periodic		
	Boundary connection	Boundary_connection1	
	Pressure drop	Off	
Comments on Solver setting			
Discretization			
	Calculation of boundary values		
	Exportable	On	
	Calculation of derivatives		
	Least Sq. Fit	On	
Simple/Simpleec/Piso/Simple-H	Simple/Piso		
Active equations			
	Momentum & continuity	Yes	
	Turbulence model	k-epsilon	
	Energy equation	Yes	
	Total/static enthalpy	Total enthalpy	
	Compressibility	Compressible	
	Wall treatment	Hybrid wall function	
	Heat transfer Wall model	Standard wall Function	
Convergence criteria			
	Type	Min. iteration	Max. iteration
Momentum	GSTB	0	50
Continuity	AMG	0	50
Turbulence	GSTB	0	50
Energy	GSTB	0	50
Scalar	GSTB	0	50
Linear solver			
	Max. number of iteration	100	
	Min. number of iteration	10	
	Reduction of residuals	On	
Comments on Module setting - Species transport			
Standard / General	Standard		

Table 4.8 (cont.): Diesel engine baseline simulation set-up.

Comments on Module setting - Combustion		
Combustion models		
Combustion models	Coherent Flame Model - ECFM-3Z	
Spark ignition	off	
Ignition models		
Auto-ignition model	Two-stage	
Comments on Module setting - Spray		
Liquid properties		
Number of fluids	On	
Set temperature [K]	293.15	
Fuel type	DIESEL-D1	
General settings for all particles		
Submodels		
Turbulent dispersion model	Enable	
Wall interaction model	Walljet1	
Evaporation model	Dukowicz	
Break-up model	Wave	
	Model constants	Value
	C1	0.61
	C2	18
	C3	1
	C4	0.15
	C5	0.1
	C6	0
	C7	0
	C8	0
Particle introduction method		
Active particle introduction from nozzle	On	
NSIZES× NINTRO× NCIRCD	3×3×3	
General nozzle data		
Start [deg]	715	
End [deg]	735	
Injected fuel mass [g]	0.0068	
Fluid temperature [K]	330	

Table 4.8 (cont.): Diesel engine baseline simulation set-up.

Geometry data	
X/Y/Z coordinate [m]	0/0/-0.00174
X/Y/Z direction	0/0/1
Nozzle diameter at hole center position [m]	330
Number of nozzle holes	5
Spray angle delta 1 [deg]	160
Spray angle delta 2 [deg]]	0
Diagrams	
Start velocity [m/s]	0
Injection rate	Table
Outer diameter [m]	0.0001
Inner diameter [m]	0
Half outer cone angle [deg]	6
Half inner cone angle [deg]	0
Particle sizes [m]	0.0001
Nozzle submodels	
Nozzle flow simulation	Diesel nozzle flow
Comments on Module setting - Emission	
NO_x models	
Model	Extended Zeldovich
Soot models	
Model	Kinetic model

4.2.2 Simulation results

The simulated DI diesel engine (Case-10) is assumed to be the reference engine, and the effects of various parameters are compared with the results of this baseline simulation. Results are presented in two sections, firstly the individual effect of injection quantity or load variation on combustion and engine-out emissions is studied, then the effects of introducing different EGR rates at part load operating conditions are investigated and compared with the reference engine results.

4.2.2.1 Engine load

In contrast to SI engine, the air flow at given speed of diesel engine is essentially unchanged and the load control is achieved by varying the amount of injected fuel per cycle. In this section, the individual effect of load variation at constant engine speed of 1500 [rpm] is evaluated in terms of ignition delay, ISFC, exhaust gas temperature and exhaust emissions. In this regard, the injection quantity is decreased and two more simulations are done for engine operation under medium and low loads (IMEP). All adopted models and operating conditions, including initial pressure, initial temperature, adopted amount of EGR, injection timing and injection duration, are the same as baseline simulation and just injected fuel mass is decreased. Injection quantity for different cases are summarized in Table 4.9.

Table 4.9 : Injected fuel mass for different loads.

	SOI @ [CAD] BTDC	Fuel mass [mg/cycle]	Equivalence ratio [-]	Load
Case-10	5	34	0.84	full
Case-11	5	20.2	0.5	medium
Case-12	5	13.5	0.33	low

The effect of injection quantity or engine load on rate of heat release and accumulated heat release are shown in Figures 4.6 and 4.7, respectively.

During the combustion process the burning proceeds in three distinguishable stages. In the first stage, the rate of burning is generally very high and lasts only for few crank angle degrees, which are shown in Table4.10. It corresponds to the period of rapid cylinder pressure rise. The second stage is the main heat release period and corresponds to a period of gradually decreasing heat release rate, while it initially reaches a second peak which is lower in magnitude. The third stage corresponds to the tail of the heat release diagram in which a small but distinguishable rate of heat release persists throughout much of the expansion stroke. The total burning period is much longer than the injection period.

Observing Figure 4.6, by decreasing the injection quantity, the amount of fuel collected in the combustion chamber during the ignition delay is reduced. Thus, maximum heat

release rate corresponding to the premixed combustion phase is higher in full load operating condition. Moreover, since more fuel is injected and more energy is released at full load, the second peak related to the main combustion phase is also higher than that of part-load.

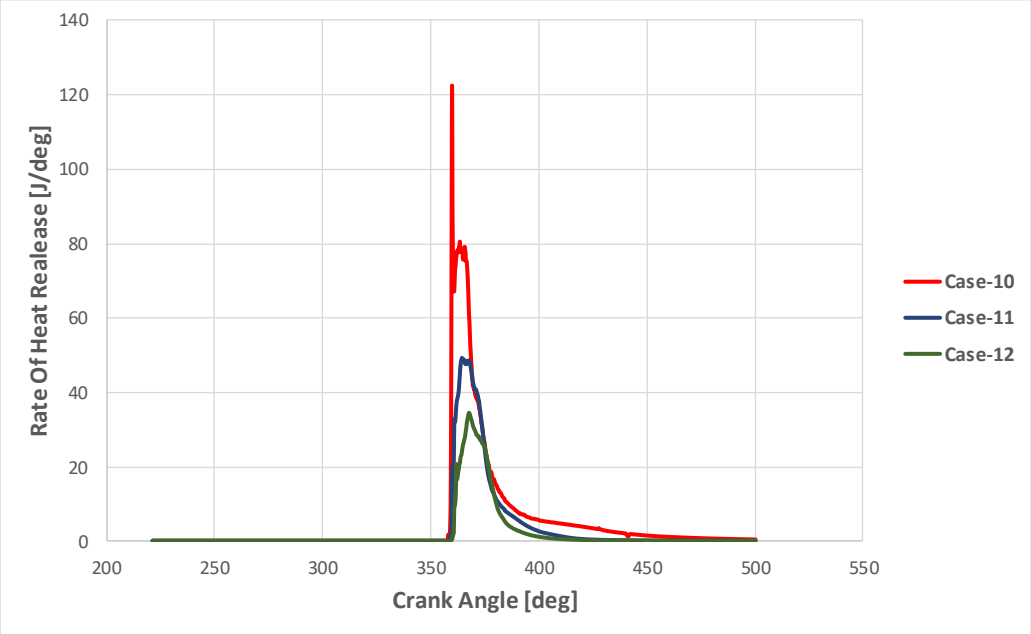


Figure 4.6 : The effect of injection quantity on rate of heat release.

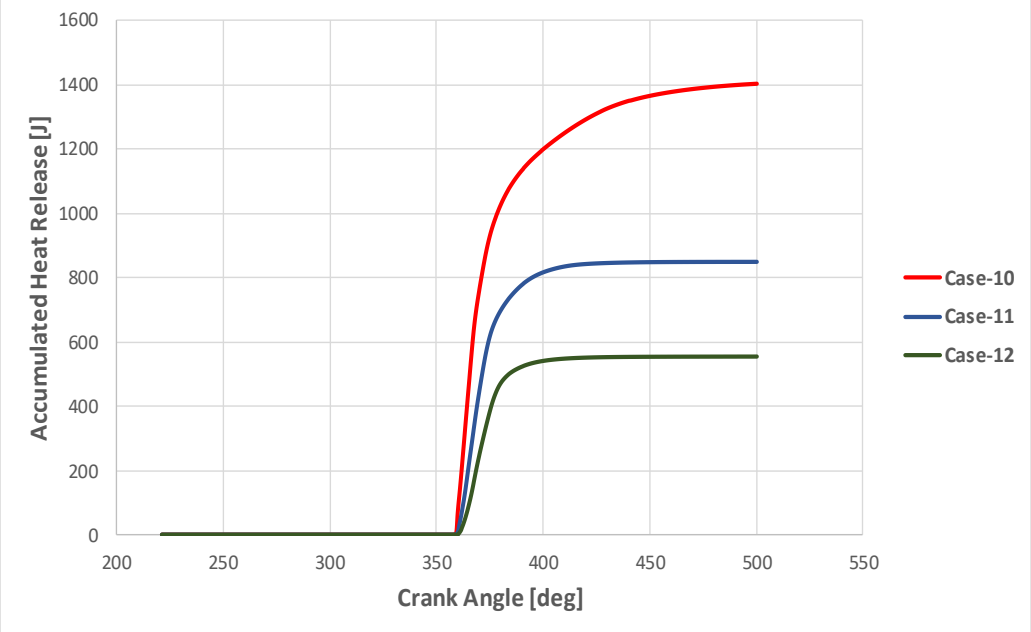


Figure 4.7 : The effect of injection quantity on accumulated heat release.

One of the most important parameters in the combustion phenomenon is the ignition delay. The period of time between the start of fuel injection into the cylinder and start of combustion is called ignition delay. Calculated ignition delay and premixed combustion duration for all cases are summarized in Table4.10. The ignition delay increases with decreasing load for this engine. As load decreases, the residual gas temperature and the wall temperature decrease and result in lower charge temperature at injection point which weaken fuel vaporization, and hence prolongs the ignition delay.

Table 4.10 : Ignition delay and premixed combustion duration under different loads.

	Ignition delay [CAD]	Premixed combustion duration [CAD]
Case-10	2	3
Case-11	3	3
Case-12	4	3

Figure 4.8 shows the effect of engine load on mean combustion temperature.

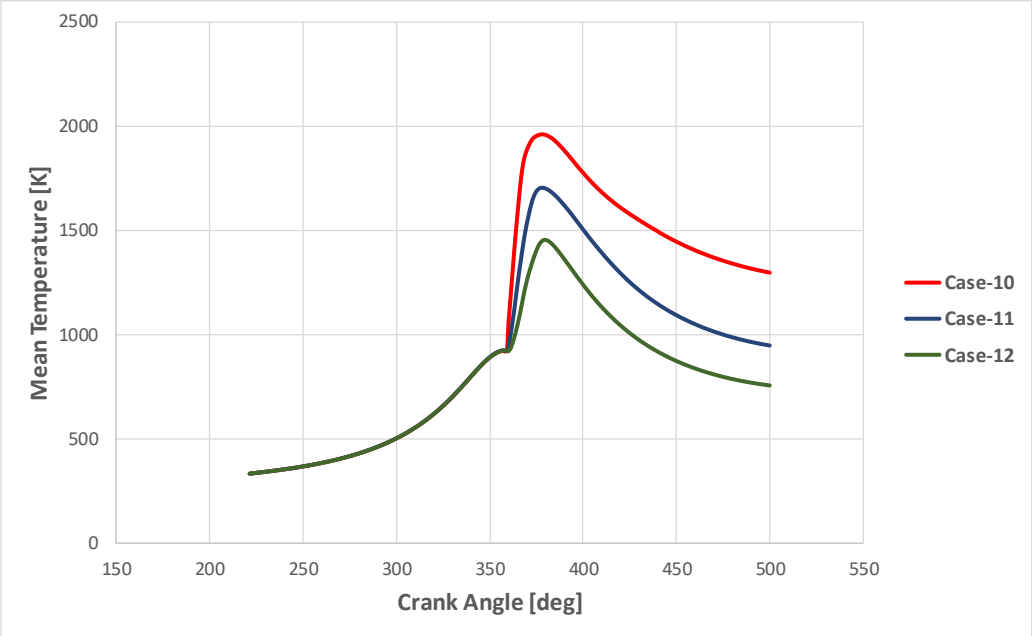


Figure 4.8 : The effect of injection quantity on mean combustion temperature.

As the load decreases, the quantity of fuel burned also decreases and releases less energy which decreases the maximum in-cylinder temperatures.

The effect of the overall equivalence ratio (engine load) on NO_x and soot emissions are illustrated in Figures 4.9 and 4.11, respectively. Reducing engine load changes the overall equivalence ratio, which is summarized in Table 4.9. Reduction of injection quantity decreases the flame temperature and affect the local charge equivalence ratio which results a change in ϕ-T plane, as shown in Figure 4.13, and afford the opportunity of avoiding soot and NO_x formation.

The critical equivalence ratio for NO formation in high-temperature burned gases is close to stoichiometric. By decreasing the injection quantity, the regions with equivalence ratio of close to stoichiometric are also decreased. At high load, with higher peak pressures, higher peak temperatures and larger regions of close to stoichiometric burned gas, NO formation increases. Compared to full load, NO_x emissions decrease by about 7% under medium load and approximately by 64% under low load.

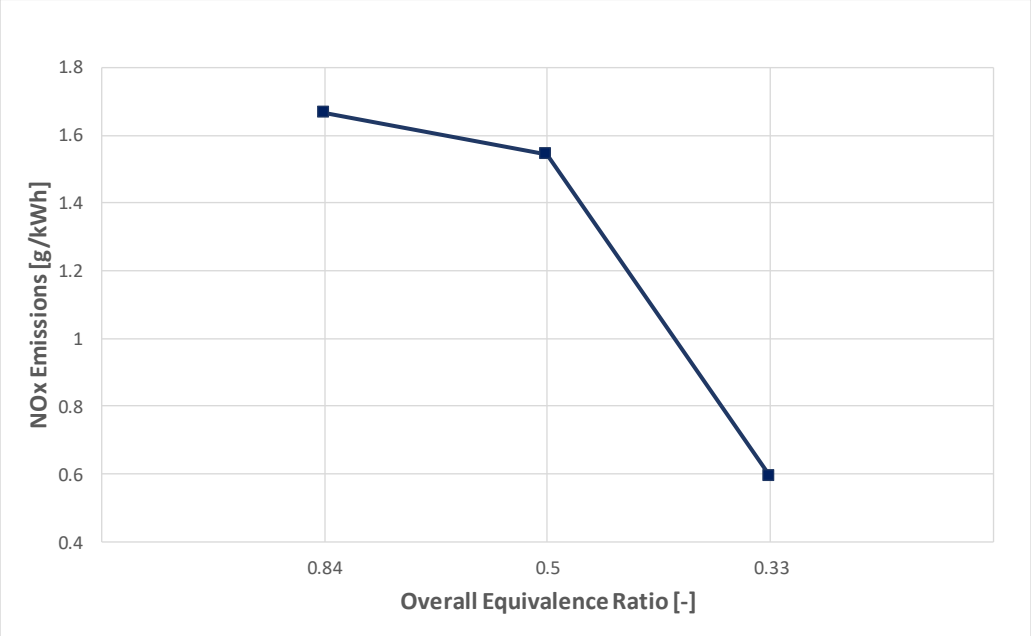


Figure 4.9 : The effect of injection quantity on NO_x emissions.

As described, load variation change the local equivalence ratio. By decreasing the injection quantity, over-rich regions are also reduced and caused an intense reduction in soot emissions. In comparison with full load condition, the amount of soot emissions decreases by about 94% under medium load and approximately by 97% under low load.

Figure 4.32 shows the in-cylinder temperature distributions and NO_x emission concentration contours for different loads at 2 [CAD] ATDC.

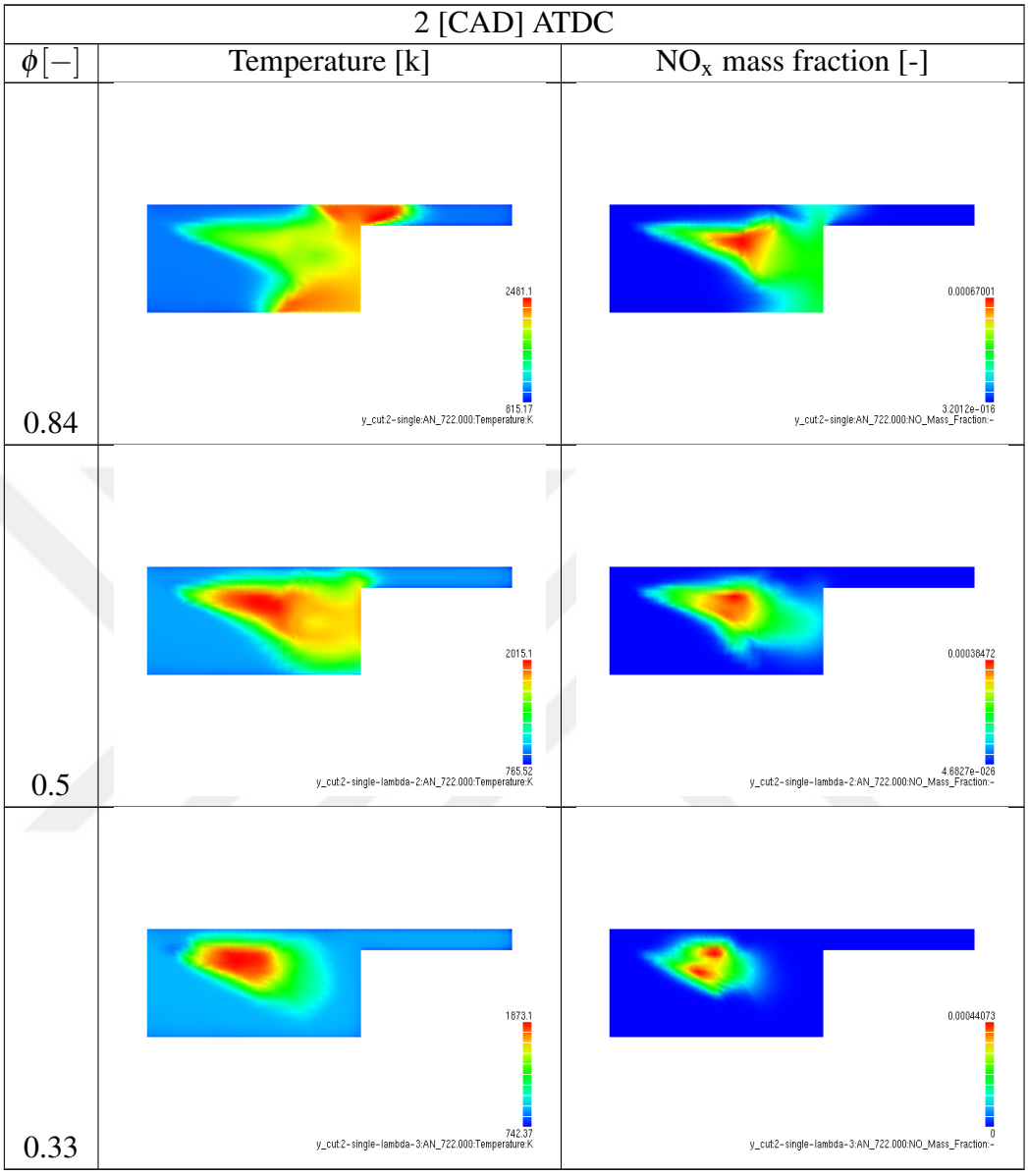


Figure 4.10 : In-cylinder distributions of temperature and NO_x emissions for different loads @ 2 [CAD] ATDC

Observing Figure 4.24, it can be seen that there is a decrease in ISFC with reduction of injection quantity and minimum ISFC is obtained under low load operating conditions (Case-12). At lower loads, the amount of fuel supplied to the combustion chamber is lower and lower energy is released which results in a reduction of the combustion temperature. Therefore, the heat losses to the walls are reduced because the burned gas temperatures are lower and ISFC is decreased by decreasing engine load.

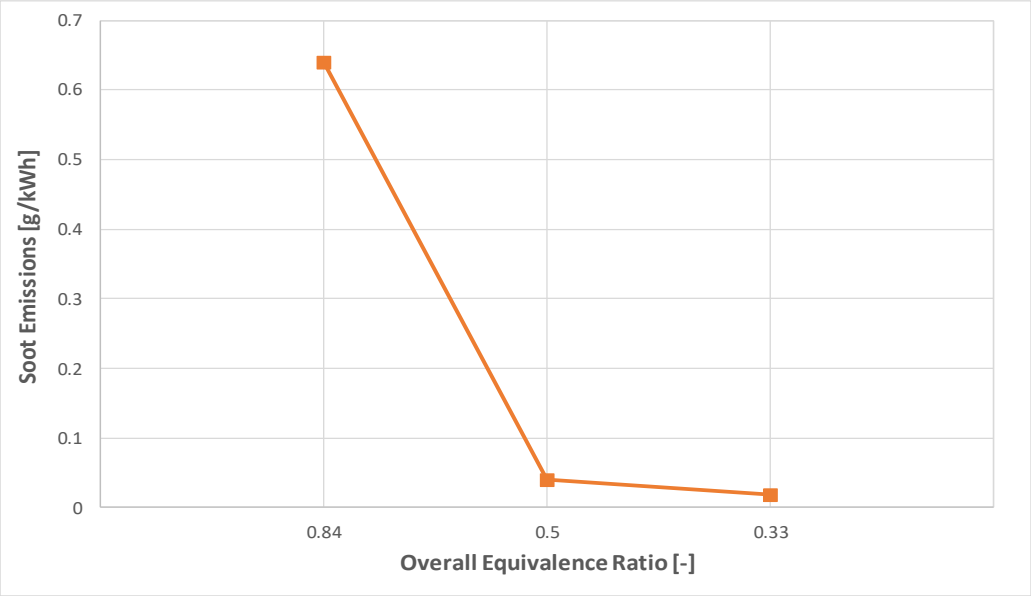


Figure 4.11 : The effect of injection quantity on soot emissions.

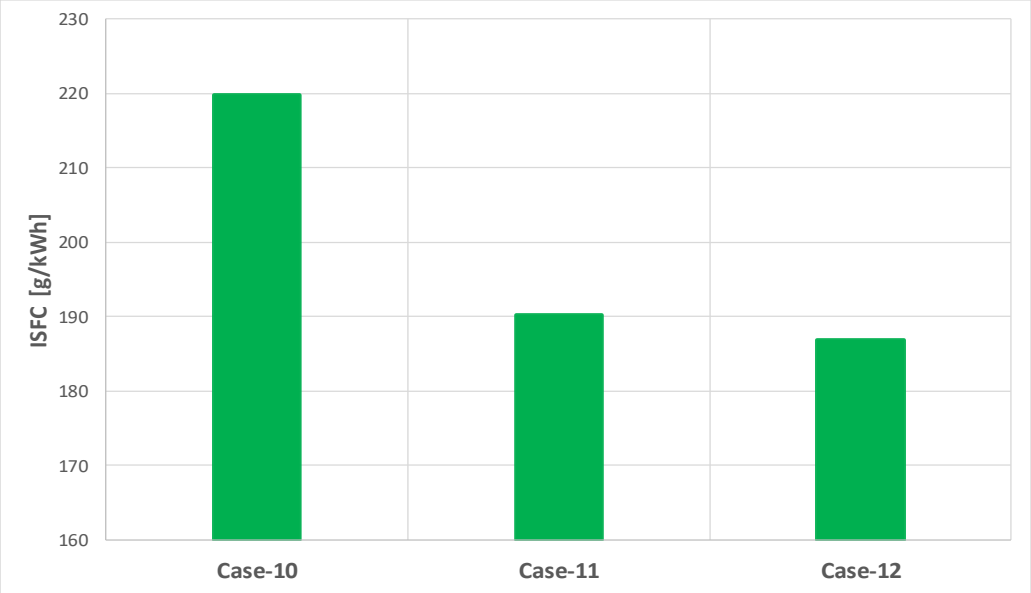
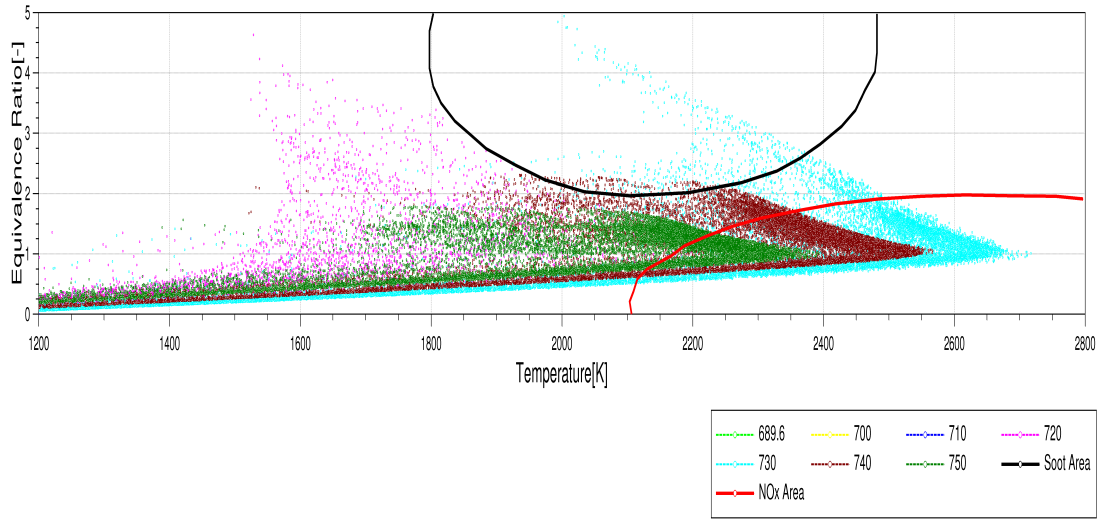
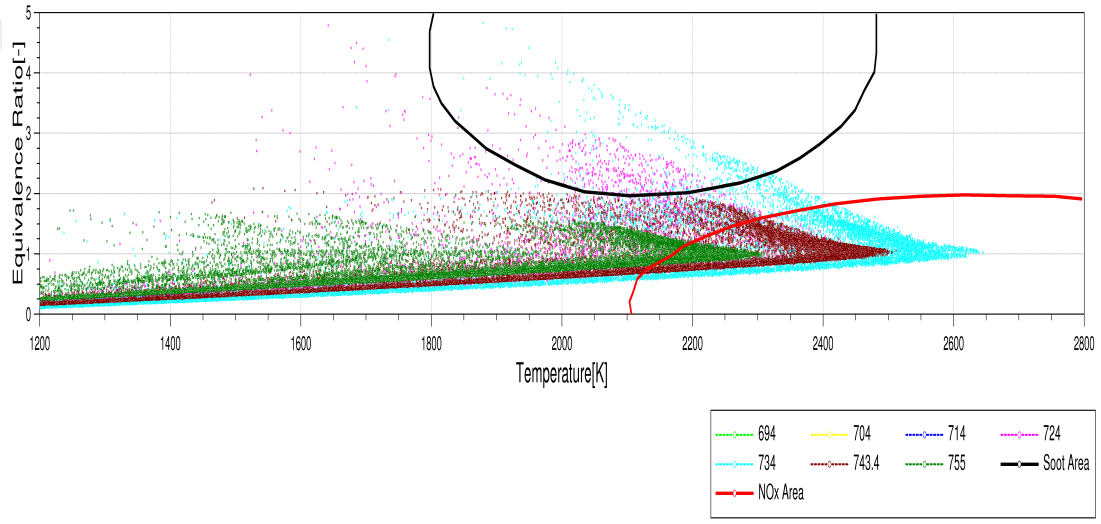


Figure 4.12 : ISFC of different cases.

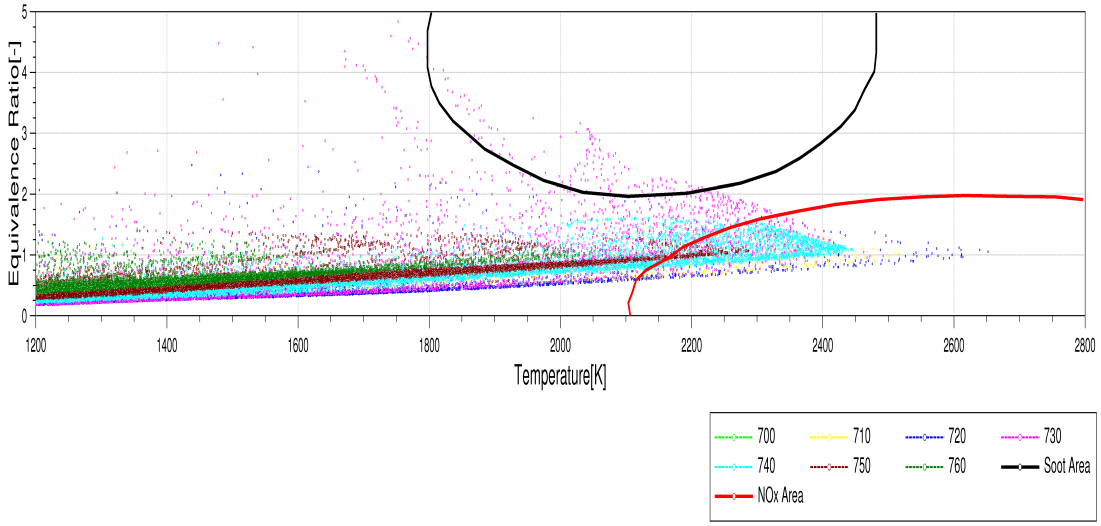
In order to better understand the effect of engine load on soot and NO_x formations, the equivalence ratio-temperature (ϕ-T) maps are developed and shown in Figure 4.13. To create ϕ-T maps 7 crank angle positions are automatically selected by AVL FIRE® , where the pink color demonstrates the crank angle with maximum rate of heat release as a central point with 3 intervals of -10 [CAD] and +10 [CAD]. A relatively large number of points for crank angle positions in a soot and NO_x area shows a good potential for reducing the emission level for this engine's operating point.



(a) Full load (Case-10)



(b) Medium load (Case-11)



(c) Low load (Case-12)

Figure 4.13 : ϕ-T plots with different injection quantities.

Specific engine outputs under different loads which are obtained by analyzing the simulation results via ESE Diesel analyser tool are summarized in Table 4.11.

Table 4.11 : Engine specific output for different loads.

	Case-10	Case-11	Case-12
Air mass at start of high pressure cycle [kg]	5.69E-04	5.83E-04	5.90E-04
Air purity [-]	0.94	0.97	0.98
Air-fuel ratio of combustion [-]	17.74	29.81	44.72
Break mean effective pressure BMEP [bar]	10.5	6.66	3.96
Break specific fuel consumption BSFC [kg/kWh]	0.2567	0.2409	0.27
Combustion Noise - A + CAV Filter [dB]	94.73	87.81	82.56
Combustion Noise - A Filter [dB]	204.79	202.53	201.01
Combustion Noise - CAV Filter [dB]	95.26	88.92	84.18
Combustion Noise [dB]	222.32	220.85	219.74
Excess air ratio [-]	1.19	2	3.01
Friction mean effective pressure FMEP [bar]	1.76	1.76	1.76
Indicated efficiency [-]	0.39	0.45	0.46
Indicated fuel consumption (total fuel mass) ISFCtt [kg/kWh]	0.2198	0.1905	0.1869
Indicated fuel consumption (trapped fuel mass) ISFCtr [kg/kWh]	0.2198	0.1905	0.1869
Indicated mean effective pressure IMEP [bar]	12.26	8.42	5.72
Indicated power [kW]	6.96	4.78	3.25
Indicated specific power [kW/l]	15.33	10.53	7.16
Indicated specific torque [Nm/l]	97.6	67.03	45.55
Indicated torque [Nm]	44.31	30.43	20.68
Injected fuel mass [kg]	3.40E-05	2.02E-05	1.35E-05
Mean mass [kg]	6.20E-04	6.13E-04	6.10E-04
Mechanical efficiency [-]	0.86	0.79	0.69
Total mass at start of high pressure cycle [kg]	6.03E-04	6.03E-04	6.03E-04
Volume displacement [m$\hat{3}$]	4.54E-04	4.54E-04	4.54E-04

4.2.2.2 Combined effects of EGR and engine load

In previous section, it was observed that the DI diesel engine produces lower amount of NO_x and soot emissions under part loads. In respect of preparing a supplementary study, different levels of EGR, 5%, 10%, 20% and 30% are used to investigate the effect of introducing EGR under part load operating conditions.

Application of EGR reduces the intake oxygen concentration by replacing part of the intake fresh air with inert combustion products such as CO_2 and water vapor. Thus, unlike to the previously simulated PFI SI engine, the equivalence ratio of mixture is changed by applying EGR in DI diesel engine, which is summarized in Table 4.12. The reason is that the amount of injected fuel for specific load is constant in DI diesel engine, while the oxygen concentration is decreased by increasing EGR rate.

Table 4.12 : Overall equivalence ratio of mixture with different EGR rates.

Load	EGR [%]	Equivalence ratio [-]
Low	5	0.33
	10	0.34
	20	0.37
	30	0.39
Medium	5	0.5
	10	0.52
	20	0.55
	30	0.59

It is obvious from Table 4.12 that the overall equivalence ratio of mixture in DI diesel engine is increased by increasing EGR.

Figures 4.14 and 4.15, respectively, illustrate the effect of various EGR rates on in-cylinder pressure at medium and low load. As it can be seen from figures, with the increase in the EGR percentage, the peak cylinder pressures and peak pressure rise rates decrease slightly. The reduction in peak cylinder pressure is due to the high specific heat capacity of mixture and its slower burning rate which resulted from adding EGR. The peak pressure values for adopted amounts of EGR at medium and low load are summarized in Table 4.13.

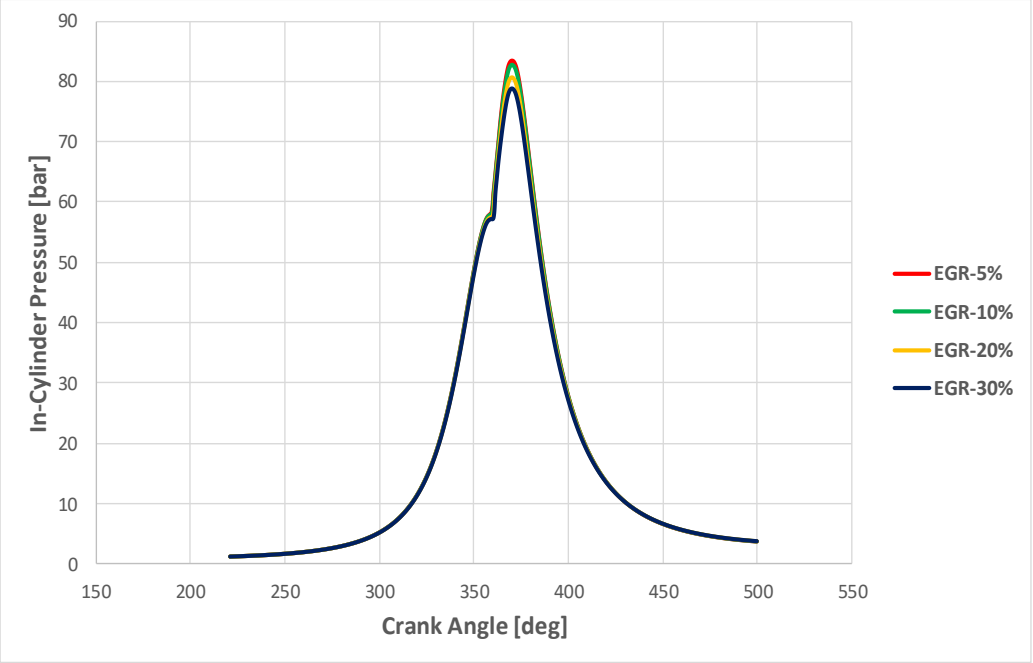


Figure 4.14 : The effect of EGR on in-cylinder pressure of Case-11.

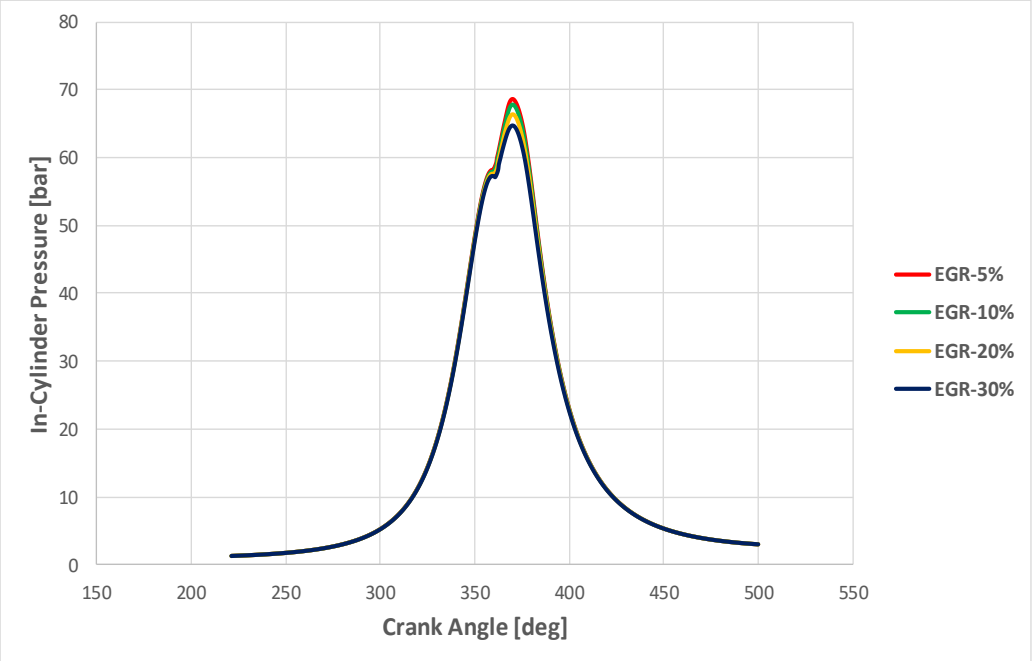


Figure 4.15 : The effect of EGR on in-cylinder pressure of Case-12.

For both cases, the peak cylinder pressures at 20% EGR rate decrease approximately by 3% and decrease by 5% at EGR rate of 30% compared with the peak cylinder pressures at 5% EGR rate.

Table 4.13 : Peak in-cylinder pressures with different EGR rates.

Load	EGR [%]	Peak pressure [bar]
Low	5	68.58
	10	67.87
	20	66.37
	30	64.73
Medium	5	83.47
	10	82.66
	20	80.75
	30	78.81

Ignition delay is affected by amount of available oxygen, in-cylinder pressure and temperature. Calculated ignition delay for all cases are summarized in Table4.14.

Table 4.14 : Ignition delay with different EGR rates.

Load	EGR [%]	Ignition delay [CAD]
Low	5	4
	10	4.4
	20	4.6
	30	4.8
Medium	5	3
	10	3.4
	20	3.6
	30	3.8

It is observed that use of EGR causes a small increase in the ignition delay period and hence retards the start of combustion. Addition of EGR increases the ignition delay mainly because of reduction of charge temperature, pressure and oxygen concentration at the point of fuel injection.

Figure 4.16 and 4.17, respectively, show the effect of various EGR rates on mean combustion temperature under medium and low load. By implementing EGR, a modest reduction in combustion temperature is observed for both cases. This results from the re-introduction of products of combustion into the cylinder, and since the recirculated inert components have higher specific heat capacities than air, they act as a heat sink. These non-reacting species increase the specific heat capacity of mixture and absorb energy during the reaction and hence act to decrease the flame temperature within the cylinder during the combustion.

The varying trend of in-cylinder mean temperature in Figures 4.16 and 4.17 suggest that applying EGR is a useful method to reduce the flame temperature for controlling NO_x formation in a diesel engine under part load.

In case of medium load, when EGR varies from 5% to 30%, the peak value of in-cylinder mean temperature decreases from 1699 [K] to 1607 [K] which means 5% reduction in peak temperature and in case of low load, when EGR varies from 5% to 30%, the peak value of in-cylinder mean temperature decreases from 1454 [K] to 1378 [K] which means 5% reduction in peak temperature.

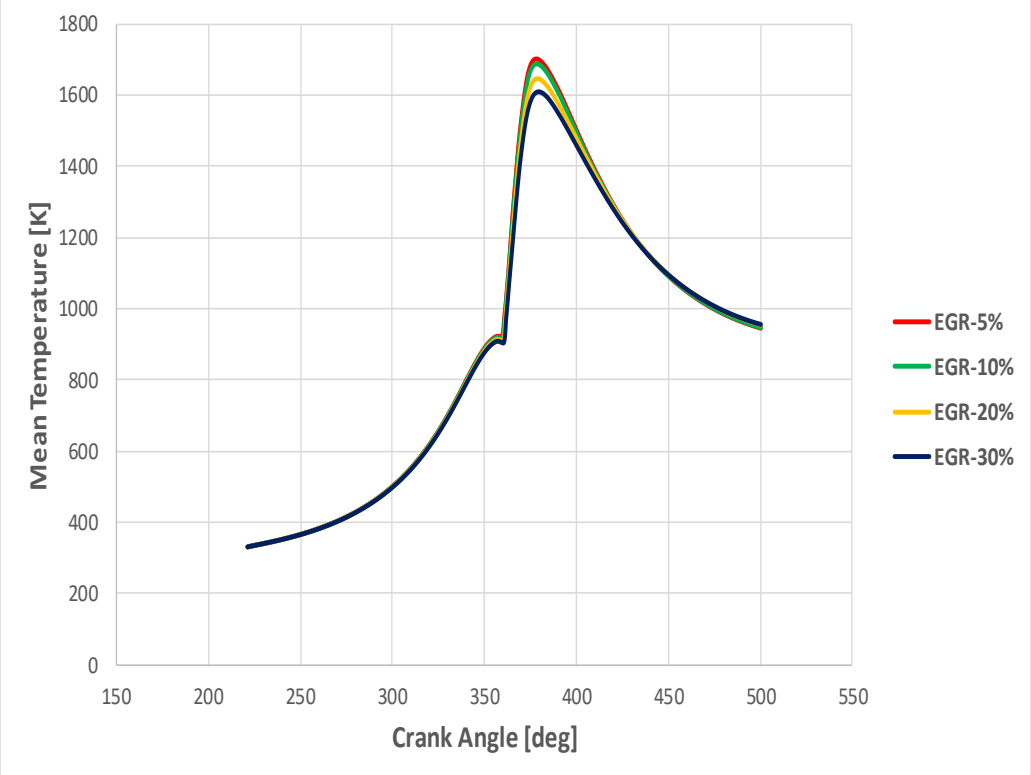


Figure 4.16 : The effect of EGR on in-cylinder temperature of Case-11.

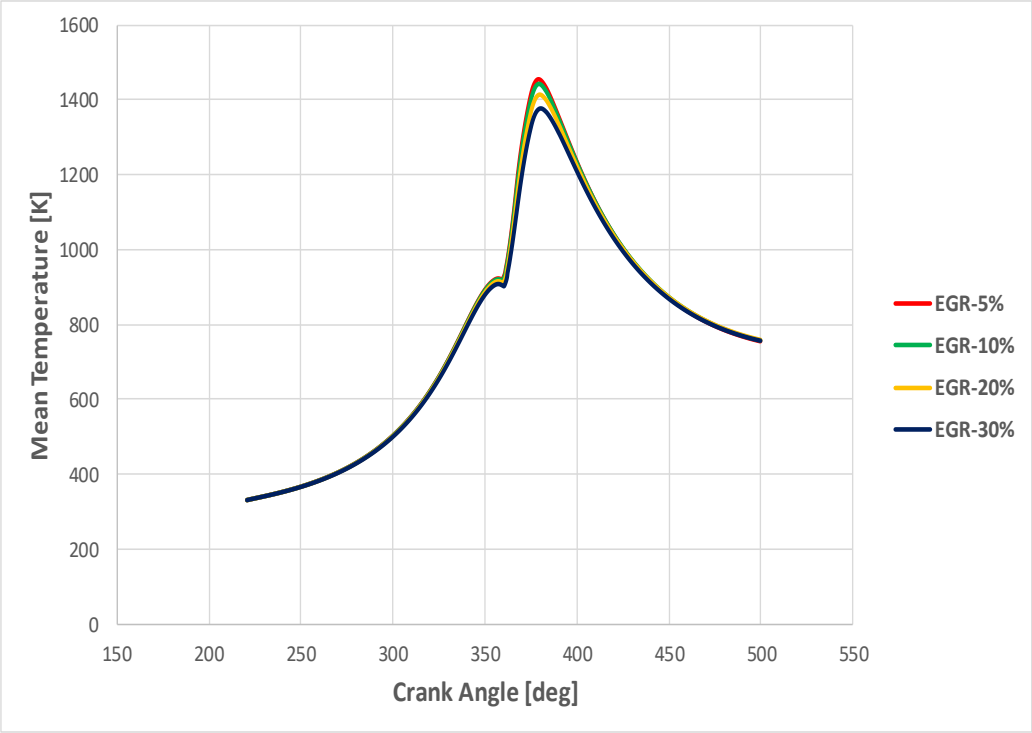


Figure 4.17 : The effect of EGR on in-cylinder temperature of Case-12.

Figures 4.18 and 4.19, respectively, show the heat release rate curves with different percentages of EGR at medium and low load. By observing these figures, it is found that the EGR greatly affects the heat release rate.

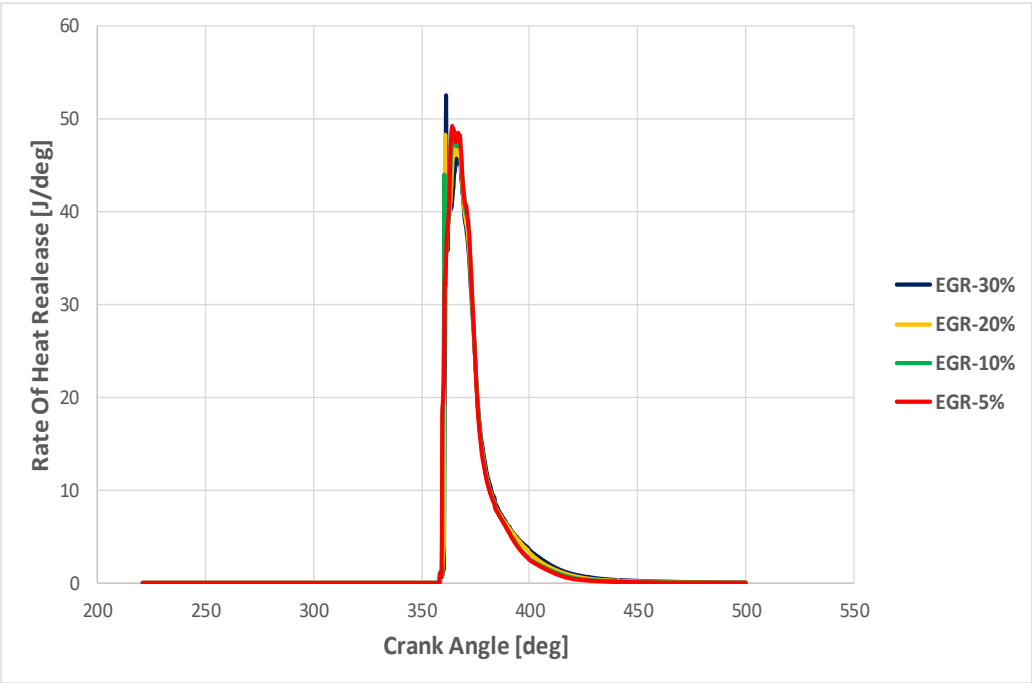


Figure 4.18 : The effect of EGR on heat release rate of Case-11.

The magnitude of the initial peak of heat release rate diagram depends on the ignition delay period, being higher for longer delays. Thus, the maximum heat release rate corresponding to the premixed combustion phase is increased intensely with an increase in EGR rate. On the other hand, lower oxygen concentration together with higher specific heat capacity of mixture as a consequence of added inert gases, reduce the in-cylinder temperature and pressure during the main combustion. Therefore, increasing the EGR rate decreases the peak heat release rate of main combustion phase (second peak). Moreover, as it can be seen from Figures 4.18 and 4.19, increase in the EGR decreases the burning velocity and shifts the combustion process further towards the expansion stroke, which results in a higher heat release rate during the late combustion phase.

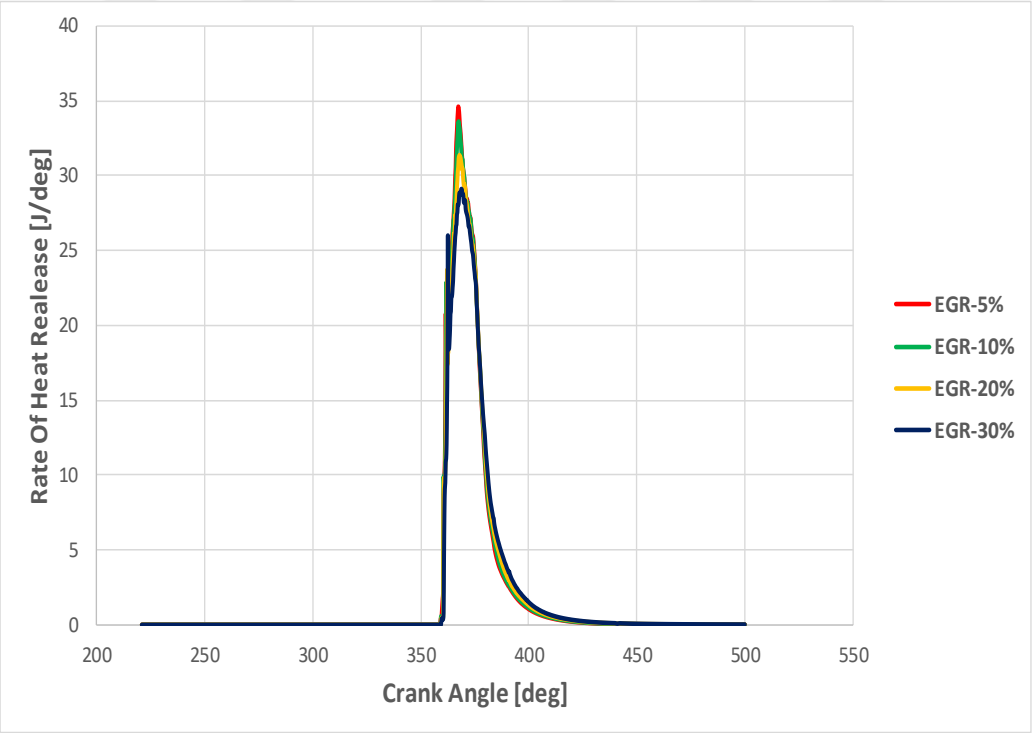


Figure 4.19 : The effect of EGR on heat release rate of Case-12.

Figure 4.20 demonstrates the effects of combination of EGR and injection quantity or engine load on NO_x emissions. The point with red color indicates the amount of NO_x emissions at full load. Observing Figure 4.20, as explained in previous section, NO_x formation decreases as the injection quantity or engine load decreases. Under part loads, with lower peak pressures, lower peak temperatures and fewer regions of close to stoichiometric burned gas, NO formation decreases.

Additionally, introducing EGR is a well known solution of NO_x emissions reduction. The efficacy of EGR can be attributed primarily to the reduction of oxygen concentration and the increased mixture specific heat capacity. As described before, the main factors affecting NO_x formation include the local temperature and the local oxygen concentration. Thus the combination of low oxygen concentration and low in-cylinder temperature result in low levels of NO_x emissions. Increasing EGR reduces the intake oxygen concentration by replacing part of the intake fresh air with inert combustion products. The higher heat capacity of inert gases together with the reduced oxygen concentration result in lowered local flame temperatures during the combustion process, as shown in Figures 4.16 and 4.17. Consequently, combination of lower oxygen concentration in the intake air and reduced flame temperature decreases the rate of NO_x formation. Since the peak combustion temperature is widely believed as the most significant parameter affecting NO_x production, EGR has proven to be very effective in reducing the exhaust NO_x emissions.

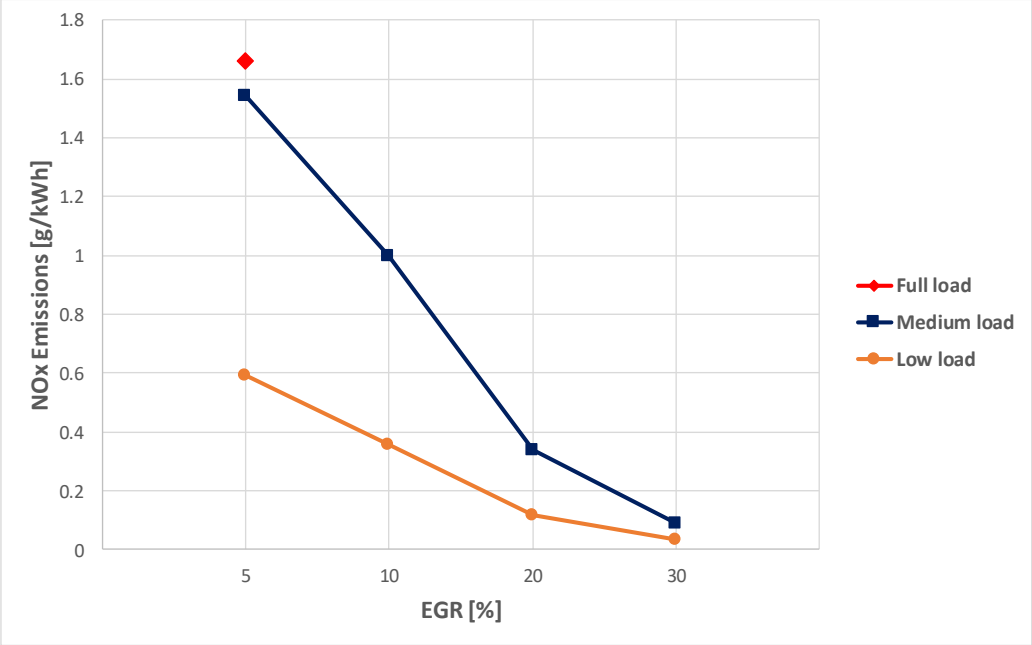


Figure 4.20 : The combined effect of EGR and injection quantity on NO_x emissions.

The results reveal that the simulated DI diesel engine produces lower NO_x emissions under part loads and it is able to realize an additional significant reduction in NO_x emissions by implementing EGR at part loads. In comparison with full load condition, the amount of NO_x emissions decreases by about 7% under medium load

and approximately by 64% under low load with 5% EGR. While by using 30% EGR, this reduction can be increased to 95% at medium load and to 98% at low load. By considering each case individually, when EGR varies from 5% to 30%, NO_x emissions experience a reduction of 94% at medium load and a decrease of 94% at low load. These results illustrate a drastic reduction in NO_x emissions under part load with high levels of EGR.

Figure 4.21 shows the effects of combination of EGR and injection quantity or engine load on soot emissions. Although NO_x formation is reduced by utilizing high levels of EGR, there is generally a trade-off with the amount of soot emissions and soot emissions tend to increase as the EGR progressively increased. Since soot emissions are a culmination of the difference between the soot formation and soot oxidation process, the balance of these two yields the total engine-out concentration of soot. The lowered combustion temperature and lowered oxygen concentration as a result of applying higher EGR rates, are thought to weaken the soot oxidation process and hence reduce the soot oxidation rates, thereby increasing the soot emissions. In another words, with increasing EGR rates, the amount of soot formed is increased only slightly, but the amount of soot oxidized during the combustion is decreased significantly. Therefore, the application of EGR is often associated with an increase in exhaust soot emissions.

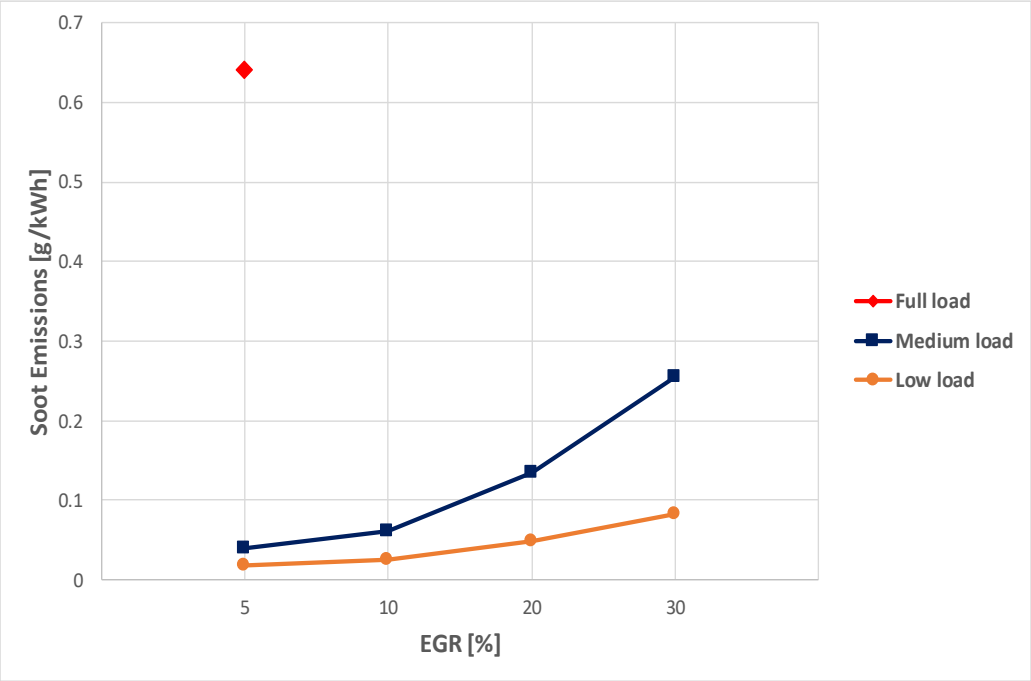


Figure 4.21 : The combined effect of EGR and injection quantity on soot emissions.

As described, load variation change the local equivalence ratio. By decreasing the injection quantity or engine load, over-rich regions are also reduced and caused a reduction in soot emissions. In comparison with full load condition, the amount of soot emissions decreases by about 94% under medium load and approximately by 97% under low load with 5% EGR. While by using 30% EGR, this reduction is decreased to 60% at medium load and to 87% at low load. By considering each case individually, when EGR varies from 5% to 30%, soot emissions increase dramatically from 0.04 to 0.255 [g/kWh] at medium load and from 0.019 to 0.083 [g/kWh] at low load.

Figures 4.25 and 4.26, respectively, show the ϕ-T maps of medium and low loads with different EGR levels.

Figure 4.22 and 4.23, respectively, show the effect of various EGR rates on IMEP and indicated power of simulated DI diesel engine under medium and low load. Since the in-cylinder pressure is decreased by increasing the percentage of EGR (Figures 4.14 and 4.15), indicated mean effective pressure is also decreased for both cases. According to Eq.(3.6), decreasing in the indicated mean effective pressure results in a reduction of indicated power.

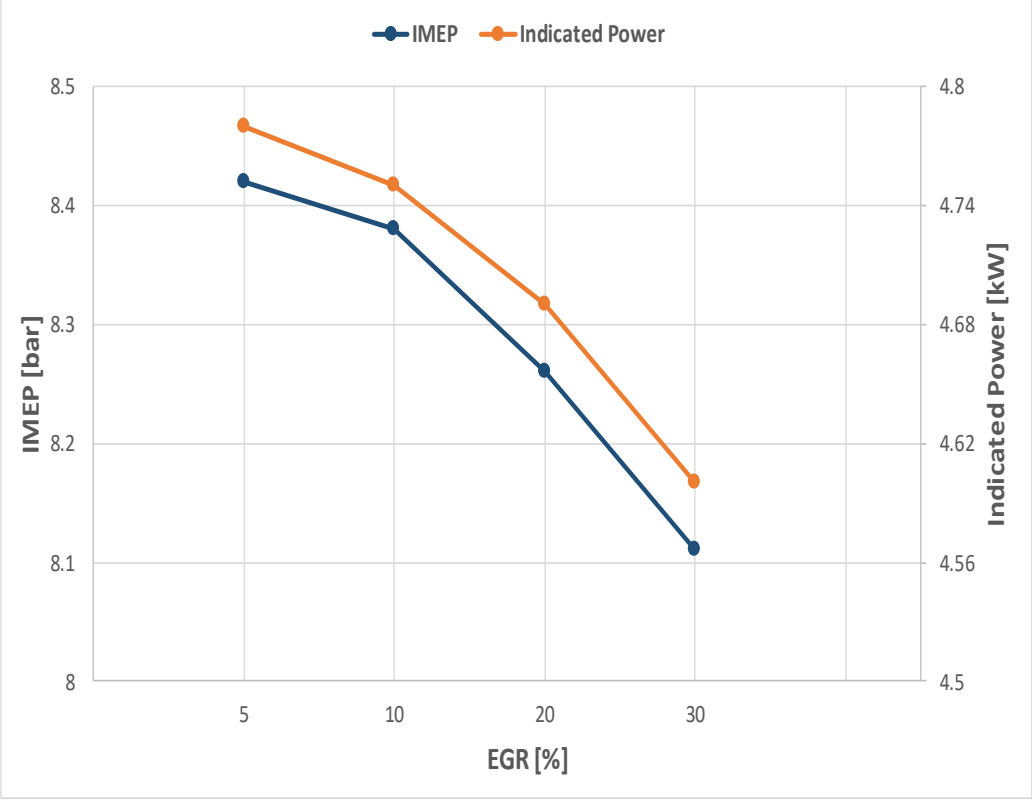


Figure 4.22 : The effect of EGR on IMEP and indicated power of Case-11.

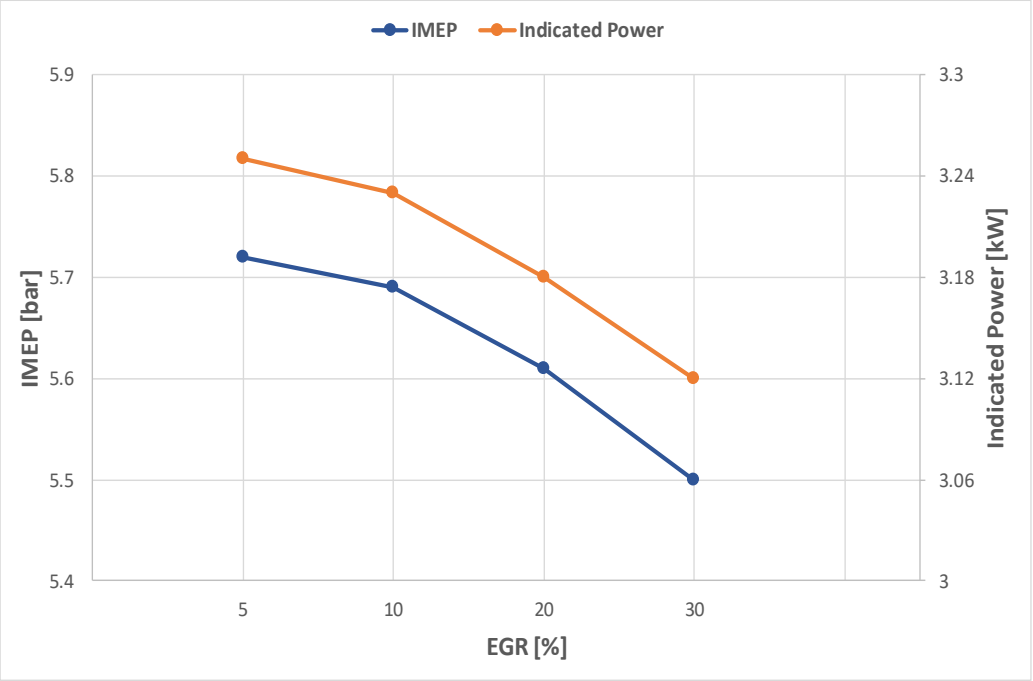


Figure 4.23 : The effect of EGR on IMEP and indicated power of Case-12.

Figure 4.24 depicts the effects of combination of EGR and injection quantity or engine load on ISFC. The ISFC is clearly a function of equivalence ratio (Heywood, 1988). At lower loads, the amount of fuel supplied to the combustion chamber is lower and lower energy is released which results in a reduction of the combustion temperature. Therefore, the heat losses to the walls are reduced because the burned gas temperatures are lower ,and hence the ISFC is decreased by decreasing engine load. On the other hand, as shown in Table 4.12, with the increase in EGR rate, oxygen available for combustion is reduced for the amount of fuel supplied, and hence the equivalence ratio is increased and results an increase of the ISFC.

In comparison with full load condition, ISFC decreases by about 13% under medium load and approximately by 15% under low load with 5% EGR. While by using 30% EGR, this reduction is decreased to 10% at medium load and to 11% at low load. By considering each case individually, when EGR varies from 5% to 30%, ISFC increases slightly from 190.2 to 197.8 [g/kWh] at medium load and from 186.9 to 194.3 [g/kWh] at low load.

Simulated engine outputs with different EGR ratios under medium and low loads, which are obtained by analyzing the simulation results via ESE Diesel analyser tool are summarized in Tables 4.15 and 4.16, respectively.

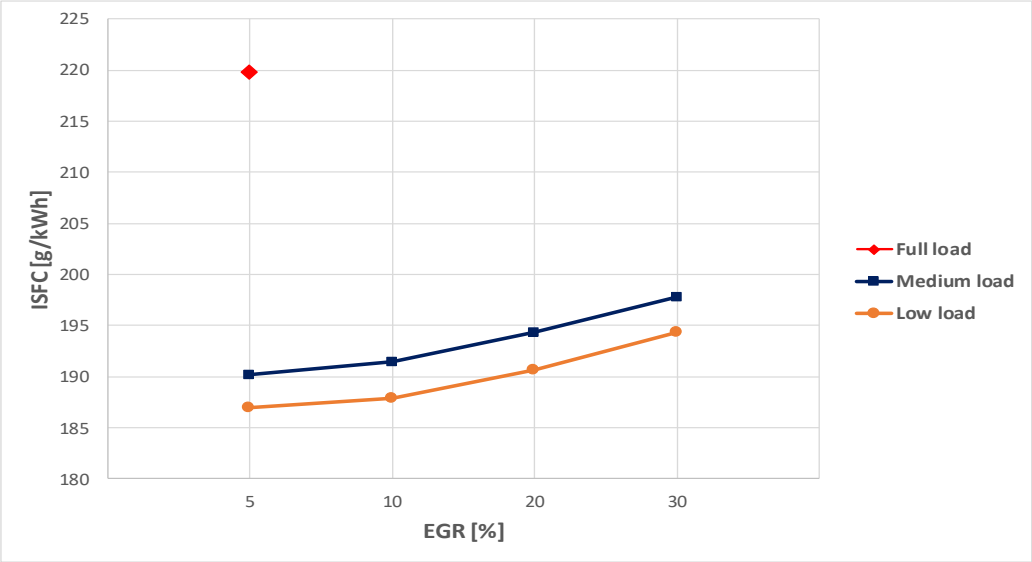


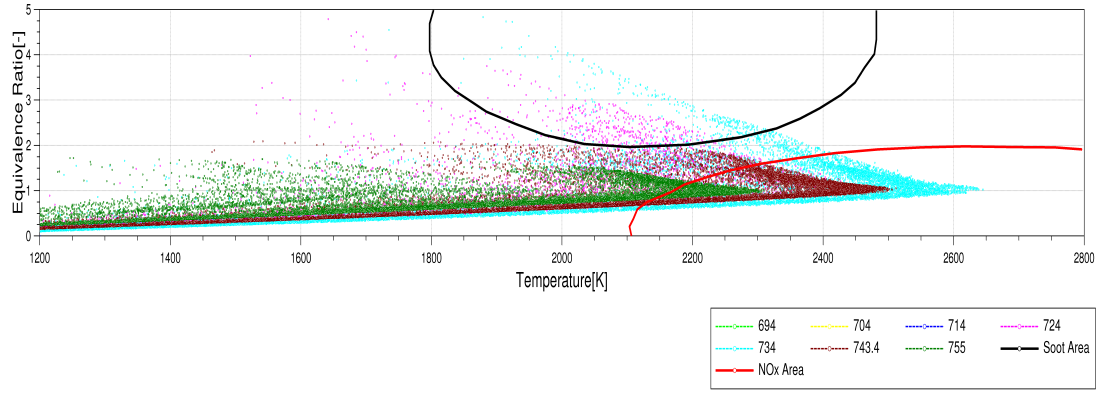
Figure 4.24 : The combined effect of EGR and injection quantity on ISFC.

Table 4.15 : Engine specific output with different EGR ratios (Medium load).

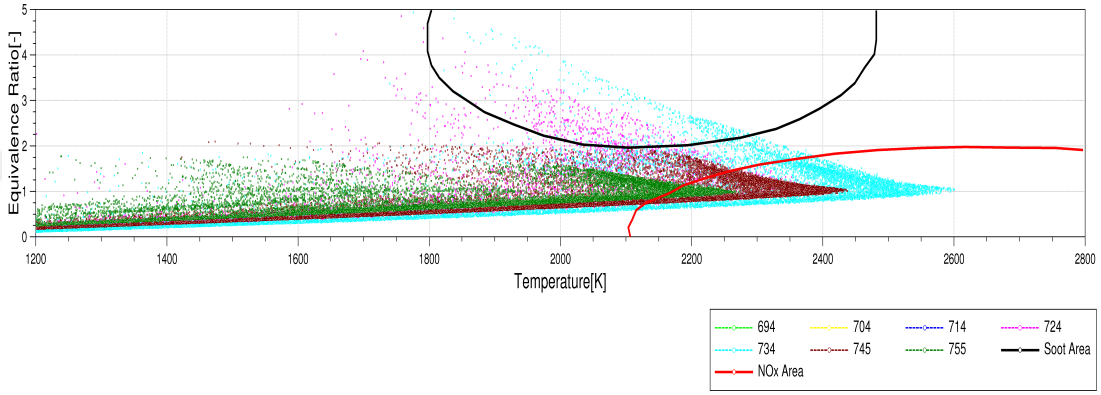
EGR [%]	5% (Case-11)	10%	20%	30%
Air mass at start of high pressure cycle [kg]	5.83E-04	5.83E-04	5.83E-04	5.83E-04
Air purity [-]	0.97	0.97	0.97	0.97
Air-fuel ratio of combustion [-]	29.81	29.82	29.83	29.84
Break mean effective pressure BMEP [bar]	6.66	6.62	6.49	6.35
Break specific fuel consumption BSFC [kg/kWh]	0.2409	0.2424	0.247	0.2527
Combustion Noise - A + CAV Filter [dB]	87.81	88.23	88.89	89.33
Combustion Noise - A Filter [dB]	202.53	202.45	202.26	202.06
Combustion Noise - CAV Filter [dB]	88.92	89.17	89.57	89.82
Combustion Noise [dB]	220.85	220.78	220.61	220.43
Excess air ratio [-]	2	1.94	1.81	1.69
Friction mean effective pressure FMEP [bar]	1.76	1.76	1.76	1.76
Indicated efficiency [-]	0.45	0.44	0.44	0.43
Indicated fuel consumption (total fuel mass) ISFCtt [kg/kWh]	0.1905	0.1915	0.1943	0.1978
Indicated fuel consumption (trapped fuel mass) ISFCtr [kg/kWh]	0.1905	0.1915	0.1943	0.1978
Indicated mean effective pressure IMEP [bar]	8.42	8.38	8.26	8.11
Indicated power [kW]	4.78	4.75	4.69	4.6
Indicated specific power [kW/l]	10.53	10.47	10.32	10.14
Indicated specific torque [Nm/l]	67.03	66.68	65.71	64.54
Indicated torque [Nm]	30.43	30.27	29.83	29.3
Injected fuel mass [kg]	2.02E-05	2.02E-05	2.02E-05	2.02E-05
Mean mass [kg]	6.13E-04	6.13E-04	6.13E-04	6.13E-04
Mechanical efficiency [-]	0.79	0.79	0.79	0.78
Total mass at start of high pressure cycle [kg]	6.03E-04	6.03E-04	6.03E-04	6.04E-04
Volume displacement [m$\hat{3}$]	4.54E-04	4.54E-04	4.54E-04	4.54E-04

Table 4.16 : Engine Specific output with with different EGR ratios (Low load).

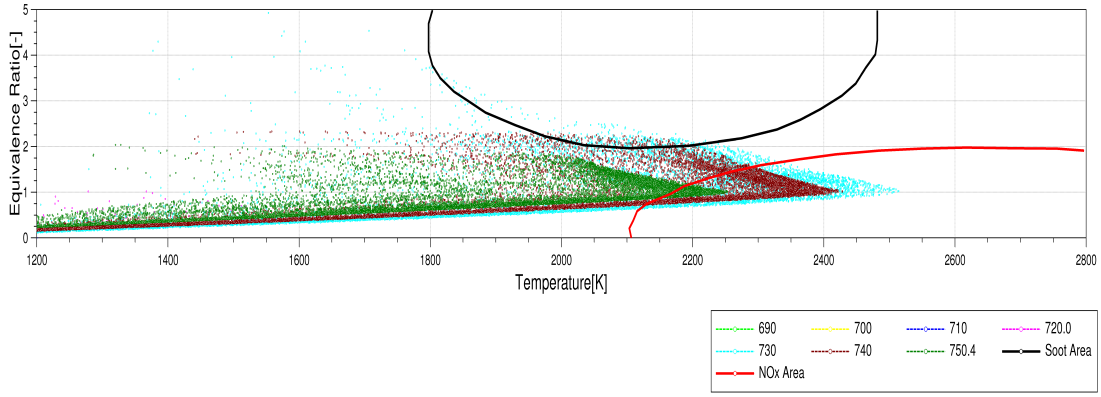
EGR [%]	5% (Case- 12)	10%	20%	30%
Air mass at start of high pressure cycle [kg]	5.90E-04	5.90E-04	5.90E-04	5.90E-04
Air purity [-]	0.98	0.98	0.98	0.98
Air-fuel ratio of combustion [-]	44.72	44.72	44.74	44.75
Break mean effective pressure BMEP [bar]	3.96	3.93	3.85	3.74
Break specific fuel consumption BSFC [kg/kWh]	0.27	0.2721	0.278	0.2859
Combustion Noise - A + CAV Filter [dB]	82.56	82.66	82.73	82.91
Combustion Noise - A Filter [dB]	201.01	200.93	200.78	200.61
Combustion Noise - CAV Filter [dB]	84.18	84.19	84.12	84.12
Combustion Noise [dB]	219.74	219.67	219.54	219.39
Excess air ratio [-]	3.01	2.91	2.72	2.53
Friction mean effective pressure FMEP [bar]	1.76	1.76	1.76	1.76
Indicated efficiency [-]	0.46	0.45	0.45	0.44
Indicated fuel consumption (total fuel mass) ISFCtt [kg/kWh]	0.1869	0.1879	0.1907	0.1943
Indicated fuel consumption (trapped fuel mass) ISFCtr [kg/kWh]	0.1869	0.1879	0.1907	0.1943
Indicated mean effective pressure IMEP [bar]	5.72	5.69	5.61	5.5
Indicated power [kW]	3.25	3.23	3.18	3.12
Indicated specific power [kW/l]	7.16	7.12	7.01	6.88
Indicated specific torque [Nm/l]	45.55	45.31	44.64	43.79
Indicated torque [Nm]	20.68	20.57	20.26	19.88
Injected fuel mass [kg]	1.35E-05	1.35E-05	1.35E-05	1.35E-05
Mean mass [kg]	6.10E-04	6.10E-04	6.10E-04	6.10E-04
Mechanical efficiency [-]	0.69	0.69	0.69	0.68
Total mass at start of high pressure cycle [kg]	6.03E-04	6.03E-04	6.03E-04	6.04E-04
Volume displacement [m$\hat{3}$]	4.54E-04	4.54E-04	4.54E-04	4.54E-04



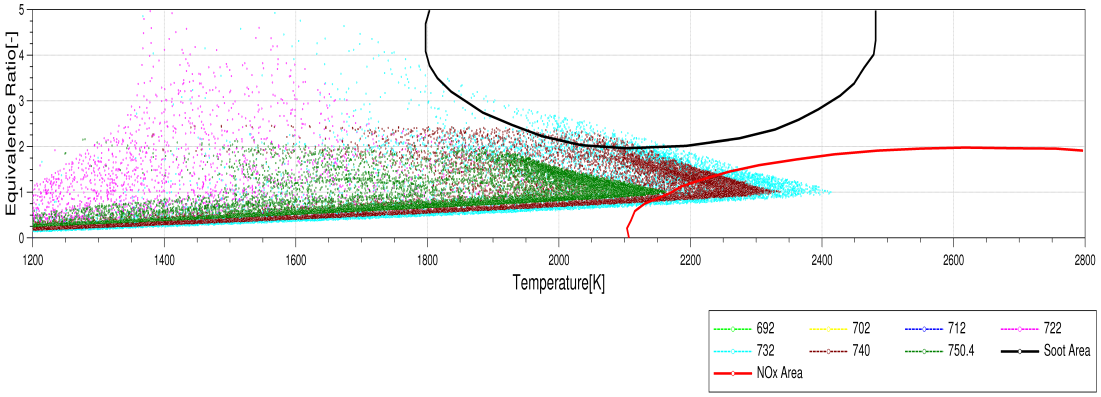
(a) EGR=5%.



(b) EGR=10%.

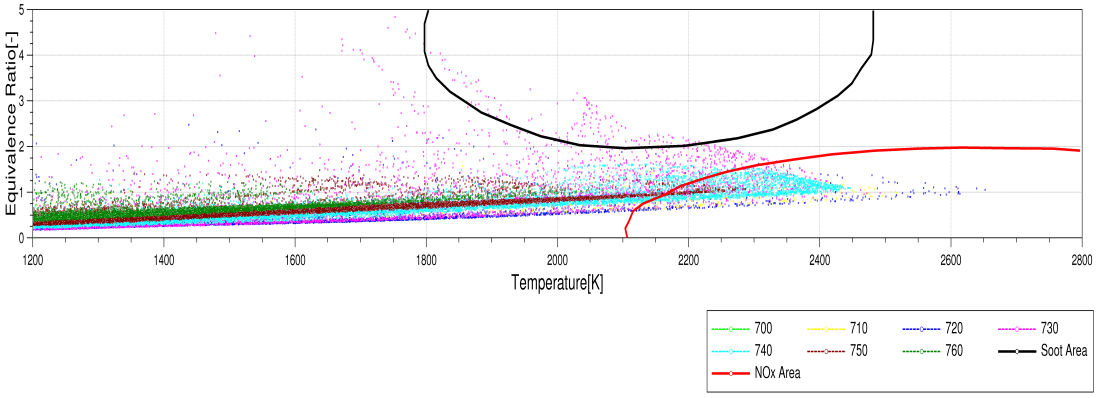


(c) EGR=20%.

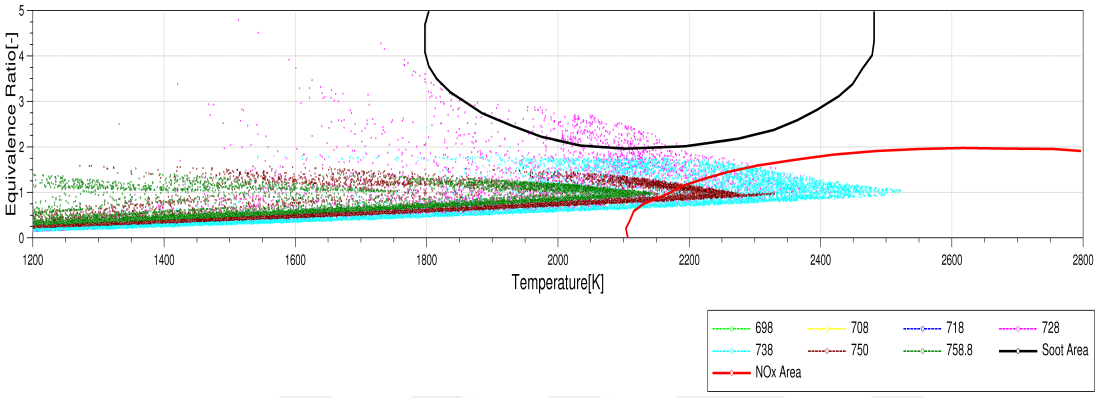


(d) EGR=30%.

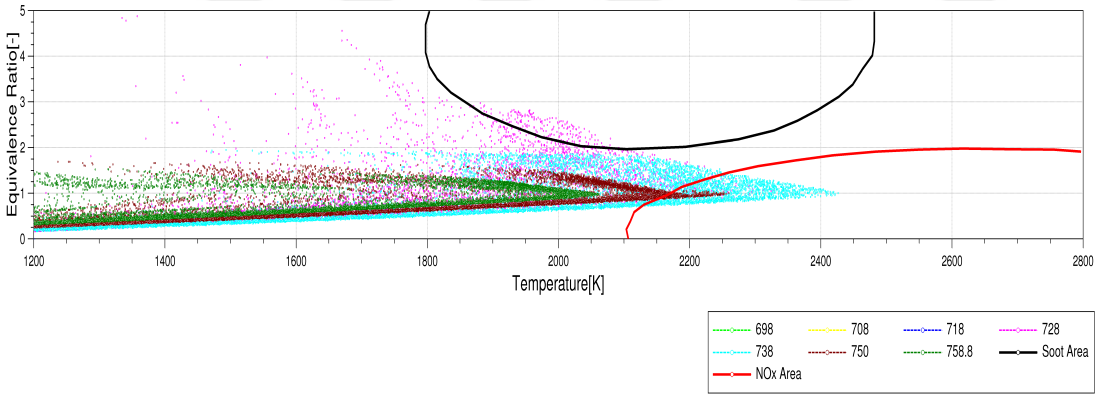
Figure 4.25 : ϕ-T plots of medium load with different EGR ratios.



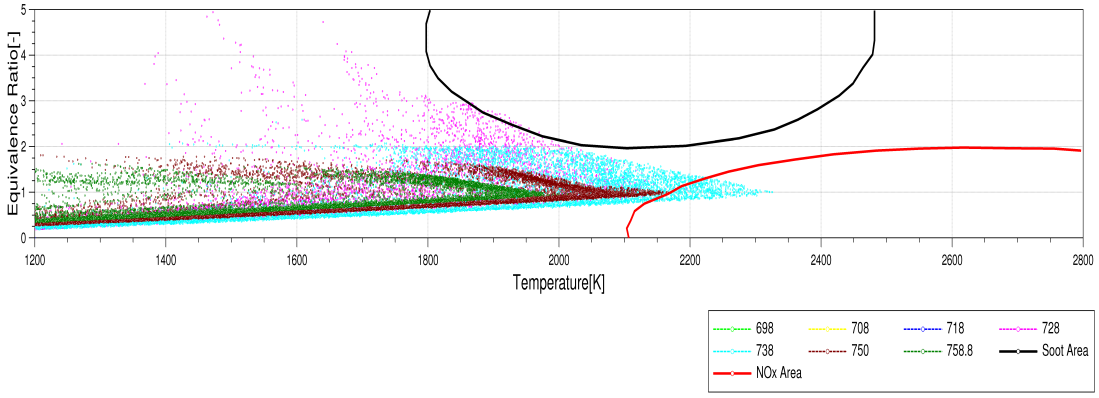
(a) EGR=5%.



(b) EGR=10%.



(c) EGR=20%.



(d) EGR=30%.

Figure 4.26 : ϕ-T plots of low load with different EGR ratios.

4.3 Simulation of Low Temperature Combustion Diesel Engine Using Double Injections

As explained before, Premixed Charge Compression Ignition (PCCI), also called Partially Premixed charge Compression Ignition (PPCI) is a kind of low temperature combustion concept that focuses on controlling the combustion process by injecting an early fuel pulse in the compression stroke that commands the start of ignition. The intake air is partially premixed with early fuel pulse to create HCCI like conditions and then the late fuel pulse is injected near TDC to control the combustion phasing by letting the combustion occur over an extended period of time compared to the instantaneous HCCI combustion.

The multiple/split injection strategy is a desirable solution to realize low temperature combustion and to control the exhaust emissions. In an effort to improve the previously simulated DI diesel engine performance and emissions, double injection strategy is implemented. Since there are no additional systems being added to the engine assembly, this strategy makes the overall system less complex and cost effective compared to other strategies, such as dual-fuel.

Additionally, this work analysis how the injection strategies including injection ratio and first injection duration can allow optimization of the emissions and fuel consumption trade-off for different operating points and engine conditions. In this regard, first the injection ratio is varied to find the optimum fuel distribution for split injection strategy, this optimum ratio is then kept constat and the first injection duration is altered and the effect of first injection duration is investigated. Finally, the simulation results of DI diesel engine which operates with optimized double injection strategy is compared with the simulation results of single injection diesel engine.

4.3.1 Effect of injection ratio

In this section, the effect of split injection on the combustion and emission of simulated diesel engine is investigated using AVL FIRE® CFD code. One of the important problems in reducing pollutant emissions from diesel engines is the trade off between soot and NO_x . Split injection is one the most powerful tools that decrease soot and

NO_x emissions simultaneously. Split injection is defined as splitting the main single injection profile in two or more injection pulses. In this regard, the results of the split injection are compared with single injection and the optimum case of split injection is investigated.

In this step, previously simulated DI diesel engine under full load operating condition is used. In order to evaluate the individual effect of injection ratio, second injection timing or start of second injection and second injection duration are not changed. Also, in respect of achieving a homogeneous air-fuel mixture, the maximum time available for mixing is selected and it is assumed that the start of first injection is immediately after the IVC (5 [CAD] after IVC) and is kept constant for all cases.

Injection fuel quantity ratio is an important parameter of optimization. It characterizes the fuel distribution between the multiple injections. In this study, the injection ratio is defined as the ratio of the injected fuel mass of the first injection (m_1) relative to the total injected fuel mass (m_{tot}), so

$$\text{Injection Ratio (IR)}[\%] = \frac{m_1}{m_{tot}} \times 100 \tag{4.1}$$

In order to investigate the effect of injection ratio on combustion, emission and fuel economy, three additional simulations are done by utilizing the injection ratios of 20, 30 and 40% , which are listed in Table 4.17 and shown in Figure 4.27.

Table 4.17 : Investigated injection ratios.

Case	Injection Mass [mg/cycle]	First Injection				Second Injection	
		SOFI @ [CAD] BTDC	Duration [CAD]	IR [%]	m_1 [mg/cycle]	SOSI @ [CAD] BTDC	Duration [CAD]
Case-10	34	-	-	0	0	5	20
Case-20	34	135	35	20	6.8	5	20
Case-30	34	135	35	30	10.2	5	20
Case-40	34	135	35	40	13.6	5	20

Figure 4.27 shows the mass of injected fuel as a function of crank angle for different cases.

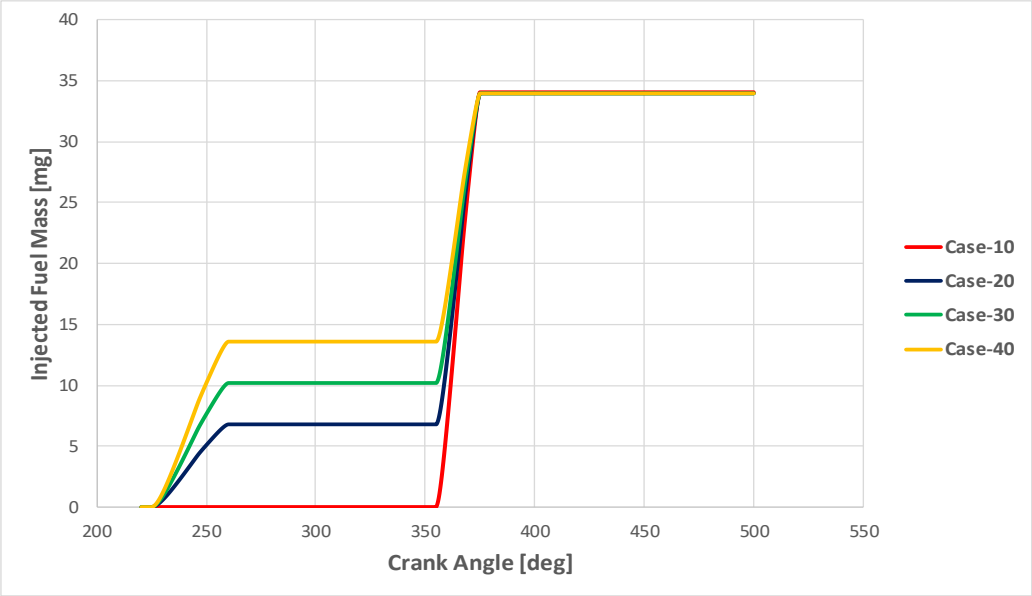


Figure 4.27 : Injected fuel mass.

Figure 4.28 depicts the effect of different injection ratios on in-cylinder pressure. The change in pressure is clearly visible which is the result of autoignition of the first injection followed by ignition of second injection. For different injection ratios from 20 to 40%, the pressure is increasing gradually until the occurrence of initially injected fuel ignition. Once the ignition of initially injected fuel occurs there is a sharp rise in cylinder pressure due to the associated heat release. With increasing the injection ratio, the intensity of pressure rise is also increased and higher peak pressures are obtained. Furthermore, as more fuel is injected initially, positions of peak pressures are advanced and reach their peak values near TDC, except for Case-20. Combustion noise which is directly relevant to pressure rise rate, would be higher for the cases with higher injection ratio. The peak pressure values and related crank angle positions of different injection ratios are summarized in Table 4.18.

Table 4.18 : Peak cylinder pressures and related crank angles of different injection ratios.

Case	Peak pressure [bar]	@ CAD
Case-10	105.62	368
Case-20	112.72	369
Case-30	118.18	367
Case-40	124.13	365

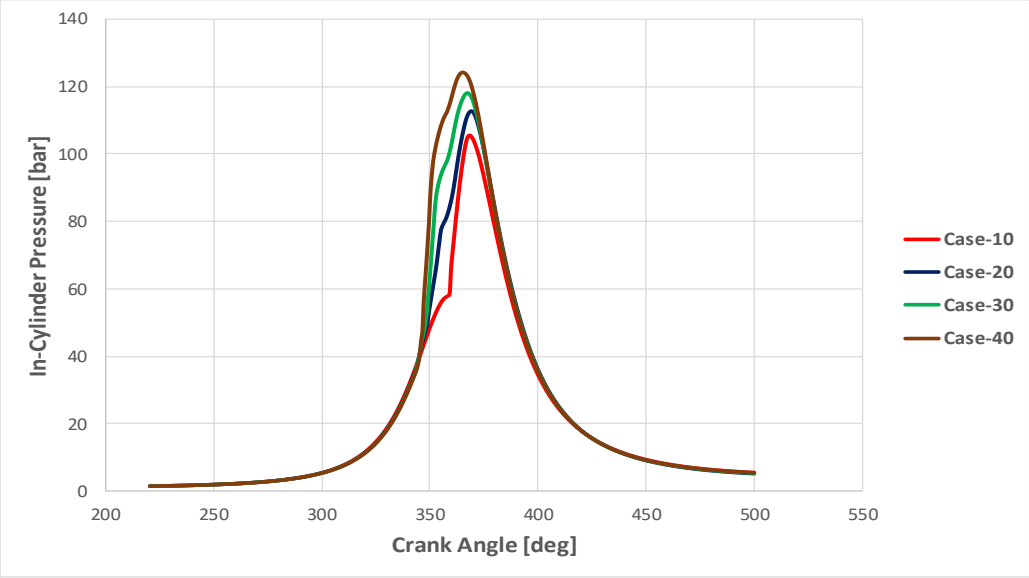


Figure 4.28 : The effect of injection ratio on in-cylinder pressure.

Figure 4.29 shows the effect of different injection ratios on mean cylinder temperatures. It can be inferred from the Figure 4.29 that the ignition of the initially injected fuel takes place only when a certain temperature (>800 [K]) is reached. For different injection ratios from 20 to 40%, the cylinder temperature is increasing gradually until the occurrence of initially injected fuel ignition. Once the ignition of initially injected fuel occurs there is a sharp rise in cylinder temperature. With increasing the injection ratio, the intensity of temperature rise is also increased and higher peak temperatures are obtained.

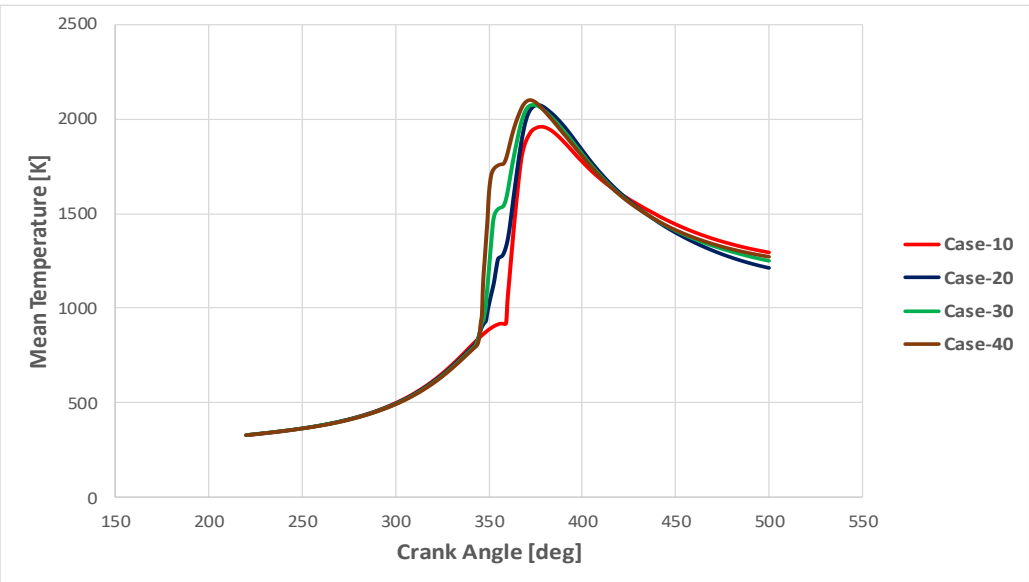


Figure 4.29 : The effect of injection ratio on temperature.

Observing Figure 4.29, with the increase of injection ratio, larger amount of fuel is burned before TDC and premixed combustion occurs earlier in the cycle, so in-cylinder temperature is increased at the start of expansion stroke, moreover, the burned gas expand through a larger temperature ratio prior to exhaust, and hence the combustion temperature is decreased at the end of expansion stroke. In another words, increasing the premixed ratio increases the in-cylinder temperature prior to the second injection timing and initiates the combustion before TDC which results in higher peak pressures, higher peak temperatures and lower exhaust temperatures.

Autoignition of the fuel plays a major role in the process of combustion in diesel engine. The PCCI chemistry determines the auto-ignition timing, the heat release rate, the reaction intermediates and the final products of combustion. Figures 4.30 and 4.31, respectively, illustrate the heat release rate and accumulated heat release curves with different injection ratios. As shown in Figure 4.30, there exists four phases in the entire heat release process;

1. premixed combustion of the first injection
2. diffusion combustion of the first injection
3. premixed combustion of the second or main injection
4. diffusion combustion of the second or main injection

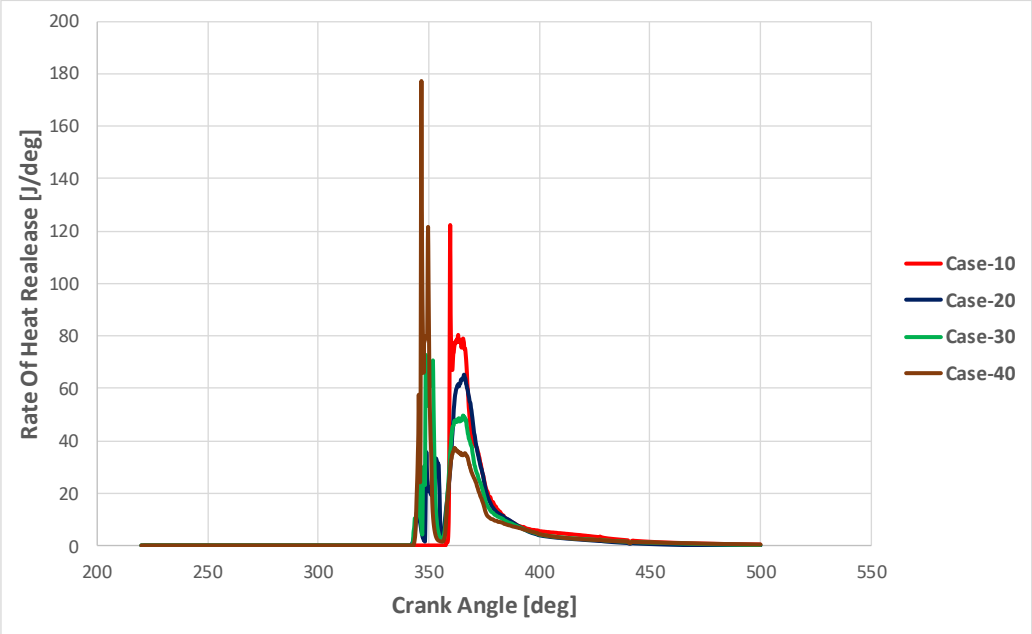


Figure 4.30 : The effect of injection ratio on rate of heat release.

The first injection promotes the premixed combustion and increase the local gas temperature and consequently develop the the combustion of main fuel that burns in diffusion mode. It is found that the increasing the first fuel quantity enables its auto-ignition prior to the second injection timing and result in predominantly premixed combustion. It is also observed that by increasing the injection ratio, larger amount of fuel is burned before the second injection. Unfortunately, in this study the initially injected fuel burns fully before the second injection timing.

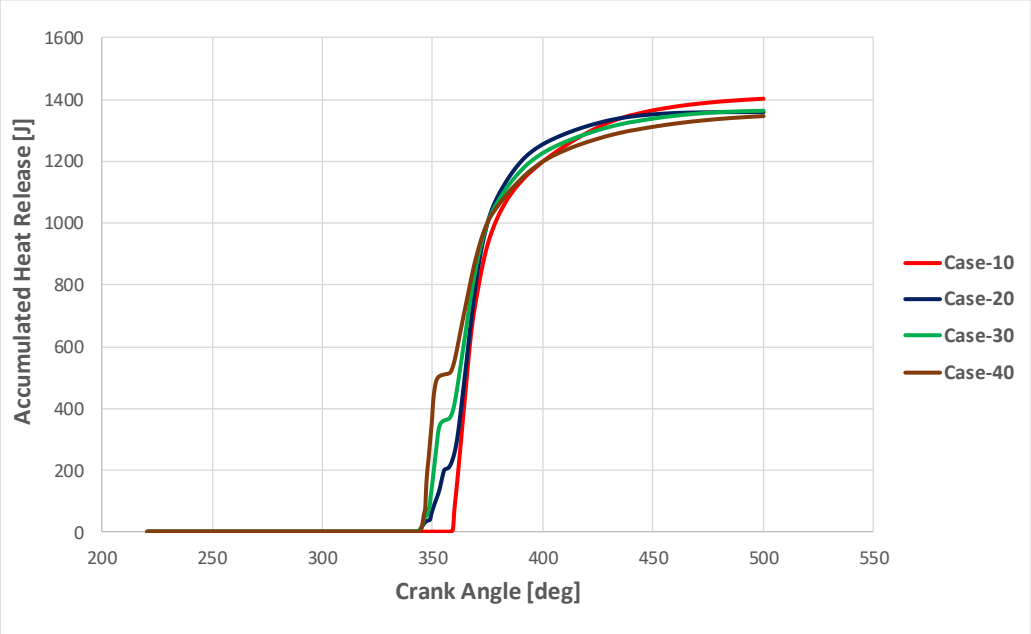


Figure 4.31 : The effect of injection ratio on accumulated heat release.

The ignition of first injection takes place at approximately 17 [CAD] BTDC in the cycle. This can be due to the temperature required for the initiation of combustion of firstly injected fuel. It is observed from the temperature profile (Figure 4.29) that the minimum temperature required for ignition of first injection is approximately equal to 800 [K]. Therefore, although the mixture is homogeneous, the ignition starts only when the required conditions are met. The chemistry of the firstly injected fuel plays an important role in the combustion and combustion phasing of the second or main injection.

Figure 4.33 shows the effect of different injection ratios on NO_x emissions. With increasing the injection ratio, higher peak temperatures are obtained. Thus NO_x emissions are increased gradually by increasing the injection ratio. As shown in Figure 4.33, for the injection ratios of higher than 20%, the amount of NO_x emissions

are higher than the single injection case. The results reveal that the only case which exhibits lower NO_x emissions in comparison with single injection is Case-20 (injection ratio of 20%). It is observed that the injection ratios greater than 20% cause the in-cylinder temperature to increase remarkably, as shown in Figure 4.29, and since a high temperature is a contributing factor to the NO_x formation, the amount of NO_x emissions are increased.

Figure 4.32 shows the in-cylinder temperature distributions and NO_x emission concentration contours with different injection ratios at 2 [CAD] ATDC.

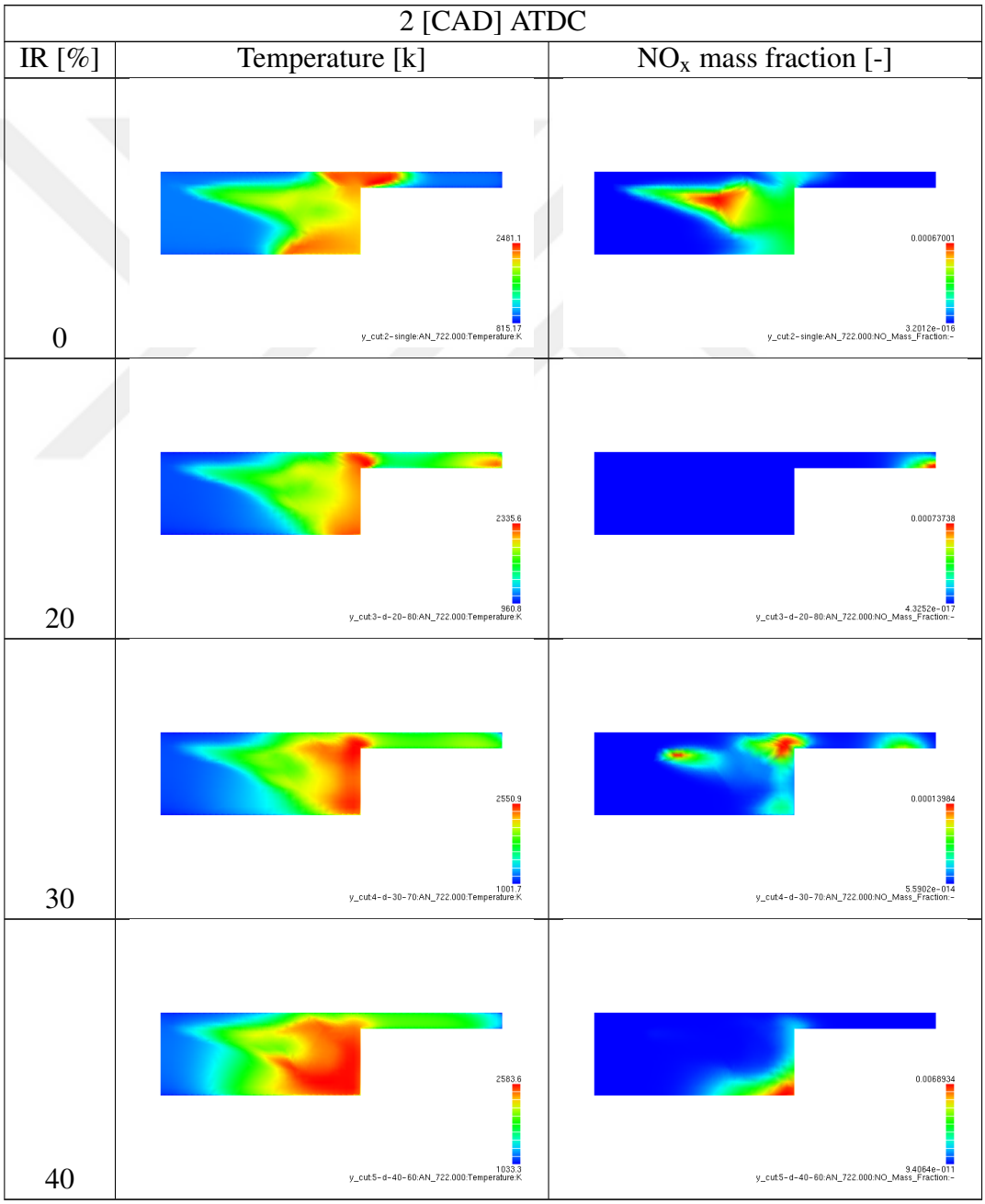


Figure 4.32 : In-cylinder distributions of temperature and NO_x emissions with different injection ratios @ 2 [CAD] ATDC

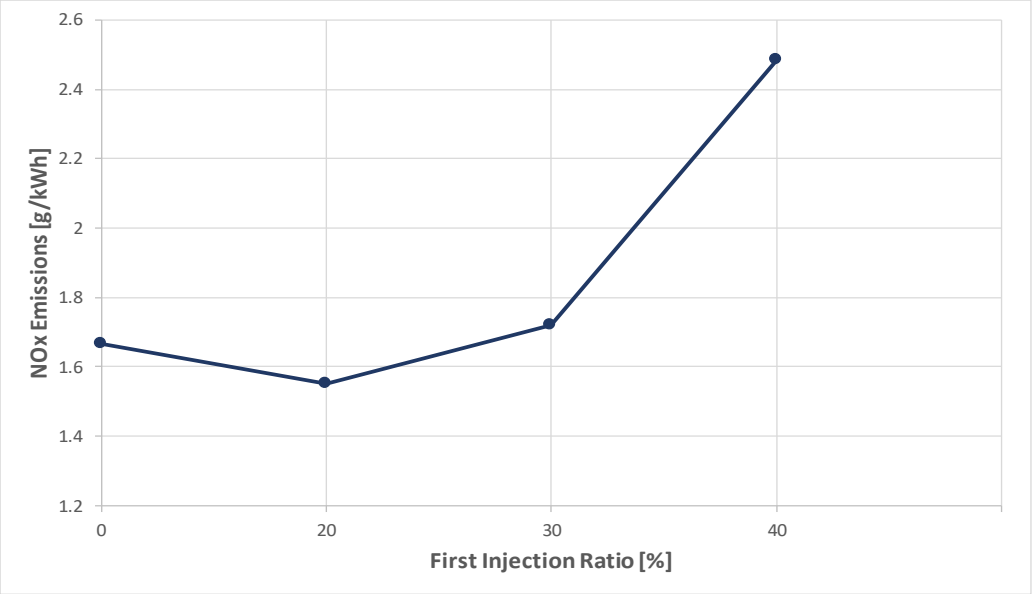


Figure 4.33 : The effect of injection ratio on NO_x emissions.

By premixing, the over-rich regions of the mixture is reduced and soot emissions are decreased. As illustrated in Figure 4.34, lower injection ratios produce noticeably lower soot emissions than single injection. However by increasing the injection ratio, soot emissions are also increased and the differences between single and multiple injection disappear, where the injection ratio of 40% produces slightly higher amount of soot emissions.

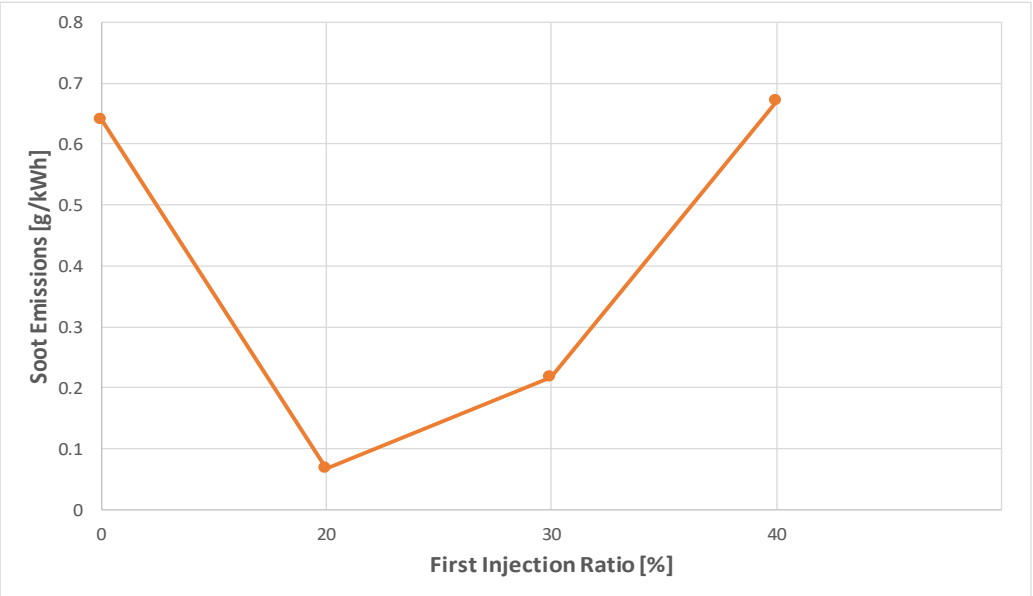


Figure 4.34 : The effect of injection ratio on soot emissions.

Figure 4.35 illustrates the effect of injection ratios on IMEP and indicated power. As it can be seen, although split injection produces higher IMEP and indicated power compared to single injection, by increasing the injection ratio, IMEP and indicated power are decreased and the differences become very low, where the injection ratio of 40% approximately has the same value of IMEP and indicated power with single injection. In comparison with single injection, IMEP and indicated power increase by about 3% with injection ratio of 20%.

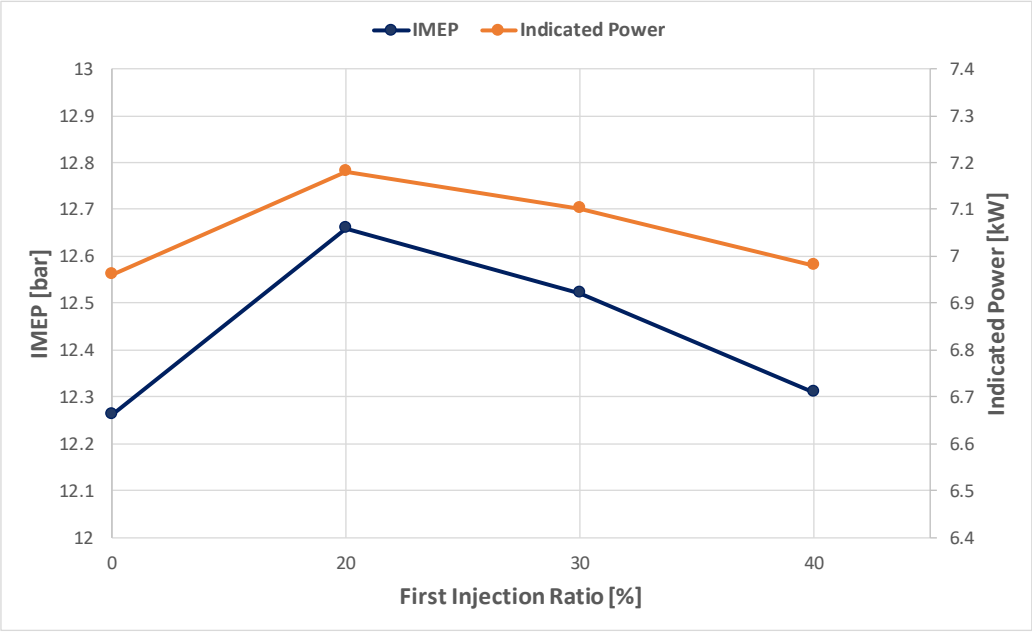


Figure 4.35 : The effect of injection ratio on IMEP and indicated power.

Figure 4.36 depicts the effect of injection ratios on ISFC. Compared to single injection, the ISFC is decreased considerably with split injection. However this reduction is decreased by increasing the injection ratio. The lowest ISFC is achieved with injection ratio of 20% which is about 213 [g/kWh]. In comparison with single injection, ISFC decreases by about 3% with injection ratio of 20%.

The engine designer's goal is obviously to achieve the best ISFC possible with emission levels low enough to satisfy the constraints imposed by emission standards. The results reveal that by using multiple injection strategy, it is possible to achieve lower engine-out emissions with an improvement in diesel engine performance. It is found that the multiple injection has the potential to reduce NO_x and soot emissions simultaneously. However, by increasing the injection ratio these advantages are diminished.

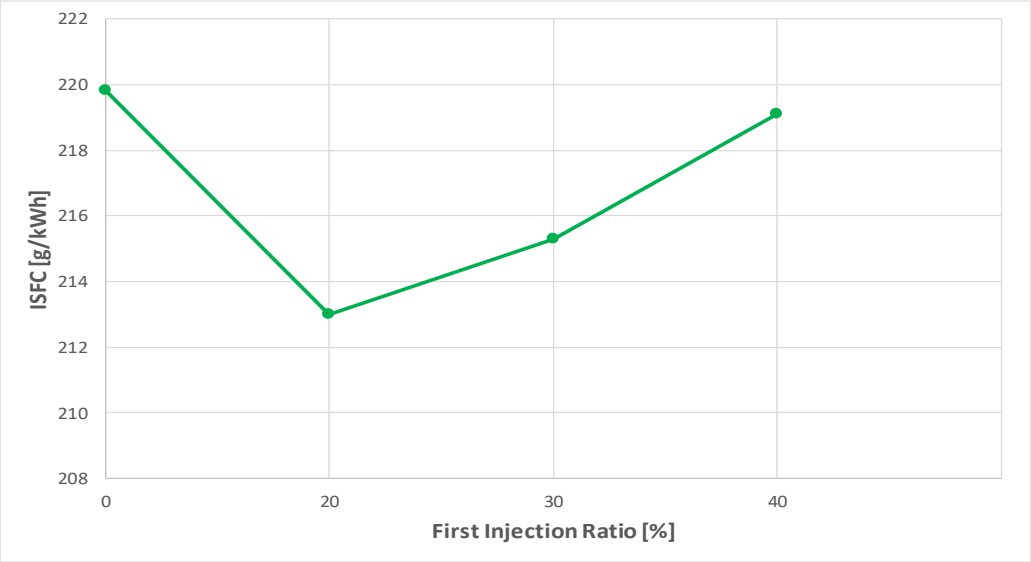


Figure 4.36 : The effect of injection ratio on ISFC.

Specific engine outputs with different injection ratios which are obtained by analyzing the simulation results via ESE Diesel analyser tool are summarized in Table 4.19.

Table 4.19 : Specific engine output with different injection ratios.

	Case-10	Case-20	Case-30	Case-40
Air mass at start of high pressure cycle [kg]	5.69E-04	5.69E-04	5.69E-04	5.69E-04
Air purity [-]	0.94	0.94	0.94	0.94
Air-fuel ratio of combustion [-]	17.74	17.74	17.74	17.74
Break mean effective pressure BMEP [bar]	10.5	10.89	10.76	10.55
Break specific fuel consumption BSFC [kg/kWh]	0.2567	0.2475	0.2506	0.2557
Combustion Noise - A + CAV Filter [dB]	94.73	91.51	94.22	95.74
Combustion Noise - A Filter [dB]	204.79	205.07	205.95	206.92
Combustion Noise - CAV Filter [dB]	95.26	92.11	94.93	96.73
Combustion Noise [dB]	222.32	223.3	223.94	224.57
Excess air ratio [-]	1.19	1.19	1.19	1.19
Friction mean effective pressure FMEP [bar]	1.76	1.76	1.76	1.76
Indicated efficiency [-]	0.39	0.4	0.39	0.39
Indicated fuel consumption (total fuel mass) ISFCtt [kg/kWh]	0.2198	0.213	0.2153	0.2191
Indicated fuel consumption (trapped fuel mass) ISFCtr [kg/kWh]	0.2198	0.213	0.2153	0.2191
Indicated mean effective pressure IMEP [bar]	12.26	12.66	12.52	12.31
Indicated power [kW]	6.96	7.18	7.1	6.98
Indicated specific power [kW/l]	15.33	15.82	15.65	15.39
Indicated specific torque [Nm/l]	97.6	100.71	99.64	97.95
Indicated torque [Nm]	44.31	45.72	45.23	44.46
Injected fuel mass [kg]	3.40E-05	3.40E-05	3.40E-05	3.40E-05
Mean mass [kg]	6.20E-04	6.22E-04	6.23E-04	6.24E-04
Mechanical efficiency [-]	0.86	0.86	0.86	0.86
Total mass at start of high pressure cycle [kg]	6.03E-04	6.03E-04	6.03E-04	6.03E-04
Volume displacement [m$\hat{3}$]	4.54E-04	4.54E-04	4.54E-04	4.54E-04

In the next sections the effects of EGR and first injection duration are investigated to check the possibility of using higher injection ratios without any negative effects on engine performance and exhaust emissions. EGR is varied from 5% to 20% and injection duration is varied from 35 [CAD] to 55[CAD] to find the optimum operating conditions.

4.3.2 Effect of EGR

In this section, effect of different EGR ratios 5%, 10%, 13%, 15%, 18%, 20% on performance and exhaust emissions of simulated engine with split injection are studied. As explained before, application of EGR reduces the intake oxygen concentration by replacing part of the intake fresh air with inert combustion products. Thus, the equivalence ratio of mixture is changed by applying EGR in DI diesel engine. The reason is that the amount of injected fuel for specific load is constant in DI diesel engine, while the oxygen concentration is decreased by increasing EGR rate.

Introducing EGR is a well known solution of NO_x emissions reduction. Figure 4.37 shows the effect of EGR on NO_x emissions. As it can be seen from the figure, NO_x emissions decrease drastically for all cases by introducing EGR. This results from the re-introduction of products of combustion into the cylinder, and since the recirculated inert components have higher specific heat capacities than air, they act as a heat sink. These non-reacting species increase the specific heat capacity of mixture and absorb energy during the reaction and hence act to decrease the flame temperature within the cylinder during the combustion.

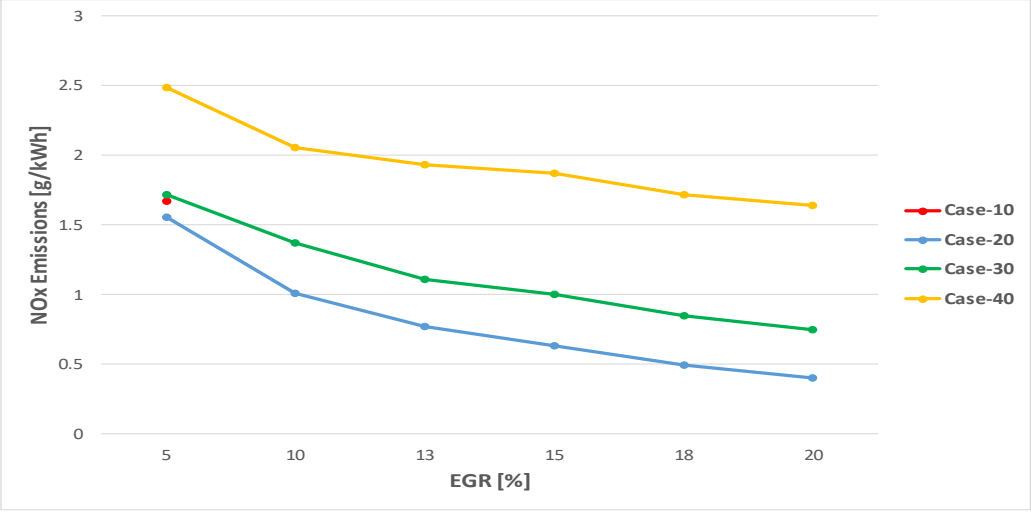


Figure 4.37 : The effect of EGR on NO_x emissions.

As described before, the main factors affecting NO_x formation include the local temperature and the local oxygen concentration. Thus the combination of low oxygen concentration and low in-cylinder temperature result in low levels of NO_x emissions. Figure 4.38 shows the effect of EGR on soot emissions. Although NO_x formation is reduced by utilizing high levels of EGR, there is generally a trade-off with the amount of soot emissions and soot emissions tend to increase as the EGR progressively increased. The lowered combustion temperature and lowered oxygen concentration as a result of applying higher EGR rates, are thought to weaken the soot oxidation process and hence reduce the soot oxidation rates, thereby increasing the soot emissions.

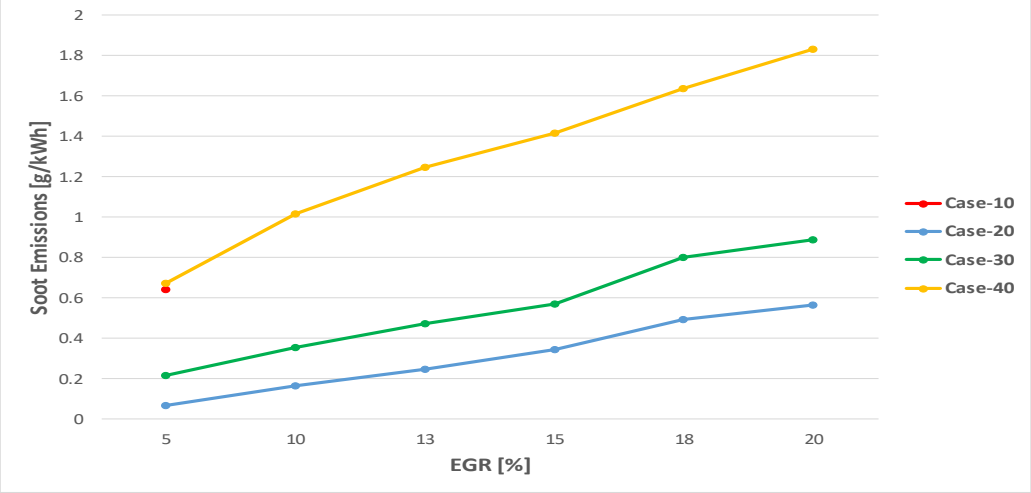


Figure 4.38 : The effect of EGR on soot emissions.

Figure 4.39 depicts the effect of various EGR rates on indicated power. As it can be seen, the indicated power is decreased steadily by increasing the EGR.

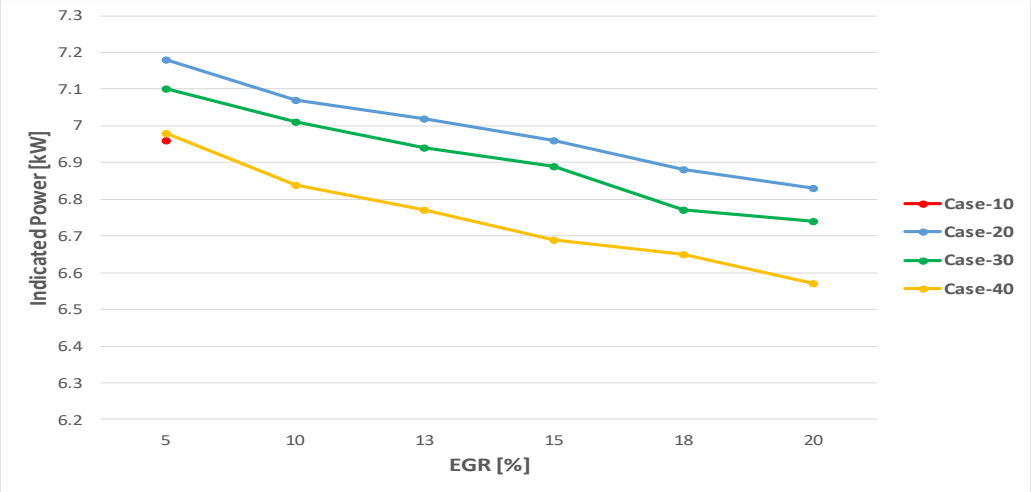


Figure 4.39 : The effect of EGR on indicated power.

Figure 4.40 illustrates the effect of EGR on ISFC for all cases. As shown in Figure 4.40 with the increase in EGR rate, oxygen available for combustion is reduced for the amount of fuel supplied, and hence the equivalence ratio is increased and results an increase of the ISFC.

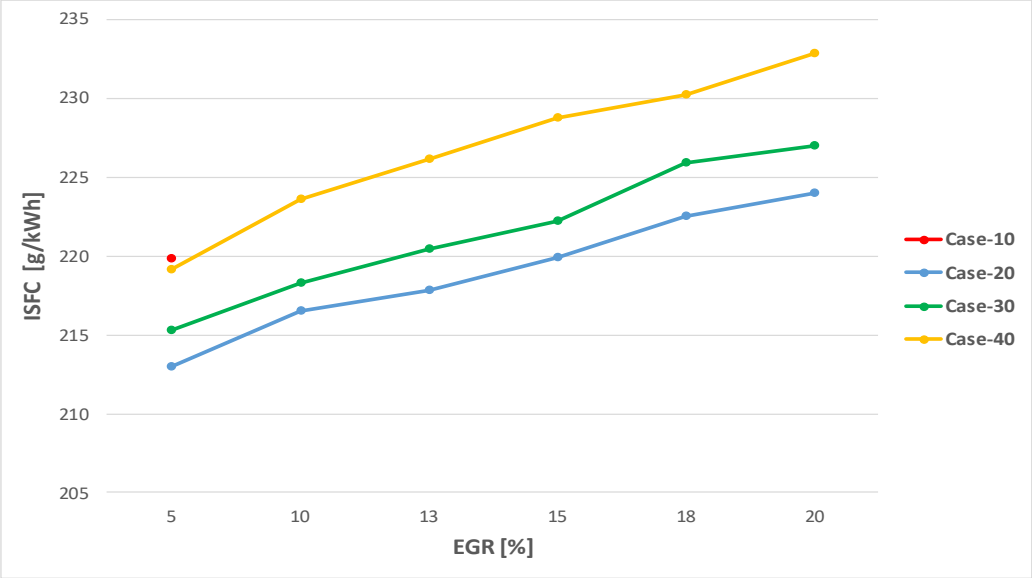


Figure 4.40 : The effect of EGR on ISFC.

As expected, although introducing EGR is an effective solution of reducing NO_x emissions, it has negative effects on indicated power output, ISFC and soot emissions. In order to reduce the EGR requirement while maintaining low NO_x and soot emissions, effect of first injection duration is investigated in the following section.

4.3.3 Effect of first injection duration with different EGR ratios

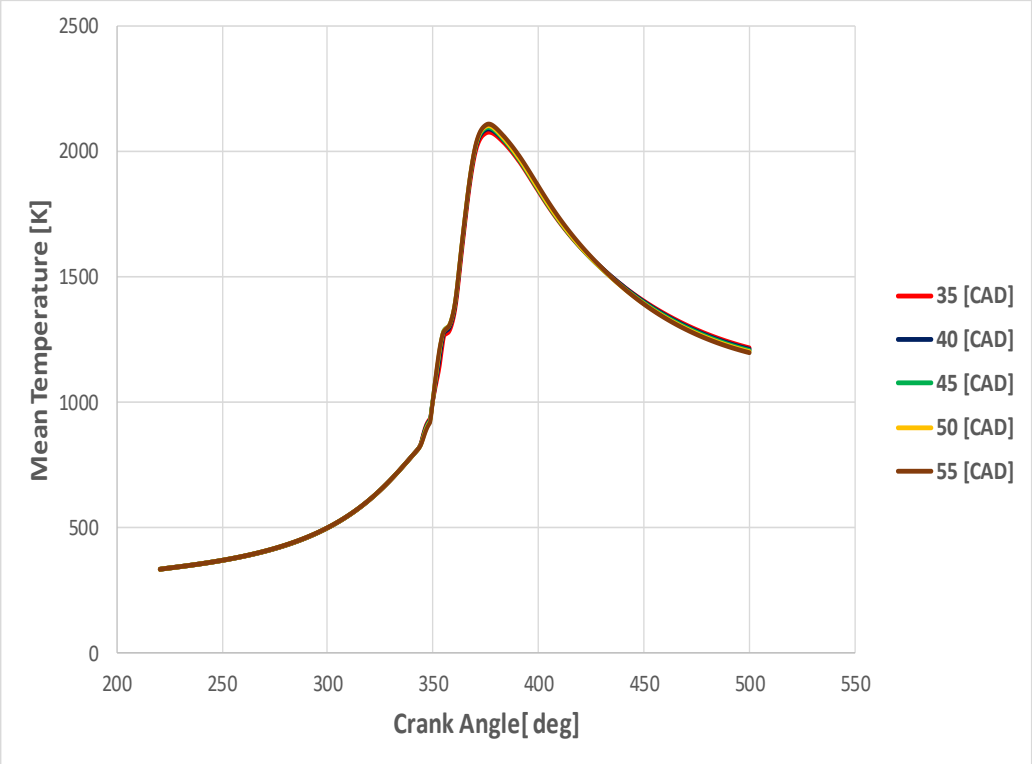
In this section the combined effects of EGR and first injection duration are investigated and compared with the previous results. In general, injection ratio and injection pressure significantly affect the injection duration. Since there is not any specific input for injection pressure in AVL FIRE® Workflow manager, by increasing the injection duration, it is assumed that the injection pressure is decreased. In this regard, various injection duration of 35, 40, 45, 50 and 55 [CAD] are set to first injection and combined effects of first injection duration with different EGR levels of 5% and 10% are studied. For identical fuel injection quantity, higher injection pressure would require shorter injection duration because of higher injection velocity from the nozzle exit. This is due to larger pressure difference between the fuel injection pressure and the ambient

pressure within the combustion chamber.

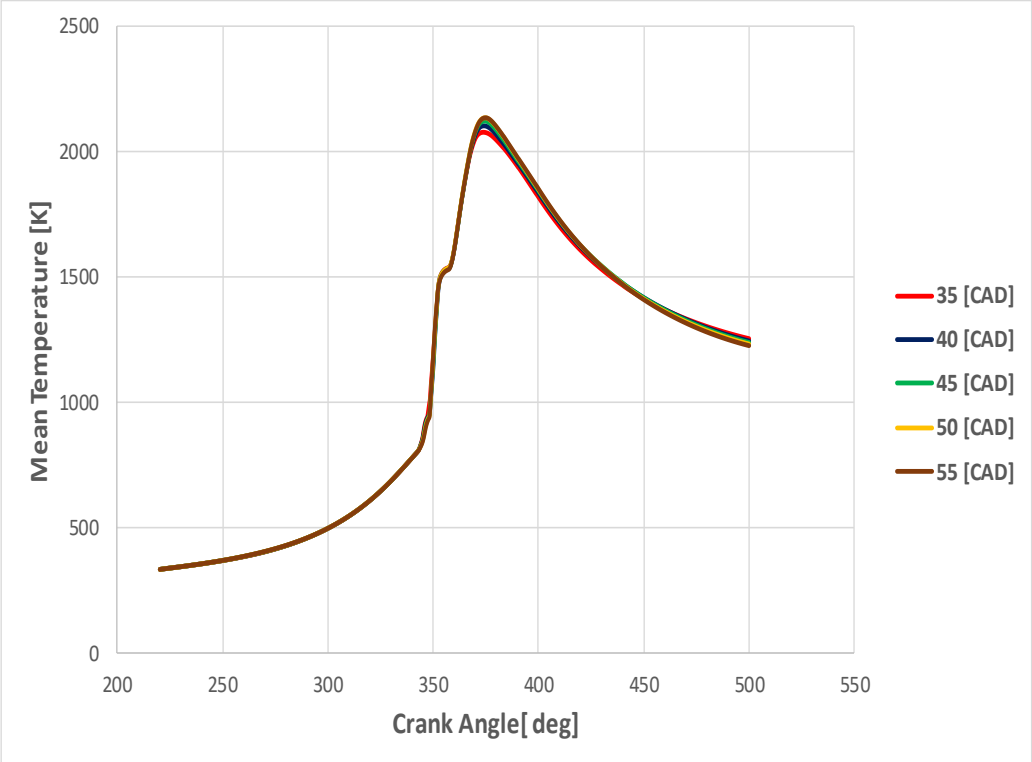
As explained, increasing the injection pressure or decreasing the injection duration, leading to finer spray droplets, which improve the fuel atomization, evaporation and hence the air-fuel mixing, thus increasing the premixed heat release that in turn, results in significant portion of heat being released during the compression stroke. As observed in section 4.3.1,the first injection duration of baseline simulations were constant for all cases and set to 35 [CAD], which means higher injection pressures for greater injection ratios. In this section by prolonging the first injection duration, the fuel evaporation and atomization are decelerated to decrease the amount of firstly injected fuel that is burned before the second injection timing.

Figure 4.41 depicts the effect of first injection duration on mean cylinder temperatures of Case-20 and Case-30, respectively. As shown in Figure 4.41, peak temperature is increased slightly with increasing the first injection duration. It is found that increasing the first injection duration weaken the atomization and resulting in a lower distributed vapor, hence poor air-fuel mixing. Therefore, some portion of firstly injected fuel added to secondly injected fuel and burn with the main injection and results in higher peak temperatures.

Figures 4.42 and 4.43, show the effect of injection duration on NO_x emissions with 5% and 10% EGR, respectively. As it can be seen, NO_x emissions increase steadily with increase of first injection duration for Case-20. For Case-30 and Case-40, it drops with injection duration of 40 [CAD] and then increase. For all cases, the highest amount of NO_x emissions are produced with longest injection duration of 55 [CAD]. In case of 5% EGR, in comparison with single injection, NO_x emissions are higher for all cases, except Case-20 with first injection duration of 35 [CAD]. While by increasing the EGR level to 10 %, as shown in Figure 4.43, NO_x emissions are decreased dramatically compared to the EGR of 5% and it is possible to achieve lower levels of NO_x emissions with 20% and 30% injection ratios in comparison with single injection. As it can be seen from the figures, with a proper combination of first injection duration and EGR level for each case, lower amount of NO_x can be produced. In case of 20% of injection ratio (Case-20) with first injection duration of 35 [CAD] and 10% EGR, NO_x emissions are decreased by 40%, and in case of 30% of injection ratio (Case-30) with first injection duration of 40 [CAD] and 10% EGR, NO_x emissions are decreased by 26%, compared to single injection.



(a) Case-20



(b) Case-30

Figure 4.41 : The effect of first injection duration on mean temperature with 5% EGR.

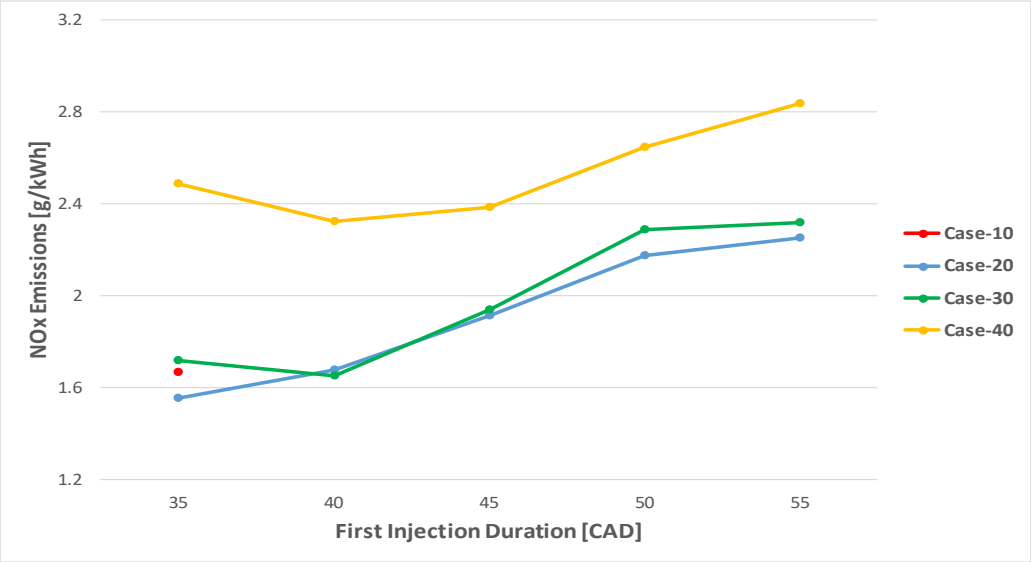


Figure 4.42 : The effect of first injection duration on NO_x emissions with 5% EGR.

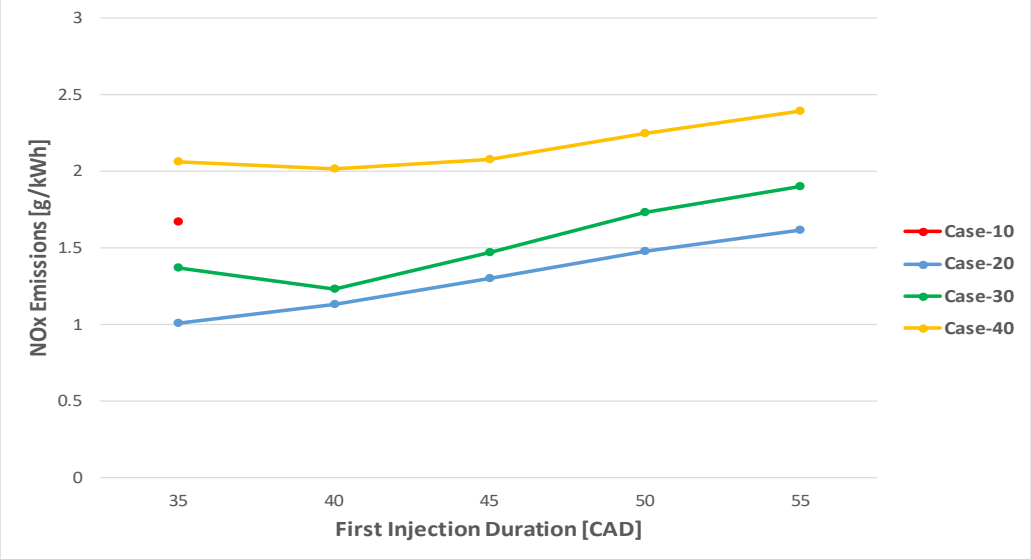


Figure 4.43 : The effect of first injection duration on NO_x emissions with 10% EGR.

Figures 4.44 and 4.38 depict the effect of injection duration on soot emissions with 5% and 10% EGR, respectively. The results indicate that soot emissions steadily fall with increase in first injection duration and this reduction occurs more intensely for Case-40. As it can be seen from Figure 4.44, compared to single injection, soot emissions of all cases are notably lower with longer duration of first injection and the lowest amount of soot emissions are produced with longest injection duration of 55 [CAD]. By increasing EGR to 10%, there is an increase in soot emissions for all cases, but with an increase in injection duration the amount of soot emission is

decreased and compared to single injection, with a proper selection of EGR and first injection duration, lower amount of soot emissions can be achieved. In case of 20% of injection ratio (Case-20) with first injection duration of 35 [CAD] and 10% EGR, soot emissions are decreased by 75%, and in case of 30% of injection ratio (Case-30) with first injection duration of 40 [CAD] and 10% EGR, soot emissions are decreased by 60%, compared to single injection. It is obvious that soot emission increases with the increase of EGR, but for simultaneous reduction of NO_x and soot emissions, 10% of EGR with 35 [CAD] of first injection duration for Case-20 and 40 [CAD] of first injection duration for Case-30 show better results than those of 5% EGR.

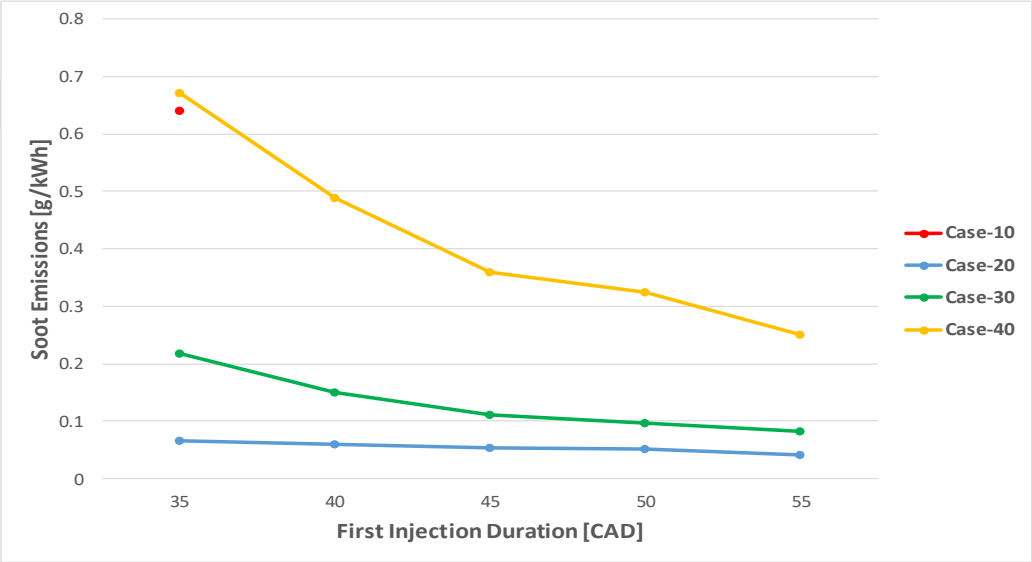


Figure 4.44 : The effect of first injection duration on soot emissions with 5% EGR.

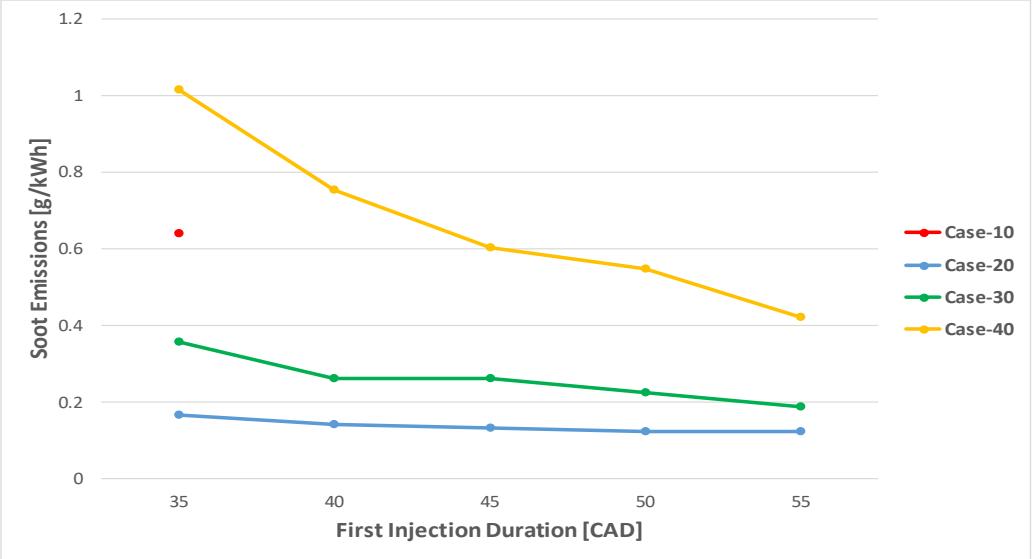


Figure 4.45 : The effect of first injection duration on soot emissions with 10% EGR.

Figures 4.46 and 4.47, illustrate the effect of injection duration on indicated power with 5% and 10% EGR, respectively. As it can be seen, indicated power increases steadily with increase of first injection duration. However, by increasing EGR to 10% the value of indicated power is decreased for all cases, in comparison with single injection, with selection of longer injection duration, higher indicated power output can be obtained. In case of 20% of injection ratio (Case-20) with first injection duration of 35 [CAD] and 5% EGR, indicated power is increased by 3%, and in case of 30% of injection ratio (Case-30) with first injection duration of 40 [CAD] and 10% EGR, indicated power is increased by 1.6%, compared to single injection.

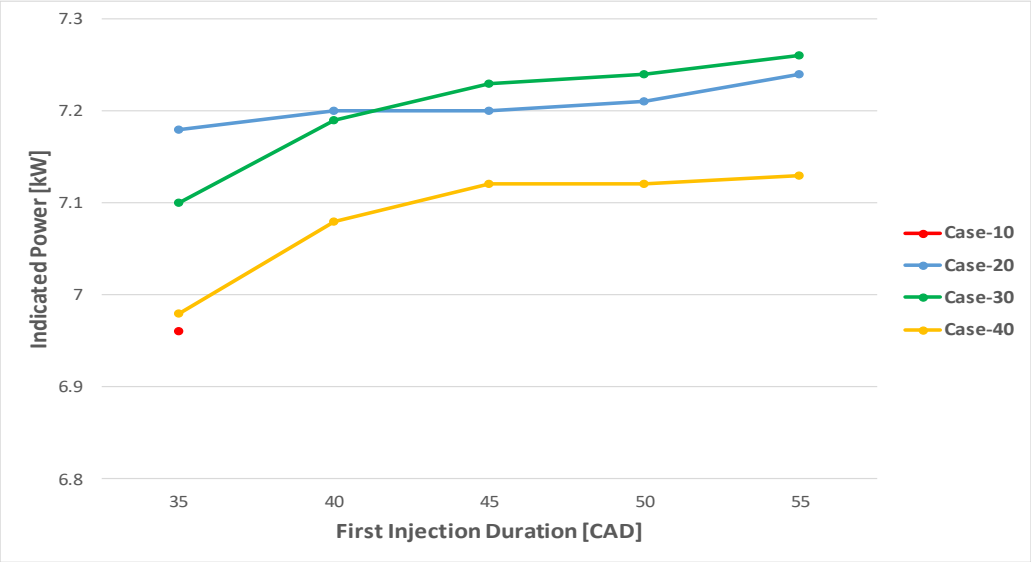


Figure 4.46 : The effect of first injection duration on indicated power with 5% EGR.

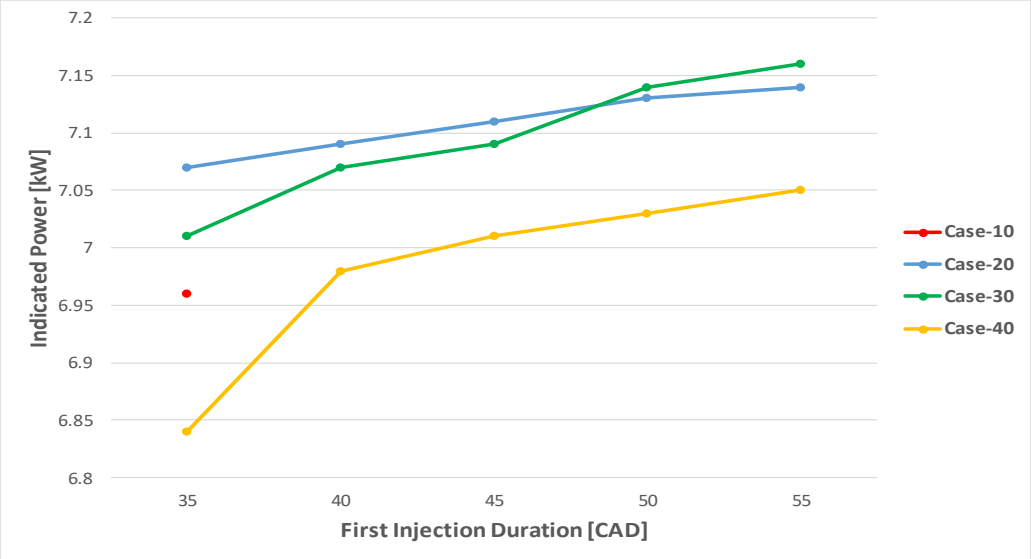


Figure 4.47 : The effect of first injection duration on indicated power with 10% EGR.

Figures 4.46 and 4.47, demonstrate the effect of injection duration on ISFC with 5% and 10% EGR, respectively. As it can be seen, ISFC decreases steadily with increase of first injection duration. However, by increasing EGR to 10% the ISFC is increased for all cases, in comparison with single injection, with selection of longer injection duration, lower ISFC can be achieved. In case of 20% of injection ratio (Case-20) with first injection duration of 35 [CAD] and 5% EGR, the ISFC is decreased by 3%, and in case of 30% of injection ratio (Case-30) with first injection duration of 40 [CAD] and 10% EGR, the ISFC is decreased by 1.6%, compared to single injection.

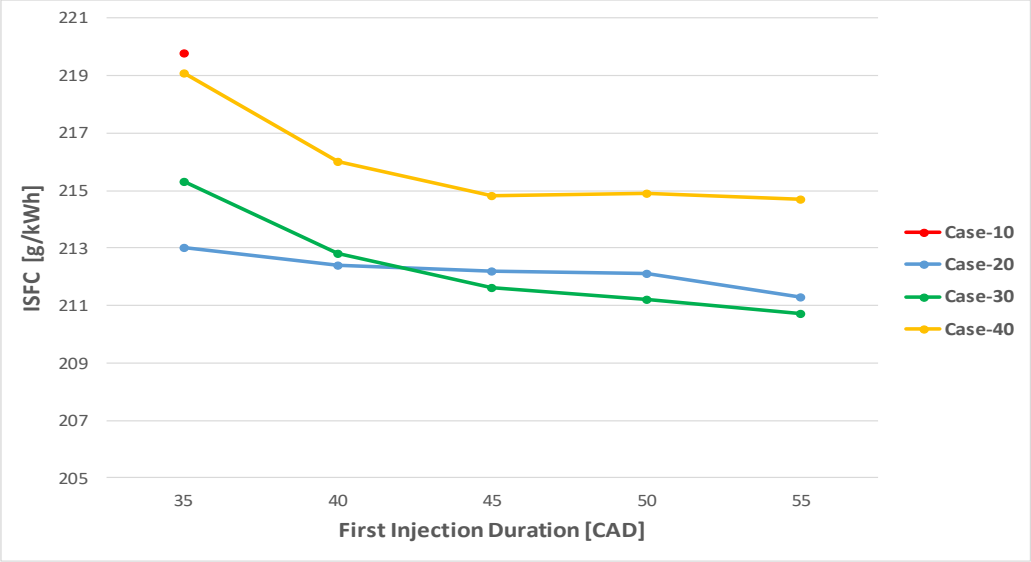


Figure 4.48 : The effect of first injection duration on ISFC with 5% EGR.

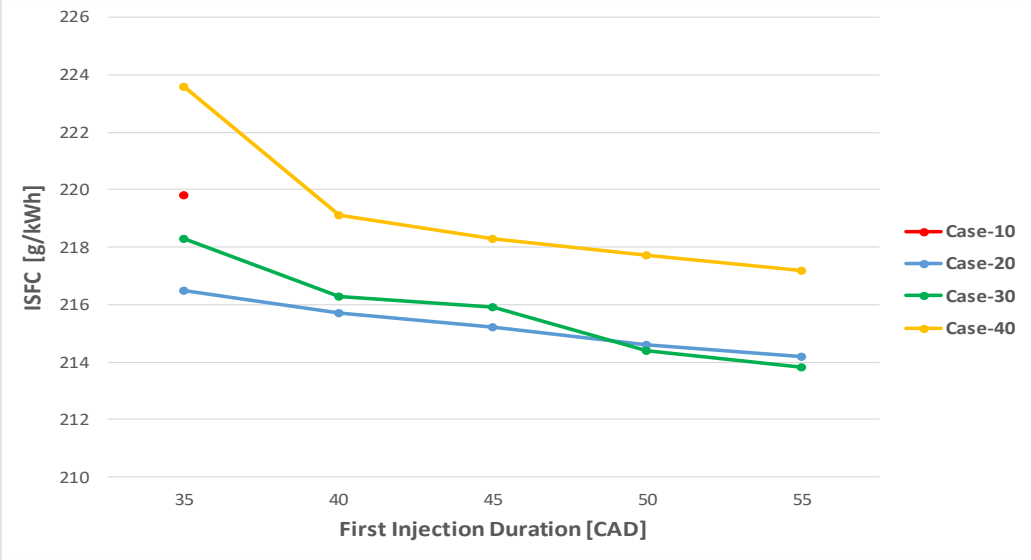


Figure 4.49 : The effect of first injection duration on ISFC with 10% EGR.

In summary, the results reveal that multiple injection strategy with proper selection of injection ratio, first injection duration and EGR level has the potential to reduce NO_x , soot emissions and ISFC simultaneously. It is found that that by using multiple injection strategy, it is possible to achieve lower engine-out emissions with an improvement in diesel engine performance, however, injection ratio of 40% shows slightly higher NO_x emissions.

5. CONCLUSIONS AND RECOMMENDATIONS

5.1 Conclusion

In this study, multi-dimensional CFD models are developed to perform the simulations of single cylinder IC engine by using the commercially available AVL FIRE® CFD code. Meshes are generated by ESE Diesel tool, then in-cylinder processes are simulated via Workflow Manager tool. The governing equations are solved from the intake valve closing (IVC) to exhaust valve opening (EVO). This section reports the result of detailed simulation of the combustion and emissions characteristics of various combustion modes using a single cylinder engine.

- **Validation**

  In the first part, a validation study is presented. The grid sensitivity of multi-dimensional engine CFD is checked by generating five different grid resolutions. The selected mesh represents a compromise between computational time and accuracy, but is found to give adequately grid independent results. The simulated SI engine is validated by available experimental test results. In this regard, in-cylinder pressure, heat release rate, specific fuel consumption, brake mean effective pressure, brake power and emissions predictions are compared with the measured experimental results at three different engine speeds of 1500[rpm], 1660 [rpm] and 1800[rpm]. The results of the simulation are in quite well qualitative and quantitative agreement with the corresponding experimental data. The peak pressure discrepancy between experiment and computation is even less than 0.6 %, which demonstrated the predictive capabilities of the adopted models. The timing of the heat release initiation and the timing of the peak heat release rate and peak value of the heat release rate are in good agreement with those of measured experimental heat release rate. Indeed in case of engine performance characteristics, it can be seen from the presented diagrams, the simulated and

experimental data matched quite well and a sufficient correlation with experimental results are achieved.

- **Parametric Study**

  The verified model is then applied to the prediction of combustion process for different EGR ratios, equivalence ratios and spark advances at the engine speed of 1500[rpm].

  - EGR

    In this regard, various levels of EGR 0, 5, 10, 13, 15, 18 and 20% are adopted in simulated SI engine to understand its effect on SI engine performance and emissions behavior.

    1. EGR showed a promising way of suppressing peak cylinder pressure and peak pressure rise rate. With the increase in the EGR percentage, the peak cylinder pressure and peak pressure rise rate decreased drastically. The peak cylinder pressure at a 10% EGR rate decreased approximately by 40% and decreased by 67% at a EGR rate of 20% compared with the peak cylinder pressure at a 0% EGR rate. However, poor combustion is occurred by applying EGR rates higher than 18% and those cases are not preferable. Attempts to increase EGR levels for higher than 18% resulted in combustion instability and misfire.
    2. Higher percentages of EGR introduce more exhaust gasses into the cylinder, thus more non-reacting species and lower combustion temperatures. Moreover peak combustion temperatures are retarded and occurs late in expansion stroke. Adding EGR decreases the flame propagation speed ,and hence the combustion duration is increased and postponed to the expansion stroke. The varying trend of in-cylinder mean temperature suggests that the applying EGR is a useful method to reduce the flame temperature for controlling NO_x formation in a SI engine. In this case, when EGR varies from 0% to 18%, the peak value of in-cylinder mean temperature decreases from 2671.5 [K] to 1851.7 [K] which means 31% reduction in peak mean temperature and also retards by 80 [CAD].

3. It is found that EGR greatly affects the heat release rate. The maximum heat release rate is decreased and the corresponding crank angle position is postponed with an increase in EGR rate. By increasing EGR from 0% to 18%, maximum rate of heat release is decreased by 78%. When EGR is applied, the in-cylinder temperature and pressure reduce due to the dilution effect of EGR along with higher specific heat capacity of mixture as a consequence of added inert gas, lead to a longer ignition delay and retarded SOC, which inhibiting the heat release.
4. By introducing EGR the flame propagation speed is decreased and hence the combustion duration is increased and moves towards the expansion stroke.It is found that, when EGR increases from 0% to 18%, combustion duration is prolonged by 57 [CAD] and the start of combustion is retarded by about 15 [CAD].
5. Since the peak combustion temperature and available oxygen concentration are widely believed as the most significant parameters affecting NO_x production, EGR has proven to be very effective in reducing the exhaust NO_x emissions. The simulated SI engine is able to realize a significant reduction in NO_x emissions by about 50% with 10% EGR and approximately 89% with 15% EGR, compared to operating with 0% EGR.
6. Due to decrease of burning rate and oxygen concentration, HC emissions increase with increasing EGR.
7. The results reveal that an increase of EGR from 0% to 18%, cause a dramatic reduction of IMEP and indicated power by 44%.
8. ISFC is found to be largely a function of combustion phasing and an increase in EGR rate results in higher fuel consumption. This is mainly result of decreased combustion efficiency due to later phasing of combustion and longer combustion duration. The ISFC increases by 47% as the EGR increases from 0% to 18%.

The results indicate that the combustion with a low level of EGR (10%) leads to a drastic reduction in NO_x emissions and a slight decrease in CO emission in parallel with a very low and negligible increase in ISFC and soot emissions.

From the viewpoints of emission and performance, 10% of EGR seems to be the most desirable amount.

- Equivalence Ratio

  Equivalence ratio (ϕ) is changed between 0.8 and 12.5 to cover the lean and rich regions.

  1. It is found that slightly rich mixture ($\phi \approx 1.1$) produces higher peak pressure and as the equivalence ratio moves leaner or richer, peak in-cylinder pressure decreases.
  2. Minimum in-cylinder temperature is obtained with an equivalence ratio of 0.8 and the maximum temperatures occur at the start of expansion stroke of a slightly rich combustion and during the end of expansion stroke of a stoichiometric combustion.
  3. The maximum value of heat release rate is gained at a slightly rich combustion with an equivalence ratio of 1.1. It is found that the combustion duration of a slightly rich mixtures , where the laminar flame speed is higher, are shorter than that of stoichiometric mixture by about 3 [CAD]. Moreover, very lean mixture burns very slowly and has the longest combustion duration, since low amount of fuel is available for combustion, the mean cylinder temperature and flame propagation speed are low in this case.
  4. Leaner mixtures give low emissions until the combustion quality becomes poor, engine operation becomes erratic and eventually misfire occurs.
  5. Although combustion temperatures of rich mixtures are high, they have low oxygen concentrations, so produce low levels of NO_x . As the mixture is leaned out, increasing oxygen concentration initially offsets the falling gas temperatures and NO_x emissions peak at $\phi \approx 0.95$. Then, decreasing temperatures dominate and NO_x emissions decrease to low levels.
  6. The indicated mean effective pressure is increased by increasing the equivalence ratio up to 1.1. The maximum value of indicated mean

effective pressure is obtained at a slightly rich combustion with an equivalence ratio of 1.1.

7. There is a decrease in ISFC with increment of equivalence ratio from 0.8 to around 1. But further increase of equivalence ratio leads to the significant increasing of ISFC due to a reduction in combustion efficiency.

– Spark Timing

The effect of various spark timings 90 [CAD] BTDC, 55 [CAD] BTDC, 49 [CAD] BTDC, 45 [CAD] BTDC, 40 [CAD] BTDC, 35 [CAD] BTDC, 30 [CAD] BTDC and 25 [CAD] BTDC) on exhaust emissions and performance characteristics of SI engine are also investigated.

1. It is found that the spark timing of 311 [CAD] or 49 [CAD] BTDC gives maximum brake torque and minimum ISFC, and hence can be selected as the optimum spark timing.
2. By retarding the spark timing from 311 [CAD](MBT) to 330 [CAD], the peak pressure value is decreased by about 40%. Retarding the sparking timing beyond MBT time leads to increasing the combustion duration. Late ignition timing extends the combustion process longer into the expansion stroke, resulting in higher exhaust temperature. By advancing the timing, combustion occurs earlier in the cycle and increases the peak cylinder pressure, since more fuel is burned before TDC and the peak pressure moves closer to TDC where the cylinder volume is smaller. Retarding the timing on the other hand decreases the peak cylinder pressure, because more fuel burns after TDC.
3. Advancing the spark timing increases the partial oxidation during the compression stroke and initiates the combustion before TDC which results in higher peak pressures, higher peak temperatures and lower exhaust temperatures. On the other hand, when the spark timing is retarded, there is less time between ignition timing and TDC to complete the chemical reaction, so large amount of fuel burns after TDC in the expansion stroke which results incomplete combustion and an increase in the exhaust temperature.

4. Higher peak cylinder pressures result in higher peak cylinder temperatures, and hence higher formation rates of NO_x . By retarding the spark timing from 49 [CAD] BTDC to 30 [CAD] BTDC, the peak cylinder temperature is decreased from 2553 [K] to 2327 [K] (9%), while the exhaust temperature is increased from 1488 [K] to 1617 [K] (9%).
5. Results reveal that, by retarding the spark timing from 49 [CAD] BTDC to 30 [CAD] BTDC, maximum rate of heat release is decreased by 26% and occurred 15 [CAD] later.
6. Retarding the sparking timing beyond MBT time leads to increasing the combustion duration. Late ignition timing extends the combustion process longer into the expansion stroke, resulting in higher exhaust temperature. Advancing the ignition timing causes combustion to occur early in the cycle that in turn, moves the peak pressure closer to TDC and increases the temperature during the combustion process, and hence increases the burning velocity.
7. As expected, an increase in burning velocity leads to reduction of the combustion duration. In comparison with retarded spark timing of 30°[CA] BTDC, it is found that the combustion duration of MBT timing is shorter by about 10[CAD].
8. NO_x emissions steadily decrease as spark timing is retarded and moved closer to TDC. Compared with MBT spark timing, 41% reduction of NO_x is possible when spark timing is retarded and set to 30 [CAD] BTDC.
9. When the exhaust temperatures increase as a result of retarded spark timing, CO emissions are decreased. At the spark timing of 25°[CA] BTDC, due to incomplete combustion some amount of CO is not oxidised ,and hence higher amount of CO emission is produced.
10. Advancing the spark timing increases the combustion temperature and reduces the combustion duration, and thus promotes more complete combustion which leads to lower levels of unburned hydrocarbon emission. While retarded timing results an inefficient combustion and hence higher amount of HC emissions.

11. For the sake of gaining high efficiency with very low ISFC, it is possible to set the spark timing to minimum spark advance of 49 [CAD] BTDC (MBT). Advancing the ignition timing to 311 [CAD](MBT) leads to 7.5% reduction of ISFC compared to the spark timing of 330 [CAD].

- **Natural gas fueled SI engine**

  In order to carry on the study, additional simulations are done by applying the natural gas (methane) as an alternative fuel and the performance and emission characteristics of CNG engine are compared with those of validated gasoline engine. The mesh structure, boundary and initial conditions, combustion and emission models, spark timing and engine speed are as same as the verified baseline model (case-44) and only the type of fuel is changed to natural gas.

  1. As described in section 3.5, the fraction of chemical energy of the natural gas which is released as sensible energy near TDC is greater. This causes an intense increase in temperature and pressure of natural gas combustion at the start of expansion stroke and subsequent reduction at the rest of stroke due to expansion and quenching.
  2. By using natural gas as fuel, peak pressure position is advanced by 4[CAD] and its value is increased by about 9.4% compared to the peak in-cylinder pressure of gasoline combustion.
  3. The combination of lower combustion temperature and lower amount of intake air leads to lower NO_x formation of CNG engine.
  4. The amount of CO emissions can be decreased by more than 40% and also NO_x reduction of 14% is possible when the engine operates on natural gas instead of gasoline.
  5. The results reveal that the engine-out unburned hydrocarbon emissions can also be reduced below the corresponding levels for gasoline engine, since the gaseous state of natural gas avoids wall wetting effects on intake manifold and cylinder liner.
  6. With same operating conditions for CNG engine lower amount of air is induced into the cylinder and the volumetric efficiency of CNG engine is reduced by 7.3%. Moreover, by considering the stoichiometric air-fuel ratio

of natural gas which is about 17.2, lower amount of intake air results in lower amount of supplied natural gas fuel to keep the air-fuel ratio of combustion equal to stoichiometric.

7. It is observed that by using natural gas as fuel the indicated power output is reduced by about 8% compared to the gasoline fueled engine under similar conditions. This is primarily because of lower density of natural gas, which requires the induction of a large volume of natural gas in order to produce similar power levels as gasoline engine.

8. The ISFC of natural gas fueled engine is 13% lower than that of gasoline engine. The reason is that, the stoichiometric air-fuel ratio of natural gas is about 17.2 and higher than that of gasoline which is about 14.9, and also LHV of natural gas is higher than gasoline which means lower amount of fuel is needed for the same work output.

- **Natural gas fueled HCCI engine**

  In addition to conventional natural gas fueled SI engine, a low temperature combustion strategy known as Homogeneous Charge Compression Ignition (HCCI) is developed by using natural gas as fuel. Proper operation of an HCCI combustion engine with natural gas is difficult mainly because of the fuel resistance to auto-ignition. Natural gas combustion in HCCI combustion engines needs high initial temperatures, achieved by high levels of pre-heating or a high compression ratio. In addition, because of the high rate of heat release, the mixture has to be heavily diluted with EGR or excess air to prevent combustion knocking. As a result, natural gas HCCI combustion is more difficult to achieve in comparison to that of other liquid fuels. For the sake of presenting a meaningful comparison with the simulation results of conventional natural gas and gasoline fueled SI engines, both gasoline and HCCI engine are considered to operate under the same load (IMEP=4.76[bar]) at engine speed of 1500 [rpm].

  1. In case of HCCI engine, because the compression ratio is higher and the whole charge reacts simultaneously, the heat is released in a very short time, resulting in an intense pressure rise and higher peak pressure compared to the conventional SI engines. Noticeable distinctions concerning with the peak

pressure value and the crank angle position corresponding to the in-cylinder peak pressure are exhibited with different engines.

2. Although both SI-Gasoline and HCCI-NG engines operate under same load (low load), fast combustion of HCCI causes very high and fast pressure rise and the peak pressure of HCCI combustion is four times higher than that of SI-Gasoline engine, and is approximately 3.6 times more than the peak pressure of SI-NG engine. The results reveal that the operating range of HCCI engine is bounded to moderate loads, by virtue of enormously rapid pressure rise (high combustion rate) occurred in high load conditions and resultant knock. This rapid rates of pressure rise and strong in-cylinder pressure waves can damage the engine over time and cause excessive noise.

3. Inasmuch as the reactions of HCCI combustion occur simultaneously, the compression effect on the burned gases is absent. As long as the HCCI engine operates with lean mixture, the overall combustion temperature is significantly reduced by the presence of excess air and the peak temperature of HCCI combustion is about 1620 [K] while in case of SI engines the temperature of a gas element burned just after spark discharge can reach over 2300 [K]. The high levels of charge dilution in HCCI cause lower in-cylinder temperatures compared with SI engines, which is important in determining the emissions characteristics of HCCI engine.

4. The HCCI engine lacks direct combustion phasing control approaches such as spark in SI engines and injection in diesel engines, and its ignition timing is predominantly determined by the chemical kinetics. As a result, the entire time history of temperature, pressure, composition and other factors has an effect on determining ignition timing. This complex interaction of parameters makes combustion timing more difficult to control in HCCI in comparison with SI engines. Also compared to SI engines, the fuel chemistry plays more important role in determining combustion characteristics of HCCI engine.

5. Since the whole charge is involved simultaneously in the combustion process, heat release of HCCI combustion has shorter overall duration with higher peak value than the conventional ones and the majority of heat release occurs in a very short period. The rapid release of heat from the fast burning process in

HCCI is one of the basic reasons for power output limitations of HCCI engine. Excessive rates of heat release and the accompanying excessive pressure rise rates can damage the engine over time.

6. From the results, the start of HCCI combustion occurs when the in-cylinder gas temperature reaches a value of 1030 [K]. This required high temperature for autoignition of natural gas is attributed to its high octane number.

7. HCCI-NG engine has the shortest duration of combustion among the engines. The combustion starts at 11 [CAD] BTDC and ends at 16 [CAD] ATDC, which means that a fast combustion occurs in a small volume and results in rapid pressure rise and higher peak pressure in comparison with SI engines in which, the combustion starts later and occurs in a larger volume.

8. Because the HCCI engine can be run under the WOT (wide open throttle) condition even for a part load operation and the equivalence ratio varies with the load, just as it does in a diesel engine, the pumping losses are extremely lower than in an SI operation at low and intermediate loads. This contributes to the relatively high efficiency of HCCI combustion at the part load operation. Other advantages over SI operation are faster combustion and the reduction in heat loss due to the low combustion temperature.

9. The HCCI-NG presents the best fuel economy among the simulated engines due to the above mentioned reasons. At part-load conditions because the HCCI engine operates with very lean mixture ($\phi = 0.355$) in absence of throttling and also delivers a power density similar to SI engine (2.7 [kW]), the ISFC of HCCI-NG engine is remarkably lower than that of SI-Gasoline and SI-NG engines. Under the condition with same engine speed of 1500 [rpm] and 4.76 [bar] of IMEP, the HCCI mode indicates the ISFC of 152.3 [g/kWh], which is approximately 37% lower than that of gasoline fueled SI engine and is lower by about 27% than the ISFC of natural gas fueled SI engine.

10. The results prove that in comparison with SI engine, a noticeable improvement in fuel economy can be achieved by implementing the HCCI strategy.

11. Given that the HCCI combustion takes advantage of highly diluted charges (lean mixture), peak in-cylinder temperature remains very low in comparison

to SI engines. As a result, HCCI engine produces tremendously lower levels of NO_x emissions compared to SI engines.

12. The results indicate that the unburned HC emissions of HCCI-NG engine are drastically higher than those of SI-Gasoline and SI-NG engines. This increase is attributed to the burned gas temperature which is too low to consume much of fuel and results in incomplete oxidations, and hence significant increase in HC emissions compared to conventional combustion. However, these levels of HC emissions can be easily reduced by means of a common oxidation catalytic convertor.

- **Diesel engine**

  In the second part of this research, first a conventional single cylinder diesel engine under full load condition at engine speed of 1500[rpm] is simulated with AVL FIRE® CFD code, and then the individual and combined effects of EGR and engine load on combustion and engine-out emissions are studied. Moreover, in order to achieve the partially premixed compression ignition and lower temperature combustion of diesel engine, the effects of multiple injection strategies including injection ratio and first injection duration on performance and exhaust emissions of diesel engine are investigated.

  - Single injection

    * Engine load

      In contrast to SI engine, the air flow at given speed of diesel engine is essentially unchanged and the load control is achieved by varying the amount of injected fuel per cycle. In this section, the individual effect of load variation at constant engine speed of 1500 [rpm] is evaluated in terms of ignition delay, ISFC, exhaust gas temperature and exhaust emissions. In this regard, the injection quantity is decreased and two more simulations are done for engine operation under medium and low loads (IMEP).

      1. The ignition delay increases with decreasing load for this engine. As load decreases, the residual gas temperature and the wall temperature decrease and result in lower charge temperature

at injection point which weaken fuel vaporization, and hence prolongs the ignition delay.

2. Reduction of injection quantity decreases the flame temperature and affect the local charge equivalence ratio which results a change in ϕ-T plane.
3. Compared to full load, NO_x emissions decrease by about 7% under medium load and approximately by 64% under low load.
4. In comparison with full load condition, the amount of soot emissions decreases by about 94% under medium load and approximately by 97% under low load.
5. At lower loads, the amount of fuel supplied to the combustion chamber is lower and lower energy is released which results in a reduction of the combustion temperature. Therefore, the heat losses to the walls are reduced because the burned gas temperatures are lower and ISFC is decreased by decreasing engine load.

* Engine load and EGR

In previous section, it was observed that the DI diesel engine produces lower amount of NO_x and soot emissions under part loads. In respect of preparing a supplementary study, different levels of EGR, 5%, 10%, 20% and 30% are used to investigate the effect of introducing EGR under part load operating conditions. Application of EGR reduces the intake oxygen concentration by replacing part of the intake fresh air with inert combustion products. Thus, unlike to the previously simulated PFI SI engine, the equivalence ratio of mixture is changed by applying EGR in DI diesel engine.

1. For both of medium and low loads, the peak cylinder pressures at 20% EGR rate decrease approximately by 3% and decrease by 5% at EGR rate of 30% compared with the peak cylinder pressures at 5% EGR rate.
2. In case of medium load, when EGR varies from 5% to 30%, the peak value of in-cylinder mean temperature decreases from 1699 [K] to 1607 [K] which means 5% reduction in peak temperature.

3. In case of low load, when EGR varies from 5% to 30%, the peak value of in-cylinder mean temperature decreases from 1454 [K] to 1378 [K] which means 5% reduction in peak temperature.
4. It is observed that use of EGR causes a small increase in the ignition delay period and hence retards the start of combustion. Addition of EGR increases the ignition delay mainly because of reduction of charge temperature, pressure and oxygen concentration at the point of fuel injection.
5. Increasing the EGR rate decreases the peak heat release rate of main combustion phase (second peak). Moreover, increase in the EGR decreases the burning velocity and shifts the combustion process further towards the expansion stroke, which results in a higher heat release rate during the late combustion phase.
6. The results reveal that the simulated DI diesel engine produces lower NO_x emissions under part loads and it is able to realize an additional significant reduction in NO_x emissions by implementing EGR at part loads.
7. In comparison with full load condition, the amount of NO_x emissions decreases by about 7% under medium load and approximately by 64% under low load with 5% EGR. While by using 30% EGR, this reduction can be increased to 95% at medium load and to 98% at low load. By considering each case individually, when EGR varies from 5% to 30%, NO_x emissions experience a reduction of 94% at medium load and a decrease of 94% at low load.
8. The lowered combustion temperature and lowered oxygen concentration as a result of applying higher EGR rates, are thought to weaken the soot oxidation process and hence reduce the soot oxidation rates, thereby increasing the soot emissions. By decreasing the injection quantity or engine load, over-rich regions are also reduced and caused a reduction in soot emissions.

9. In comparison with full load condition, the amount of soot emissions decreases by about 94% under medium load and approximately by 97% under low load with 5% EGR. While by using 30% EGR, this reduction is decreased to 60% at medium load and to 87% at low load. By considering each case individually, when EGR varies from 5% to 30%, soot emissions increase dramatically from 0.04 to 0.255 [g/kWh] at medium load and from 0.019 to 0.083 [g/kWh] at low load.
10. In comparison with full load condition, ISFC decreases by about 13% under medium load and approximately by 15% under low load with 5% EGR. While by using 30% EGR, this reduction is decreased to 10% at medium load and to 11% at low load. By considering each case individually, when EGR varies from 5% to 30%, ISFC increases slightly from 190.2 to 197.8 [g/kWh] at medium load and from 186.9 to 194.3 [g/kWh] at low load.

– Multiple injection

  This work also analysis how the injection strategies including injection ratio and first injection duration can allow optimization of the emissions and fuel consumption trade-off for different operating points and engine conditions.

  * Injection ratio

    In order to evaluate the individual effect of injection ratio, second injection timing or start of second injection and second injection duration are not changed and three additional simulations are done by utilizing the injection ratios of 20, 30 and 40%.

    1. For different injection ratios from 20 to 40%, the pressure is increasing gradually until the occurrence of initially injected fuel ignition. Once the ignition of initially injected fuel occurs there is a sharp rise in cylinder pressure due to the associated heat release. With increasing the injection ratio, the intensity of pressure rise is also increased and higher peak pressures are obtained.
    2. The ignition of the initially injected fuel takes place only when a certain temperature (>800 [K]) is reached. For different injection

ratios from 20 to 40%, the cylinder temperature is increasing gradually until the occurrence of initially injected fuel ignition. Once the ignition of initially injected fuel occurs there is a sharp rise in cylinder temperature.

3. Increasing the premixed ratio increases the in-cylinder temperature prior to the second injection timing and initiates the combustion before TDC which results in higher peak pressures, higher peak temperatures and lower exhaust temperatures.
4. The ignition of first injection takes place at approximately 17 [CAD] BTDC in the cycle. This can be due to the temperature required for the initiation of combustion of firstly injected fuel. It is observed from the temperature profile that the minimum temperature required for ignition of first injection is approximately equal to 800 [K].
5. For the injection ratios of higher than 20%, the amount of NO_x emissions are higher than the single injection case. The results reveal that the only case which exhibits lower NO_x emissions in comparison with single injection is Case-20 (injection ratio of 20%).
6. By premixing, the over-rich regions of the mixture is reduced and soot emissions are decreased. Lower injection ratios produce noticeably lower soot emissions than single injection. However by increasing the injection ratio, soot emissions are also increased and the differences between single and multiple injection disappear, where the injection ratio of 40% produces slightly higher amount of soot emissions.
7. Although split injection produces higher IMEP and indicated power compared to single injection, by increasing the injection ratio, IMEP and indicated power are decreased and the differences become very low, where the injection ratio of 40% approximately has the same value of IMEP and indicated power with single

injection. In comparison with single injection, IMEP and indicated power increase by about 3% with injection ratio of 20%.

8. Compared to single injection, the ISFC is decreased considerably with split injection. However this reduction is decreased by increasing the injection ratio. The lowest ISFC is achieved with injection ratio of 20% which is about 213 [g/kWh]. In comparison with single injection, ISFC decreases by about 3% with injection ratio of 20%.

* EGR and first injection duration

It is found that the multiple injection has the potential to reduce NOx and soot emissions simultaneously. However, by increasing the injection ratio these advantages are diminished. In this regard the effects of EGR and first injection duration are investigated to check the possibility of using higher injection ratios without any negative effects on engine performance and exhaust emissions. In this regard, various injection duration of 35, 40, 45, 50 and 55 [CAD] are set to first injection and combined effects of first injection duration with different EGR levels of 5% and 10% are studied.

1. The peak temperature is increased slightly with increasing the first injection duration. It is found that increasing the first injection duration weaken the atomization and resulting in a lower distributed vapor, hence poor air-fuel mixing. Therefore, some portion of firstly injected fuel added to secondly injected fuel and burn with the main injection and results in higher peak temperatures.

2. NO_x emissions increase steadily with increase of first injection duration for Case-20. For Case-30 and Case-40, it drops with injection duration of 40 [CAD] and then increase. For all cases, the highest amount of NO_x emissions are produced with longest injection duration of 55 [CAD].

3. In case of 5% EGR, in comparison with single injection, NO_x emissions are higher for all cases, except Case-20 with first

injection duration of 35 [CAD]. While by increasing the EGR level to 10%, NO_x emissions are decreased dramatically compared to the EGR of 5% and it is possible to achieve lower levels of NO_x emissions with 20% and 30% injection ratios in comparison with single injection.

4. The results reveal that with a proper combination of first injection duration and EGR level for each case, lower amount of NO_x can be produced. In case of 20% of injection ratio (Case-20) with first injection duration of 35 [CAD] and 10% EGR, NO_x emissions are decreased by 40%, and in case of 30% of injection ratio (Case-30) with first injection duration of 40 [CAD] and 10% EGR, NO_x emissions are decreased by 26%, compared to single injection.
5. The results indicate that soot emissions steadily fall with increase in first injection duration and this reduction occurs more intensely for Case-40. Compared to single injection, soot emissions of all cases are notably lower with longer duration of first injection and the lowest amount of soot emissions are produced with longest injection duration of 55 [CAD].
6. By increasing EGR to 10%, there is an increase in soot emissions for all cases, but with an increase in injection duration the amount of soot emission is decreased and compared to single injection, with a proper selection of EGR and first injection duration, lower amount of soot emissions can be achieved.
7. In case of 20% of injection ratio (Case-20) with first injection duration of 35 [CAD] and 10% EGR, soot emissions are decreased by 75%, and in case of 30% of injection ratio (Case-30) with first injection duration of 40 [CAD] and 10% EGR, soot emissions are decreased by 60%, compared to single injection. It is obvious that soot emission increases with the increase of EGR, but for simultaneous reduction of NO_x and soot emissions, 10% of EGR with 35 [CAD] of first injection duration for Case-20 and 40

[CAD] of first injection duration for Case-30 show better results than those of 5% EGR.

8. According to the results indicated power increases steadily with increase of first injection duration. However, by increasing EGR to 10% the value of indicated power is decreased for all cases, in comparison with single injection, with selection of longer injection duration, higher indicated power output can be obtained.
9. In case of 20% of injection ratio (Case-20) with first injection duration of 35 [CAD] and 5% EGR, indicated power is increased by 3%, and in case of 30% of injection ratio (Case-30) with first injection duration of 40 [CAD] and 10% EGR, indicated power is increased by 1.6%, compared to single injection.
10. ISFC decreases steadily with increase of first injection duration. However, by increasing EGR to 10% the ISFC is increased for all cases, in comparison with single injection, with selection of longer injection duration, lower ISFC can be achieved.
11. In case of 20% of injection ratio (Case-20) with first injection duration of 35 [CAD] and 5% EGR, the ISFC is decreased by 3%, and in case of 30% of injection ratio (Case-30) with first injection duration of 40 [CAD] and 10% EGR, the ISFC is decreased by 1.6%, compared to single injection.
12. The results reveal that multiple injection strategy with proper selection of injection ratio, first injection duration and EGR level has the potential to reduce NO_x , soot emissions and ISFC simultaneously. It is found that that by using multiple injection strategy, it is possible to achieve lower engine-out emissions with an improvement in diesel engine performance, however, injection ratio of 40% shows slightly higher NO_x emissions.

By considering engine performance and emissions characteristics, the optimum results are listed briefly in Table 5.1.

Table 5.1 : Optimum results.

Spark Ignition					
Case	NO_x [g/kWh]	Soot [g/kWh]	IMEP [bar]	Indicated power [kW]	ISFC [g/kWh]
SI [validated model, 10% EGR, ϕ=1, SOS = 330 [CAD]]	4.492	4.2E-06	4.76	2.7	240.1
SI [10% EGR, ϕ=1, SOS = 311 [CAD] (MBT)]	7.668	2.3E-07	5.14	2.91	222.7
SI [natural gas fueled, 10% EGR, ϕ=1, SOS =330[CAD]]	3.893	0.00106	4.39	2.49	208.9
HCCI [natural gas fueled, 10% EGR, ϕ= 0.35]	0.0051	1.7E-09	4.76	2.7	152.2
Diesel					
Case	NO_x [g/kWh]	Soot [g/kWh]	IMEP [bar]	Indicated power [kW]	ISFC [g/kWh]
Diesel [single injection, 5% EGR, full load]	1.66	0.64025	12.26	6.96	219.83
Diesel [multiple injection, 5% EGR, injection ratio=20%, full load]	1.55	0.0665	12.66	7.18	213
Diesel [single injection, 10% EGR, medium load]	0.996875	0.06164	8.38	4.75	191.5
DIesel [single injection, 10% EGR, low load]	0.356039	0.02525	5.69	3.23	187.9

5.2 Recommendations And Future Work

The following are some recommendations to further aid fundamental research in the area of various combustion strategies relative to this document.

- Using appropriate combustion chamber shape
- Investigating the combined effects of EGR, Equivalence ratio and spark timing on SI engine
- Using various alternative fuels
- Implementing SI-HCCI-SI engine
- Effect of supercharging and boosting pressure on multiple injection strategy
- Further exploration of multiple injection strategy by adding more injection pulses
- Implementing NADI strategy

REFERENCES

Aceves, Salvador M. and **Flowers, Daniel L.** A detailed chemical kinetic analysis of low temperature non-sooting diesel combustion. In *SAE Technical Paper*. SAE International, 04 2005. doi: 10.4271/2005-01-0923. URL http://dx.doi.org/10.4271/2005-01-0923.

Agafonov, GL, **Nullmeier, M**, **Vlasov, PA**, **Warnatz, J**, and **Zaslonko, IS**. Kinetic modeling of solid carbon particle formation and thermal decomposition during carbon suboxide pyrolysis behind shock waves. *Combustion science and technology*, 174(5-6):185–213, 2002.

Agarwal, Avinash Kumar. Experimental investigation on intake air temperature and air-fuel ratio dependence of random and deterministic cyclic variability in a homogeneous charge compression ignition engine. In *SAE Technical Paper*. SAE International, 04 2011. doi: 10.4271/2011-01-1183. URL http://dx.doi.org/10.4271/2011-01-1183.

Alriksson, Malin and **Denbratt, Ingemar**. Low temperature combustion in a heavy duty diesel engine using high levels of egr. In *SAE Technical Paper*. SAE International, 04 2006. doi: 10.4271/2006-01-0075. URL http://dx.doi.org/10.4271/2006-01-0075.

Anselmi, Patricia, **Kashdan, Julian**, **Bression, Guillaume**, **Ferrero-Lesur, Edouard**, **Thirouard, Benoist**, and **Walter, Bruno**. Improving emissions, noise and fuel economy trade-off by using multiple injection strategies in diesel low temperature combustion (ltc) mode. In *SAE Technical Paper*. SAE International, 10 2010. doi: 10.4271/2010-01-2162. URL http://dx.doi.org/10.4271/2010-01-2162.

Aoyama, Taro, **Hattori, Yoshiaki**, **Mizuta, Jun'ichi**, and **Sato, Yasuo**. An experimental study on premixed-charge compression ignition gasoline engine. In *SAE Technical Paper*. SAE International, 02 1996. doi: 10.4271/960081. URL http://dx.doi.org/10.4271/960081.

Appel, Jörg, **Bockhorn, Henning**, and **Frenklach, Michael**. Kinetic modeling of soot formation with detailed chemistry and physics: laminar premixed flames of {C2} hydrocarbons. *Combustion and Flame*, 121(1–2):122 – 136, 2000. ISSN 0010-2180. doi: http://dx.doi.org/10.1016/S0010-2180(99)00135-2. URL http://www.sciencedirect.com/science/article/pii/S0010218099001352.

Arcoumanis, C, **Gavaises, Manolis**, and **others**. Linking nozzle flow with spray characteristics in a diesel fuel injection system. *Atomization and Sprays*, 8(3): 307–348, 1998.

Asad, Usman and **Zheng, Ming**. Efficacy of egr and boost in single-injection enabled low temperature combustion. *SAE Int. J. Engines*, 2:1085–1097, 04 2009. doi: 10.4271/2009-01-1126. URL http://dx.doi.org/10.4271/2009-01-1126.

Asad, Usman, **Divekar, Prasad**, **Zheng, Ming**, and **Tjong, Jimi**. Low temperature combustion strategies for compression ignition engines: Operability limits and challenges. In *SAE Technical Paper*. SAE International, 04 2013. doi: 10.4271/2013-01-0283. URL http://dx.doi.org/10.4271/2013-01-0283.

Asad, Usman, **Zheng, Ming**, and **Tjong, Jimi**. Experimental investigation of diesel-ethanol premixed pilot-assisted combustion (ppac) in a high compression ratio engine. *SAE Int. J. Engines*, 9:1059–1071, 04 2016. doi: 10.4271/2016-01-0781. URL http://dx.doi.org/10.4271/2016-01-0781.

AVL. *AVL FIRE® v.2013 USER MANUAL*. AVL List GmbH, 2013.

Bahng, Gun Woong, **Jang, Dongsoon**, **Kim, Youngtae**, and **Shin, Misoo**. A new technology to overcome the limits of HCCI engine through fuel modification. *Appl. Therm. Eng.*, 98:810–815, 2016. ISSN 13594311. doi: 10.1016/j.applthermaleng.2015.12.076. URL http://dx.doi.org/10.1016/j.applthermaleng.2015.12.076.

Bakker, P.C., **Goes, J.E. De Abreu**, **Somers, L.M.T.**, and **Johansson, B.H.** Characterization of low load ppc operation using ron70 fuels. In *SAE Technical Paper*. SAE International, 04 2014. doi: 10.4271/2014-01-1304. URL http://dx.doi.org/10.4271/2014-01-1304.

Bao, Zufeng, **Cheng, Xiaobei**, **Qiu, Liang**, and **Luan, Xingcun**. Investigation into partially premixed combustion in a light-duty diesel engine based on different injection strategies. In *SAE Technical Paper*. SAE International, 10 2014. doi: 10.4271/2014-01-2681. URL http://dx.doi.org/10.4271/2014-01-2681.

Baumgarten, C. *Mixture Formation in Internal Combustion Engines*. Heat and Mass Transfer. Springer Berlin Heidelberg, 2010. ISBN 9783642068089. URL https://books.google.com.tr/books?id=VI2AcgAACAAJ.

Beatrice, Carlo, **Avolio, Giovanni**, **Giacomo, Nicola Del**, and **Guido, Chiara**. Compression ratio influence on the performance of an advanced single-cylinder diesel engine operating in conventional and low temperature combustion mode. In *SAE Technical Paper*. SAE International, 06 2008. doi: 10.4271/2008-01-1678. URL http://dx.doi.org/10.4271/2008-01-1678.

Bockhorn, H., **Fetting, F.**, **Heddrich, A.**, and **Wannemacher, G.** Investigation of the surface growth of soot in flat low pressure hydrocarbon oxygen flames. *Symposium (International) on Combustion*, 20(1):979 – 988, 1985. ISSN 0082-0784. doi: http://dx.doi.org/10.1016/S0082-0784(85)80587-7. URL http://www.sciencedirect.com/science/article/pii/S0082078485805877. Twentieth Symposium (International) on Combustion.

Bogensperger, M. A comparative study of different calculation approaches for the numerical simulation of thermal no formation. *Diss. U. Graz*, 1996.

Bogensperger, M, **Ban, M**, **Priesching, P**, and **Tatschl, R**. Modeling of premixed si-engine combustion using avl fire–a validation study. In *International Multidimensional Engine Modeling User's Group Meeting at the SAE Congress April*, volume 13, 2008.

Boot, M. D., **Luijten, C. C. M.**, **Somers, L. M. T.**, **Eguz, U.**, **van Erp, D. D. T. M.**, **Albrecht, A.**, and **Baert, R. S. G.** Uncooled egr as a means of limiting wall-wetting under early direct injection conditions. In *SAE Technical Paper*. SAE International, 04 2009a. doi: 10.4271/2009-01-0665. URL http://dx.doi.org/10.4271/2009-01-0665.

Boot, M.D., **Luijten, C.C.M.**, **Rijk, E.P.**, **Albrecht, B.A.**, and **Baert, R.S.G.** Optimization of operating conditions in the early direct injection premixed charge compression ignition regime. In *SAE Technical Paper*. Consiglio Nazionale delle Ricerche, 09 2009b. doi: 10.4271/2009-24-0048. URL http://dx.doi.org/10.4271/2009-24-0048.

Bose, AK and **Pei, DCT**. Evaporation rates in spray drying. *The Canadian Journal of Chemical Engineering*, 42(6):259–262, 1964.

Bowman, Craig T. Kinetics of pollutant formation and destruction in combustion. *Progress in Energy and Combustion Science*, 1(1):33 – 45, 1975. ISSN 0360-1285. doi: http://dx.doi.org/10.1016/0360-1285(75)90005-2. URL http://www.sciencedirect.com/science/article/pii/0360128575900052.

Boyarski, Nicholas J. and **Reitz, Rolf D.** Premixed compression ignition (pci) combustion with modeling-generated piston bowl geometry in a diesel engine. In *SAE Technical Paper*. SAE International, 04 2006. doi: 10.4271/2006-01-0198. URL http://dx.doi.org/10.4271/2006-01-0198.

Bression, Guillaume, **Soleri, Dominique**, **Savy, Sylvain**, **Dehoux, Stéphane**, **Azoulay, David**, **Hamouda, Hedi Ben-Hadj**, **Doradoux, Laurent**, **Guerrassi, Noureddine**, and **Lawrence, Nick**. A study of methods to lower hc and co emissions in diesel hcci. *SAE Int. J. Fuels Lubr.*, 1:37–49, 04 2008. doi: 10.4271/2008-01-0034. URL http://dx.doi.org/10.4271/2008-01-0034.

Cao, Li, **Bhave, Amit**, **Su, Haiyun**, **Mosbach, Sebastian**, **Kraft, Markus**, **Dris, Antonis**, and **McDavid, Robert M.** Influence of injection timing and piston bowl geometry on pcci combustion and emissions. *SAE Int. J. Engines*, 2:1019–1033, 04 2009. doi: 10.4271/2009-01-1102. URL http://dx.doi.org/10.4271/2009-01-1102.

Caton, Jerald A. Thermodynamic advantages of low temperature combustion (ltc) engines using low heat rejection (lhr) concepts. In *SAE Technical Paper*. SAE International, 04 2011. doi: 10.4271/2011-01-0312. URL http://dx.doi.org/10.4271/2011-01-0312.

Cheng, Xiaobei, **Chen, Liang**, **Yan, Fangqin**, **Hong, Guang**, **Yin, Yong**, and **Liu, Huan**. Investigations of split injection strategies for the improvement of combustion and soot emissions characteristics based on the two-color method in a heavy-duty diesel engine. In *SAE Technical Paper*. SAE International, 10 2013. doi: 10.4271/2013-01-2523. URL http://dx.doi.org/10.4271/2013-01-2523.

Cheng, Xiaobei, **LI, Shuai**, **Yang, Jin**, **Dong, Shijun**, and **Bao, Zufeng**. Effect of n-butanol-diesel blends on partially premixed combustion and emission characteristics in a light-duty engine. In *SAE Technical Paper*. SAE International, 10 2014. doi: 10.4271/2014-01-2675. URL http://dx.doi.org/10.4271/2014-01-2675.

Çinar, Can, **Uyumaz, Ahmet**, **Polat, Seyfi**, **Yilmaz, Emre**, **Can, Özer**, and **Solmaz, Hamit**. Combustion and performance characteristics of an HCCI engine utilizing trapped residual gas via reduced valve lift. *Appl. Therm. Eng.*, 100(x):586–594, 2016. ISSN 13594311. doi: 10.1016/j.applthermaleng.2016.02.080. URL http://dx.doi.org/10.1016/j.applthermaleng.2016.02.080.

Colin, O. and **Benkenida, A.** The 3-zones extended coherent flame model (ecfm3z) for computing premixed/diffusion combustion. *Oil & Gas Science and Technology-revue De L Institut Francais Du Petrole*, 59:593–609, 2004. doi: 10.2516/ogst:2004043.

Colin, Olivier, **da Cruz, António Pires**, and **Jay, Stéphane**. Detailed chemistry-based auto-ignition model including low temperature phenomena applied to 3-d engine calculations. *Proceedings of the Combustion Institute*, 30(2):2649 – 2656, 2005. ISSN 1540-7489. doi: http://dx.doi.org/10.1016/j.proci.2004.08.058. URL http://www.sciencedirect.com/science/article/pii/S0082078404001122.

Cong, Shenghui, **McTaggart-Cowan, Gordon**, and **Garner, Colin**. Effects of fuel injection parameters on low temperature diesel combustion stability. In *SAE Technical Paper*. SAE International, 04 2010. doi: 10.4271/2010-01-0611. URL http://dx.doi.org/10.4271/2010-01-0611.

Cunningham, E. On the velocity of steady fall of spherical particles through fluid medium. *Proceedings of the Royal Society of London A: Mathematical, Physical and Engineering Sciences*, 83(563):357–365, 1910. ISSN 0950-1207. doi: 10.1098/rspa.1910.0024. URL http://rspa.royalsocietypublishing.org/content/83/563/357.

D'Ambrosio, S. and **Ferrari, A.** Effects of exhaust gas recirculation in diesel engines featuring late PCCI type combustion strategies. *Energy Convers. Manag.*, 105(x): 1269–1280, 2015. ISSN 01968904. doi: 10.1016/j.enconman.2015.08.001. URL http://dx.doi.org/10.1016/j.enconman.2015.08.001.

Das, Pranab, **Subbarao, P.M.V.**, and **Subrahmanyam, J.P.** Effect of cetane number and fuel properties on combustion and emission characteristics of an hcci-di combustion engine using a novel dual injection strategy. In *SAE Technical Paper*. SAE International, 01 2015. doi: 10.4271/2015-26-0023. URL http://dx.doi.org/10.4271/2015-26-0023.

Das, Pranab, **Selokar, Mayur**, **Subbarao, P.M.V.**, and **Subrahmanyam, J.P.** Effect of injection timing, premixed equivalence ratio and egr on combustion characteristics of an hcci-di combustion engine using in-cylinder dual injection strategy. In *SAE Technical Paper*. SAE International, 04 2016. doi: 10.4271/2016-01-0752. URL http://dx.doi.org/10.4271/2016-01-0752.

Dec, John E. A conceptual model of di diesel combustion based on laser-sheet imaging. Technical report, SAE technical paper, 1997.

Dec, John E. Advanced compression-ignition engines—understanding the in-cylinder processes. *Proceedings of the Combustion Institute*, 32(2):2727 – 2742, 2009. ISSN 1540-7489. doi: http://dx.doi.org/10.1016/j.proci.2008.08.008. URL http://www.sciencedirect.com/science/article/pii/S1540748908001739.

Dec, John E. and **Sjöberg, Magnus**. A parametric study of hcci combustion - the sources of emissions at low loads and the effects of gdi fuel injection. In *SAE Technical Paper*. SAE International, 03 2003. doi: 10.4271/2003-01-0752. URL http://dx.doi.org/10.4271/2003-01-0752.

Demirdzic, I., **Lilek, Z.**, and **Peric, M.** A collocated finite volume method for predicting flows at all speeds. *International Journal for Numerical Methods in Fluids*, 16(12):1029–1050, 1993. ISSN 1097-0363. doi: 10.1002/fld.1650161202. URL http://dx.doi.org/10.1002/fld.1650161202.

Dijkstra, Rutger, **Blasio, Gabriele Di**, **Boot, Michael**, **Beatrice, Carlo**, and **Bertoli, Claudio**. Assessment of the effect of low cetane number fuels on a light duty ci engine: Preliminary experimental characterization in pcci operating condition. In *SAE Technical Paper*. SAE International, 09 2011. doi: 10.4271/2011-24-0053. URL http://dx.doi.org/10.4271/2011-24-0053.

Diwakar, Ramachandra and **Singh, Satbir**. Importance of spray-bowl interaction in a di diesel engine operating under pcci combustion mode. In *SAE Technical Paper*. SAE International, 04 2009. doi: 10.4271/2009-01-0711. URL http://dx.doi.org/10.4271/2009-01-0711.

Doğru, B. *Skip cycle method investigation at part load conditions of spark ignition engines*. PhD thesis, Istanbul Technical University, 2013.

Dukowicz, John K. Quasi-steady droplet phase change in the presence of convection. Technical report, Los Alamos Scientific Lab., 1979.

Dukowicz, John K. A particle-fluid numerical model for liquid sprays. *Journal of Computational Physics*, 35(2):229 – 253, 1980. ISSN 0021-9991. doi: http://dx.doi.org/10.1016/0021-9991(80)90087-X. URL http://www.sciencedirect.com/science/article/pii/002199918090087X.

Dumitrescu, Cosmin E., **Stuart Neill, W.**, **Guo, Hongsheng**, **Hosseini, Vahid**, and **Chippior, Wallace L.** Fuel Property Effects on PCCI Combustion in a Heavy-Duty Diesel Engine. *J. Eng. Gas Turbines Power*, 134(5):052801, 2012. ISSN 07424795. doi: 10.1115/1.4005213.

Ehleskog, Malin, **Gjirja, Savo**, and **Denbratt, Ingemar**. Effects of high injection pressure, egr and charge air pressure on combustion and emissions in an hd single cylinder diesel engine. *SAE Int. J. Engines*, 2:341–354, 11 2009. doi: 10.4271/2009-01-2815. URL http://dx.doi.org/10.4271/2009-01-2815.

Evans, R. L. and **Blaszczyk, J**. A comparative study of the performance and exhaust emissions of a spark ignition engine fuelled by natural gas and gasoline. *Proceedings of the Institution of Mechanical Engineers, Part D: Journal of Automobile Engineering*, 211(1):39–47, 1997. doi: 10.1243/0954407971526209. URL http://pid.sagepub.com/content/211/1/39.abstract.

Fang, Tiegang, **Coverdill, Robert E.**, **fon F. Lee, Chia**, and **White, Robert A.** Combustion and soot visualization of low temperature combustion within an hsdi diesel engine using multiple injection strategy. In *SAE Technical Paper*. SAE International, 04 2006. doi: 10.4271/2006-01-0078. URL http://dx.doi.org/10.4271/2006-01-0078.

Flynn, Patrick F, **Durrett, Russell P**, **Hunter, Gary L**, **zur Loye, Axel O**, **Akinyemi, OC**, **Dec, John E**, and **Westbrook, Charles K**. Diesel combustion: an integrated view combining laser diagnostics, chemical kinetics, and empirical validation. 1999.

Frolov, S. 1d soot clustering model. *N.N. Semenov Institute of Chemical Physics, Moscow*, June 2011.

Gao, T Y, **Divekar, P**, **Asad, U**, **Han, X Y**, **Reader, G T**, **Wang, M P**, **Zheng, M**, and **Tjong, J**. An Enabling Study of Low Temperature Combustion with Ethanol in a Diesel Engine. *Proc. Asme Intern. Combust. Engine Div. Fall Tech. Conf. - 2012*, 135(December):217–226, 2012. ISSN 0195-0738. doi: 10.1115/1.4024027. URL {\T1\textless}GotoISI{\T1\textgreater}://WOS:000335097100022.

Gharahbaghi, Shadi, **Wilson, Trevor S**, **Xu, Hongming**, **Cryan, Simon**, and **Richardson, Steve**. Modelling and Experimental Investigations of Supercharged HCCI Engines. 2006(724), 2006.

Gharehghani, A, **Mirsalim, M**, **Jazayeri, A**, and **Hosseini, R**. Experimental Study on Low Temperature Combustion Dual Fuel Biodiesel/Natural Gas Engine.

Vol. 1 Large Bore Engines; Fuels; Adv. Combust., page V001T03A001, 2015. doi: 10.1115/ICEF2015-1006. URL http://proceedings.asmedigitalcollection.asme.org/proceeding.aspx?doi=10.1115/ICEF2015-1006.

Gülder, Ö.L. Correlations of laminar combustion data for alternative s.i. engine fuels. In *SAE Technical Paper*. SAE International, 08 1984. doi: 10.4271/841000. URL http://dx.doi.org/10.4271/841000.

Gosman, AD and **Loannides, E**. Aspects of computer simulation of liquid-fueled combustors. *Journal of Energy*, 7(6):482–490, 1983.

Gowthaman, S. and **Sathiyagnanam, A.P.** Effects of charge temperature and fuel injection pressure on HCCI engine. *Alexandria Eng. J.*, 55(1):119–125, 2016. ISSN 11100168. doi: 10.1016/j.aej.2015.12.025. URL http://linkinghub.elsevier.com/retrieve/pii/S1110016815002185.

Gray, Allen W. (Bill) and **Ryan, Thomas W.** Homogeneous charge compression ignition (hcci) of diesel fuel. In *SAE Technical Paper*. SAE International, 05 1997. doi: 10.4271/971676. URL http://dx.doi.org/10.4271/971676.

Görner, K. Technische verbrennungssysteme, grundlagen, modellbildung. *Simulation*, 1991.

Halstead, M. P., **Kirsch, L. J.**, **Prothero, A.**, and **Quinn, C. P.** A mathematical model for hydrocarbon autoignition at high pressures. *Proceedings of the Royal Society of London A: Mathematical, Physical and Engineering Sciences*, 346(1647): 515–538, 1975. ISSN 0080-4630. doi: 10.1098/rspa.1975.0189. URL http://rspa.royalsocietypublishing.org/content/346/1647/515.

Han, Sangwook and **Bae, Choongsik**. The influence of fuel injection pressure and intake pressure on conventional and low temperature diesel combustion. In *SAE Technical Paper*. SAE International, 09 2012. doi: 10.4271/2012-01-1721. URL http://dx.doi.org/10.4271/2012-01-1721.

Han, Sangwook, **Shim, Euijoon**, **Jang, Jinyoung**, **Park, Jungseo**, **Bae, Choongsik**, **Park, Jongnam**, and **Kim, Hyunok**. Operating range of low temperature diesel

combustion with supercharging. In *SAE Technical Paper*. SAE International, 04 2009. doi: 10.4271/2009-01-1440. URL http://dx.doi.org/10.4271/2009-01-1440.

Hanson, Ronald K. and **Salimian, Siamak**. *Survey of Rate Constants in the N/H/O System*, pages 361–421. Springer US, New York, NY, 1984. ISBN 978-1-4684-0186-8. doi: 10.1007/978-1-4684-0186-8_6. URL http://dx.doi.org/10.1007/978-1-4684-0186-8_6.

Hardy, W. L. and **Reitz, Rolf D.** A study of the effects of high egr, high equivalence ratio, and mixing time on emissions levels in a heavy-duty diesel engine for pcci combustion. In *SAE Technical Paper*. SAE International, 04 2006. doi: 10.4271/2006-01-0026. URL http://dx.doi.org/10.4271/2006-01-0026.

Hashimoto, Kohtaro. Effect of ethanol on the hcci combustion. In *SAE Technical Paper*. SAE International, 07 2007. doi: 10.4271/2007-01-2038. URL http://dx.doi.org/10.4271/2007-01-2038.

Heywood, John B. *INTERNAL COMBUSTION ENGINE FUNDAMENTALS*. 87-15251. McGraw-Hill, Inc., 1988. ISBN 0-07-028637-X.

Hildingsson, Leif, **Johansson, Bengt**, **Kalghatgi, Gautam T.**, and **Harrison, Andrew J.** Some effects of fuel autoignition quality and volatility in premixed compression ignition engines. *SAE Int. J. Engines*, 3:440–460, 04 2010. doi: 10.4271/2010-01-0607. URL http://dx.doi.org/10.4271/2010-01-0607.

Hou, Junxing, **Wen, Zhenhua**, **Liu, Jianwei**, and **Jiang, Zhiqiang**. Study on Knock Characteristics of Dimethyl Ether Fueled Homogenous Charge Compression Ignition-Direct Injection Combustion Engines. *J. Energy Resour. Technol.*, 137 (6):062202, 2015. ISSN 0195-0738. doi: 10.1115/1.4030726. URL http://www.engineeringvillage.com/blog/document.url?mid=cpx{_}M3c1463c14e4fa3ceaaM783010178163171{&}database=cpx$\delimiter"026E30F$nhttp://www.scopus.com/inward/record.url?eid=2-s2.0-84934942452{&}partnerID=tZOtx3y1.

Jamsran, Narankhuu, **Putrasari, Yanuandri**, and **Lim, Ocktaeck**. A computational study on the autoignition characteristics of an HCCI engine fueled with natural gas. *J. Nat. Gas Sci. Eng.*, 29:469–478, 2016. ISSN 18755100. doi: 10.1016/j.jngse.2016.01.008. URL http://dx.doi.org/10.1016/j.jngse.2016.01.008.

Jia, Ming, **Li, Yaopeng**, **Xie, Maozhao**, **Wang, Tianyou**, **Wang, Hu**, and **Reitz, Rolf D.** The Potential of High-load Extension by Using Late Intake Valve Closing for a Diesel Premixed Charge Compression Ignition (PCCI) Engine. *Phys. Procedia*, 66(x):33–36, 2015. ISSN 18753892. doi: 10.1016/j.egypro.2015.02.018. URL http://dx.doi.org/10.1016/j.egypro.2015.02.018.

Jiro, Senda, **Kobayashi, Masaaki**, **Iwashita, Seiji**, and **Fujimoto, Hajime**. Modeling of diesel spray impingement on a flat wall. Technical report, SAE Technical Paper, 1994.

Jun, Daesu and **Iida, Norimasa**. A study of high combustion efficiency and low co emission in a natural gas hcci engine. In *SAE Technical Paper*. SAE International, 06 2004. doi: 10.4271/2004-01-1974. URL http://dx.doi.org/10.4271/2004-01-1974.

Jung, Yongjin, **Bae, Choongsik**, **Jang, Jinyoung**, and **Kim, Duksang**. Improvement of premixed compression ignition combustion using various injector configurations. In *SAE Technical Paper*. SAE International, 04 2011. doi: 10.4271/2011-01-1357. URL http://dx.doi.org/10.4271/2011-01-1357.

Juttu, S., **Thipse, S. S.**, **Marathe, N. V.**, and **Babu, M. K. Gajendra**. Homogeneous charge compression ignition (hcci): A new concept for near zero nox and particulate matter (pm) from diesel engine combustion. In *SAE Technical Paper*. The Automotive Research Association of India, 01 2007. doi: 10.4271/2007-26-020. URL http://dx.doi.org/10.4271/2007-26-020.

Kalghatgi, Gautam T. and **Head, R. A.** The available and required autoignition quality of gasoline - like fuels in hcci engines at high temperatures. In *SAE Technical Paper*. SAE International, 06 2004. doi: 10.4271/2004-01-1969. URL http://dx.doi.org/10.4271/2004-01-1969.

Kamimoto, Takeyuki and **Bae, Myurng-hoan**. High combustion temperature for the reduction of particulate in diesel engines. In *SAE Technical Paper*. SAE International, 02 1988. doi: 10.4271/880423. URL http://dx.doi.org/10.4271/880423.

Kanoto, Yoshihiko, **Ohmura, Tetsuo**, and **Iida, Norimasa**. An investigation of combustion control using egr for small and light hcci engine fuelled with dme. In *SAE Technical Paper*. SAE International, 07 2007. doi: 10.4271/2007-01-1876. URL http://dx.doi.org/10.4271/2007-01-1876.

Kashdan, Julian T., **Anselmi, Patricia**, and **Walter, Bruno**. Advanced injection strategies for controlling low-temperature diesel combustion and emissions. *SAE Int. J. Engines*, 2:1835–1856, 06 2009. doi: 10.4271/2009-01-1962. URL http://dx.doi.org/10.4271/2009-01-1962.

Kawano, Daisuke, **Naito, Hiroyoshi**, **Suzuki, Hisakazu**, **Ishii, Hajime**, **Hori, Shigeo**, **Goto, Yuichi**, and **Odaka, Matsuo**. Effects of fuel properties on combustion and exhaust emissions of homogeneous charge compression ignition (hcci) engine. In *SAE Technical Paper*. SAE International, 06 2004. doi: 10.4271/2004-01-1966. URL http://dx.doi.org/10.4271/2004-01-1966.

Kawasaki, Kiyoshi, **Kubo, Soichiro**, **Yamane, Koji**, and **Kondo, Chihiro**. The Effect of the Induction of Nitrogen Oxides on Natural Gas HCCI Combustion. *SAE Int. J. Fuels Lubr.*, 7(3):2014–01–2697, 2014. ISSN 1946-3960. doi: 10.4271/2014-01-2697. URL http://papers.sae.org/2014-01-2697/.

Kim, Myung Yoon and **Lee, Chang Sik**. Effect of a narrow fuel spray angle and a dual injection configuration on the improvement of exhaust emissions in a HCCI diesel engine. *Fuel*, 86(17-18):2871–2880, 2007. ISSN 00162361. doi: 10.1016/j.fuel.2007.03.016.

Kim, Yungjin, **Park, Sangki**, and **Lee, Kihyung**. Investigation of the Optimal Injection Conditions for a PCCI Diesel Engine. *ASME 2012 Intern. Combust. Engine Div. Fall Tech. Conf.*, pages 457–464, 2012. doi: 10.1115/ICEF2012-92178. URL http://proceedings.asmedigitalcollection.asme.org/proceeding.aspx?articleid=1721013.

Kimura, Shuji, **Aoki, Osamu**, **Ogawa, Hiroshi**, **Muranaka, Shigeo**, and **Enomoto, Yoshiteru**. New combustion concept for ultra-clean and high-efficiency small di diesel engines. In *SAE Technical Paper*. SAE International, 10 1999. doi: 10.4271/1999-01-3681. URL http://dx.doi.org/10.4271/1999-01-3681.

Kimura, Shuji, **Aoki, Osamu**, **Kitahara, Yasuhisa**, and **Aiyoshizawa, Eiji**. Ultra-clean combustion technology combining a low-temperature and premixed combustion concept for meeting future emission standards. In *SAE Technical Paper*. SAE International, 03 2001. doi: 10.4271/2001-01-0200. URL http://dx.doi.org/10.4271/2001-01-0200.

Kiplimo, Robert, **Tomita, Eiji**, **Kawahara, Nobuyuki**, and **Yokobe, Sumito**. Effects of spray impingement, injection parameters, and EGR on the combustion and emission characteristics of a PCCI diesel engine. *Appl. Therm. Eng.*, 37:165–175, 2012. ISSN 13594311. doi: 10.1016/j.applthermaleng.2011.11.011. URL http://dx.doi.org/10.1016/j.applthermaleng.2011.11.011.

Kitamura, Takaaki and **Ito, Takayuki**. Mixing-controlled, low temperature diesel combustion with pressure modulated multiple-injection for hsdi diesel engine. *SAE Int. J. Engines*, 3:461–478, 04 2010. doi: 10.4271/2010-01-0609. URL http://dx.doi.org/10.4271/2010-01-0609.

Knight, Bryan M., **Bittle, Joshua A.**, and **Jacobs, Timothy J.** Characterizing the influence of egr and fuel pressure on the emissions in low temperature diesel combustion. In *SAE Technical Paper*. SAE International, 04 2011. doi: 10.4271/2011-01-1354. URL http://dx.doi.org/10.4271/2011-01-1354.

Kokjohn, Sage L and **Reitz, Rolf D**. Ices2009-76030 Investigation of Design Parameters in Partially Premixed. *Differences*, pages 1–11, 2009. doi: 10.1115/ICES2009-76030.

Kondo, T and **Nakagawa, T**. A Numerical Simulation of Fuel Premixing for Pcci Combustion by Direct Injection. *Proc. Asme Power Conf. - 2011, Vol 1*, 2011(Power):153–159, 2012. doi: 10.1115/POWER2011-55380. URL {\T1\textless}GotoISI{\T1\textgreater}://WOS:000320008200021.

Kong, Song-Charng, **Han, Zhiyu**, and **Reitz, Rolf D.** The development and application of a diesel ignition and combustion model for multidimensional engine simulation. In *SAE Technical Paper*. SAE International, 02 1995. doi: 10.4271/950278. URL http://dx.doi.org/10.4271/950278.

Kook, Sanghoon, **Bae, Choongsik**, **Miles, Paul C.**, **Choi, Dae**, and **Pickett, Lyle M.** The influence of charge dilution and injection timing on low-temperature diesel combustion and emissions. In *SAE Technical Paper*. SAE International, 10 2005. doi: 10.4271/2005-01-3837. URL http://dx.doi.org/10.4271/2005-01-3837.

Krestinin, A.V. Detailed modeling of soot formation in hydrocarbon pyrolysis. *Combustion and Flame*, 121(3):513 – 524, 2000. ISSN 0010-2180. doi: http://dx.doi.org/10.1016/S0010-2180(99)00167-4. URL http://www.sciencedirect.com/science/article/pii/S0010218099001674.

Kulkarni, Anup M., **Stricker, Karla C.**, **Blum, Angeline**, and **Shaver, Gregory M.** Pcci control authority of a modern diesel engine outfitted with flexible intake valve actuation. In *SAE Technical Paper*. SAE International, 06 2009. doi: 10.4271/2009-01-1882. URL http://dx.doi.org/10.4271/2009-01-1882.

Kulzer, Andre, **Nier, Tobias**, and **Karrelmeyer, Roland**. A thermodynamic study on boosted hcci: Experimental results. In *SAE Technical Paper*. SAE International, 04 2011. doi: 10.4271/2011-01-0905. URL http://dx.doi.org/10.4271/2011-01-0905.

Kumar, Pravin and **Rehman, A.** Bio-diesel in homogeneous charge compression ignition (HCCI) combustion. *Renew. Sustain. Energy Rev.*, 56:536–550, 2016. ISSN 18790690. doi: 10.1016/j.rser.2015.11.088. URL http://dx.doi.org/10.1016/j.rser.2015.11.088.

Kumar, Raj and **Zheng, Ming**. Fuel efficiency improvements of low temperature combustion diesel engines. In *SAE Technical Paper*. SAE International, 04 2008. doi: 10.4271/2008-01-0841. URL http://dx.doi.org/10.4271/2008-01-0841.

Kutlar, O.A. Dört zamanlı otto (rochas) Çevrimli motorlarda kısmi yükte yakıt tüketimini azaltmak İçin yeni bir yöntem. 1998.

Lam, SH. Reduced chemistry modeling and sensitivity analysis. *lecture notes for Aerothermochemistry for Hypersonic Technology*, 1995:3, 1994.

Lechner, Guntram A., **Jacobs, Timothy J.**, **Chryssakis, Christos A.**, **Assanis, Dennis N.**, and **Siewert, Robert M.** Evaluation of a narrow spray cone angle, advanced injection timing strategy to achieve partially premixed compression ignition combustion in a diesel engine. In *SAE Technical Paper*. SAE International, 04 2005. doi: 10.4271/2005-01-0167. URL http://dx.doi.org/10.4271/2005-01-0167.

Lee, Sangsuk and **Reitz, Rolf D.** Spray targeting to minimize soot and co formation in premixed charge compression ignition (pcci) combustion with a hsdi diesel engine. In *SAE Technical Paper*. SAE International, 04 2006. doi: 10.4271/2006-01-0918. URL http://dx.doi.org/10.4271/2006-01-0918.

Lee, Sunyoup, **Oh, Seungmook**, **Kim, Junghwan**, and **Kim, Duksang**. Icef2014-5406 Enhancing Low Temperature Combustion With Biodiesel Blending in. *ASME Intern. Combust. Engine Fall 2014*, pages 1–11, 2014.

Leermakers, C.A.J., **Luijten, C.C.M.**, **Somers, L.M.T.**, **Kalghatgi, G.T.**, and **Albrecht, B.A.** Experimental study of fuel composition impact on pcci combustion in a heavy-duty diesel engine. In *SAE Technical Paper*. SAE International, 04 2011. doi: 10.4271/2011-01-1351. URL http://dx.doi.org/10.4271/2011-01-1351.

Li, Hailin, **Neill, W. Stuart**, **Chippior, Wally**, **Graham, Lisa**, **Connolly, Trevor**, and **Taylor, Joshua D.** An experimental investigation on the emission characteristics of hcci engine operation using n-heptane. In *SAE Technical Paper*. SAE International, 07 2007a. doi: 10.4271/2007-01-1854. URL http://dx.doi.org/10.4271/2007-01-1854.

Li, Tie, **Izumi, Hiroyuki**, **Shudo, Toshio**, **Ogawa, Hideyuki**, and **Okabe, Yukihiro**. Characterization of low temperature diesel combustion with various dilution gases.

In *SAE Technical Paper*. SAE International, 04 2007b. doi: 10.4271/2007-01-0126. URL http://dx.doi.org/10.4271/2007-01-0126.

Li, Tie, **Suzuki, Masaru**, and **Ogawa, Hideyuki**. Characteristics of smokeless low temperature diesel combustion in various fuel-air mixing and expansion of operating load range. In *SAE Technical Paper*. SAE International, 04 2009. doi: 10.4271/2009-01-1449. URL http://dx.doi.org/10.4271/2009-01-1449.

Liu, Alex B, **Mather, Daniel**, and **Reitz, Rolf D**. Modeling the effects of drop drag and breakup on fuel sprays. Technical report, DTIC Document, 1993.

Liu, Bei, **Cheng, Xiaobei**, **Qiu, Liang**, **Dong, Shijun**, and **Wang, Xin**. Numerical simulation and experimental research on ppc combustion and emissions characteristics of diesel engine. In *SAE Technical Paper*. SAE International, 04 2015. doi: 10.4271/2015-01-0401. URL http://dx.doi.org/10.4271/2015-01-0401.

Lu, Yingying, **Yu, Wenbin**, and **Su, Wanhua**. Using multiple injection strategies in diesel pcci combustion: Potential to extend engine load, improve trade-off of emissions and efficiency. In *SAE Technical Paper*. SAE International, 04 2011. doi: 10.4271/2011-01-1396. URL http://dx.doi.org/10.4271/2011-01-1396.

Maas, U. and **Pope, S.B.** Simplifying chemical kinetics: Intrinsic low-dimensional manifolds in composition space. *Combustion and Flame*, 88(3):239 – 264, 1992. ISSN 0010-2180. doi: http://dx.doi.org/10.1016/0010-2180(92)90034-M. URL http://www.sciencedirect.com/science/article/pii/001021809290034M.

Magnussen, B.F. and **Hjertager, B.H.** On mathematical modeling of turbulent combustion with special emphasis on soot formation and combustion. *Symposium (International) on Combustion*, 16(1):719 – 729, 1977. ISSN 0082-0784. doi: http://dx.doi.org/10.1016/S0082-0784(77)80366-4. URL http://www.sciencedirect.com/science/article/pii/S0082078477803664.

Makkapati, Satheesh and **Curtis, Eric W.** Boosted hcci - experimental observations in a single cylinder engine. In *SAE Technical Paper*. SAE International, 04

2014. doi: 10.4271/2014-01-1277. URL http://dx.doi.org/10.4271/2014-01-1277.

Mancaruso, Ezio and **Vaglieco, Bianca Maria**. Characterization of pcci combustion in a single cylinder ci engine fuelled with rme and bio-ethanol. In *SAE Technical Paper*. SAE International, 04 2013. doi: 10.4271/2013-01-1672. URL http://dx.doi.org/10.4271/2013-01-1672.

Masuda, Yutaka and **Chen, Zhili**. Combustion and emission characteristics of a pci engine fueled with ethanol-diesel blends. In *SAE Technical Paper*. SAE International, 06 2009. doi: 10.4271/2009-01-1854. URL http://dx.doi.org/10.4271/2009-01-1854.

Mathivanan, K., **J. M. Mallikarjuna**, and **Ramesh, A.** Influence of multiple fuel injection strategies on performance and combustion characteristics of a diesel fuelled HCCI engine – An experimental investigation. *Exp. Therm. Fluid Sci.*, 77:337–346, 2016. ISSN 08941777. doi: 10.1016/j.expthermflusci.2016.05.010. URL http://linkinghub.elsevier.com/retrieve/pii/S0894177716301261.

Maurya, Rakesh Kumar and **Agarwal, Avinash Kumar**. Combustion and emission behavior of ethanol fuelled homogeneous charge compression ignition (hcci) engine. In *SAE Technical Paper*. The Automotive Research Association of India, 01 2008. doi: 10.4271/2008-28-0064. URL http://dx.doi.org/10.4271/2008-28-0064.

McTaggart-Cowan, G. P., **Cong, S.**, **Garner, C. P.**, **Wahab, E.**, and **Peckham, M.** Experimental Study of Low Temperature Diesel Combustion Sensitivity to Engine Operating Parameters. *J. Eng. Gas Turbines Power*, 134(8):082805, 2012. ISSN 07424795. doi: 10.1115/1.4006377. URL http://gasturbinespower.asmedigitalcollection.asme.org/article.aspx?articleid=1430080.

Mendez, Sylvain, **Kashdan, Julian T.**, **Bruneaux, Gilles**, **Thirouard, Benoist**, and **Vangraefschepe, Franck**. Formation of unburned hydrocarbons in low temperature

diesel combustion. *SAE Int. J. Engines*, 2:205–225, 11 2009. doi: 10.4271/2009-01-2729. URL http://dx.doi.org/10.4271/2009-01-2729.

Michailidis, a. D., **Stobart, R. K.**, and **McTaggart-Cowan, G. P.** Low Temperature Combustion Optimization and Cycle-by-Cycle Variability Through Injection Optimization and Gas-to-Liquid Fuel-Blend Ratio. *J. Eng. Gas Turbines Power*, 135(7):071504, 2013. ISSN 0742-4795. doi: 10.1115/1.4024090. URL http://gasturbinespower.asmedigitalcollection.asme.org/article.aspx?doi=10.1115/1.4024090.

Mochizuki, Keisuke, **Shima, Takahiro**, **Suzuki, Hirotaka**, **Ishikawa, Yoshihiro**, **Iijima, Akira**, **Yoshida, Koji**, and **Shoji, Hideo**. A study of supercharged hcci combustion using blended fuels of propane and dme. In *SAE Technical Paper*. SAE International, 11 2014. doi: 10.4271/2014-32-0005. URL http://dx.doi.org/10.4271/2014-32-0005.

Munehiro Matsuishi, Yasuhide Abe, Yuya Higuchi, **Yuma Ishizawa, Akira Iijima**, **Hideo Shoji, Hiraku Kojima, Kazuhito Misawa**, and **Nakama, Kenjiro**. Experimental and Numerical Study of HCCI Combustion using Cooled EGR. *SAE Technical Paper*, SETC2015, 2015. ISSN 0148-7191.

Musculus, Mark P. B., **Lachaux, Thierry**, **Pickett, Lyle M.**, and **Idicheria, Cherian A.** End-of-injection over-mixing and unburned hydrocarbon emissions in low-temperature-combustion diesel engines. In *SAE Technical Paper*. SAE International, 04 2007. doi: 10.4271/2007-01-0907. URL http://dx.doi.org/10.4271/2007-01-0907.

Naber, Jeffrey and **Reitz, Rolf D**. Modeling engine spray/wall impingement. Technical report, SAE Technical Paper, 1988.

Nagle, J and **Constable, S.RF**. Oxidation of carbon between 1000-2000 c. In *Proceedings of the fifth carbon conference*, volume 1, page 154. Pergamon Oxford, 1962.

Najafabadi, Mohammad Izadi, **Dam, Nico**, **Somers, Bart**, and **Johansson, Bengt**. Ignition sensitivity study of partially premixed combustion by using shadowgraphy and oh* chemiluminescence methods. In *SAE Technical Paper*. SAE International,

04 2016. doi: 10.4271/2016-01-0761. URL http://dx.doi.org/10.4271/2016-01-0761.

Najt, Paul M. and **Foster, David E.** Compression-ignited homogeneous charge combustion. In *SAE Technical Paper*. SAE International, 02 1983. doi: 10.4271/830264. URL http://dx.doi.org/10.4271/830264.

Nakagome, Keiichi, **Shimazaki, Naoki**, **Niimura, Keiichi**, and **Kobayashi, Shinji**. Combustion and emission characteristics of premixed lean diesel combustion engine. In *SAE Technical Paper*. SAE International, 02 1997. doi: 10.4271/970898. URL http://dx.doi.org/10.4271/970898.

NASA, Glenn Research Center. Technical report, May 2015.

Northrop, William F., **Bohac, Stanislav V.**, and **Assanis, Dennis N.** Premixed low temperature combustion of biodiesel and blends in a high speed compression ignition engine. *SAE Int. J. Fuels Lubr.*, 2:28–40, 04 2009. doi: 10.4271/2009-01-0133. URL http://dx.doi.org/10.4271/2009-01-0133.

Ogawa, Hideyuki, **Miyamoto, Noboru**, **Kaneko, Naoya**, and **Ando, Hirokazu**. Combustion control and operating range expansion in an hcci engine with selective use of fuels with different low-temperature oxidation characteristics. In *SAE Technical Paper*. SAE International, 05 2003. doi: 10.4271/2003-01-1827. URL http://dx.doi.org/10.4271/2003-01-1827.

Ogawa, Hideyuki, **Setiapraja, Hari**, and **Nakamura, Toshihiro**. Improvements to premixed diesel combustion with ignition inhibitor effects of premixed ethanol by intake port injection. In *SAE Technical Paper*. SAE International, 04 2010. doi: 10.4271/2010-01-0866. URL http://dx.doi.org/10.4271/2010-01-0866.

Ogawa, Hiroshi, **Kimura, Shuji**, **Koike, Masao**, and **Enomoto, Yoshiteru**. A study of heat rejection and combustion characteristics of a low-temperature and pre-mixed combustion concept based on measurement of instantaneous heat flux in a direct-injection diesel engine. In *SAE Technical Paper*. SAE International, 10 2000. doi: 10.4271/2000-01-2792. URL http://dx.doi.org/10.4271/2000-01-2792.

Okude, Keiichi, **Mori, Kazutoshi**, **Shiino, Shiroh**, and **Moriya, Takeshi**. Premixed compression ignition (pci) combustion for simultaneous reduction of nox and soot in diesel engine. In *SAE Technical Paper*. SAE International, 06 2004. doi: 10.4271/2004-01-1907. URL http://dx.doi.org/10.4271/2004-01-1907.

Park, Su Han, **Yoon, Seung Hyun**, and **Lee, Chang Sik**. HC and CO emissions reduction by early injection strategy in a bioethanol blended diesel-fueled engine with a narrow angle injection system. *Appl. Energy*, 107(x):81–88, 2013. ISSN 03062619. doi: 10.1016/j.apenergy.2013.02.015. URL http://dx.doi.org/10.1016/j.apenergy.2013.02.015.

Park, Youngsoo and **Bae, Choongsik**. Effects of single and double post injections on diesel pcci combustion. In *SAE Technical Paper*. SAE International, 03 2013. doi: 10.4271/2013-01-0010. URL http://dx.doi.org/10.4271/2013-01-0010.

Patankar, Suhas. *Numerical heat transfer and fluid flow*. CRC press, 1980.

Patankar, Suhas V and **Spalding, D Brian**. A calculation procedure for heat, mass and momentum transfer in three-dimensional parabolic flows. *International journal of heat and mass transfer*, 15(10):1787–1806, 1972.

Patterson, Mark A. and **Reitz, Rolf D.** Modeling the effects of fuel spray characteristics on diesel engine combustion and emission. In *SAE Technical Paper*. SAE International, 02 1998. doi: 10.4271/980131. URL http://dx.doi.org/10.4271/980131.

Peng, Zhijun, **Zhao, Hua**, and **Ladommatos, Nicos**. Effects of air/fuel ratios and egr rates on hcci combustion of n-heptane, a diesel type fuel. In *SAE Technical Paper*. SAE International, 03 2003. doi: 10.4271/2003-01-0747. URL http://dx.doi.org/10.4271/2003-01-0747.

Persson, Håkan, **Agrell, Mats**, **Olsson, Jan-Ola**, **Johansson, Bengt**, and **Ström, Hans**. The effect of intake temperature on hcci operation using negative valve overlap. In *SAE Technical Paper*. SAE International, 03 2004. doi: 10.4271/2004-01-0944. URL http://dx.doi.org/10.4271/2004-01-0944.

Pickett, Lyle M. and **Siebers, Dennis L.** Non-sooting, low flame temperature mixing-controlled di diesel combustion. In *SAE Technical Paper*. SAE International, 03 2004. doi: 10.4271/2004-01-1399. URL http://dx.doi.org/10.4271/2004-01-1399.

Poinsot, Thierry and **Veynante, Denis**. *Theoretical and numerical combustion*. RT Edwards, Inc., 2005.

Polat, Seyfi. An experimental study on combustion, engine performance and exhaust emissions in a HCCI engine fuelled with diethyl ether-ethanol fuel blends. *Fuel Process. Technol.*, 143:140–150, 2016. ISSN 03783820. doi: 10.1016/j.fuproc.2015.11.021.

Polifke, W. Fundamental and practical limitations of no, reduction in lean-premixed combustion, presented at euroconference—premixed turbulent combustion: Introduction to the state of the art, aachen. 1995.

Ra, Y and **Reitz, R**. Numerical Study of Fuel Composition Effects on Low Temperature Diesel Combustion With a Discrete Multi-Component Vaporization Model. *Asme Ices2009*, pages 1–11, 2009.

Rajput, RK. *Internal combustion engines*. Laxmi Publications, 2005.

Ranz, WE and **Marshall, WR**. Evaporation from drops. *Chemical Engineering Progress*, 48(3):141446, 1952.

Renganathan, Manimaran and **Rajagopal, Thundil Karuppa Raj**. Computational study of hcci-di combustion at preheated and supercharged inlet air conditions. In *SAE Technical Paper*. SAE International, 04 2014. doi: 10.4271/2014-01-1108. URL http://dx.doi.org/10.4271/2014-01-1108.

Richard, S., **Colin, O.**, **Vermorel, O.**, **Benkenida, A.**, **Angelberger, C.**, and **Veynante, D.** Towards large eddy simulation of combustion in spark ignition engines. *Proceedings of the Combustion Institute*, 31(2):3059 – 3066, 2007. ISSN 1540-7489. doi: http://dx.doi.org/10.1016/j.proci.2006.07.086. URL http://www.sciencedirect.com/science/article/pii/S1540748906001040.

Saravanan, S., **Pitchandi, K.**, and **Suresh, G.** An experimental study on premixed charge compression ignition-direct ignition engine fueled with ethanol and gasohol. *Alexandria Eng. J.*, 54(4):897–904, 2015. ISSN 11100168. doi: 10.1016/j.aej.2015.07.010. URL http://dx.doi.org/10.1016/j.aej.2015.07.010.

Sasaki, Ito T., S. and **Iguchi, S.** "Smoke-less Rich Combustion by Low Temperature Oxidation in Diesel Engines. *Proceedings of the 9th Aachener Kolloquium Fahrzeug- und Motorentechnik 2000, Aachen, Germany.*, 2000, 2000.

Sharma, Priybrat and **Dhar, Atul**. Development of chemical kinetics based hydrogen HCCI combustion model for parametric investigation. *Int. J. Hydrogen Energy*, 41 (14):6148–6154, 2016. ISSN 03603199. doi: 10.1016/j.ijhydene.2015.12.021. URL http://dx.doi.org/10.1016/j.ijhydene.2015.12.021.

Shen, Mengqin, **Tuner, Martin**, and **Johansson, Bengt**. Close to stoichiometric partially premixed combustion -the benefit of ethanol in comparison to conventional fuels. In *SAE Technical Paper*. SAE International, 04 2013a. doi: 10.4271/2013-01-0277. URL http://dx.doi.org/10.4271/2013-01-0277.

Shen, Mengqin, **Tuner, Martin**, **Johansson, Bengt**, and **Cannella, William**. Effects of EGR and Intake Pressure on PPC of Conventional Diesel, Gasoline and Ethanol in a Heavy Duty Diesel Engine. *SAE Tech. Pap.*, 01(X), 2013b. doi: 10.4271/2013-01-2702. URL http://dx.doi.org/10.4271/2013-01-2702.

Shibata, Gen and **Ogawa, Hideyuki**. Hcci combustion control by dme-ethanol binary fuel and egr. In *SAE Technical Paper*. SAE International, 09 2012. doi: 10.4271/2012-01-1577. URL http://dx.doi.org/10.4271/2012-01-1577.

Shibata, Gen and **Urushihara, Tomonori**. Auto-ignition characteristics of hydrocarbons and development of hcci fuel index. In *SAE Technical Paper*. SAE International, 04 2007. doi: 10.4271/2007-01-0220. URL http://dx.doi.org/10.4271/2007-01-0220.

Shibata, Gen, **Oyama, Koji**, **Urushihara, Tomonori**, and **Nakano, Tsuyoshi**. The effect of fuel properties on low and high temperature heat release and resulting performance of an hcci engine. In *SAE Technical Paper*. SAE International, 03

2004. doi: 10.4271/2004-01-0553. URL http://dx.doi.org/10.4271/2004-01-0553.

Singh, Akhilendra Pratap and **Agarwal, Avinash Kumar**. Effect of intake charge temperature and egr on biodiesel fuelled hcci engine. In *SAE Technical Paper*. SAE International, 02 2016. doi: 10.4271/2016-28-0257. URL http://dx.doi.org/10.4271/2016-28-0257.

Soloiu, Valentin, **Duggan, Marvin**, **Ochieng, Henry**, **Williams, David**, **Molina, Gustavo**, and **Vlcek, Brian**. Investigation of Low Temperature Combustion Regimes of Biodiesel With n-Butanol Injected in the Intake Manifold of a Compression Ignition Engine. *J. Energy Resour. Technol.*, 135(4):41101, 2013. ISSN 0195-0738. doi: 10.1115/1.4023743.

Song, Hyunwoo and **Song, Soonho**. Predicting performance of a methane-fueled HCCI engine with hydrogen addition considering knock resistance. *Int. J. Hydrogen Energy*, 40(45):15749–15759, 2015. ISSN 03603199. doi: 10.1016/j.ijhydene.2015.09.019. URL http://dx.doi.org/10.1016/j.ijhydene.2015.09.019.

Spalding, D Brian. *Combustion and Mass Transfer: a textbook with multiple-choice exercises for engineering students*. Elsevier, 2013.

Su, Wanhua, **Lu, Yingying**, **Yu, Wenbin**, **Wang, Changqing**, **Pei, Yiqiang**, **Sun, Yongliang**, **Li, Yunqiang**, **Yu, Zhongfu**, and **Wang, Jinfeng**. High density-low temperature combustion in diesel engine based on technologies of variable boost pressure and intake valve timing. In *SAE Technical Paper*. SAE International, 06 2009. doi: 10.4271/2009-01-1911. URL http://dx.doi.org/10.4271/2009-01-1911.

Sundararajan, Karthikayan, **Janathanan, Krishnaraj**, **Pandian, Vasanthakumar**, **Dhandapani, Madhankumar**, and **Kanagara, Kalaiyarasan**. A performance, combustion and emission study on hcci engine: Trends and innovations. In *SAE Technical Paper*. SAE International, 02 2016. doi: 10.4271/2016-28-0013. URL http://dx.doi.org/10.4271/2016-28-0013.

Takahiro Shima, Hirotaka Suzuki Keisuke Mochizuki Akira Iijima Koji Yoshida Hideo Shoji, Yuki Takamura. Influence of combustion chamber wall temperature on combustion in an hcci engine using an alternative fuel. In *SAE Technical Paper*. SAE International, 04 2015.

Takashi Shimada, Chibin Rin Masanori Yamada Naoya Ito Akira Iijima Koji Yoshida Hideo Shoji, Yuki Yoshida. Influence of internal egr on knocking in an hcci engine. In *SAE Technical Paper*. SAE International, 04 2015.

Takeda, Yoshinaka, **Keiichi, Nakagome**, and **Keiichi, Niimura**. Emission characteristics of premixed lean diesel combustion with extremely early staged fuel injection. In *SAE Technical Paper*. SAE International, 05 1996. doi: 10.4271/961163. URL http://dx.doi.org/10.4271/961163.

Tanov, Slavey, **Collin, Robert**, **Johansson, Bengt**, and **Tuner, Martin**. Combustion stratification with partially premixed combustion, ppc, using nvo and split injection in a ld - diesel engine. *SAE Int. J. Engines*, 7:1911–1919, 10 2014. doi: 10.4271/2014-01-2677. URL http://dx.doi.org/10.4271/2014-01-2677.

Taritas, Ivan, **Kozarac, Darko**, and **Sjeric, Momir**. Numerical study of boosting configurations and valve strategies for high load hcci engine in wide range of engine speed. In *SAE Technical Paper*. SAE International, 04 2014. doi: 10.4271/2014-01-1267. URL http://dx.doi.org/10.4271/2014-01-1267.

Tatschl, R, **Pachler, K**, **Fuchs, H**, and **Almer, W**. Multidimensional simulation of diesel engine combustion-modeling and experimental verification. In *Proceedings of the Fifth Conference'The Working Process of the Internal Combustion Engine', Graz, Austria*, 1995.

Tesner, PA, **Smegiriova, TD**, and **Knorre, VG**. Kinetics of dispersed carbon formation. *Combustion and Flame*, 17(2):253–260, 1971.

Theobald, M. A. and **Cheng, W. K**. A numerical study of diesel ignition. *ASME Energy Sources Technology Conference*, ASME Paper 87-FE-2, February 1987.

Thring, R. H. Homogeneous-charge compression-ignition (hcci) engines. In *SAE Technical Paper*. SAE International, 09 1989. doi: 10.4271/892068. URL http://dx.doi.org/10.4271/892068.

Tompkins, Brandon T., **Song, Hoseok**, and **Jacobs, Timothy J.** Low temperature heat release of palm and soy biodiesel in late injection low temperature combustion. *SAE Int. J. Fuels Lubr.*, 7:106–115, 04 2014. doi: 10.4271/2014-01-1381. URL http://dx.doi.org/10.4271/2014-01-1381.

Torregrosa, A. J., **Broatch, A.**, **Garcia, A.**, and **M??nico, L. F.** Sensitivity of combustion noise and NOx and soot emissions to pilot injection in PCCI Diesel engines. *Appl. Energy*, 104(x):149–157, 2013. ISSN 03062619. doi: 10.1016/j.apenergy.2012.11.040. URL http://dx.doi.org/10.1016/j.apenergy.2012.11.040.

Tsujimura, Taku, **Oguma, Mitsuharu**, and **Goto, Shinichi**. A study of fuel auto-ignitability on premixed compression ignition characteristics. In *SAE Technical Paper*. SAE International, 04 2008. doi: 10.4271/2008-01-0062. URL http://dx.doi.org/10.4271/2008-01-0062.

Tsurushima, Tadashi, **Harada, Akira**, **Iwashiro, Yuki**, **Enomoto, Yoshiteru**, **Asaumi, Yasuo**, and **Aoyagi, Yuzo**. Thermodynamic characteristics of premixed compression ignition combustions. In *SAE Technical Paper*. SAE International, 05 2001. doi: 10.4271/2001-01-1891. URL http://dx.doi.org/10.4271/2001-01-1891.

Valentino, Gerardo, **Corcione, Felice**, **Iannuzzi, Stefano**, and **Serra, Simone**. Effects of premixed low temperature combustion of fuel blends with high resistance to auto-ignition on performances and emissions in a high speed diesel engine. In *SAE Technical Paper*. SAE International, 09 2011. doi: 10.4271/2011-24-0049. URL http://dx.doi.org/10.4271/2011-24-0049.

Valentino, Gerardo, **Corcione, Felice E.**, **Iannuzzi, Stefano**, and **Serra, Simone**. An experimental analysis on diesel/n-butanol blends operating in partial premixed combustion in a light duty diesel engine. In *SAE Technical Paper*. SAE International, 04 2012. doi: 10.4271/2012-01-1127. URL http://dx.doi.org/10.4271/2012-01-1127.

Veltman, Matthias K., **Karra, Prashanth K.**, and **Kong, Song-Charng**. Effects of biodiesel blends on emissions in low temperature diesel combustion. In *SAE*

Technical Paper. SAE International, 04 2009. doi: 10.4271/2009-01-0485. URL http://dx.doi.org/10.4271/2009-01-0485.

Versteeg, Henk Kaarle and **Malalasekera, Weeratunge**. *An introduction to computational fluid dynamics: the finite volume method*. Pearson Education, 2007.

Wang, Buyu, **Shuai, Shi-Jin**, **Yang, Hong-Qiang**, **Wang, Zhi**, **Wang, Jian-Xin**, and **Xu, Hongming**. Experimental study of multiple premixed compression ignition engine fueled with heavy naphtha for high efficiency and low emissions. In *SAE Technical Paper*. SAE International, 10 2014. doi: 10.4271/2014-01-2678. URL http://dx.doi.org/10.4271/2014-01-2678.

Wang, Hai and **Frenklach, Michael**. A detailed kinetic modeling study of aromatics formation in laminar premixed acetylene and ethylene flames. *Combustion and Flame*, 110(1):173 – 221, 1997. ISSN 0010-2180. doi: http://dx.doi.org/10.1016/S0010-2180(97)00068-0. URL http://www.sciencedirect.com/science/article/pii/S0010218097000680.

Wang, Zhenkan, **Tanov, Slavey**, **Wang, Hua**, **Richter, Mattias**, **Johansson, Bengt**, and **Alden, Marcus**. High-speed particle image velocimetry measurement of partially premixed combustion (ppc) in a light duty engine for different injection strategies. In *SAE Technical Paper*. SAE International, 09 2015. doi: 10.4271/2015-24-2454. URL http://dx.doi.org/10.4271/2015-24-2454.

Wang, Zhi, **Liu, Haoye**, **Ma, Xiao**, **Wang, Jianxin**, **Shuai, Shijin**, and **Reitz, Rolf D.** Homogeneous charge compression ignition (HCCI) combustion of polyoxymethylene dimethyl ethers (PODE). *Fuel*, 183:206–213, 2016. ISSN 00162361. doi: 10.1016/j.fuel.2016.06.033. URL http://dx.doi.org/10.1016/j.fuel.2016.06.033.

Wendt, John. *Computational fluid dynamics: an introduction*. Springer Science & Business Media, 2008.

William, J. P. and **Charles, K. W.** Technical report, California, United States: Lawrence Livermore National Laboratory, 2011.

Xie, Hui, **Wei, Zhipeng**, **He, Bangquan**, and **Zhao, Hua**. Comparison of hcci combustion respectively fueled with gasoline, ethanol and methanol through the

trapped residual gas strategy. In *SAE Technical Paper*. SAE International, 04 2006. doi: 10.4271/2006-01-0635. URL http://dx.doi.org/10.4271/2006-01-0635.

Xie, Kelvin, **Yanai, Tadanori**, **Yang, Zhenyi**, **Reader, Graham**, and **Zheng, Ming**. Emission analysis of hcci combustion in a diesel engine fueled by butanol. In *SAE Technical Paper*. SAE International, 04 2016. doi: 10.4271/2016-01-0749. URL http://dx.doi.org/10.4271/2016-01-0749.

Yin, Lianhao, **Ingesson, Gabriel**, **Shamun, Sam**, **Tunestal, Per**, **Johansson, Rolf**, and **Johansson, Bengt**. Sensitivity analysis of partially premixed combustion (ppc) for control purposes. In *SAE Technical Paper*. SAE International, 04 2015. doi: 10.4271/2015-01-0884. URL http://dx.doi.org/10.4271/2015-01-0884.

Yu, Hanzhengnan, **Guo, Yong**, **Li, Donghai**, **Liang, Xingyu**, **Shu, Ge-Qun**, **Wang, Yuesen**, **Wang, Xiangxiang**, and **Dong, Lihui**. Numerical investigation of the effect of spray cone angle on mixture formation and co/soot emissions in an early injection hcci diesel engine. In *SAE Technical Paper*. SAE International, 04 2015. doi: 10.4271/2015-01-1070. URL http://dx.doi.org/10.4271/2015-01-1070.

Yun, Hanho and **Reitz, Rolf D.** An Experimental Investigation on the Effect of Post-Injection Strategies on Combustion and Emissions in the Low-Temperature Diesel Combustion Regime. *J. Eng. Gas Turbines Power*, 129(1):279, 2007. ISSN 07424795. doi: 10.1115/1.2180812. URL http://gasturbinespower.asmedigitalcollection.asme.org/article.aspx?articleid=1424662.

Zeldovich, Y.B., **Sadovnikov, P.Y.**, and **Kamenetskii, D.A.F.** *Oxidation of nitrogen in combustion*. Translation by M. Shelef,Publishing House of the Acad of Sciences of USSR, 1947.

Zhang, F., **Liu, H.F.**, **Yu, J.**, and **Yao, M.** Direct numerical simulation of n-heptane/air auto-ignition with thermal and charge stratifications under partially-premixed charge compression ignition (PCCI) engine related conditions. *Appl. Therm. Eng.*,

104:516–526, 2016. ISSN 13594311. doi: 10.1016/j.applthermaleng.2016.05.100. URL http://linkinghub.elsevier.com/retrieve/pii/S1359431116307566.

Zhang, Yan, **He, Bang-Quan**, **Xie, Hui**, and **Zhao, Hua**. The combustion and emission characteristics of ethanol on a port fuel injection hcci engine. In *SAE Technical Paper*. SAE International, 04 2006. doi: 10.4271/2006-01-0631. URL http://dx.doi.org/10.4271/2006-01-0631.

Zheng, Zunqing, **Yao, Mingfa**, **Chen, Zheng**, and **Zhang, Bo**. Experimental study on hcci combustion of dimethyl ether(dme)/methanol dual fuel. In *SAE Technical Paper*. SAE International, 10 2004. doi: 10.4271/2004-01-2993. URL http://dx.doi.org/10.4271/2004-01-2993.

CURRICULUM VITAE



Name Surname: Mobin MAJIDI DOLAT ABADI

Place and Date of Birth: IRAN, 1987

E-Mail: majidi.mobin@yahoo.com

EDUCATION:

- **B.Sc.:** 2011, Mohaghegh Ardabili State University, Mechanical Engineering Department
- **M.Sc.:** 2016, Istanbul Technical University, Mechanical engineering Department